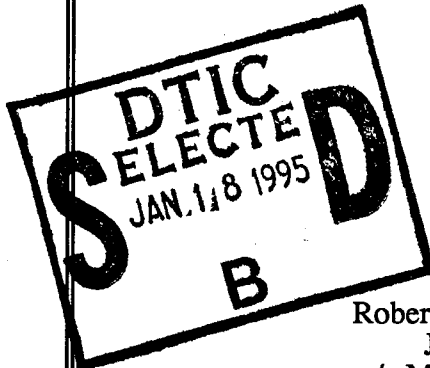


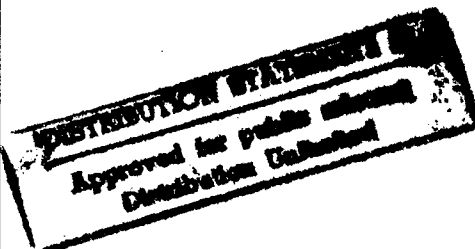
# Semiannual Technical Report

## Interface Properties of Wide Bandgap Semiconductor Structures

Supported under Grant #N00014-92-J-1477  
Office of the Chief of Naval Research  
Report for the period 7/1/94-12/31/94



Robert F. Davis, Salah Bedair,\* Jerry Bernholc,\*\*  
Jeffrey T. Glass and R. J. Nemanich\*\*  
c/o Materials Science and Engineering Department  
\*Electrical and Computer Engineering Department  
and \*\*Department of Physics  
North Carolina State University  
Campus Box 7907  
Raleigh, NC 27695-7907



DTIC QUALITY INSPECTED 3

December, 1994

19950117 030

# REPORT DOCUMENTATION PAGE

Form Approved  
OMB No. 0704-0188

Public reporting burden for this collection of information is estimated to average 1 hour per response, including the time for reviewing instructions, searching existing data sources, gathering and maintaining the data needed, and completing and reviewing the collection of information. Send comments regarding this burden estimate or any other aspect of this collection of information, including suggestions for reducing this burden to Washington Headquarters Services, Directorate for Information Operations and Reports, 1215 Jefferson Davis Highway, Suite 1204, Arlington, VA 22202-4302, and to the Office of Management and Budget Paperwork Reduction Project (0704-0188), Washington, DC 20503.

1. AGENCY USE ONLY (Leave blank)

2. REPORT DATE

December, 1994

3. REPORT TYPE AND DATES COVERED

Semiannual Technical 7/1/94-12/31/94

4. TITLE AND SUBTITLE

Interface Properties of Wide Bandgap Semiconductor Structures

5. FUNDING NUMBERS

uri41114a-01  
1114SS  
N00179  
N66005  
4B855

6. AUTHOR(S)

Robert F. Davis and R. J. Nemanich

7. PERFORMING ORGANIZATION NAME(S) AND ADDRESS(ES)

North Carolina State University  
Hillsborough Street  
Raleigh, NC 27695

8. PERFORMING ORGANIZATION  
REPORT NUMBER

N00014-92-J-1477

9. SPONSORING/MONITORING AGENCY NAMES(S) AND ADDRESS(ES)

Sponsoring: ONR, 800 N. Quincy, Arlington, VA 22217-5660  
Monitoring: Administrative Contracting Officer, Office of Naval Research  
Regional Office Atlanta, 101 Marietta Tower, Suite 2805  
101 Marietta Street  
Atlanta, GA 30332-0490

10. SPONSORING/MONITORING  
AGENCY REPORT NUMBER

11. SUPPLEMENTARY NOTES

12a. DISTRIBUTION/AVAILABILITY STATEMENT

Approved for Public Release; Distribution Unlimited

12b. DISTRIBUTION CODE

13. ABSTRACT (Maximum 200 words)

The initial stages of epitaxial growth of SiC on 6H-SiC substrates were studied by UHV STM. The results showed single bilayer undulating steps and stepped structures that were related to the annealing temperature. A new method of cleaning SiC based on silane exposure was developed, and the surfaces examined by UV photoemission showed the presence of surface electronic states. Gas source MBE growth of SiC on 2H-AlN indicated the potential of the formation of 2H-SiC, and doped 3C- and 6H-SiC have been grown on 6H-SiC. Pt films on 6H-SiC exhibited 1.26eV Schottky barrier with nearly ideal electrical properties. A planar RF system was developed for large area diamond deposition. Bias-enhanced nucleation of diamond on TiC(111) has been demonstrated. Theoretical studies of F-based ALE of diamond indicated that HF desorption is a crucial step. The negative electron affinity of H-terminated diamond was verified with combined theoretical and experimental studies. Future studies of NEA diamond surfaces will involve a new plasma system integrated into the UHV transfer line. A system for measuring electron emission has been designed. High purity GaN powder has been synthesized. ALE of GaN and InGaN has been analyzed to address several growth related difficulties. AlN and SiC/AlN pseudomorphic heterostructures have been grown by plasma assisted GSMBE. A computer controlled CVD system has been constructed for the growth of AlN, GaN and InN. OMVPE techniques have been used to prepare doped GaN monocrystalline thin films. A system has been designed for ECR deposition of the nitrides. Photo- and cathodo-luminescence of the nitrides displayed band edge and defect signatures. Theoretical studies indicated that the N vacancy in GaN acts as a shallow donor, and other deep levels were identified. Reactive ion etching of GaN and AlN was demonstrated. The electronic states of AlN/6H-SiC heterostructures indicated a negative electron affinity.

14. SUBJECT TERMS

diamond, 6H-SiC, 3C-SiC, 2H-SiC, AlN, GaN, InN, step structure, cleaning, Schottky barrier, negative electron affinity, defects, surface structure, ALE, gas source MBE, plasma assisted gas source MBE, CVD, plasma CVD, OMVPE, ECR-plasma CVD, reactive ion etching, UHV STM, angle resolved uv-photoemission, photoluminescence, cathodoluminescence, TEM

15. NUMBER OF PAGES

199

16. PRICE CODE

17. SECURITY CLASSIFICATION  
OF REPORT

UNCLAS

18. SECURITY CLASSIFICATION  
OF THIS PAGE

UNCLAS

19. SECURITY CLASSIFICATION  
OF ABSTRACT

UNCLAS

20. LIMITATION OF ABSTRACT

SAR

## Table of Contents

I.	Introduction	1
	<b>Carbon-based Materials</b>	
II.	Scanning Tunneling Microscopy of Vicinal and On-axis Surfaces of Epitaxial 6H-SiC (0001) Films <i>S. Tanaka and R. F. Davis</i>	3
III.	Silane Plasma and CVD Preparation of 6H SiC Surfaces for Growth of Epitaxial Films <i>M. C. Benjamin, R. S. Kern, S. W. King, R. F. Davis, and R. J. Nemanich</i>	8
IV.	Growth of 2H-Silicon Carbide using Pseudomorphic 2H-Aluminum Nitride Layer on 6H-Silicon Carbide Substrates by Gas-source Molecular Beam Epitaxy <i>S. Tanaka and R. F. Davis</i>	13
V.	Growth of SiC Thin Films by Gas-Source Molecular Beam Epitaxy and Their Electrical Characterization <i>S. Kern and R. F. Davis</i>	19
VI.	Chemistry, Microstructure, and Electrical Properties at Interfaces between Thin Films of Platinum and Alpha (6H) Silicon Carbide (0001) <i>L. M. Porter and R. F. Davis</i>	24
VII.	Diamond Deposition Using a Planar Radio Frequency Inductively Coupled Plasma <i>S. P. Bozeman, D. A. Tucker, B. R. Stoner, W. M. Hooke and J. T. Glass</i>	39
VIII.	Bias-enhanced Nucleation of Highly Oriented Diamond on TiC(111) <i>M. McClure and J. T. Glass</i>	47
IX.	Fluorine-based Mechanisms for ALE Growth on Diamond (110) <i>M. G. Wensell, Z. Zhang and J. Bernholc</i>	52
X.	Surface Structures and Electron Affinities of Bare and Hydrogenated Diamond C(100) Surfaces <i>Z. Zhang, M. Wensell, and J. Bernholc</i>	65
XI.	Negative Electron Affinity Effects on H Plasma Exposed Diamond (100) Surfaces <i>P. Baumann and R. J. Nemanich</i>	86
XII.	Growth and Characterization of Homoepitaxial Diamond Negative Electron Affinity Surfaces <i>A. Sowers and R. J. Nemanich</i>	95
XIII.	Characterization of Electron Emission from Cold Cathode Emitters <i>B. Ward and R. J. Nemanich</i>	100
	<b>Nitrogen-based Materials</b>	
XIV.	High Purity Gallium Nitride Powder Synthesis for Bulk Crystal Growth Studies <i>C. Balkas and R. F. Davis</i>	105
XV.	Atomic Layer Epitaxy of GaN and GaInN <i>S. Bedair</i>	113

XVI.	Characterization of AlN and AlN-SiC Pseudomorphic Heterostructures on $\alpha(6H)$ -SiC(0001) Grown by Plasma-assisted, Gas-source Molecular Beam Epitaxy <i>S. Kern and R. F. Davis</i>	118
XVII.	Novel Computer-controlled CVD System for the Deposition and Doping of AlN, GaN, InN and Their Solid Solutions and Heterostructures of These Materials <i>D. Hanser and R. F. Davis</i>	124
XVIII.	Deposition, Doping and Characterization of OMVPE Grown GaN on Various SiC(0001) Substrates using High-temperature Monocrystalline AlN Buffer Layers <i>W. Weeks and R. F. Davis</i>	128
XIX.	Electron Cyclotron Resonance Growth of AlN, GaN, and InN <i>J. Christman and R. J. Nemanich</i>	137
XX.	Luminescence Studies of GaN, AlN, InN and Their Solid Solutions <i>B. Perry and R. F. Davis</i>	140
XXI.	Native Defects in Wurtzite GaN and AlN <i>P. Boguslawski, E. Briggs, T. A. White, M. G. Wensell and J. Bernholc</i>	148
XXII.	Theory of Native Defects and of Carbon Doping in Wurtzite GaN <i>P. Boguslawski, E. Briggs and J. Bernholc</i>	154
XXIII.	Reactive Ion Etching of GaN, AlN and InN <i>K. Gruss and R. F. Davis</i>	158
XXIV.	Contact Formation to n-type and p-type GaN <i>L. Smith and R. F. Davis</i>	169
XXV.	AlN/SiC Electronic Structures <i>M. C. Benjamin, R. S. Kern, S. W. King, R. F. Davis and R. J. Nemanich</i>	188
XXVI.	Distribution List	199

Accession For	
NTIS GRA&I	<input checked="" type="checkbox"/>
DTIC TAB	<input type="checkbox"/>
Unannounced	<input type="checkbox"/>
Justification	
By _____	
Distribution/_____	
Availability Codes	
Dist	Avail and/or Special
A-1	



## I. Introduction

Heteroepitaxy is the growth of a crystal (or a film) on a foreign crystalline substrate that determines its orientation. Such oriented growth requires that lattice planes in both materials have similar structure. In general, an epitaxial relationship is probable whenever the orientation of the substrate and overgrowth produces an interface with a highly coincident atomic structure having low interfacial energy relative to a random arrangement.

During the past decade, nonequilibrium techniques have been developed for the growth of epitaxial semiconductors, superconductors, insulators and metals which have led to new classes of artificially structured materials. In many cases, the films were deposited on substrates having a different chemistry from that of the film, and heteroepitaxy was achieved. Moreover, layered structures with a periodicity of a few atomic layers have also been produced by the sequential heteroepitaxial deposition of a film of one type on another. Metastable structures can be generated which possess important properties not present in equilibrium systems. A consideration of the materials under consideration for next generation electronic and optoelectronic devices, e.g., the III-V nitrides show that only a few of them can currently be grown in bulk, single crystal form having a cross-sectional area of  $>3\text{cm}^2$ . Thus other, commercially available substrates must be used. This introduces a new set of challenges for the successful growth of device quality films which are not present in homoepitaxial growth and which must be surmounted if these materials are to be utilized in device structures.

In addition to providing structures which do not exist in nature, applications of advanced heteroepitaxial techniques permit the growth of extremely high quality heterostructures involving semiconductors, metals, and insulators. These heterostructures offer the opportunity to study relationships between the atomic structure and the electrical properties of both the film itself and the interface between the two dissimilar materials. They also allow the study of epitaxial growth between materials exhibiting very different types (ionic, covalent, or metallic) of bonding.

While the potential of heteroepitaxial deposition has been demonstrated, significant advances in theoretical understanding, experimental growth and control of this growth, and characterization are required to exploit the capabilities of this process route. It is particularly important to understand and control the principal processes which control heteroepitaxy at the atomic level. It is this type of research, as well as the chemistry of dry etching via laser and plasma processing, which forms the basis of the research in this grant.

The materials of concern in this report are classified as wide bandgap semiconductors and include diamond, the III-V nitrides, SiC, GaP and AlP. The extremes in electronic and thermal properties of diamond and SiC allow the types and numbers of current and conceivable applications of these materials to be substantial. However, a principal driving force for the interest in the III-V nitrides and GaP and AlP is their potential for solid-state optoelectronic

devices for light emission and detection from the visible through the far ultraviolet range of the spectrum.

The principal objectives of the research program are the determination of (1) the fundamental physical and chemical processes ongoing at the substrate surface and substrate/film interface during the heteroepitaxial deposition of both monocrystalline films of the materials noted above, as well as metal contacts on these materials, (2) the mode of nucleation and growth of the materials noted in (1) on selected substrates and on each other in the fabrication of multilayer heterostructures, (3) the resulting properties of the individual films and the layered structures and the effect of interfacial defects on these properties, (4) the development and use of theoretical concepts relevant to the research in objectives (1-3) to assist in the fabrication of improved films and structures and (5) the determination of process chemistry which leads to the laser assisted and plasma etching of these wide bandgap compound semiconductors.

This is the fifth bi-annual report since the initiation of the project. The following sections introduce each topic, detail the experimental approaches, report the latest results and provide a discussion and conclusion for each subject. Each major section is self-contained with its own figures, tables and references.

# Carbon-based Materials

## II. Scanning Tunneling Microscopy of Vicinal and On-axis Surfaces of Epitaxial 6H-SiC (0001) Films

### A. Introduction

Silicon carbide exists in >250 polytypes or stacking arrangements along the c-axis. The single cubic (zinc-blende) polytype is known as  $\beta$ - or 3C-SiC, where the 3 refers to the number of planes in the periodic sequence. The hexagonal (wurtzite) structure also occurs alone and in combination with 3C to form the remaining hexagonal or rhombohedral forms, known collectively as  $\alpha$ -SiC, of which 6H is the most common. It has become an important semiconductor material because of its considerable potential for high-temperature, -power and -frequency device applications [1]. Homoepitaxial growth of 6H and 4H thin films is now commonly reported because of the availability of wafers of these polytypes. Chemical vapor deposition (CVD) is the primary process route (for a review of this work for SiC see Ref. [1]); however, molecular beam epitaxy (MBE) [2, 3] has also been used, as in the case of the present research. Films of 6H-SiC can be deposited via step flow mechanism on vicinal 6H-SiC (0001) surfaces as a result of the closely spaced steps which allow the retention of the same stacking sequence as the substrate [4, 5]. In contrast, the wider terraces on the surfaces of on-axis 6H material are unfavorable for sufficient mass transport to the steps for step flow growth. Instead, the terraces become the areas on which occur the nucleation and growth of islands of the 3C polytype [5]. The 6H substrates are also being increasingly used for the epitaxial growth of AlN and GaN due to the small mismatches in lattice parameters relative to most other available substrates [6, 7]. The defect density observed in AlN films has been shown to be sensitive to the 6H surface structure [8]. As such, knowledge of the step/terrace configuration and surface reconstruction on 6H-SiC substrates is important, as they determine film characteristics as well as surface chemistries.

Low energy electron diffraction (LEED) has been employed to determine the surface reconstruction on 6H(0001) and 3C(001) surfaces as a function of temperature [see, e.g., Refs. [9, 10]. Ultra high vacuum scanning tunneling microscopy (UHV-STM) has been used to investigate both 3C(111) films deposited via CVD on 6H-SiC(0001) [11] and the C-terminated surfaces of bulk crystals derived via sublimation (Lely process) [12].

In this study we have observed for the first time via UHV STM both the vicinal ( $\sim 3.5^\circ$  off 6H-SiC(0001) towards  $\langle 11\bar{2}0 \rangle$ ) and on-axis, Si-terminated surfaces of 6H-SiC(0001) epitaxial layers having a thickness and donor carrier concentration of  $\sim 750 \text{ \AA}$  and  $\sim 6 \times 10^{17} \text{ cm}^{-3}$ , respectively, and grown commercially by CVD on 6H-SiC(0001) substrates. Each layer contained an  $\sim 1.5 \text{ mm}$  thick thermally grown  $\text{SiO}_2$  layer which acted both to remove the thin layer of C-containing material frequently present on the SiC film surface following the CVD process and to protect this surface prior to observation.

## B. Experimental

The oxide layer was removed prior to loading using a 10 % HF solution for 5-8 min. To obtain clean surfaces, the sample was desorbed at 400-550 °C for 2-14 hrs and annealed at 1000-1250 °C for 3-5 min. in an Omicron 1 STM chamber. The sample temperature was monitored using an optical pyrometer. The STM study was performed at room temperature. Tungsten tips and a tunneling current and bias of 0.3 nA and -3.5 V, respectively, were used to image the surface.

## C. Results and Discussion

Observations of the vicinal surface after annealing at 1150 °C for 3 min. revealed a strongly undulating step/terrace configuration, as shown in Fig. 1. Similar morphological features have been observed on GaAs film surfaces grown by metalorganic vapor phase epitaxy (MOVPE) at a relatively lower growth temperature compared to normal GaAs deposition temperatures [13]. Increasing the growth temperature of the latter material resulted in smoother step edges. It is

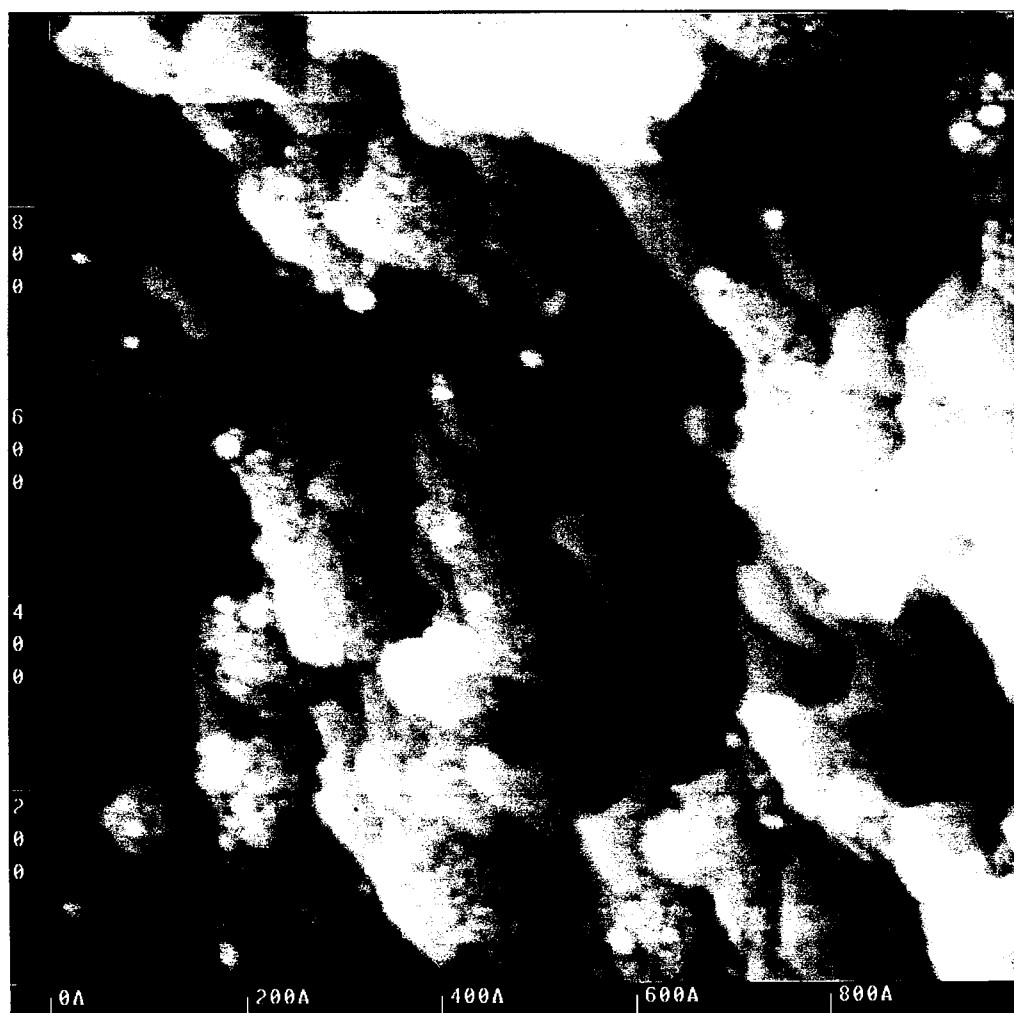


Figure 1. Surface feature of the vicinal 6H-SiC.

believed that the undulating step features are a result of insufficient surface diffusion lengths of adatoms. A honeycomb-like microstructure and contamination (white spots) were also observed on some terraces (see Fig. 1). The spots are believed to be residual silicon oxide which was not removed during the cleaning procedure. The cause of the honeycomb-like features will be discussed below in conjunction with surface chemistry. Most step heights were  $\sim 2.5$  Å corresponding to single bilayer steps consisting of one Si and one C layer. The  $(1\times 1)$  hexagonal surface crystallography could not be resolved using the imaging parameters of this study.

Relatively wider terraces separated primarily by single bilayer steps were observed on the on-axis surface of a sample after annealing at 1000 °C for 3 min. in UHV, as shown in Fig. 2. In general, the steps descend along the direction, possibly as a result of step flow growth of the epitaxial layer. Some terraces, contain single bilayer deep holes (black region), similar to the feature shown in 6H-SiC, in reference [12] as well as islands (white region) of SiC. No honeycomb-like features were observed.

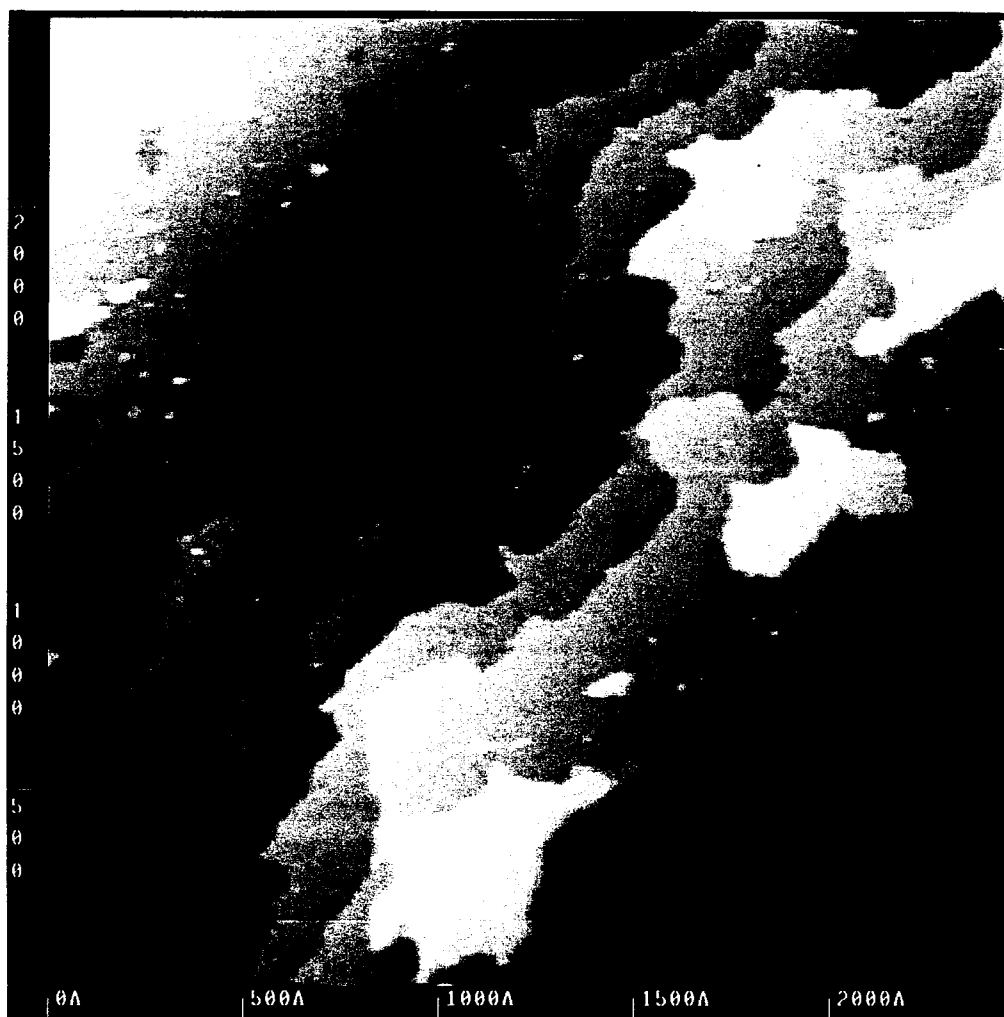


Figure 2. Surface feature of the on-axis 6H-SiC.

Figure 3 shows a high magnification image of a honeycomb-like feature observed on the on-axis terrace region after sequential annealing at 1000 °C and 1100 °C for 3 min. at each temperature in UHV. The unit cell of this structure was measured to be  $\sim 18.5$  Å. According to surface chemical studies on 6H-SiC(0001) by Auger electron spectroscopy (AES), surface graphitization begins to occur above 1027 °C [14]. A model of a graphite monolayer has been proposed by Chang, et al. [11] based on their STM observations, which is in agreement with the aforementioned AES analysis and our results. Therefore, the honey-comb-like structure is very likely the result of surface graphitization due to Si sublimation during annealing.

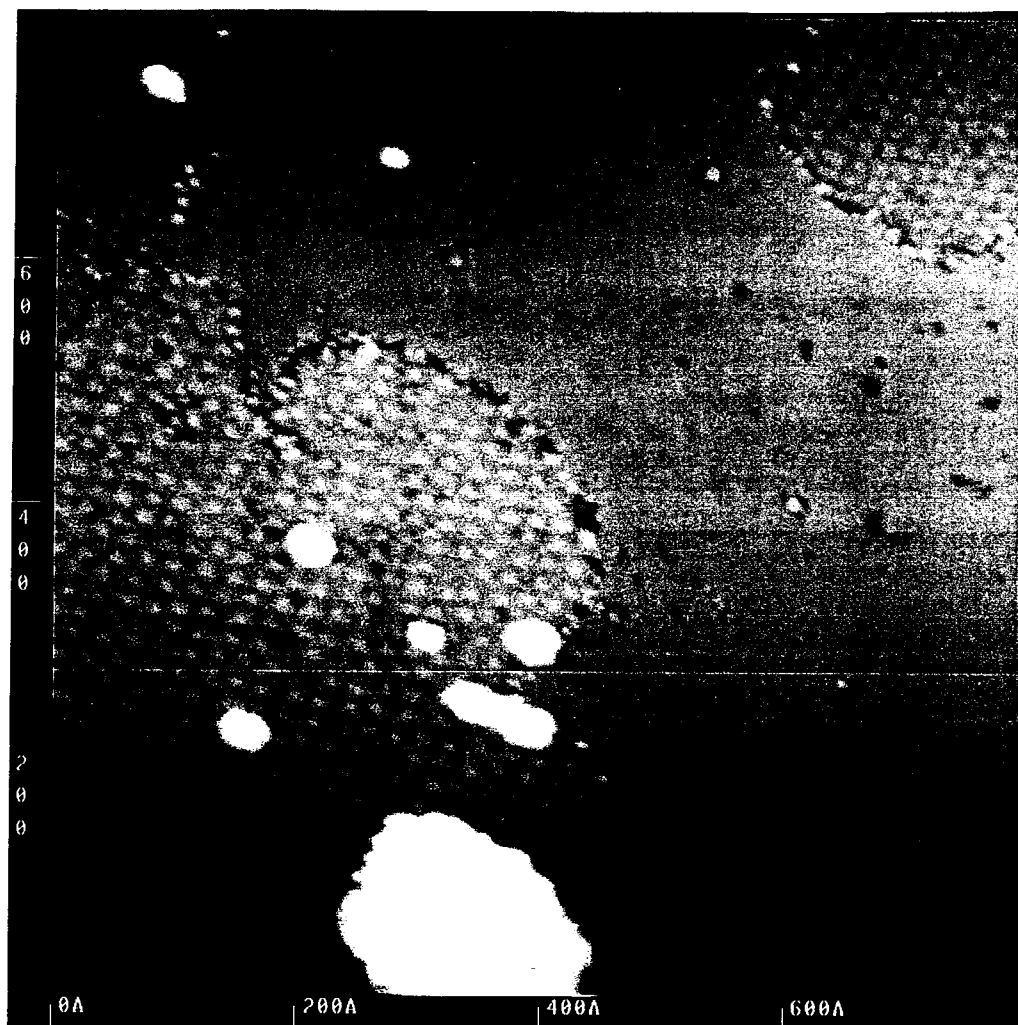


Figure 3. Honeycomb-like structure observed in the on-axis 6H-SiC substrate after annealed at 1100 °C

#### D. Conclusions

In summary, STM observations on the Si face of homoepitaxial layers deposited on commercially available vicinal and on-axis 6H-SiC(0001) wafers has been performed. A

strongly undulating step/terrace configuration was observed in the vicinal surface. By contrast, relatively wide terraces were observed on the on-axis surface. Single Si/C bilayer steps were dominant on both surfaces. A surface phase transformation due to Si sublimation from the Si-terminated surface and resultant graphitization during the cleaning procedure at  $T \geq 1100^\circ\text{C}$ , were observed in both vicinal and on-axis surfaces. The effects of surface structures on both thin film growth by molecular beam epitaxy and defect formation will be published in the near future.

#### E. Future Research

The 6H-SiC wafers which have no epitaxial layer, as grown wafers, will be examined by the similar technique used in this study. In addition, the surfaces of the epitaxial layers grown in our GSMBE system will be investigated in terms of occurrence of step bunching and step flow. It is also interesting to investigate the atomistic structure of the step in 6H-SiC surfaces by a higher resolution STM.

#### F. References

1. R. F. Davis, *Physica B* **185**, 1 (1993).
2. L. Rowland, R. S. Kern, S. Tanaka, and R. F. Davis, *J. Mater. Res.* **8**, 2753 (1993).
3. T. Yoshinobu, M. Nakayama, H. Shiomi, T. Fuyuki, and H. Matsunami, *J. Cryst. Growth* **99**, 520 (1990).
4. T. Kimoto, H. Nishino, W. S. Yoo, and H. Matsunami, *J. Appl. Phys.* **73**, 726 (1993).
5. S. Tanaka, R. S. Kern, and R. F. Davis, *Appl. Phys. Lett.*, to be published.
6. Z. Sitar, M. J. Paisley, Y. J. Ruan, W. J. Choyke, and R. F. Davis, *J. Vac. Sci. Technol. B* **8**, 316 (1990).
7. C. Wang and R. F. Davis, *Appl. Phys. Lett.* **63**, 990 (1993).
8. S. Tanaka, R. S. Kern, and R. F. Davis, *Appl. Phys. Lett.*, to be published in Jan. 3 (1994).
9. A. J. Van Bommel, J. E. Crombeen, and A. Van Tooren, *Surf. Sci.* **48**, 463 (1975).
10. R. Kaplan, *Surf. Sci.* **215**, 111 (1989).
11. C. S. Chang, I. S. T. Tsong, Y. C. Wang, and R. F. Davis, *Surf. Sci.* **256**, 354 (1991).
12. M. A. Kulakov, P. Heuvel, V. F. Tsvetkov, and B. Bullemer, *Surf. Sci.* **315**, 248 (1994).
13. M. Shinohara, M. Tanimoto, H. Yokoyama, and N. Inoue, *Appl. Phys. Lett.* **65**, 1418 (1994).
14. L. Muehlhoff, W. J. Choyke, M. J. Bozack, and J. T. Yates, Jr., *J. Appl. Phys.* **60**, 2842 (1986).



### III. Silane Plasma and CVD Preparation of 6H SiC Surfaces for Growth of Epitaxial Films

#### A. Introduction

As the need increases for electronic devices that have higher performance characteristics, surface cleaning without damage becomes especially important. Hydrogen plasma processing have been demonstrated in cleaning silicon wafers.[1] Recently, silane/hydrogen mixtures have been used to clean silicon.[2] As SiC tends to graphitize with annealing, this technique should work for SiC. R. Kaplan has investigated this by annealing  $\beta$  and 6H SiC samples in a silicon flux.[3] We demonstrate in this report surface cleaning of 6H SiC both by silane ( $\text{SiH}_4$ ) chemical vapor deposition (CVD) and by silane plasma treatment.

UPS is used to examine the electronic states of the processed surface. Surface states, possibly caused by dangling bonds on a clean surface, are observed. Surface states appear as distinctive features in the spectra.

#### B. Experimental Procedures

These studies have been performed in an integrated vacuum transfer system. The capabilities include plasma processing, UPS, XPS, MBE, LEED and Auger electron spectroscopy (AES).

The plasma system has a base pressure of  $1.0 \times 10^{-9}$  Torr but operates in the milli-Torr range of pressure. Hydrogen of up to 100 sccm can flow into the system. One may also flow at a rate of 10 sccm, a mixture of 1% silane/ $\text{H}_2$ . Power is coupled into the chamber through rf induction. Typical values are from 20 to 400 watts depending on the type of cleaning/etching desired. Figure 1 depicts the chamber.

We have cleaned the surface two different ways. Both involve an *ex situ* HF dip to remove thick oxide. The first method is simply to anneal the sample in a silane flux. A temperature of 825 °C is reached and held for 5 minutes in a flow of 10 sccm of 1% silane/ $\text{H}_2$ . AES of this process, along with the LEED pattern, is shown in Fig. 2 and compared to an *ex situ* clean. The second method involves the rf plasma. The effect of this processing is shown in Fig. 3. Our parameters are: a temperature of 800 °C, power of 400 watts, a flow of 10 sccm, and a pressure of 25 mTorr. Both parameters result in substantial removal of oxygen and surface hydrocarbons. The CVD clean results in a  $3 \times 3$  reconstruction, possibly due to a silicon adatom structure, indicating a Si rich surface.[4] The plasma clean results in a  $1 \times 1$  surface showing the stoichiometry of the bulk.

The UPS chamber has a base pressure of  $2 \times 10^{-10}$  Torr. Operating conditions involve pressures up to  $1 \times 10^{-9}$  Torr, but the higher pressure is due to the helium inflow and does not contaminate the sample. The UPS system utilizes a helium resonance lamp (the He I line) to

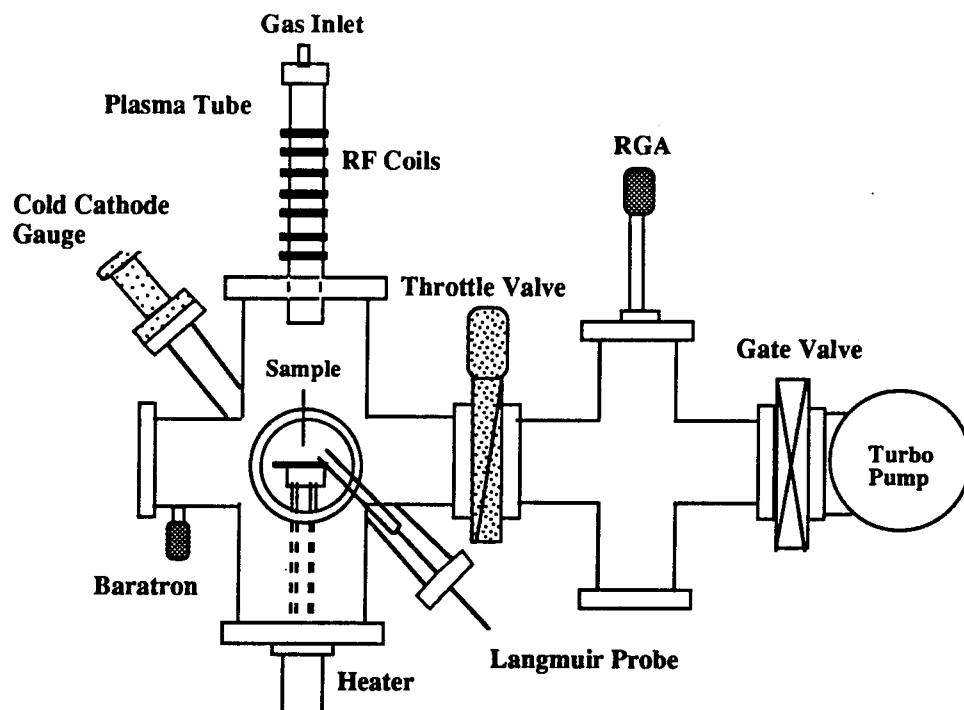


Figure 1. The plasma/CVD chamber.

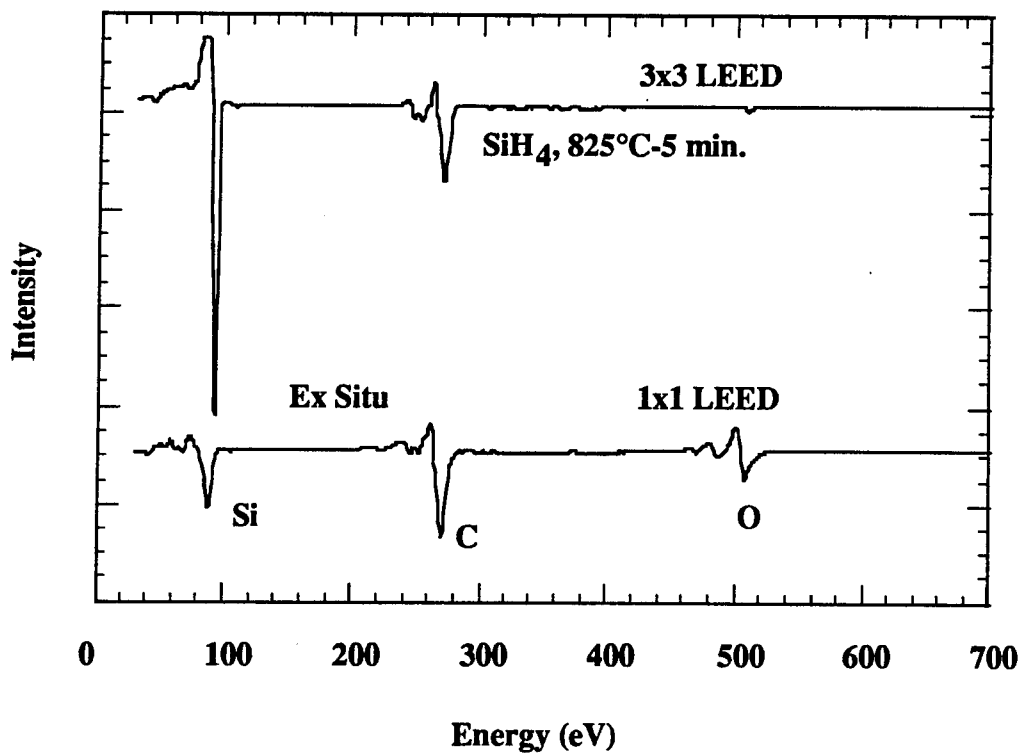


Figure 2. Silane CVD clean of 6H SiC.

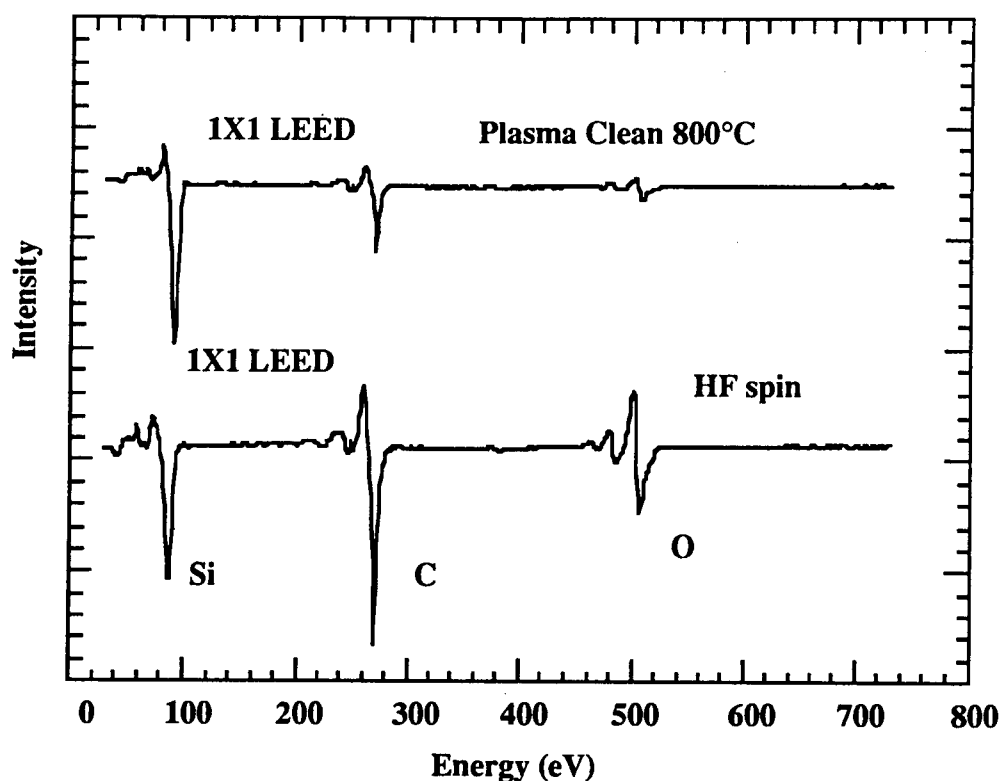


Figure 3. Remote silane plasma clean.

provide a source of 21.2 eV light. Photoemitted electrons are measured with a 50 mm mean radius hemispherical electron analyzer operated at a 0.15 eV energy resolution and a  $2^\circ$  angular resolution. The analyzer (VSW HA50) is mounted on a double goniometer and can be tilted with respect to the sample in two independent directions. The SiC samples were fastened by tantalum wire to a molybdenum sample holder. The sample holder is biased by up to 4 V to allow low energy electrons to overcome the work function of the analyzer. The Fermi level of the system (sample and analyzer) is determined by UPS measurement of the sample holder with no sample bias (i.e., grounded). The sample holder can be heated to 1150 °C.

Scans were performed on the CVD cleaned sample, a reconstructed sample and a hydrogen terminated clean sample. The reconstructed sample was the  $\sqrt{3} \times \sqrt{3}$  R30° surface. This surface is prepared by annealing to 960 °C without a silane flow and is silicon deficient. The hydrogen terminated surface is a CVD cleaned sample which had a LEED pattern of 1×1. It was exposed to a hydrogen plasma to investigate the role of dangling bonds in the UPS spectra. The UPS data appears in Fig. 4.

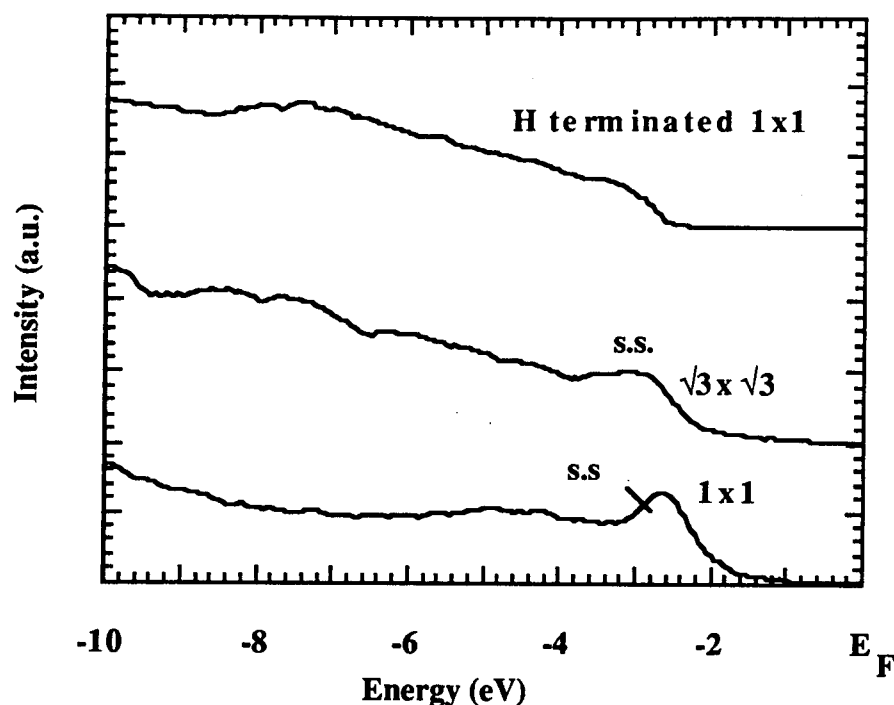


Figure 4. Surface states of SiC.

#### C. Results

The CVD clean removes substantial amounts of oxygen and hydrocarbons. We have an ordered surface with a  $3 \times 3$  reconstruction. From the Auger spectra, we determine a Si/C ratio of 1.8 indicating a silicon rich surface. The LEED pattern is attributed to a Si adatom structure.

The plasma clean also removes contaminants yet gives us a  $1 \times 1$  surface in registry with the bulk. The Si/C ratio is 1.2 so the surface is still slightly silicon rich.

The UPS investigation yielded very interesting results. We see a feature, a "bump," on the  $1 \times 1$  surface which may be a surface state. The feature appeared diminished on a reconstructed surface. To test the origin of the state, we used the plasma system to terminate the surface with hydrogen. This resulted in the extinction of the feature. We attribute this extinction to the passivation of the surface. The dangling bonds are satisfied by the hydrogen atoms which terminate the surface.

#### D. Conclusions

We demonstrate cleaning of 6H SiC substrates by silane plasma and CVD methods. Currently we are unable to achieve the low temperature plasma clean which works so well for silicon. Yet, we have improved upon the pure chemical etch method. Lower processing temperatures are desired for industrial purposes. An advantage over silicon processing is that the temperature need not be as low, due to differences in diffusion of dopants.

We have made the observation of surface states on SiC. To our knowledge, this is the first report of such phenomena for SiC.

#### E. Future Plans

Refinement of the plasma processing parameters will be made with the goal being achievement of a lower processing temperature.

Further investigation of the surface state structure will be made by UPS. The  $3\times 3$  surface will be examined. This probe of the surface structure should lead to a better understanding of surface kinetics which in turn should help further develop the cleaning process.

#### F. Acknowledgment

This work was supported in part by the Office of Naval Research through grants N0014-92-J-1477 and N0014-92-J-1604. The SiC substrates used were supplied by Cree Research.

#### G. References

1. R. A. Rudder, S. V. Hattangady, J. B. Posthill, and R. J. Markunas, Mat. Res. Soc. Symp. **116** 529 (1988).
2. J. P. Barnak, Private Communication.
3. R. Kaplan, Surface Science **215** 111 (1989).
4. R. Kaplan.

#### **IV. Growth of 2H-Silicon Carbide using Pseudomorphic 2H-Aluminum Nitride Layer on 6H-Silicon Carbide Substrates by Gas-source Molecular Beam Epitaxy**

##### **A. Introduction**

High purity, monocrystalline silicon carbide (SiC) is being extensively studied for high-temperature, -power and -frequency electronic device applications [1]. More than 250 polytypes or stacking arrangements of the closest packed Si/C bilayers along the crystallographic axes of closest packing have been reported [2]. The 3C or  $\beta$ , 15R, 6H and 4H polytypes are the most common; the numerals and the letters refer to the number of bilayers needed to form a unit cell and the cubic or hexagonal nature of the cell, respectively. 3C and 6H films have been grown successfully by many researchers [3]. Another polytype, 2H, has also been desired for electronic device applications because it has the largest band gap of any SiC polytype (3.3 eV) and a higher electron mobility than 6H and 15R [4]. However, deposition of the 2H polytype has been unsuccessful until recently, and then only in the form of small whiskers [4-7]. Recently, NASA's group has reported the first successful growth of 2H-SiC films on 6H-SiC substrates by pulsed laser ablation [8]. The structural study using transmission electron microscopy (TEM) showed the symmetry of a film grown at 1270°C as c-axis oriented 2H-SiC containing columnar grains with average diameter of 20 nm and length of 100 nm.

In general, films having the same polytypes as the substrate can be deposited, if the growth mode is 'step flow.' Step flow can be achieved kinetically when the deposited adatoms reach surface step sites and retain the identical stacking sequence as the substrate. Thus, 6H films can be formed on 6H(0001) substrates with the availability of steps even at growth temperatures <1500°C, i.e., in the temperature regime where 3C is found by experiment [2] to be the more commonly deposited phase (although quantum mechanical calculation [9] predicts 6H to be more stable than 3C). The steps serve as the primary surface template which forces replication of the substrate polytype in the growing film. Step flow has been achieved experimentally via CVD in the homoepitaxial growth of 6H and 4H films between 1200 and 1600°C [3, 10, 11]. By contrast, previous SiC film growth studies via MBE at lower growth temperatures (<1200°C) on 6H-SiC substrates did not result in step flow and homoepitaxial reproduction of the 6H substrate. Recently, however, we have successfully achieved step flow growth and even control of polytypes by changing the gas flow ratio of  $C_2H_4/Si_2H_6$  [12]. The problem in growing 2H-SiC film is potentially the lack of 2H-SiC substrates. Since AlN has the wurtzite (2H) structure and is closely lattice matched to SiC, this material may be used as a template of the 2H structure to achieve our goal.

In this study, we have investigated the possibility of forming the 2H-SiC and growing SiC by step flow under certain growth conditions on a 2H-AlN which is grown on 6H-SiC substrates by plasma-assisted(PA) GSMBE [13]. Under the ethylene rich conditions, i. e., the gas flow ratio of  $C_2H_4/Si_2H_6 = 5$ , we have observed the formation of 2H-SiC on 2H-AlN. It should, however, be noted that since the film of 2H-SiC was very thin, further investigations is necessary to confirm this result.

### B. Experimental Procedure

The very thin,  $\sim 15$  Å, AlN films were first grown via PAGSMBE on the Si(0001) surfaces of either vicinal ( $3-4^\circ$  off from (0001) toward  $\langle 11\bar{2}0 \rangle$ ) or on-axis  $\alpha$ (6H)-SiC substrates. A detailed description of the deposition technique has been published [14]. After the growth of AlN films followed by taking RHEED patterns, SiC films were deposited under the various conditions given in Table I. Following growth and RHEED observation, each sample was cut and glued face-to-face and thinned to electron transparency using standard cross-sectional TEM preparation techniques [15]. Each sample was examined along the  $\langle \bar{2}110 \rangle$  zone axis using a Topcon EM-002B operated at a 200kV acceleration voltage.

Table I. Range of growth conditions for the SiC films

Substrate	2H-AlN/6H-SiC
Temperature	1050 °C
$Si_2H_6$ flow rate	0.1 sccm
$C_2H_4$ flow rates	0.1, 0.5 sccm
$C_2H_4/Si_2H_6$ flow rate ratios	1.0, 5.0
Growth rates and time	$\approx 10-50$ Å/hr, 1 hr.

### C. Results

Figure 1 shows a cross-sectional TEM micrograph of the multi-layer structure including 3C-SiC, 2H-AlN, and 6H-SiC substrate. The top SiC layer was grown at the gas flow ratio ( $C_2H_4/Si_2H_6$ ) of 1. Island-like 3C-SiC is evident on 2H-AlN thin film, which is  $\sim 15$  Å in thickness. It should be noted that under the same condition as used in this film growth step flow is occurred on 6H-SiC substrate because of ( $3 \times 3$ ) surface reconstruction according to our recent study [12]. This implies that nucleation of 3C phase is enhanced probably by the presence of Al- or N- dangling bonds on the AlN(0001) surface. Either Si or C adatoms (molecules) may reduce their diffusion lengths on the AlN surface and thus very small numbers of adatoms might reach the step sites where crystallographic information of 2H structure can only be supplied.

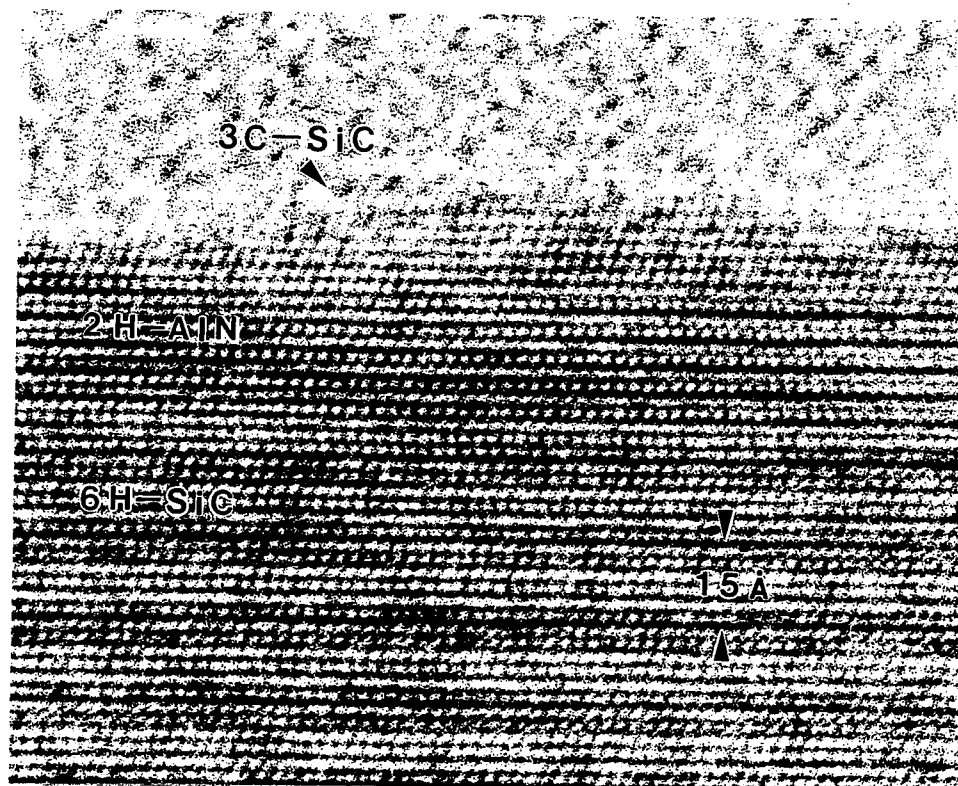


Figure 1. HRTEM image of the multi-layer structure of 3C-SiC/2H-AlN/6H-SiC. The SiC film was grown at the gas flow ratio of 1.

In contrast, no 3C region can be observed in the sample which was grown at the gas flow ratio ( $C_2H_4/Si_2H_6$ ) of 5, as seen in Fig. 2. Surface morphology appeared to be step flow pattern. The film thickness of SiC, however, is too small to clearly discern the SiC layer. Our preliminary investigation of SiC film growth on 6H-SiC substrate indicated the presence of SiC film under more ethylene-rich conditions and that the growth rates of SiC film on AlN and SiC surfaces were comparable. In combining these results, the presence of 2H-SiC layer is plausible. Further experiments are necessary to elucidate this problem.

#### D. Discussion

The gas flow ratio of  $C_2H_4/Si_2H_6$  was found to affect polytypes of SiC films on the 2H-AlN(0001) surfaces. Under equal flow rates of each gas the 3C nuclei and island-like surface morphology was observed. In contrast, ethylene-rich condition might give rise to 2H polytype of SiC on the 2H-AlN surfaces. The change in polytypes under the two different growth conditions should be discussed in terms of surface chemistry of AlN(0001) and bonding configurations of SiC/AlN interface including step sites.



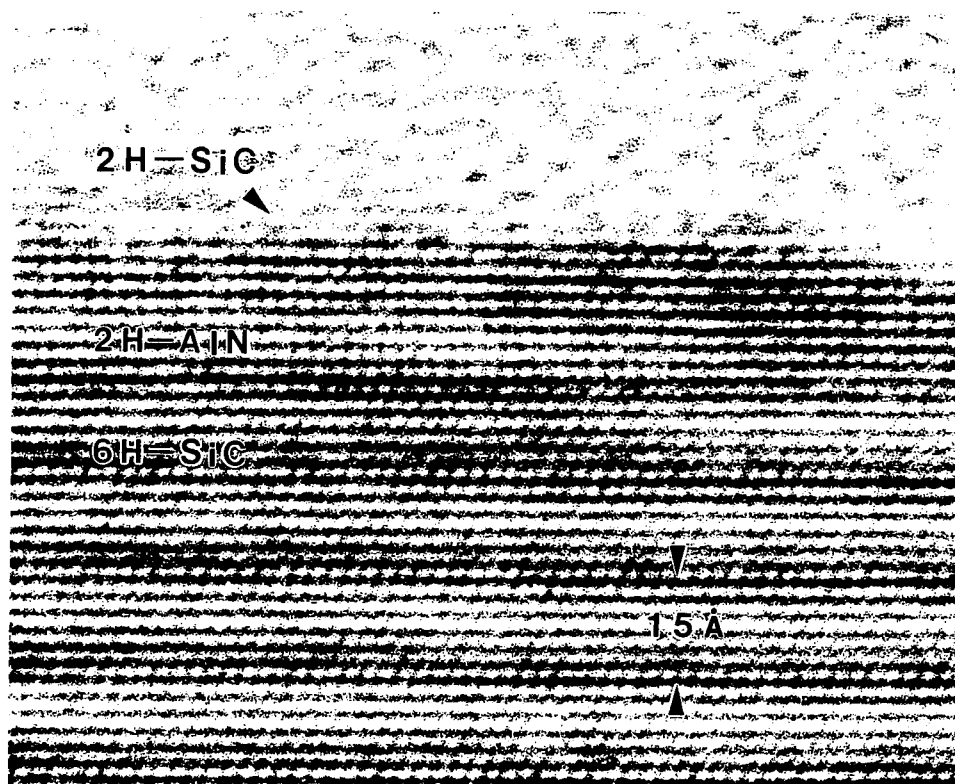


Figure 2. HRTEM image of the multi-layer structure of 2H-SiC/2H-AlN/6H-SiC. The SiC film was grown at the gas flow ratio of 5. The thickness of 2H-SiC is ~2-3 bilayers.

AlN(0001) surface is assumed to be Al-terminated because the 6H-SiC substrate used in this study was Si face on which preferentially formed Si-N bonding at the AlN/6H-SiC interface[16]. Thus, there are Al dangling bonds on the AlN surface except at the step sites, which may possess N dangling bonds, as indicated in Fig. 3. An energetic calculation [16] predicts that adatoms (molecules) of Si and C species react the AlN surface to form either Si-N and C-Al bonds, respectively. The Al-Si bond is rather unfavorable in the calculation, however, under the gas flow ratio (R) of 1 it may be created kinetically to form 3C nuclei on the terrace sites, as was observed in Fig. 1. On the other hand, majority of  $C_2H_4$  gas molecules at  $R = 5$  may cover the Al dangling bonds by forming C-Al bonding configuration which hinder the formation of 3C nuclei on the terrace sites.  $Si_2H_6$  molecules can reach the step site and form Si-N bond to retain the same stacking sequence of 2H-AlN. It should be noted here that 2H retention is only possible at step sites and 3C nucleation occurs on terrace sites due to thermodynamic point of view.

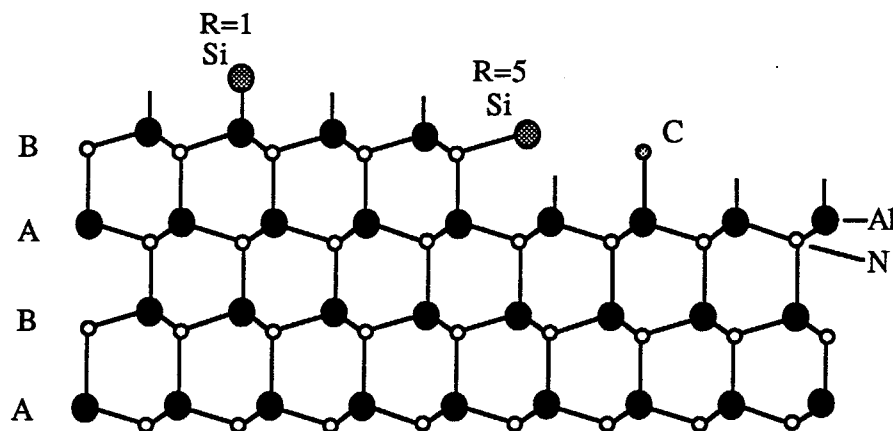


Figure 3. AlN surface structure.

#### E. Conclusion

2H polytype of SiC film has been kinetically stabilized on very thin 2H-AlN thin films, which were pseudomorphically deposited on 6H-SiC substrates. The AlN thin layer plays a role as a template of 2H structure. Under the different gas flow ratios of  $C_2H_4/Si_2H_6$  during SiC growth the difference in polytypes of SiC films have been observed. Ethylene-rich condition is considered to kinetically stabilize the 2H-SiC structure at the growth temperature of  $1050^\circ C$  mainly due to prevention of 3C nuclei on the terrace sites by C-Al bondings. The detailed mechanisms of 3C nucleation on the terrace sites is still unknown, however, it is probably related to Si-Al bonding characteristics.

#### F. Future Plans

The strong evidence for the presence of 2H-SiC is desired. Several attempts should be made to grow thicker 2H-SiC in the same experimental methods. Based on the previous study including the growth mechanism of SiC film on 6H-SiC substrate [12], thicker 2H-SiC will probability be deposited on very thin 2H-SiC layer obtained in this experiment using the gas flow ratio of 1, which enhances step flow. Dependence of growth temperature of SiC will also be studied.

#### G. References

1. R. F. Davis, *Physica B* **185**, 1 (1993).
2. N. W. Jepps and T. F. Page, *Progress in Crystal Growth and Characterization* vol. 7, edited by P. Krishna (Pergamon Press, New York, 1983), 259.
3. For example see, H. S., Kong, J. T. Glass, and R. F. Davis, *J. Appl. Phys.* **64**, 2672 (1988).
4. L. Patrick, *J. Appl. Phys.* **37**, 4911 (1966).
5. R. F. Adamsky and K. M. Merz, *Z. Krist.* **111**, 350 (1959).

6. M. I. Sokhor and V. P. Glukhov, *Sov. Phys. Crystallogr.* **10**, 341 (1963).
7. J. A. Powell, *J. Appl. Phys.* **40**, 4660 (1969).
8. M. A. Stan, M. O. Patton, and J. D. Warner, *Appl. Phys. Lett.* **64**, 2667 (1994).
9. V. Heine, C. Chen, and R. J. Needs, *J. Am. Ceram. Soc.* **74**, 2630 (1991).
10. H. Matsunami, T. Ueda, and H. Nishino, *Mater. Res. Soc. Symp. Proc.* **162**, 397 (1990).
11. L. B. Rowland, R. S. Kern, S. Tanaka, and R. F. Davis, *J. Mater. Res.* **8**, 2753 (1993).
12. S. Tanaka, R. S. Kern, and R. F. Davis, *Appl. Phys. Lett.*, to be published in Nov. 28 (1994).
13. S. Tanaka, R. S. Kern, and R. F. Davis, *Appl. Phys. Lett.*, to be published in Jan. 3 (1995).
14. L. B. Rowland, R. S. Kern, S. Tanaka, and R. F. Davis, *J. Mater. Res.* **8**, 2310 (1993).
15. C. H. Carter, Jr., R. F. Davis, and S. R. Nutt, *J. Mater. Res.* **1**, 811 (1986).
16. W. R. L. Lambrecht and B. Segall, *Phys. Rev. B* **43**, 7070 (1991).

## V. Growth of SiC Thin Films by Gas-Source Molecular Beam Epitaxy and Their Electrical Characterization

### A. Introduction

Silicon carbide (SiC) is a wide bandgap material that exhibits polytypism, a one-dimensional polymorphism arising from the various possible stacking sequences of, e. g., the silicon and carbon layers along the directions of closest packing. There are approximately 250 SiC polytypes[1]. Included in these is one cubic polytype. This single cubic polytype,  $\beta$ -SiC, crystallizes in the zincblende structure, has a room temperature bandgap of 2.3 eV, and is commonly referred to as 3C-SiC. (In the Ramsdell notation, the three (3) refers to the number of Si and C bilayers necessary to produce a unit cell and the C indicates its cubic symmetry.) The other rhombohedral and hexagonal polytypes are classed under the heading of  $\alpha$ -SiC. The most common of these latter polytypes is 6H-SiC with a room temperature bandgap of  $\approx 3.0$  eV.

Since the 1950's, monocrystalline single crystals of 6H-SiC have been grown at using the Lely sublimation process[2]. However, nucleation was uncontrolled using this process and control of resultant polytypes was difficult. SiC single crystals inadvertently formed during the industrial Acheson process have also been used as substrates for SiC growth. However, neither these nor those formed using the Lely process are large enough for practical device applications. Recently, using a seeded sublimation-growth process, boules of single polytype 6H-SiC of >1 inch diameter of much higher quality of that obtained using the Lely process have been grown. The use of single crystals of the 6H polytype cut from these boules has given a significant boost to SiC device development.

SiC epitaxial thin film growth on hexagonal SiC substrates has been reported since the 1960's. The use of nominally on-axis SiC substrates has usually resulted in growth of 3C-SiC films. Films of 3C-SiC(111) grown by CVD have been formed on 6H-SiC substrates less than  $1^\circ$  off (0001)[3]. Films of 3C-SiC on 6H-SiC substrates have typically had much lower defect densities than those grown on Si substrates. The major defects present in  $\beta$ -SiC/6H-SiC films have been double positioning boundaries (DPB)[4]. Despite the presence of DPBs, the resultant material was of sufficient quality to further device development of SiC. The use of off-axis 6H-SiC(0001) substrates has resulted in growth of high-quality monocrystalline 6H-SiC layers with very low defect densities[5].

In addition, the use of more advanced deposition techniques, such as molecular beam epitaxy (MBE), has been reported for SiC in order to reduce the growth temperature and from about 1400-1500°C on 6H-SiC substrates. Si and C electron-beam sources have been used to epitaxially deposit SiC on 6H-SiC (0001) at temperatures of 1150°C[6]. Previous reports by all investigators have documented 3C-SiC growth only on 6H-SiC(0001) by MBE.

## B. Experimental Procedure

Thin, epitaxial films of SiC were grown on the Si and C faces of 6H-SiC(0001) substrates supplied by Cree Research, Inc. These included both vicinal 6H-SiC(0001) wafers oriented 3-4° towards [11 $\bar{2}$ 0] containing a 0.75  $\mu\text{m}$  epitaxial 6H-SiC layer deposited via CVD and on-axis 6H-SiC(0001) wafers. All wafers were received with a thermally oxidized 50 nm layer to aid in wafer cleaning. Wafers are prepared for growth by a 10% HF dip and a 10 minute anneal at 1050°C in UHV as well as a disilane exposure and boil-off, a technique detailed in previous reports and based on the work of Kaplan[8].

All films were grown using a specially designed and previously described [9] GSMBE system. The base and operating pressures were  $10^{-9}$  Torr and  $10^{-3}$ – $10^{-6}$  Torr, respectively. All films were grown between 1050–1250°C using 1:1 ratios of disilane ( $\text{Si}_2\text{H}_6$ , 99.99% purity) and ethylene ( $\text{C}_2\text{H}_4$ , 99.99% purity) with total source inputs ranging from 0.6–4.0 sccm on off-axis  $\alpha$ (6H)-SiC(0001) and thin 2H-AlN(0001) buffer layers on on-axis  $\alpha$ (6H)-SiC(0001). The thin AlN layers were grown for 1 minute in the same system at 1050°C using a standard Al (99.9999% purity) effusion cell source, operating at 1260°C, and a compact electron cyclotron resonance (ECR) source to activate 3.5 sccm of  $\text{N}_2$  (99.9995% purity). (This procedure has been described previously [10, 11]). As described in previous reports, both 3C- and 6H-SiC have been grown on vicinal  $\alpha$ (6H)-SiC(0001) substrates depending on the chemistry of the gas phase and the substrate temperature. For the purposes of the doping studies, the 6H polytype was the only one investigated and only those films grown at 1250°C using 1.0 sccm  $\text{Si}_2\text{H}_6$  and 1.0 sccm  $\text{C}_2\text{H}_4$ . Solid aluminum, evaporated from a standard MBE effusion cell, was used for p-type doping and ammonia ( $\text{NH}_3$ , diluted to 50 ppm in Ar) was used for p-type doping.

Reflection high-energy electron diffraction (RHEED) at 10 kV and high-resolution transmission electron microscopy (HRTEM) were used for structure and microstructure analyses. Samples were prepared for HRTEM using standard techniques[7]. A Topcon EM 002B high-resolution transmission electron microscope was used at 200 kV for the HRTEM analysis. Secondary ion mass spectrometry (SIMS), using a Cameca IMS-3f ion microprobe operating at 10 keV with  $\text{O}^+$  ions, was employed to determine the atomic concentration of Al. Carrier concentrations for undoped SiC films, grown on insulating AlN layers, as well as p-type and n-type doped films were measured at room temperature by standard Hall techniques at 3.5 kG. Nickel contacts, RF sputtered at room temperature then annealed at 1000°C for 30 s in Ar, were used on the undoped and n-type films and aluminum contacts, evaporated in a standard evaporator and annealed at 500°C for 30 seconds in Ar, were used on p-type films.

## C. Results

*Undoped  $\beta$ -SiC Films.* Undoped films of  $\beta$ -SiC(111) have been grown on thin, insulating layers of 2H-AlN(0001) at 1050°C using 1.0 sccm  $\text{Si}_2\text{H}_6$  and 1.0 sccm  $\text{C}_2\text{H}_4$ . Growth rates

approaching 1000 Å per hour were achieved. Hall electrical measurements made on some of the thicker SiC films ( $\approx 0.75 \mu\text{m}$ ) have showed the films to be n-type with electron concentrations as low as  $3 \times 10^{15} \text{ cm}^{-3}$  and mobilities as high as  $648 \text{ cm}^2 \text{ V}^{-1} \text{ s}^{-1}$ .

*P-type Doping.* Homoepitaxial SiC films on n-type substrates were doped p-type with Al at several different impurity concentrations. Carrier concentrations were measured on a number of Al-doped 6H-SiC films by the Hall technique. These films were grown under the previously stated conditions. Four different doping levels were achieved with Al effusion cell temperatures held at 700°C, 800°C, 900°C and 1000°C. The results are shown in Table I.

Table I. Hall Concentrations and Mobilities of Various P-type SiC Films

Aluminum Cell Temperature (°C)	Hole Concentration ( $\text{cm}^{-3}$ )	Hole Mobility ( $\text{cm}^2 \text{ V}^{-1} \text{ s}^{-1}$ )
700	$4.6 \times 10^{15}$	39
800	$7.1 \times 10^{16}$	33
900	$8.8 \times 10^{17}$	26
1000	$3.8 \times 10^{18}$	19

Figure 1 shows SIMS profiles for the same p-type films as displayed in Table I. Compared to our previously reported[12] p-type doped films, these profiles are very smooth and uniform.

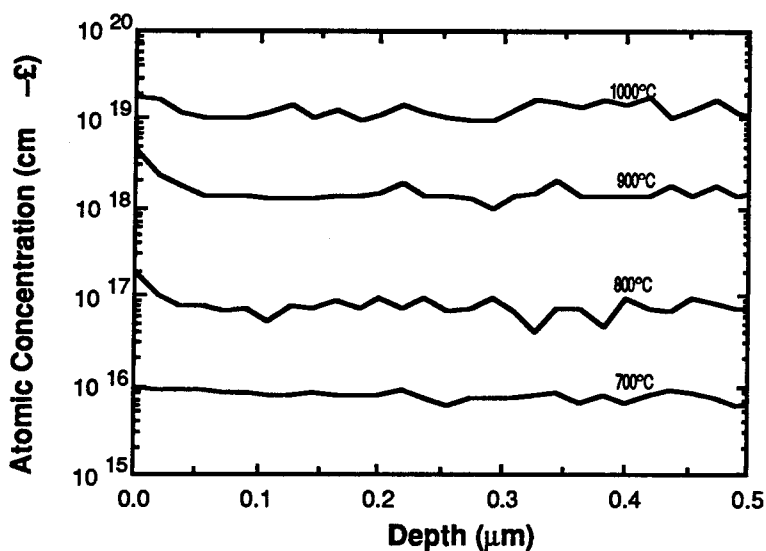


Figure 1. SIMS profiles for 6H-SiC films doped with Al from an MBE effusion cell at different source temperatures.

*N-type Doping.* Homoepitaxial SiC films on p-type substrates were doped n-type using NH<sub>3</sub>, diluted to 50 ppm in Ar, at several different impurity concentrations. Carrier concentrations were measured on a number of N-doped 6H-SiC films by the Hall technique. These films were grown under the previously-stated conditions. Three different doping levels were achieved with NH<sub>3</sub>/Ar flow rates at 0.33, 0.5 and 1.0 sccm. The results are shown in Table II. No SIMS analysis has been performed on these films.

Table II. Hall Concentrations and Mobilities of Various N-type SiC Films

NH <sub>3</sub> /Ar Flow Rate (sccm)	Electron Concentration (cm <sup>-3</sup> )	Electron Mobility (cm <sup>2</sup> V <sup>-1</sup> s <sup>-1</sup> )
0.33	8.9×10 <sup>16</sup>	378
0.50	3.2×10 <sup>17</sup>	289
1.00	5.4×10 <sup>17</sup>	245

#### D. Discussion

The results of the Hall measurements on undoped  $\beta$ -SiC, grown on AlN on on-axis 6H-SiC, represent some of the lowest unintentional doping levels ever reported in the cubic polytype. The Hall measurements listed in Tables I and II and the SIMS data displayed in Fig. 1 represent the first intensive attempt at SiC doping ever attempted by MBE. As expected, the concentration of both impurity atoms and carriers increased as the source flux increased. The profiles in Fig. 1 and the data in Table I are of the same order of magnitude indicating a much higher activation efficiency in p-type SiC than previously reported by CVD [13]. In this case, the ratio of carrier concentration to impurity concentration is about 1 to 3. Unfortunately, the same data are currently unavailable on the n-type samples.

#### E. Conclusions

Films of 3C- and 6H-SiC have been grown between 1050-1250°C by GSMBE using Si<sub>2</sub>H<sub>6</sub> and C<sub>2</sub>H<sub>4</sub> on different orientations of  $\alpha$ (6H)-SiC(0001) and on thin buffer layers of AlN. Growth of SiC on AlN represents a possible means of growing higher quality  $\beta$ -SiC(111) than previously reported. Hall electrical measurements on these films revealed carrier concentration as low as 3×10<sup>15</sup> cm<sup>-3</sup> and mobilities as high as 648 cm<sup>2</sup>V<sup>-1</sup>s<sup>-1</sup>.

Doped films of 6H-SiC have been grown on vicinal  $\alpha$ (6H)-SiC(0001) at 1250°C. The films (doped p-type with Al and n-type with N) showed carrier concentrations that increased

with increasing impurity flux. SIMS profiles for Al incorporation are of the same order of magnitude indicating a much higher activation efficiency than previously reported by CVD.

#### F. Future Research Plans and Goals

Further work on doping both 3C- and 6H-SiC will be performed. Simple device structures (i.e., p-n junctions) will be fabricated. Additionally, further studies will be initiated to study the role that hydrogen and other gases may play in the activation efficiency of carriers in SiC films. Since no hydrogen is used in MBE, aside from that released during the decomposition of the precursor gases, hydrogen incorporation is postulated[14] as a possible retardant to impurity activation. Experiments will be conducted with various levels of H<sub>2</sub> present to check the validity of this postulate.

#### G. References

1. G. R. Fisher and P. Barnes, *Philos. Mag. B* **61**, 217 (1990).
2. J. A. Lely, *Ber. Deut. Keram. Ges.* **32**, 229 (1955).
3. H. S. Kong, J. T. Glass, and R. F. Davis, *Appl. Phys. Lett.* **49**, 1074 (1986).
4. H. S. Kong, B. L. Jiang, J. T. Glass, G. A. Rozgonyi, and K. L. More, *J. Appl. Phys.* **63**, 2645 (1988).
5. H. S. Kong, J. T. Glass, and R. F. Davis, *J. Appl. Phys.* **64**, 2672 (1988).
6. S. Kaneda, Y. Sakamoto, T. Mihara, and T. Tanaka, *J. Cryst. Growth* **81**, 536 (1987).
7. S. P. Withrow, K. L. More, R. A. Zuhr, and T. E. Haynes, *Vacuum* **39**, 1065 (1990).
8. R. Kaplan, *Surface Sci.* **215**, 111 (1989).
9. L. B. Rowland, S. Tanaka, R. S. Kern and R. F. Davis, in *Proceedings of the Fourth International Conference on Amorphous and Crystalline Silicon Carbide and Related Materials*, edited by C. Y. Yang, M. M. Rahman and G. L. Harris (Springer-Verlag, Berlin, 1992) p. 84.
10. L. B. Rowland, R. S. Kern, S. Tanaka and R. F. Davis, *J. Mater. Res.* **8**, 2310 (1993).
11. L. B. Rowland, R. S. Kern, S. Tanaka and R. F. Davis, *Appl. Phys. Lett.* **62**, 3333 (1993).
12. R. S. Kern, S. Tanaka and R. F. Davis, in *Transactions of the Second International High Temperature Electronics Conference*, P-141, (1994).
13. H. J. Kim and R. F. Davis, *J. Electrochem. Soc.* **133**, 2350 (1986).
14. E. Bringuier, personal communication.



**VI. Chemistry, Microstructure, and Electrical Properties at  
Interfaces Between Thin Films of Platinum and Alpha (6H)  
Silicon Carbide (0001)**

Manuscript Submitted

to

Journal of Materials Research

for

Consideration for Publication

by

**L.M. Porter and R.F. Davis**

*Department of Materials Science and Engineering, North Carolina State University,  
Raleigh, NC 27695-7907*

**J.S. Bow, M.J. Kim, and R.W. Carpenter**

*Center for Solid State Science, Arizona State University, Tempe, AZ 85287-1704*

## Abstract

Thin films (4–1000Å) of Pt were deposited via UHV electron beam evaporation at room temperature on monocrystalline, n-type  $\alpha$  (6H)-SiC (0001) substrates and examined in terms of chemistry, microstructure, and electrical properties. The as-deposited contacts were polycrystalline and showed excellent rectifying behavior with low ideality factors ( $n < 1.1$ ) and leakage currents of  $5 \times 10^{-8}$  A/cm<sup>2</sup> at -10 V. The Schottky barrier height increased from 1.06 eV before annealing to 1.26 eV after successive 20 min. anneals at 450, 550, 650, and 750°C. In addition, the leakage currents decreased to  $2 \times 10^{-8}$  A/cm<sup>2</sup> at -10 V. Interfacial reactions were not observed at annealing temperatures below 750°C; above this temperature, which Pt<sub>2</sub>Si and C precipitates were identified in the reaction zone.

## A. Introduction

The high strength and extreme thermal and electronic properties of SiC coupled with the high melting point, high work function, and metallic properties of Pt have led to interest in the Pt/SiC system for both structural and electronic applications. Chou [1] investigated Pt/SiC diffusion couples (1-2 mm thick) for ceramic reinforced metal composites. Similar to the results in the present study, both Pt silicides and free C were identified in the reaction zones after annealing at temperatures between 900 and 1000°C. An extension of this work [2] showed the presence of several silicides after annealing at  $1100^\circ\text{C} \leq 4$  h. In contrast to the present research in which thin films ( $\leq 1000\text{\AA}$ ) were used, annealing the thick Pt/SiC samples at high temperatures resulted in the formation of alternating silicide and C layers. Significant differences in the product phases are often observed for annealed thick and thin films of Pt on SiC particularly if the thin films are completely consumed.

The interfacial chemistry and structure of ultrathin ( $\leq 8\text{\AA}$ ) films of Pt deposited on  $\beta$ -SiC (001) were studied by Auger electron spectroscopy (AES) and low energy electron diffraction (LEED).[3] The results indicated no chemical reaction after annealing for 10 s at 800–900°C and silicide and graphite formation after annealing for 10 s at 1000°C.

Papanicolaou *et al.* [4] studied the electrical characteristics of Pt on n-type  $\beta$ -SiC annealed for 20 min. at temperatures between 300 and 800°C. The study showed that Pt was a good Schottky contact with a high Schottky barrier (0.95–1.35 eV) throughout the annealing sequence. However, the reverse current densities were at least six orders of magnitude higher than those observed in the present study. The higher reverse currents are likely due to a higher defect density in the  $\beta$ -SiC films than in the 6H-SiC substrates and/or the difference in surface preparation. High voltage Pt Schottky barrier diodes have been fabricated on n-type 6H-SiC at 140°C.[5] The as-deposited diodes displayed a high breakdown voltage ( $>425$  V), a low forward voltage drop, low leakage currents, and excellent switching characteristics.

While there have been a number of studies of the Pt/SiC interface highlighting its potential applications, this is the first to correlate the electrical, chemical, and microstructural properties between thin Pt films ( $\leq 1000\text{\AA}$ ) and semiconductor quality 6H-SiC as a function of annealing. In this study analytical techniques, including high resolution transmission electron microscopy (HRTEM), x-ray photoelectron spectroscopy (XPS), and current-voltage (I-V) measurements, were used to understand the chemistry, microstructure, and electronics at interfaces between Pt and monocrystalline, n-type  $\alpha$ (6H)-SiC (0001) substrates. These properties were examined for both as-deposited interfaces and after annealing between 450 and 750°C. The Schottky barrier height (SBH), a critical property for determining the electrical properties, was also calculated through the annealing series.

#### B. Experimental Procedure

Vicinal, single crystal, nitrogen-doped, n-type ( $\approx 10^{18}\text{ cm}^{-3}$ ) wafers of 1" diameter  $\alpha$  (6H)-SiC (0001) containing 0.5-1.5  $\mu\text{m}$  thick, unintentionally doped n-type ( $\approx 10^{16}\text{--}10^{17}\text{ cm}^{-3}$ ) homoepitaxial films thermally oxidized to a thickness of 500-1000 $\text{\AA}$  in dry oxygen at 1300°C were provided by Cree Research, Inc. Epitaxial layers, intentionally doped with nitrogen during growth to achieve an n-type carrier concentration of  $\approx 2 \times 10^{18}\text{ cm}^{-3}$ , were also employed in this research. The Si-terminated (0001) surface, tilted 3°-4° towards  $[11\bar{2}0]$  was used for all depositions and analyses.

The substrates were simultaneously cleaned and the oxide layer etched from the surface using a 10 min. dip in a 10% hydrofluoric acid solution. This was followed by a quick rinse in deionized water. The substrates were loaded immediately into a vacuum system transfer tube (base pressure  $\approx 10^{-9}$  Torr), thermally desorbed at 700°C for 15 min. to remove any residual hydrocarbon contamination, and transferred to the metal deposition chamber.

A UHV dual source 270°, 10 cc electron beam evaporation system was used to deposit the Pt films having thicknesses ranging from 4 - 1000  $\text{\AA}$  onto the substrates described above. A 330 l/s turbomolecular pump was used for roughing the system and during processing. A 500 l/s diode ion pump and a Ti sublimation pump were employed to achieve and maintain UHV base pressures of  $< 2 \times 10^{-10}$  Torr. Prior to the depositions, approximately 25-50  $\text{\AA}$  was typically evaporated from the source to liberate any foreign material which may have collected on its surface. Each substrate was covered by a shutter during this operation. To commence the deposition, the emission current was increased very slowly until a deposition rate of 10-12  $\text{\AA}/\text{min}$  was stabilized according to the thickness monitor, and the shutter subsequently removed from in front of the sample. The pressure during the depositions was between  $5 \times 10^{-9}$  and  $5 \times 10^{-8}$  Torr. Throughout each deposition the substrates were rotated to ensure uniform thickness across the sample. The substrates were not intentionally heated during the depositions.

Patterned contact structures consisting of 500  $\mu\text{m}$  (0.02") and 750  $\mu\text{m}$  (0.03") diameter circular contacts of 100 nm thickness were created for electrical characterization by depositing the Pt through a Mo mask in contact with the SiC epitaxial layer. Silver paste served as the large area back contact. All subsequent annealing, which consisted of successive heating at 450, 550, 650, and 750°C for 20 min. at each temperature, was conducted in UHV. Current-voltage (I-V) measurements were taken with a Rucker & Kolls Model 260 probe station in tandem with an HP 4145A Semiconductor Parameter Analyzer.

Pt/SiC samples were prepared in cross-section for analysis by TEM. High resolution images were obtained with an ISI EM 002B operating at 200 kV with an interpretable resolution limit of 0.18 nm. These images were typically recorded at an electron-optical magnification of 490,000 to 590,000. Some of the HRTEM micrographs were digitized using a 512 $\times$ 512 camera and the resulting images analyzed by using the SEMPER program.[6] Lattice spacings (d-spacings) and interplanar angles were measured from optical digital diffraction patterns and used to identify the reaction product phases. The values of the lattice spacings were calculated using the (0006) d-spacing in 6H-SiC as a baseline measured near the phase to be identified. Thus, any change in d-spacing due to different focusing conditions was negated. A data base of d-spacings for each possible reaction product phase was compared to the experimentally-determined values. The d-spacings from the data base which were within 2% of the measured values were compared with interplanar angles for the identification of phases. Most of the measured values were within 1% of the theoretical values. Unknown phases were identified uniquely by these procedures.

Analytical electron microscopy was performed using a Gatan 666 parallel electron energy loss spectrometer (PEELS) with a spatial resolution of approximately 3 nm attached to a Philips 400 FEG operating at 100 kV. Energy dispersive spectrometry (EDS) was performed using a JEOL 2000 FX operating at 200 kV with a probe size of approximately 40 nm. For fixed position PEELS and EDS, the probe position was adjusted in the diffraction mode by monitoring the shadow image in the Bragg disk of the transmitted beam. The image was created by defocusing the second condenser lens. A liquid nitrogen cooled double-tilt holder was used for all analytical experiments to minimize specimen contamination.

The surface and interface chemistry of the Pt/SiC assembly were studied using a Riber XPS system containing a Mac2 semi-dispersive electron energy analyzer and accessible by UHV transfer from the deposition chamber. The Mg K $\alpha$  (1253.6 eV) x-ray source was operated at 14 kV with an emission-controlled current of 15 mA. Scans of individual photoelectron peaks were obtained at 0.8 eV resolution and contained 500-750 data points and a 20-30 eV binding energy range. This technique also allowed the calculation of the Schottky barrier height for thin films of Pt on SiC.

### C. Results and Discussion

**Electrical Properties.** Platinum contacts displayed excellent and very stable rectifying characteristics both in the as-deposited state and after successive 20 min. anneals at 450, 550, 650, and 750°C. Before annealing, the leakage currents and ideality factors were typically  $5 - 10 \times 10^{-8}$  A/cm<sup>2</sup> and  $n < 1.1$ , respectively. An I vs. V plot which is representative of the results after each successive stage of the annealing series is shown in Fig. 1. Leakage currents at -10 V of the annealed samples were  $2 \times 10^{-8}$  A/cm<sup>2</sup>.

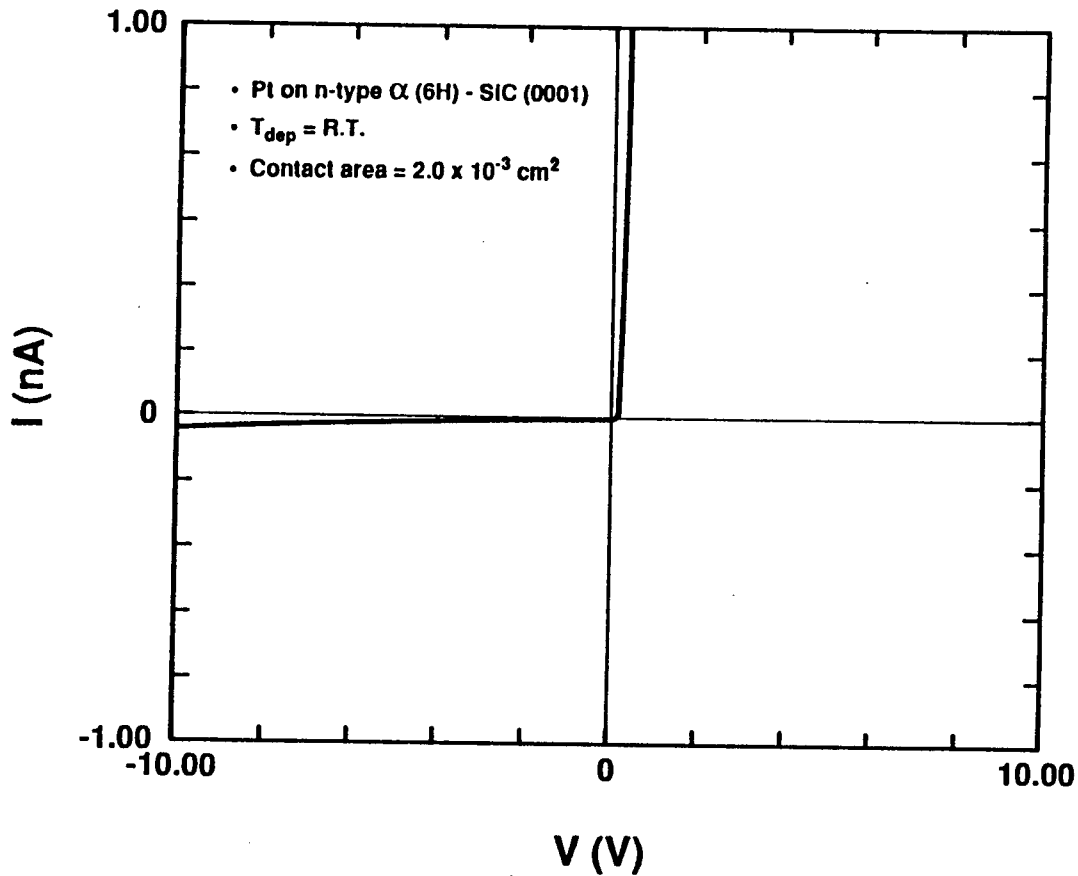


Figure 1. Representative current vs. voltage measurement for Pt/SiC contact after successive annealings for 20 min. at 450, 550, 650, and 750°C.

The semilogarithmic plot of  $I$  vs.  $V$  in Fig. 2 shows that the characteristics maintained the same slope (and, therefore, ideality factor) but shifted to a higher voltage with each successive anneal. Calculations based on these results show that the SBH increased from 1.06 eV for the as-deposited contacts to 1.26 eV after annealing at 750°C, as presented in graphical form in Fig. 3. These results are similar to those reported by Papanicolaou et al.[4] in which the SBH of Pt on  $\beta$ -SiC (001) increased steadily after annealing for 20 min. each at 450, 600, 700, and 800°C. The SBH was 0.95 eV for as-deposited contacts and 1.35 eV after annealing at 800°C.

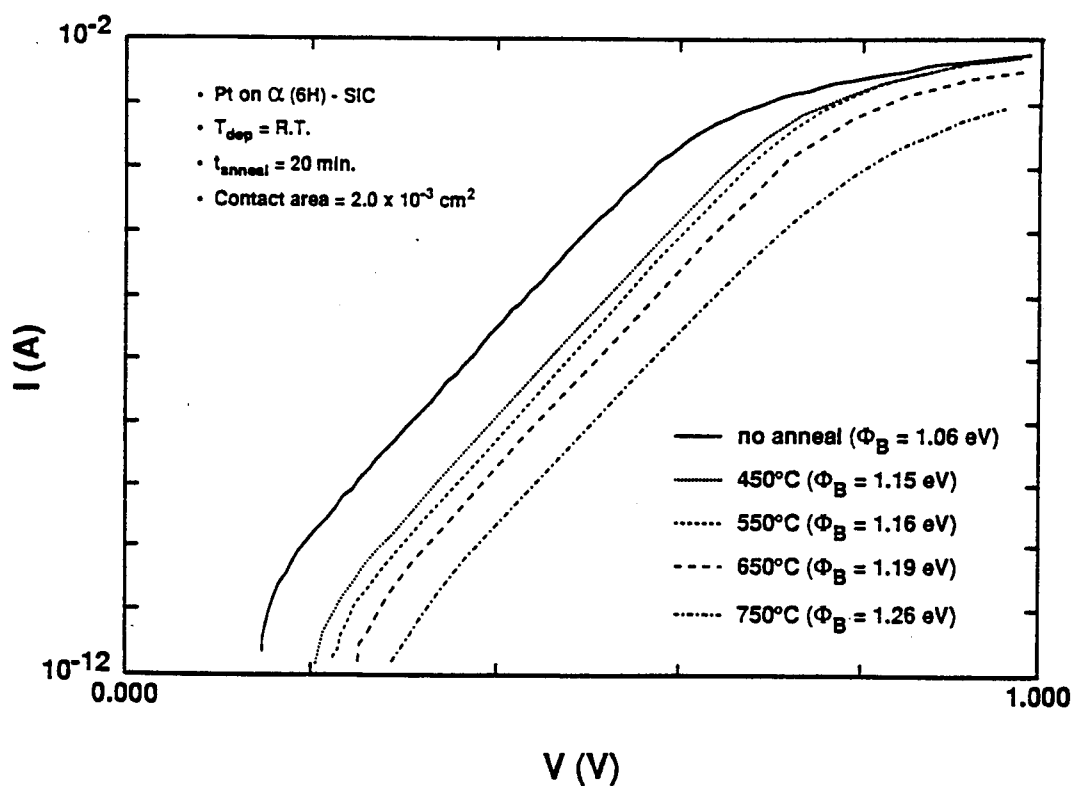


Figure 2. Semilogarithmic current vs. voltage plot for as-deposited Pt/SiC through successive annealing series at 450, 550, 650, and 750°C for 20 min. at each temperature.

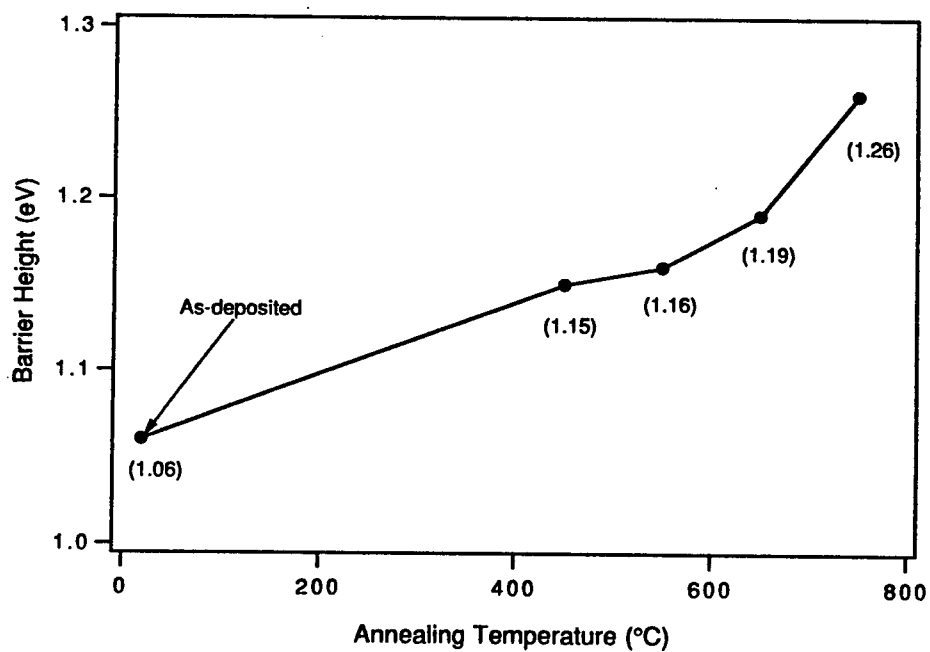


Figure 3. Schottky barrier heights of Pt/SiC vs. annealing temperature.

The SBH was also calculated for very thin, as-deposited Pt films from XPS data using the method described in Ref. 7. The Si 2p and C 1s peaks were used to determine the amount of band bending at the SiC surface/interface before and after deposition. Table I lists the binding energies of these peaks.

Table I. Binding energies of Si 2p (Si-bound-to-C) and C 1s (C-bound-to-Si) peaks from SiC with various thicknesses of Pt. These binding energies have been corrected according to the Au 4f<sub>7/2</sub> binding energy. Units are in electron-volts.

Peak	0 Å Pt	4 Å Pt	8 Å Pt	12 Å Pt
Si 2p	101.58	101.32	101.24	100.64
C 1s	283.80	283.56	283.50	282.96

It is important to assure complete coverage by the Pt films after the depositions. The growth mode was examined following the procedure outlined in Ref. 7. For Pt, which is fcc ( $a = 3.92$  Å), one monolayer was taken to be 2.26 Å. The calculated C 1s and Si 2p reduced intensities are plotted vs. Pt thickness in Fig. 4. The measured intensities attenuated more

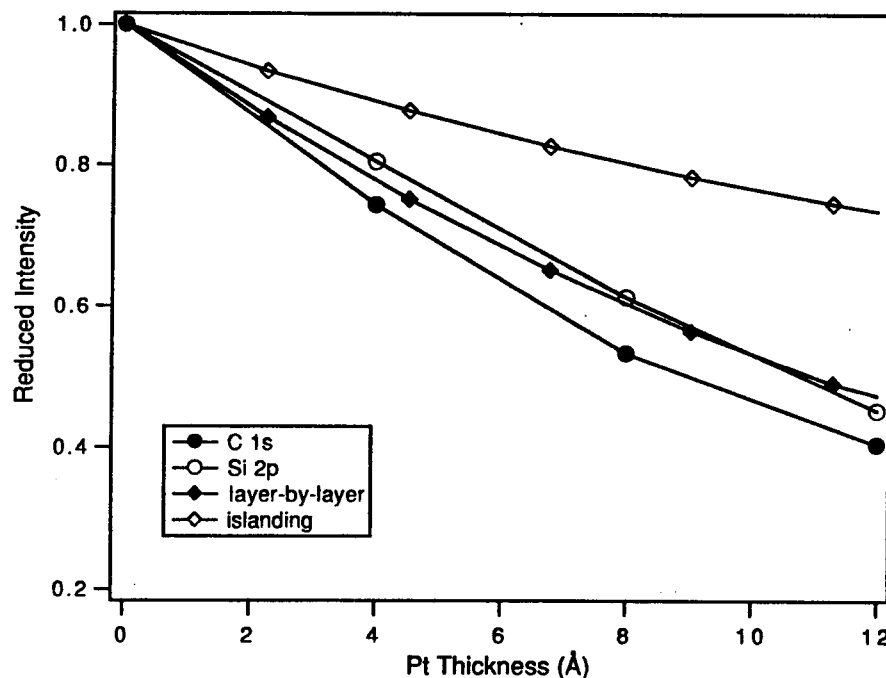


Figure 4. Plot of C 1s and Si 2p reduced intensities vs. Pt overlayer thickness as measured by the growth thickness monitor. The theoretical curves represent two-dimensional layer-by-layer (Frank van der Merwe) and three-dimensional island (Volmer-Weber) growth.

rapidly than the theoretical curve for three-dimensional, or island, growth (assuming 50% coverage). Less attenuation of the substrate intensities is expected for island growth because some regions of the substrate are not covered by the deposited film. The data is shown to follow the theoretical curve for two-dimensional, or layer-by-layer, growth, indicating complete coverage of the SiC substrate by the Pt film.

The C 1s and Si 2p peaks for a Pt deposition sequence are displayed in Fig. 5. The band bending at the SiC surface prior to deposition was determined from the C 1s binding energy. Subtracting the C 1s binding energy of 283.80 eV from 284.30 eV (see Ref. 7) indicates that the energy difference between the bottom of the conduction band and the Fermi level was 0.50 eV. After depositing 4 Å of Pt the C 1s and Si 2p binding energies were reduced by 0.24 and 0.26 eV, respectively. After depositing a total of 12 Å, these binding energies were reduced by a total of 0.84 and 0.82 eV, respectively.

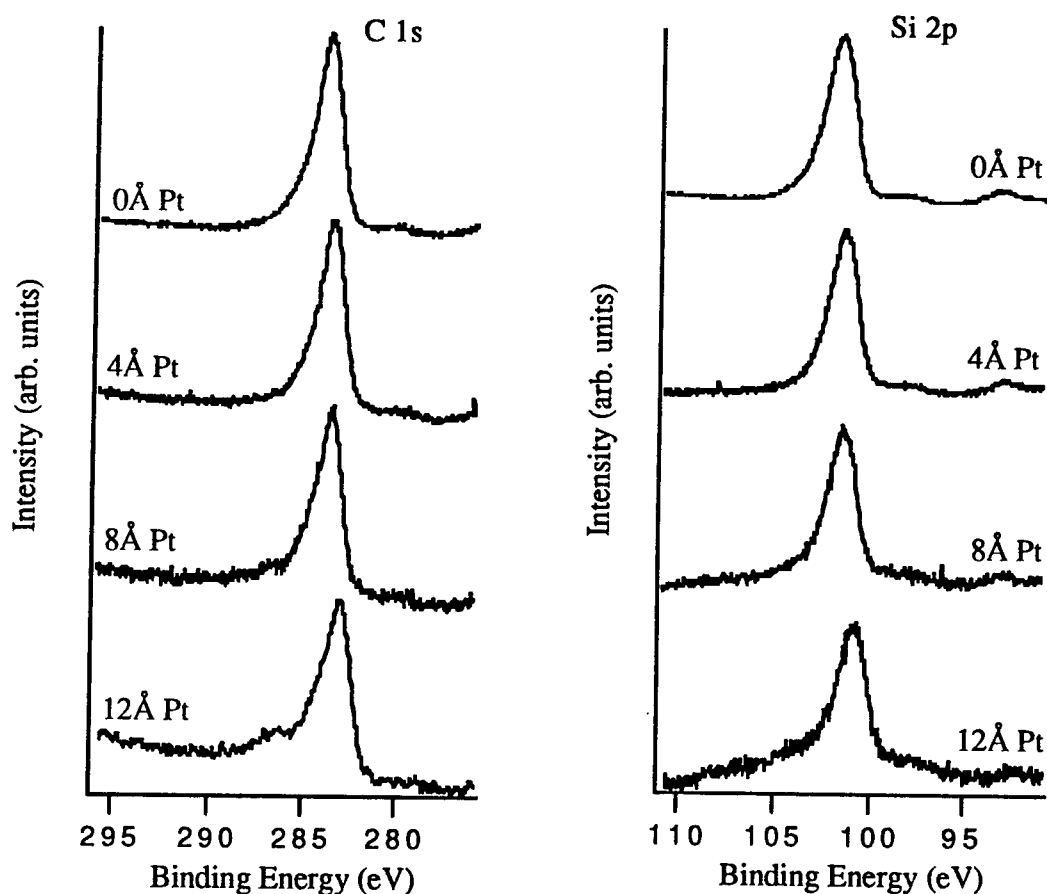


Figure 5. XPS C 1s and Si 2p photoelectron peaks from SiC (0001) before and after deposition of 4, 8, and 12 Å of Pt.



The possibility that the decreasing binding energies with increasing metal overlayer thickness was a result of a corresponding decrease in sample charging was considered. However, the amount of change in the binding energies as shown in Table I was much larger than the corresponding differences found in clean SiC surfaces, the latter of which were attributed to sample charging. Thus, the results indicate that most of the binding energy changes can be attributed to both increasing coverage and charge transfer from thicker Pt layers. Comparison of the XPS data to the I-V measurements indicates that films thicker than 12 Å should not cause significant, additional changes in the barrier height. Taking the average of the binding energy reductions and adding it to the initial amount of band bending gives a barrier height of  $1.33 \pm 0.1$  eV. This calculated value is 0.27 eV higher than the value calculated from I-V measurements. The possible reason for this discrepancy will be discussed in the following section.

*Microstructure.* Transmission electron microscopy analysis showed that the as-deposited Pt films were random polycrystalline with grain sizes of  $10 \pm 3$  nm (Fig. 6). As the annealing temperature was increased from 450 to 650°C, the  $[111]_{\text{Pt}} \parallel [0001]_{\text{SiC}}$  oriented grains grew at the expense of the other grains. The average grain sizes after annealing at 550 and 650°C were 40 and 65 nm, respectively. The increase in grain size may be observed by comparing Fig. 7, which shows a cross-sectional TEM micrograph of a sample annealed at 650°C, to Fig. 6. No evidence of an interface reaction zone was observed via HRTEM in any of the samples annealed at or below 650°C; however, a limited amount of interdiffusion was detected in the samples annealed at 650°C. Platinum had diffused several nanometers into the SiC at some localized regions. Some steps a few nanometers thick were also observed at the interface. The crystallographic relationships between Pt and SiC in these latter samples were determined from SAD patterns of a sample in cross-section:

$$[011]_{\text{Pt}} \parallel [11\bar{2}0]_{\text{SiC}}$$

$$(111)_{\text{Pt}} \parallel (0001)_{\text{SiC}}$$

$$[111]_{\text{Pt}} \parallel [0001]_{\text{SiC}}$$

$$(220)_{\text{Pt}} \parallel (11\bar{2}0)_{\text{SiC}}$$

The mismatch between Pt and SiC was  $\{|d_{(220)\text{Pt}} - d_{(11\bar{2}0)\text{SiC}}| + d_{(11\bar{2}0)\text{SiC}}\} \times 100\% = 9.70\%$ . Although this mismatch is not small, the mismatches between other low index crystal planes of Pt and SiC are even higher. Table II lists the calculated lattice mismatches between some of the low index crystal planes. These results indicate that the preferential grain growth with annealing occurred in order to decrease the strain associated with the interface.

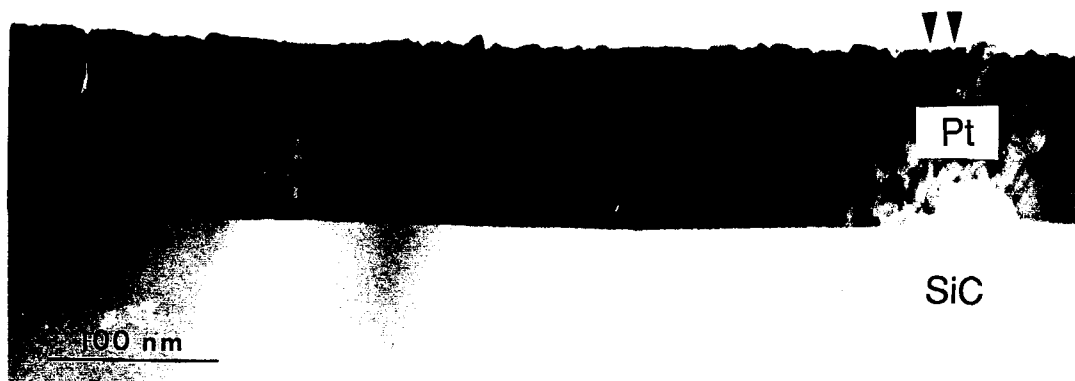


Figure 6. Cross-sectional TEM image of Pt deposited at room temperature onto 6H-SiC (0001). The average grain size of the Pt film was 10 nm.



Figure 7. Cross-sectional TEM image of Pt/SiC annealed at 650°C for 20 min. The arrows delineate the grain boundaries. The average grain size of the Pt film was 65 nm.

The evolution in the preferred orientation of the Pt grains noted above may be correlated with the increasing SBH determined via I-V measurements as a function of annealing temperature to 650°C (Fig. 3) by comparing SBH's determined from XPS and I-V measurements. The smaller value calculated for the as-deposited sample from the latter technique is likely due to inhomogeneities at the polycrystalline metal-semiconductor interface produced by the variety of grain orientations, interfacial strain, defects, and/or trace O (~3 at. %) detected at the the interface by PEELS. The microstructural inhomogeneities are believed to cause variations in the SBH as a function of position along the interface.

Table II. Calculated lattice mismatches between low index planes in Pt and 6H-SiC.

(h k l)SiC	d-spacing (Å)	(h k l)Pt	d-spacing (Å)	mismatch (%)
(1 $\bar{1}$ 00)	2.661	(111)	2.2650	14.88
(1 $\bar{1}$ 00)	2.661	(200)	1.9616	26.28
(1 $\bar{1}$ 00)	2.661	(220)	1.3875	47.86
(11 $\bar{2}$ 0)	1.5365	(111)	2.2650	47.41
(11 $\bar{2}$ 0)	1.5365	(200)	1.9616	27.67
(11 $\bar{2}$ 0)	1.5365	(220)	1.3875	9.70

Current-transport at inhomogeneous interfaces is dominated by the regions with the lowest SBH, which results in calculated SBH's from I-V measurements which are lower than the arithmetic average of the entire interface.[8-13] This phenomenon would explain why the SBH calculated from I-V measurements was 0.27 eV lower than that calculated from XPS analyses, the latter of which should yield a value closer to the average value. While capacitance-voltage measurements should also yield a value closer to the average SBH, the results were bias dependent and somewhat erratic, a result which also may be due to the resulting microstructure.

Both the randomness of the grain orientations and the interfacial O decreased after annealing. This change was accompanied by and directly correlated with an increase in the SBH calculated from I-V measurements.

Interfaces along which the SBH varies usually are associated with ideality factors which are bias dependent; however, interfaces which contain a distribution of low SBH areas, as opposed to one large area, display much less dependence of the ideality factor on bias.[13] Bias dependence of the ideality factors was not found for the Pt contacts below voltages at which the current became limited by the resistance of the SiC. The Pt contacts before and after annealing displayed low ideality factors over three to four decades of current. The electrical properties, along with the observation of the small grain size in the Pt films, indicate that inhomogeneities in microstructure and SBH exist and are finely-dispersed throughout the interface.

*Chemistry.* The annealed Pt/SiC interfacial chemistry has been investigated with high resolution TEM and its associated analysis techniques. After annealing at 750°C for 20 min., a 45 nm thick reaction zone formed as shown in Fig. 8. This zone was composed of an amorphous, irregular-shaped, white phase layer of C and a dark, crystalline Pt<sub>2</sub>Si phase. Parallel electron energy loss point spectra of this sample indicated that the C phase also contained trace amounts of Pt. Particles of C with diameters of 0.5 to 2.0 nm were also distributed throughout the otherwise unreacted Pt film.

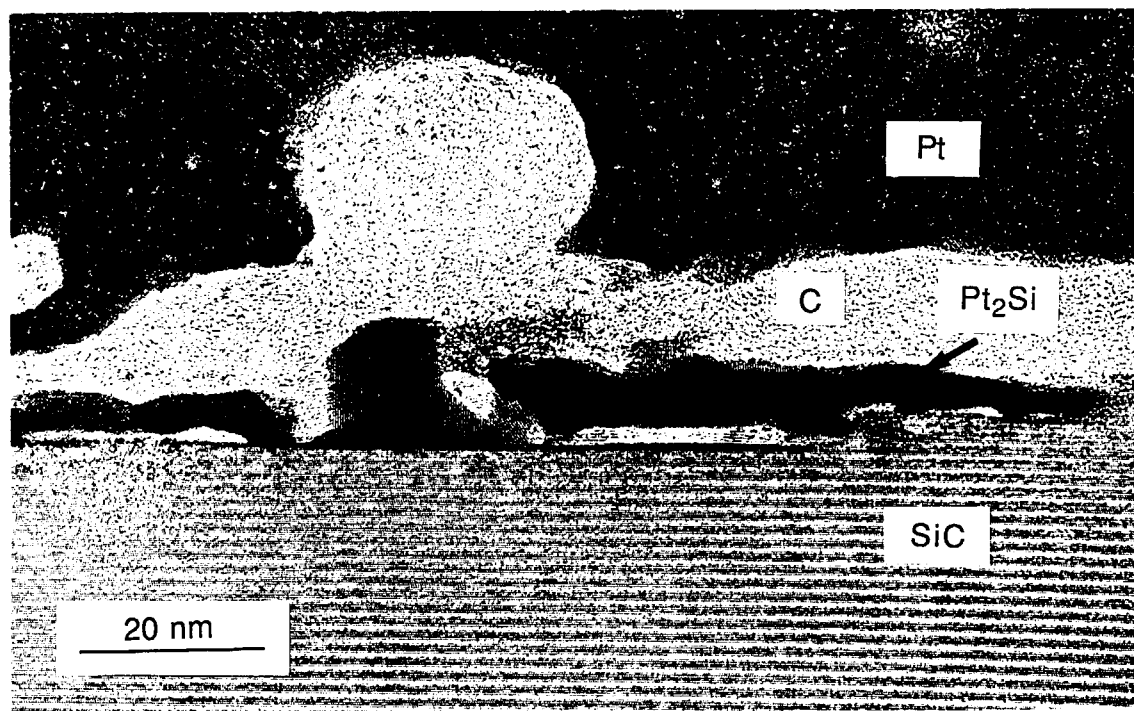


Figure 8. High resolution TEM image of the Pt/SiC interface after annealing at 750°C for 20 min.

Two sets of orthogonal d-spacings of 0.2015 and 0.2785 nm were measured from both optical digital diffraction patterns and micro-diffraction patterns. These experimentally determined d-spacings matched within 0.5% the orthogonal planes with d-spacings  $d_{(1\bar{1}2)} = 0.2025$  nm and  $d_{(110)} = 0.2781$  nm in Pt<sub>2</sub>Si. The platinum silicide was epitaxially related to the SiC with  $[1\bar{1}2]_{\text{Pt}_2\text{Si}} \parallel [0001]_{\text{SiC}}$  and  $[110]_{\text{Pt}_2\text{Si}} \parallel [1\bar{1}00]_{\text{SiC}}$ .

It can also be seen from Fig. 8 that neither the amorphous phase nor the Pt<sub>2</sub>Si phase was completely isolated from either the Pt or the SiC. Most of the SiC contacted Pt<sub>2</sub>Si. However, there were also some regions where the amorphous C phase made contact with the SiC. There were also tunnels (darker gray) through the C-rich phase where Pt<sub>2</sub>Si connected to the Pt phase. The most important interface in terms of electrical properties is, of course, the interface with SiC. As discussed above, most of this interface was comprised of epitaxial Pt<sub>2</sub>Si,

indicating that most of the interface has very high structural quality. On the other hand, the C phase which comprises the remainder of the interface has not resulted in a degradation in the electrical properties of the annealed contacts.

These results are to be compared with those of Chou [1] who produced diffusion couples from hot-pressed  $\beta$ -SiC and Pt of about 1 to 2 mm thickness and annealed them in flowing He at 900 and 1000°C for various times. Scanning electron microscopy and energy dispersive spectrometry showed that the interface contained periodic layers of Pt<sub>3</sub>Si and C. Pt<sub>2</sub>Si did not form until after annealing at 1000°C for an unspecified time. These results are in contrast to the results in the present study in which Pt<sub>2</sub>Si, the first silicide observed, formed at 750°C. Differences between these two studies include the SiC polytypes, sample thicknesses, and the annealing conditions. All or one of these differences may explain the differing results; however a definitive explanation based on the research performed is not known at this time.

Localized chemical bonding at the interface for the as-deposited interface was investigated with XPS. Platinum-carbon bonding was not expected to form since there are no equilibrium platinum carbides [14], and the Pt-C bond has been theoretically determined to be very weak.[15] As expected, only C-Si bonding was displayed in the C 1s peak after depositing 4, 8, or 12 Å of Pt. The shifts in the C 1s and Si 2p binding energies (Fig. 5) are attributed to changes in band bending.

The results regarding silicide formation were somewhat inconclusive. Deconvolution of the Pt 4f<sub>7/2</sub> and 4f<sub>5/2</sub> peaks revealed two chemical bonding states. The binding energy due to the major bonding state was 70.94 - 71.58 eV, and that for the minor bonding state was 72.12 - 72.76 eV. The major bonding state is attributed to Pt-Pt bonding.[16] The minor peak at the higher binding energy could be due to either Pt-Si [16] or Pt-O bonding. The reported Si 2p binding energies for Si-bound-to-Pt in Pt silicide (e.g., Pt<sub>2</sub>Si and PtSi [16]) and for Si-bound-to-C in SiC [17] are virtually identical. Therefore, it cannot be confirmed from the Si 2p peak whether a Pt silicide formed. There is, however, indication from the Si 2p peak that the oxygen present at the SiC surface before deposition of Pt remained at the interface after the depositions.

Bermudez and Kaplan [3] thermally evaporated thin layers ( $\leq 8$  Å) of Pt onto  $\beta$ -SiC (001). Preliminary results for Pt on  $\beta$ -SiC (111) and  $\alpha$ -SiC (0001) were also reported. Prior to deposition of Pt, the substrates were dipped in HF and cleaned in alcohol. An atomic oxygen concentration of 3.5% was found in all Pt films deposited on  $\beta$ -SiC (001) substrates at low temperature (sample temp.  $\approx 270^\circ\text{C}$  due to radiative heating from the Pt source). Somewhat smaller oxygen concentrations (2.5%) were found in films deposited on  $\alpha$ -SiC (0001). The authors suggested that the O contamination resulted from "dissociative adsorption of H<sub>2</sub>O in the UHV background."

In the unannealed Pt films deposited in this work, a trace amount of O ( $\approx 3$  at. %) localized at the interface was detected by PEELS. This result is in good agreement with that of Bermudez and Kaplan and indicates that Pt-O bonding contributed to the second bonding state revealed in the XPS analyses. However, considering the  $\approx 30\%$  contribution of the minor Pt  $4f_{7/2}$  peak to the total integrated peak area, Pt-Si bonding was also likely present. Furthermore, the fact that the percent contribution did not decrease significantly with increasing Pt thickness suggests that there may have been some intermixing of Pt and Si.

#### D. Conclusions

A study of the chemistry, microstructure, and electrical properties at interfaces between Pt and monocrystalline, n-type 6H-SiC (0001) was performed for the specific application of contacts in SiC devices. The room temperature deposition of Pt by UHV electron beam evaporation onto these chemically and thermally cleaned substrates resulted in excellent Schottky contacts, which were characterized by low ideality factors ( $n < 1.1$ ) and leakage currents of  $5 \times 10^{-8}$  A/cm<sup>2</sup> at -10 V. The SBH's calculated from I-V measurements (1.06 to 1.26 eV) increased after each successive 20 min. anneal at 450, 550, 650, and 750°C with a corresponding reduction in the leakage currents.

The as-deposited films were polycrystalline with an average grain size of  $10 \pm 3$  nm. Increasing the annealing temperature from 450 to 650°C caused the [111] Pt grains to grow at the expense of the other grains to an average size of 65 nm. The increase in the SBH's calculated from I-V measurements was attributed to this grain growth and corresponding increase in the film homogeneity.

The first reaction phases, crystalline Pt<sub>2</sub>Si and an amorphous C phase, were observed to form between the Pt and the SiC after annealing at 750°C. The interfacial reaction should reduce any adherence problems associated with Pt contacts deposited in non-UHV environments, a problem which has been expressed by a number of scientists. In this study the excellent electrical properties after annealing have shown Pt to be a viable choice for Schottky contacts in SiC devices.

#### E. Future Research Plans and Goals

The current technology of SiC devices is driving the need for ohmic contacts to p-type SiC which have low contact resistivities at both room and elevated temperatures. Aluminum alloys are currently used because the Al degeneratively dopes the surface of the SiC, which reduces the contact resistance. However, these contacts cause problems at elevated temperatures due to melting and extensive diffusion.

We are currently investigating three metal systems, one of which should be much more stable at elevated temperatures. The materials, which are comprised of 2-3 components, were chosen based on chemistry and doping considerations in addition to thermal stability. All three

contact materials have been deposited onto p-type (and in one case n-type) 6H-SiC and have been characterized electrically after annealing at low-moderate temperatures.

Annealing at or near 1000°C has been performed on the contact material with high thermal stability. This system has already shown ohmic behavior. Once the preliminary studies involving annealing conditions and electrical properties have been performed, the chemistry and physics of these interfaces will be thoroughly investigated to understand the mechanisms related to the electrical behavior. The contact resistivity will also be measured as a function of both carrier concentration and temperature.

#### F. Acknowledgments

The authors would like to thank the Office of Naval Research under Contracts N00014-92-J-1500 and N00014-92-J-1477 for funding the research performed at NCSU. The research performed at ASU was supported by NSF-DMR-8901841. The microscopy was performed at the NSF/ASU HREM facility under grant NSF-DMR-9115680.

#### G. References

1. T.C. Chou, J. Mater. Res., **5**, 601 (1990).
2. T.C. Chou, A. Joshi, and J. Wadsworth, J. Mater. Res., **6**, 796 (1991).
3. V.M. Bermudez and R. Kaplan, J. Mater. Res., **5**, 2882 (1990).
4. N.A. Papanicolaou, A. Christou, and M.L. Gipe, J. Appl. Phys., **65**, 3526 (1989).
5. M. Bhatnagar, P.K. McLarty, and B.J. Baliga, IEEE Elec. Dev. Lett., **13**, 501 (1992).
6. W.O. Saxton, T.J. Pitt, and M. Horner, Ultramicroscopy, **4**, 343 (1979).
7. L.M. Porter, J.S. Bow, R.C. Glass, M.J. Kim, R.W. Carpenter, and R.F. Davis, J. Mater. Res., In Press.
8. I. Ohdomari and K.N. Tu, J. Appl. Phys., **51**, 3735 (1980).
9. J.L. Freeouf, T.N. Jackson, S.E. Laux, and J.M. Woodall, J. Vac. Sci. Technol., **21**, 570 (1982).
10. J.M. Woodall and J.L. Freeouf, J. Vac. Sci. Technol., **21**, 574 (1982).
11. R.T. Tung, Appl. Phys. Lett., **58**, 2821 (1991).
12. J.H. Werner and H.H. Guttler, J. Appl. Phys., **69**, 1522 (1991).
13. R.T. Tung, Phys. Rev. B, **45**, 13509 (1992).
14. *Binary Alloy Phase Diagrams* 2nd ed. (ASM International, Materials Park, Ohio, 1990), Vol. 1, edited by T.B. Massalski, H. Okamoto, P.R. Subramanian, and L. Kacprzak.
15. A.B. Anderson and C. Ravimohan, Phys. Rev. B, **38**, 974 (1988).
16. P.J. Grunthaner, F.J. Grunthaner, and A. Madhukar, J. Vac. Sci. Technol., **20**, 680 (1982).
17. K.L. Smith and K.M. Black, J. Vac. Sci. Technol. A, **2**, 744 (1984).

## VII. Diamond Deposition Using a Planar Radio Frequency Inductively Coupled Plasma

### A. Introduction

A substantial amount of research has been undertaken in the field of diamond chemical vapor deposition (CVD) because of diamond's unique and extreme properties. One of the present areas of development in diamond CVD is the production of uniform films over large areas. Large area deposition has been pursued using a number of techniques, including flat flame combustion burners [1], hot filament arrays [2], scanned combustion torches [3], and RF torches [4]. This report describes a new deposition method with the possibility of improved scaling to large area coverage using planar radio frequency (RF) inductively coupled plasma (ICP).

Growth of diamond films using RF inductively coupled plasmas has been reported by several researchers [5,6]. This growth method is attractive because of the high plasma densities and high growth rates which have been achieved using it. In addition, high power RF sources are significantly less expensive per kW than microwave sources. Growth over large areas has also been examined in this system, and deposition over areas as large as 4" in diameter has been reported using a rotating substrate and RF torch [4]. Ultimately, however, the scalability of systems based on conventional helical induction coils is limited by the RF skin depth.

This limitation arises in the conventional RF inductively coupled geometry consisting of a solenoidal coil generating a plasma which impinges on a downstream substrate. At the pressures typically used for diamond deposition ( $> 1$  Torr), the RF skin depth and electron and ion diffusion lengths are of the order of a few centimeters. As the diameter of the coil becomes large compared to the skin depth, the plasma tends to form only at the walls of the tube, producing a ring-shaped discharge [7]. Consequently, there is a strong variation in the rate and nature of the deposition over a substrate oriented perpendicular to the axis of the RF coil.

The planar RF ICP has been developed recently to overcome this limitation and applied to large area semiconductor processing [8]. It consists of a spiral coil wound in a plane rather than around a cylinder and has primarily been used at relatively low pressures ( $< 100$  mTorr) for etching, plasma surface treatments, and deposition of diamond-like carbon (DLC) [9,10]. In processing devices using the new geometry, the coil and substrate are in parallel planes and the primary skin effect gradients are perpendicular to the substrate and should not lead to inhomogeneities across the substrate surface. Therefore, the planar induction coils may scale to large plasmas of uniform cross section more easily than the standard helical coil.

This report describes the growth of well faceted diamond particles using such a planar RF ICP. The studies reported here include observations of particle morphology, quality and area of deposition as a function of methane/hydrogen ratio and substrate position in the plasma. The



use of a planar RF ICP is expected to facilitate the future scaling of RF plasma based diamond deposition systems to cover larger substrates. It should be emphasized, however, that film morphology and quality rather than uniformity are the focus of this preliminary work. In fact, the spiral coil produces relatively weak electric fields on axis so that plasma generation is inhomogeneous. This inhomogeneity is the result of the particular spiral configuration rather than the skin depth attenuation of the RF radiation. Separate experimental investigations [11] have shown that the plasma uniformity can be improved by using flat coil configurations which are substantially different from the spiral geometry.

#### B. Experimental Procedure

The deposition system used in this work (Fig. 1) consists of a quartz vessel attached to a stainless steel chamber via a viton gasket. The spiral induction coil is placed against the flat upper surface of the quartz, resulting in a separation of 6 mm between the coil and plasma. The center of the coil is connected to a RF generator (13.6 MHz) via an impedance matching network and the outside of the coil is grounded to the chamber. Deposition experiments were carried out at 4 Torr. In pure argon at this pressure the discharge is roughly the shape of a hemisphere. When the methane and hydrogen are added, the plasma contracts to a torus with a major diameter of about 7 cm and a minor diameter of about 3 cm. The major diameter of the torus is about half the diameter of the coil (6 cm). The extent of the torus coincides with the region of strongest induced electric field which also occurs at about half the coil diameter [12].

The molybdenum substrate holder is electrically isolated and is attached to a stainless steel positioning rod via an insulating BN spacer. Substrate heating is provided by the plasma. The temperature of the substrate holder was measured by an infrared pyrometer and sampled from the side. It was not possible to view the surface of the sample during growth because of obstruction by the coil and plasma.

The deposition experiments were performed at 1kW of RF power in a mixture of argon, methane and hydrogen at a total pressure of 4 Torr. The argon was added to sustain the plasma and its concentration was fixed at 95%, while the ratio of methane to hydrogen and the position in the plasma were varied. Deposition was performed on 2 and 4 inch silicon wafers which were pretreated by scratching with diamond particles and wet cleaning to remove the residue. The deposition time was 8 hours.

Table I summarizes the conditions under which samples (A) through (D) were grown. The ratio of hydrogen to methane and the distance between the substrate and window were varied. The distance of 1.5 cm corresponds to growth immersed in the plasma, with the substrate approximately 0.5 cm inside the area of most intense optical emission from the plasma. The distance of 2.5 cm corresponds to remote growth with the substrate about 0.5 cm below the

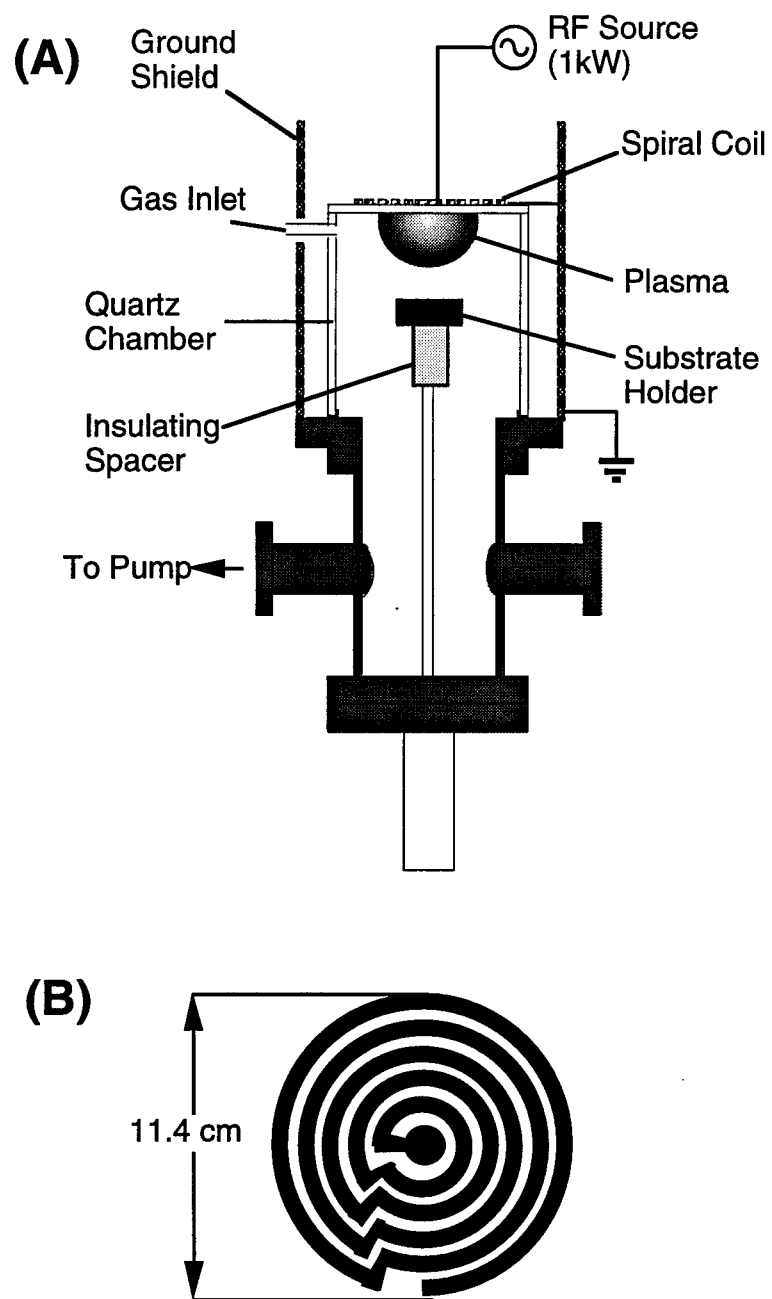


Figure 1. Schematic diagram of planar radio frequency inductively coupled plasma deposition system (a), and detail of spiral induction coil (b).

region of brightest emission from the plasma. The temperature of the substrate holder varied from 550 to 600°C during these runs.

Table I. Deposition conditions for the samples discussed in the text.

Samples	CH <sub>4</sub> /H <sub>2</sub> (%)	Distance From Window (cm)
A	1.7	1.5
B	3.5	1.5
C	1.7	2.5
D	3.5	2.5

The RF power was 1kW and the deposition time 8 hours. The total pressure of argon, methane, and hydrogen was 4 Torr, and the argon concentration was 95%.

### C. Results

Deposition of either diamond or diamond-like carbon occurred under all of the conditions listed and SEM micrographs of these films are shown in Fig. 2. The particle morphology was uniform across the films, while the nucleation density varied across the wafer with the highest nucleation density near the discharge region. The particle morphologies varied substantially between the various deposition conditions but were reproducible. The highest quality films as determined from Raman and SEM were obtained at low methane concentration with the substrate immersed in the plasma (sample (A)) and consisted of well-faceted particles about 1  $\mu\text{m}$  in size. While this particle size after the eight hour growth time corresponds to a growth rate  $\leq 0.2 \mu\text{m/hr}$ , the growth rate could probably be improved by increasing the power density and reducing the argon dilution. At higher methane concentrations when the substrate was still immersed (B), facets could also be observed but the particles exhibited a greater amount of twinning. This change in morphology has also been observed with increasing methane concentration in other deposition systems [14]. The deposits on the remote substrates were nanocrystalline films (C) and highly twinned clusters (D). Thus, the only faceted particles were grown with the substrate immersed in the plasma.

Raman spectra were also measured for samples (A) through (D). The Raman spectra of the films varied more from point to point than did the morphology, probably because of the small amount of material present. Figure 3 shows a spectrum from a film grown under the conditions of sample (A) which exhibits a peak at  $1332 \text{ cm}^{-1}$ , characteristic of diamond. The Raman spectrum also shows a luminescent background and features characteristic of non-diamond carbon [14].

To better characterize the deposition pattern and area, two additional films were grown on 4" wafers under conditions similar to samples (A) and (D). In both cases the deposition pattern was an annulus similar in size to the plasma. The smaller deposition ring was observed on the

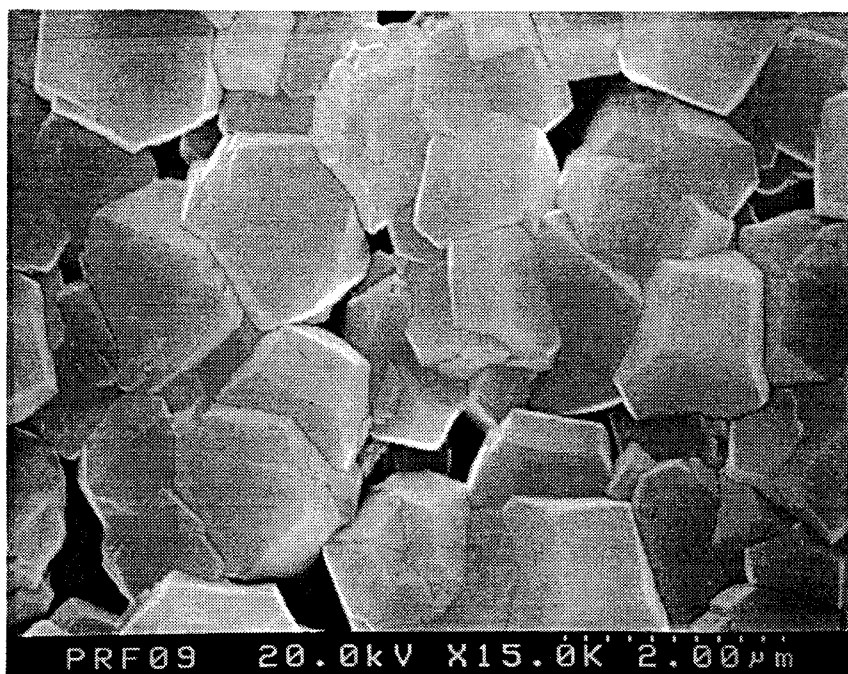


Figure 2 (a). SEM micrograph of diamond film produced on sample (A).

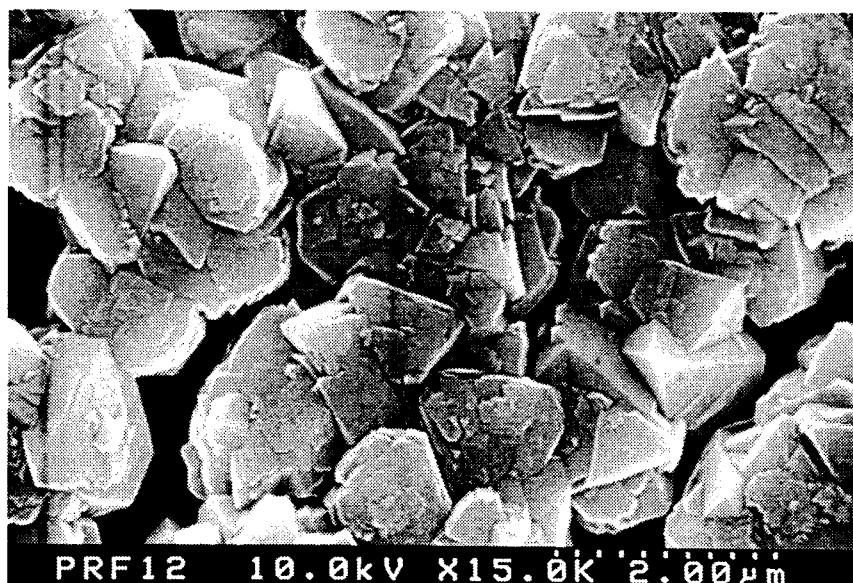


Figure 2 (b). SEM micrograph of diamond film produced on sample (B).

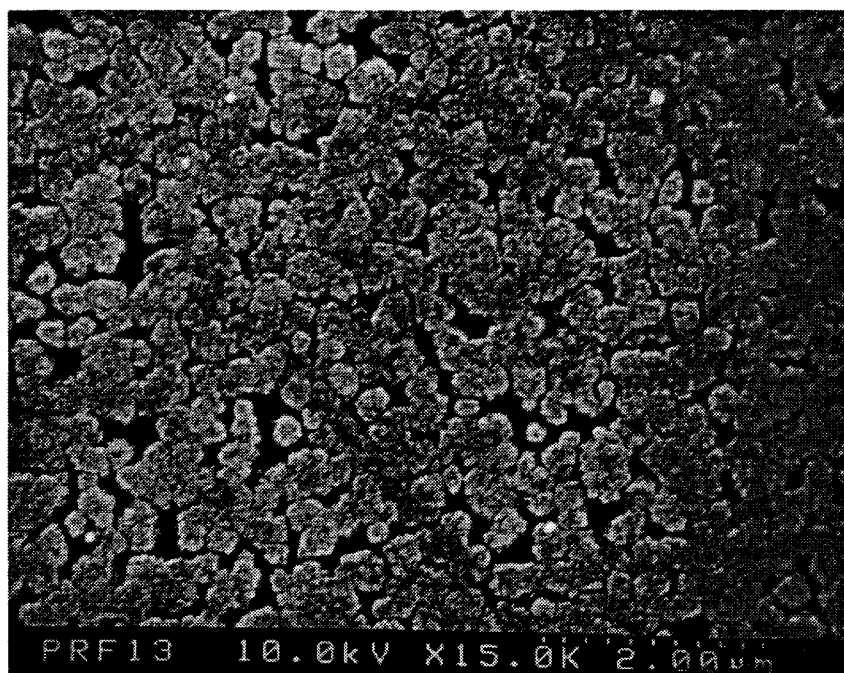


Figure 2 (c). SEM micrograph of diamond film produced on sample (C).

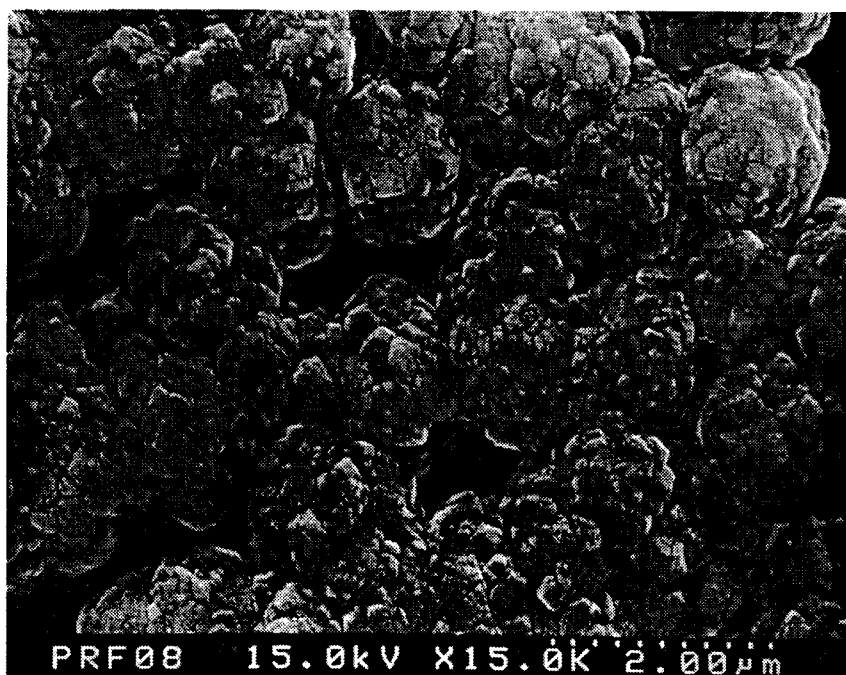


Figure 2 (d). SEM micrograph of diamond film produced on sample (D).

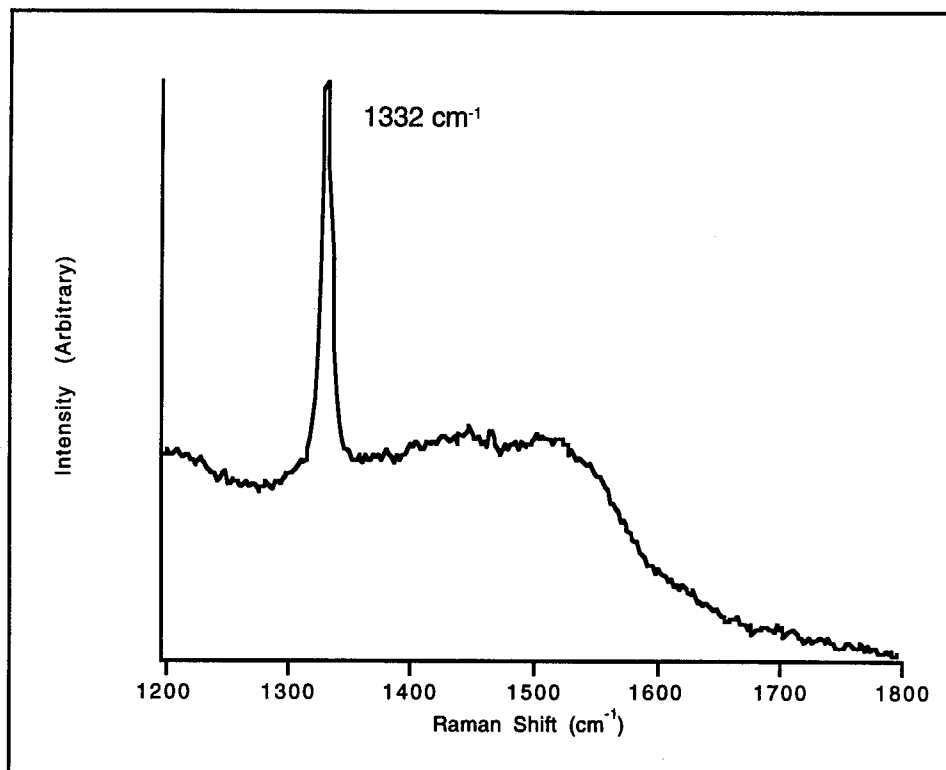


Figure 3. Raman spectrum of film grown in planar RF ICP system, showing diamond peak at  $1332\text{ cm}^{-1}$ .

immersed sample and was 1.2 cm wide and 9.6 cm in outer diameter. The deposition area of the remote sample was larger, being 2.6 cm wide and 9.4 cm in outer diameter.

#### D. Conclusions

In summary, the first diamond deposition using a planar RF ICP has been achieved. The use of a planar RF ICP is expected to facilitate the future scaling of plasma based diamond deposition systems to cover larger areas. Deposition occurs in an annulus which corresponds with the area of most intense optical emission from the plasma. It appears to be necessary to immerse the substrate in the plasma to produce high-quality diamond films as determined via SEM and Raman spectroscopy. Future work will include further characterization of the deposition parameters and attempts to increase the deposition area.

The authors wish to thank A. Somashekhar and R. J. Nemanich of North Carolina State University and Glenn Tessmer of Kobe Steel USA Inc. for measurement of the Raman spectra. Helpful discussions with T. L. Munsat, and S. Washburn of the University of North Carolina at Chapel Hill are gratefully acknowledged. A portion of the equipment necessary for the

construction of the deposition system was loaned by UNC-Chapel Hill. This work was partially supported by the University Research Initiative through the Office of Naval Research.

#### E. Future Research Plans and Goals

Future work will include further characterization of the deposition parameters and attempts to increase the deposition area. It may be possible to improve the uniformity of the deposition via off axis rotation of the substrate or by utilizing alternate coil geometries [7].

#### F. References

1. N. G. Glumac and D. G. Goodwin, *Materials Letters* **18**, 119-122 (1993).
2. L. Schäffer, M. Sattler, and C. P. Klages in *Applications of Diamond Films and Related Materials*, ed. Y. Tzeng, M. Yoshikawa, M. Murakawa, and A. Feldman (Elsevier, 1991) p. 453.
3. Y. Tzeng, R. Phillips, C. C. Tin, Y. Chen, T. Srivinyunon, and C. Cutshaw in *Diamond, Silicon Carbide, and Related Wide Bandgap Semiconductors*, ed. J. T. Glass, R. Messier, and N. Fujimori (MRS: Pittsburgh, 1990) p. 145.
4. M. Kohzaki, K. Uchida, K. Higuchi, and S. Noda, *Japanese Journal of Applied Physics*, **32**, L438 (1993).
5. S. Matsumoto, *Journal of Materials Science Letters* **4**, 600 (1985).
6. M. A. Capelli, T. G. Owano, and C. H. Kruger, *Journal of Materials Research* **5**, 2326 (1990).
7. Boulos, *Pure and Applied Chemistry* **57**, 1321-1352 (1985).
8. J. Hopwood, *Plasma Sources Science and Technology* **1**, 109-116 (1992).
9. D. L. Pappas and J. Hopwood, *Journal of Vacuum Science and Technology A* **12**, 1576-1581 (1994).
10. D. F. Beale, A. E. Wendt, and L. J. Mahoney, *Journal of Vacuum Science and Technology A* **12**, 2775-2779.
11. T. Munsat, W. M. Hooke, S. P. Bozeman, and S. Washburn, submitted to *Applied Physics Letters* (1994).
12. J. Hopwood, C. R. Guarnieri, S. J. Whitehair, and J. J. Cuomo, *Journal of Vacuum Science and Technology A* **11**, 147-151 (1993).
13. K. Kobashi, K. Nishimura, Y. Kawate, and T. Horiuchi, *Phys. Rev. B* **38**, 4067 (1988).
14. D. S. Knight and W. B. White, *Journal of Material Research* **4**, 385-393 (1989).

## VIII. Bias-enhanced Nucleation of Highly Oriented Diamond on TiC(111)

### A. Introduction

Diamond has received much attention for use in a wide variety of applications. These include tribological, thermal management, optical, and microelectronic applications. In order to exploit this material's extreme properties, high quality diamond crystals must be formed. And in some cases, through process advancements, the properties of synthetic diamond have surpassed those exhibited by natural diamond.[1]

Diamond utilized for microelectronic application such as a semiconductor device is desirable but must contend with other materials possessing similar attributes, such as SiC. Both diamond and SiC exhibit high temperature semiconducting properties allowing for higher current densities, which may be used for higher power or smaller-scale circuitry applications. SiC, however, has undergone much more development and very large bulk crystals of this material may now be formed.

In regards to diamond deposition, epitaxial diamond has been achieved on both cBN and diamond,[2, 3] but these materials are expensive and large area substrates of these materials are difficult to obtain. There has been past research to suggest that diamond heteroepitaxy may be achieved on non-diamond or related substrates, however, the recent deposition on  $\beta$ -SiC, Si, and Ni have shown the most dramatic results.[4-7] In the case of the work conducted on  $\beta$ -SiC and Si, bias-enhanced nucleation (BEN) was used for the formation of these epitaxial diamond crystals.[8, 9] The term highly oriented diamond (HOD) has been used to describe these aligned particles rather than epitaxial diamond since once these particles coalesce, they have been observed to form low angle grain boundaries on the order of  $6^\circ$  to  $10^\circ$ . [8] The origin of this misalignment in the form of particle tilting or azimuthal misorientation is a result of an approximately 20% mismatch at the diamond/SiC interface. Zhu *et al.*[10] have shown that the misfit dislocations that form at the interface account for the misorientation.

It has been revealed through continued research of BEN that the carbide forming nature of the substrate appears to be an important attribute for the effective utilization of this nucleation pretreatment process.[11] Later work, on a study of several refractory metal substrates, indicated that a correlation was observed for both the induction time to the onset of significant diamond nucleation and the nucleation density to material properties exhibited by these metals.[12] It was proposed that this class of material would be likely candidates for further heteroepitaxy studies using BEN.

This letter discusses early results using BEN on single crystal TiC(111) substrates. Also, it was speculated in previous work that the refractory materials may be potential diamond heteroepitaxy substrates when using this unique diamond nucleation pretreatment.[11] In



general, the refractory metals are similar to silicon in the respect that they are carbide formers but quite different in other respects. One of these differences is that TiC, like the other refractory monocarbides, possess a different crystal structure to that of SiC (TiC-rock salt structure; SiC-zinc blende structure). Epitaxial diamond was formed on  $\beta$ -SiC and Si when utilizing this diamond nucleation pretreatment[4] and served as a guide for this research. Similar experimental conditions to the work performed by Stoner *et al.*[9] on  $\beta$ -SiC was used on TiC(111) to investigate the possibility of obtaining diamond heteroepitaxy using BEN.

## B. Experimental Approach

*Sample Preparation.* The substrate material used in these experiments was TiC(111) which was obtained from Advanced Technology Materials, Inc. The single crystal material was cut into 10mm  $\times$  5mm  $\times$  1mm pieces and was polished using 30, 6, 1, and 0.1 $\mu$ m diamond grit followed by 1 hour of polishing using 0.05 $\mu$ m Al<sub>2</sub>O<sub>3</sub> to remove any residual diamond that may have been embedded in the TiC surface. The substrates were subsequently cleaned in acetone, methanol, and isopropanol. Prior to entering into the chemical vapor deposition (CVD) reactor, a de-ionized water rinse was performed.

*Experimental Conditions.* The deposition system which was used in this study was an ASTeX 2.45 MHz, 1.5kW system that has been described in detail elsewhere.[13, 14] The samples were initially cleaned *in situ* in a H<sub>2</sub> plasma for 30 minutes to remove any oxygen present on the surface followed immediately by the BEN process for approximately 10 minutes. Following the *in situ* H<sub>2</sub> plasma cleaning procedure and BEN, the process parameters for yielding well faceted diamond particles were employed. The specific system parameters for each stage of the diamond deposition are listed in Table I.

Table I. System parameters for each process.

System parameter	H <sub>2</sub> plasma clean	BEN	Growth
Power (W)	600	600	600
Pressure (Torr)	25	15	40
CH <sub>4</sub> :H <sub>2</sub> ratio	—	5%	0.2%
Bias current (mA)	—	120	—
Bias voltage (Vdc)	—	225 $\pm$ 10	—
Temperature (°C)	660 $\pm$ 20	785 $\pm$ 20	900
Duration	30 min	10-15 min	8 hours

## C. Results and Discussion

It was observed that the diamond nucleation density was significantly enhanced which supports previous work regarding diamond nucleation via bias enhanced nucleation on carbide

forming substrates.[11] Micrographs (Figs. 1 and 2) taken throughout the substrate showed (111) textured diamond particles having the same orientation to one another. However, a dense region of diamond particles oriented to each other could not be found. Since these particles were oriented to each other across the substrate and to pyramidal etch pits in the TiC(111) surface, it is assumed that these particles are highly oriented with respect to the substrate. These etch pits were observed after the polishing and cleaning procedures.

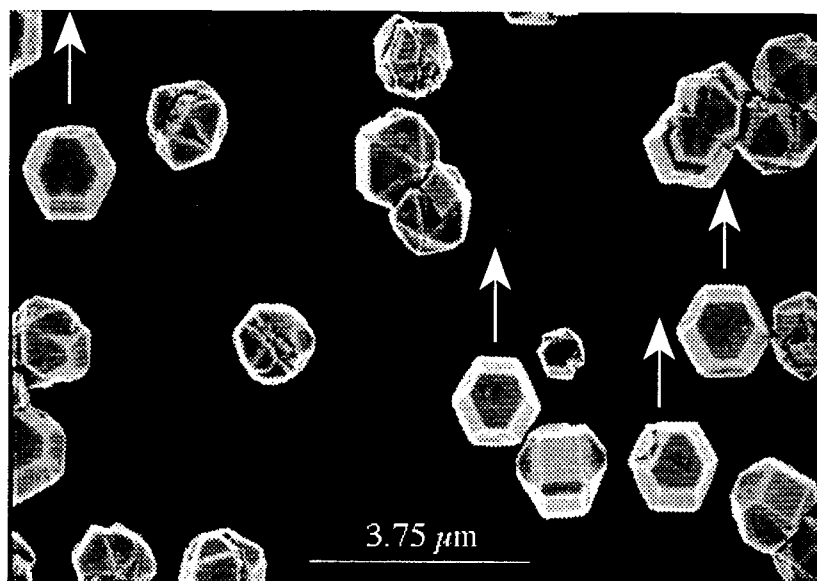


Figure 1. SEM micrograph of oriented diamond particles on the TiC (111) substrate with arrows showing orientation direction. The marker is 3.75μm in length.

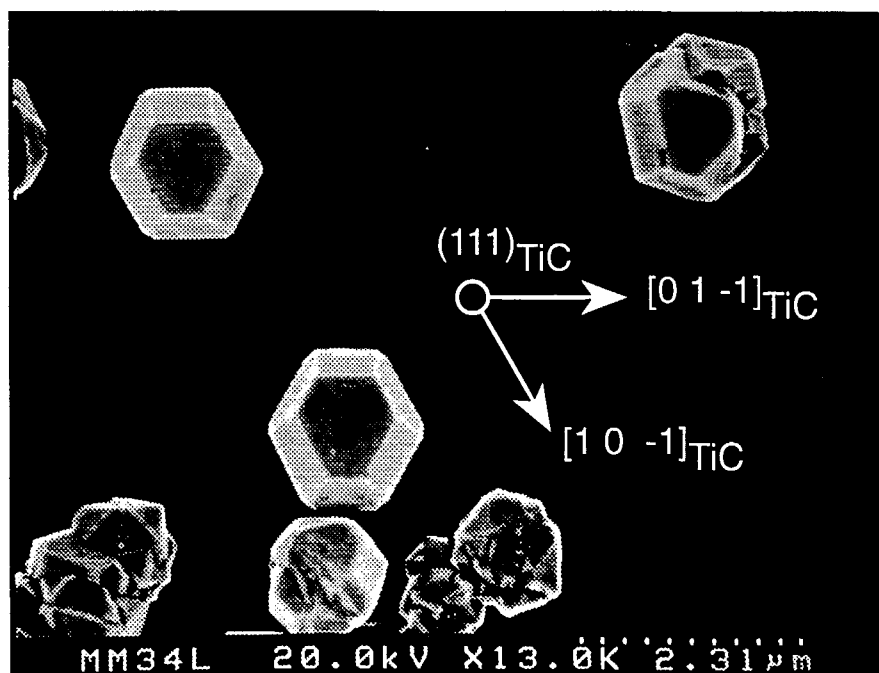


Figure 2. SEM micrograph of oriented diamond particles showing orientation of the TiC(111) substrate

The absence of a dense region with oriented diamond particles may be due the short BEN duration used. A moderate to low nucleation density was preferred to observed diamond particles separated from one another and to prevent coalescence into a complete film. Since the coefficient of thermal expansion are significantly different for TiC and diamond, delamination would have occurred upon the formation of a complete film. Also, the deposition conditions used for the growth of well faceted diamond crystals were not optimized and twinning on the diamond (111) face resulted. Therefore, a short BEN duration and growth conditions not favorable for suppressing twinning on the (111) face resulted in the low density of oriented diamond particles. The Raman spectra of the diamond particles in shown in Fig. 3 and indicates the characteristic diamond feature at  $1332\text{ cm}^{-1}$ . The  $1480\text{ cm}^{-1}$  and  $1602\text{ cm}^{-1}$  features are indicative of  $\text{sp}^2$ -bonded carbon and may be a result of the large occurrence of twinning.

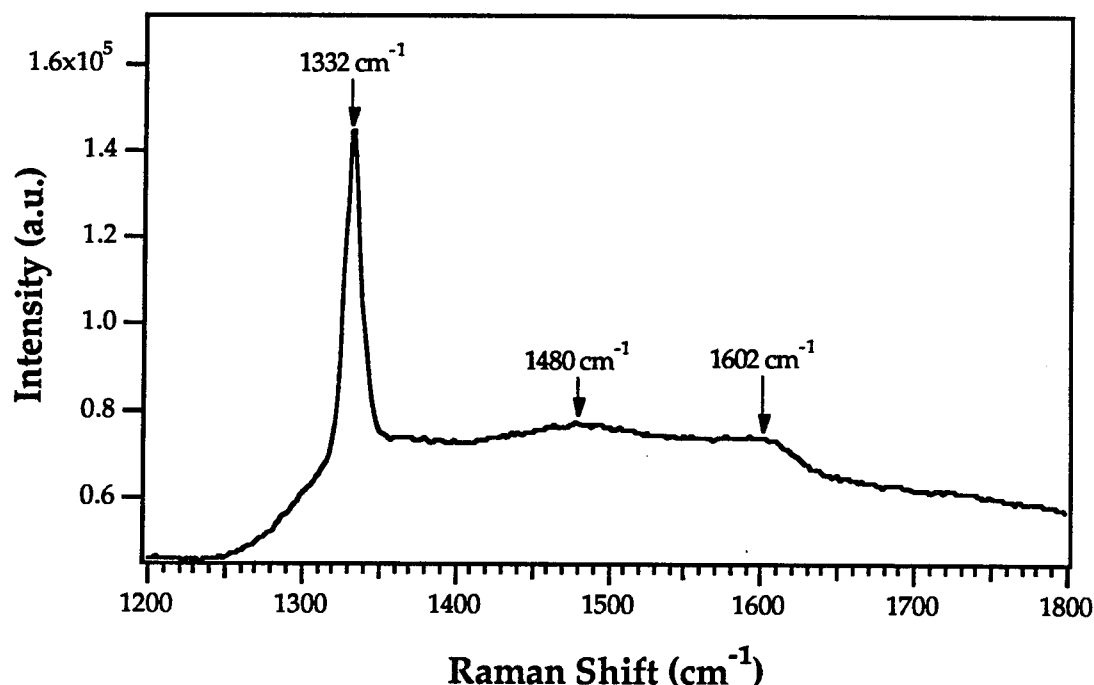


Figure 3. Micro-Raman spectrum of the diamond particles on the TiC(111) substrate. The spectrum shows a sharp peak at  $1332\text{ cm}^{-1}$  characteristic of diamond and the features at  $1480\text{ cm}^{-1}$  and  $1602\text{ cm}^{-1}$  are characteristic of  $\text{sp}^2$ -bonded carbon.

#### D. Conclusions

Bias enhanced nucleation was utilized on TiC(111) single crystal substrates in order to explore the possibility of obtaining epitaxial diamond. This nucleation pretreatment process was observed to enhance the diamond nucleation density on this material. This supports previous work in this area claiming that the carbide forming nature of the substrate is important in order to obtain enhanced nucleation of diamond. A preferred orientation of diamond (111)

textured particles was observed on the TiC(111) substrate. These particles were observed to be aligned with the substrate in the  $\langle 110 \rangle$  direction.

#### E. Acknowledgments

The authors wish to thank Advanced Technologies and Materials, Inc. for supplying the substrates. This work was funded by the Ballistic Missile Defense Organization/Innovative Science and Technology program through the Office of Naval Research.

#### F. References

1. T. R. Anthony, W. F. Banholzer, J. F. Fleischer, L. Wei, P. K. Kuo, R. L. Thomas and R. W. Pryor, *Phys. Rev. B*, **42** (1990) 1104-1111.
2. M. Kamo, H. Yurimoto and Y. Sato, *Proceedings of the Fourth International Conference on Solid Films and Surfaces (ICSFS-4)*, Hamamatsu, Jpn., 1987 Aug 23-27, **33-34** (1988) 553-560.
3. S. Koizumi, T. Murakami, T. Inuzuka and K. Suzuki, *Appl. Phys. Lett.*, **57** (1990) 563.
4. B. R. Stoner, Doctor of Philosophy, North Carolina State University, 1992.
5. B. R. Stoner and J. T. Glass, *Appl. Phys. Lett.*, **60** (1992) 698-700.
6. P. C. Yang, W. Zhu and J. T. Glass, *J. of Mat. Res.*, **8** (1993) 1773-1776.
7. S. D. Wolter, B. R. Stoner, J. T. Glass, P. J. Ellis, D. S. Buhaenko, C. E. Jenkins and P. Southworth, *Appl. Phys. Lett.*, **62** (1993) 1215.
8. B. R. Stoner, S. R. Sahaida, J. P. Bade, P. Southworth and P. J. Ellis, *J. Mat. Res.*, **8** (1993) 1334-1340.
9. B. R. Stoner, G. H. Ma, S. D. Wolter, W. Zhu, Y.-C. Wang, R. F. Davis and J. T. Glass, *Diamond and Relat. Mater.*, **2** (1993) 142.
10. W. Zhu, X. H. Wang, B. R. Stoner, G. H. M. Ma, H. S. Kong, M. W. H. Braun and J. T. Glass, *Phys. Rev. B*, **47** (1993) 6529-6542.
11. S. D. Wolter, B. R. Stoner and J. T. Glass, *Diamond and Relat. Mater.*, **3** (1994) 1188.
12. S. D. Wolter, Master of Science, North Carolina State University, 1994.
13. B. R. Stoner, G.-H. M. Ma, S. D. Wolter and J. T. Glass, *Phys. Rev. B*, **45** (1992) 11067.
14. B. R. Stoner, B. E. Williams, S. D. Wolter, K. Nishimura and J. T. Glass, *J. Mat. Res.*, **7** (1992) 257.

## IX. Fluorine-based Mechanisms for ALE Growth on Diamond (110)

M.G. Wensell, Z. Zhang and J. Bernholc

*Department of Physics, North Carolina State University, Raleigh, North Carolina 27695-8202*

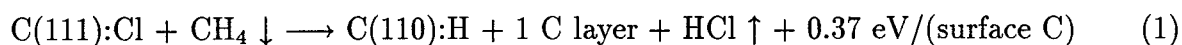
(November 18, 1994)

### Abstract

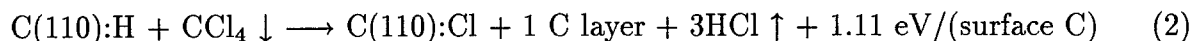
Endpoint energetics for atomic layer epitaxial growth mechanisms have been studied using *ab initio* molecular dynamics. Hydrocarbons and fluorocarbons are the principle gas species used in the growth reactions. The mechanisms employ the switching of H- and F-terminated terminated (110) surfaces to yield self-limiting growth. The reaction of atomic and diatomic hydrogen with fluorinated surfaces and the reaction of atomic and diatomic fluorine with hydrogenated surfaces has also been studied. The desorption of the HF molecule was found to be crucial for H- and F-based growth mechanisms.

Atomic layer epitaxial (ALE) growth has the promise of yielding high quality diamond films. An ALE process has the characteristic of depositing a layer of the growth material onto the substrate via self-limiting reactions. A growth mechanism consisting of self-limiting reactions has the desirable feature of prohibiting any additional growth until the entire layer has been uniformly covered. Repetition of the ALE process results in the layer-by-layer growth of high-quality single crystal films. This technique has been well-demonstrated for the growth of II-VI and III-V semiconductor thin films [1,2]. For binary semiconductors, the formation of a polar bond in the solid and self-limiting adsorption of the precursor gases directly benefits from the difference in the electronegativity of the elements. However, these advantages do not exist to assist ALE growth of homogenous group IV semiconductors such as diamond. Alternative methods have been proposed for ALE growth of silicon that rely on the sequential exposure of precursor gases to the substrate that result in alternating the adatoms terminating the surface [3-5]. Our efforts have been directed at identifying novel mechanisms for growing diamond films employing the alternating surface termination scheme with fluorine and hydrogen.

Halogen-based mechanisms for ALE growth on diamond have typically been based on chlorocarbons and hydrocarbons as the precursor growth gas species. Recently, an ALE diamond growth process has been proposed [6] involving the successive deposition of CH<sub>4</sub> and CCl<sub>4</sub> onto an initially chlorinated diamond (111) surface. From an elementary molecular bond strength calculation their reactions:



and



are found to yield the growth of a double layer per cycle and implicitly assume growth in the [111] direction. However, from the results of *ab initio* molecular dynamics studies of this process, we found that while the reactions are energetically favorable, there are significant

steric repulsions between adatoms that makes the (111) surface inherently unsuitable for ALE growth. Since the covalent radius of Cl is 33% greater than C, the density of coverage required to fully terminate the (111) surface leads to substantial steric repulsion. A more serious drawback to this growth process is that the (111):3H surface is an unstable structure. To achieve the triple-hydrogen termination on the (111) surface requires a  $60^\circ$  rotation of every other methyl group where one H atom has to move up 0.5 Å and the other two H atoms move downward by 0.2 Å (see Fig. 1). We performed a low-temperature molecular dynamics simulation of the surface and found that it readily becomes disordered. The inherent difficulties in obtaining the starting surfaces for the growth reactions should inhibit the growth mechanism.

As a result of these findings, this Letter proposes three alternative ALE diamond growth mechanisms based on fluorocarbons and hydrocarbons to achieve growth on the diamond (110) surface. Fluorine has the advantage of having a smaller covalent radius than chlorine, which reduces the steric repulsion between halogen adatoms on a diamond surface. Therefore, we would expect a lowering of the growth barriers relative to those found in Cl gas-species adsorption. The (110) surface was chosen because each surface carbon has only one dangling bond, independent of the placement of the surface plane. This results in a simpler surface structure for ALE growth mechanisms than the (111) surface. The growth precursor gases are either  $C_2H_4$  or  $C_2F_4$  and are exposed to the C(110):F or C(110):H surfaces, respectively. These reactions result in the growth of a monolayer of diamond and the switching of the terminating surface adatoms from H to F or vice versa. We can thus define a bilayer growth per cycle mechanism using both growth reactions in sequence. Reaction of hydrogen and fluorine diatomic and ionic gas species with the (110) surface has also been studied. These reactions have the effect of switching the type of the terminating adatoms without growing a layer. Thus we can also define monolayer growth per cycle mechanisms using a combination of a growth reaction and a switching reaction.

In our investigation, we have performed large-scale *ab initio* calculations using the Car-Parrinello method [7] which combines the density-functional theory with molecular dynam-

ics. The electrons are described in the local density approximation with their wavefunctions expanded in a plane wave basis. The ions were modeled with soft-core, norm-conserving pseudopotentials. Pseudopotentials for carbon were generated using a modified Hamann procedure [8] and the hydrogen and fluorine were generated using the Li and Rabii procedure [9]. Due to the lack of  $p$  electrons in the core, the  $p$  pseudopotential for fluorine is very deep. This requires choosing a cutoff that includes plane wave with kinetic energies smaller than 50 Ry. Pseudopotentials generated with the Li and Rabii method are optimized for this cutoff [10].

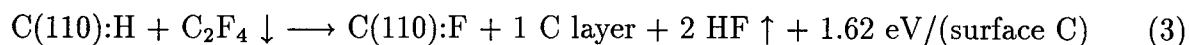
The diamond surfaces were modeled in supercells as slabs of 9–11 atomic layers separated by more than 10 Å of vacuum. The large amount of vacuum was necessary to minimize interactions between slab surfaces. The bottom layer of each slab was held fixed to perfect crystal lattice positions and the dangling bonds were passivated with hydrogen. The top layer of the slab was terminated with either hydrogen or fluorine adatoms. An example of a ten-layer fluorine-terminated diamond (110) surface is depicted in Fig. 2. The gas-species used in the growth mechanisms were calculated in supercells of 10 cubic Å volume containing a single molecule or atom. Ground state total energies were calculated for each slab and gas species by simultaneous relaxation of the atomic and electronic structure. These total energies are then used to determine the energetics of the mechanisms.

The energetics of a reaction are defined to be the total energies of a slab and the precursor gas species minus the total energies of the slab with a fully deposited layer and the desorbed gas species. In each supercell the total number of atoms of each element are conserved throughout each reaction. Barriers to growth due to orientation of the precursor gas species relative to surface sites are not included in the scope of this paper.

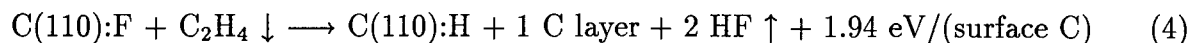
We have studied several reactions that when combined in appropriate sequences, are good candidates for ALE diamond growth mechanisms. Two reactions for growth of a monolayer of carbon are proposed. The first involves exposure of a  $C_2F_4$  gas to a uniformly hydrogenated C(110) surface. The reactions assume that addition of vinyl-like dimers occurs uniformly across the surface. The result is the adsorption of a monolayer of carbon,



the desorption of two HF molecules per C<sub>2</sub>F<sub>4</sub> molecule, and an energy gain of 1.62 eV per surface C. Similarly, we can model the symmetric counterpart of this reaction by switching the hydrogen and fluorine atoms in the reaction. Thus, in the second reaction, a C<sub>2</sub>H<sub>4</sub> gas is exposed to a uniformly fluorinated surface resulting in the growth of a carbon monolayer, the desorption of two HF molecules per C<sub>2</sub>H<sub>4</sub> molecule, and a similar energy gain of 1.94 eV/(surface C). The reactions can be detailed as



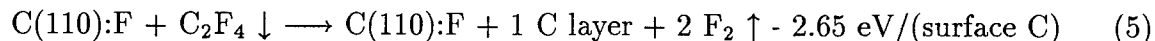
and



and are shown in Figs. 3 and 4, respectively. The differences in energy gain can be attributed to the differences in the covalent radii of the surface terminating adatoms. Since the energy gain is smaller for fluorine gas-species adsorption, the steric repulsion plays a role in the reaction but the favorable size of the fluorine adatoms prevents the repulsion from becoming a prohibitive barrier to adsorption. The desorption of HF is an important part of the reactions. Since the H-F bond is stronger than either the H-C or the C-F bond, the formation of this bond results in the large energy gain per surface carbon as the surface terminating adatoms are alternated. With these two reactions, one could combine them in to a two step cycle alternating the surface terminating adatoms and the incident gas-species. The reciprocal cycle would result in two layers of growth per cycle, but further reactions must be examined to show that the growth is self-limiting.

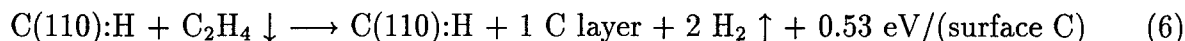
To study the self-limiting aspect of the reactions, we examined reactions that would result in additional growth on uniformly covered surfaces where the surface terminating adatoms are the same as those contained in the gas-species. For example, C<sub>2</sub>F<sub>4</sub> continues to be exposed to the fluorinated surface that is the result of reaction (3). For continued growth on this surface, we would expect to see the desorption of two F<sub>2</sub> molecules per each C<sub>2</sub>F<sub>4</sub> adsorbed. To achieve the growth of a layer of carbon using this reaction, we would have to

add 2.65 eV per surface carbon atom to achieve growth. The reaction can be expressed as



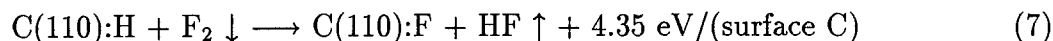
As this is a very large barrier to the reaction, reaction (3) can be characterized as a self-limiting reaction in the sense that continued adsorption of  $\text{C}_2\text{F}_4$  onto the completely fluorinated surface is very unfavorable energetically.

The self-limiting character of the second reaction was examined in a similar way. Continued exposure of  $\text{C}_2\text{H}_4$  to the completely hydrogenated surface would require the desorption of two  $\text{H}_2$  molecules per each  $\text{C}_2\text{H}_4$  adsorbed. To achieve a monolayer of carbon using this reaction, an energy gain of 0.53 eV per surface carbon atom is realized. The reaction can be expressed as



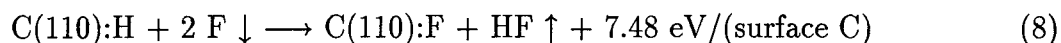
From reaction (6), it would appear that reaction (4) is not a self-limiting reaction due to the slight energy gain. However, to gain energy by addition of  $\text{C}_2\text{H}_4$  to  $\text{C(110):H}$  a two-center reaction must take place. When the vinyl-like dimers are formed, we assume that the dimer's carbon-carbon double bond breaks and that  $\text{H}_2$  formation occurs simultaneously. Experimentally, the reaction of  $\text{C}_2\text{H}_4$  with hydrogen terminated diamond surfaces has not been observed in the absence of plasma or glow discharge. Thus, both growth reactions are most likely self-limiting and when used in an alternating cycle will form a bi-layer growth per cycle ALE mechanism.

In addition to the two main growth reactions, reactions of atomic and diatomic fluorine and hydrogen gas species with an oppositely terminated diamond (110) surface have been investigated. These reactions have the effect of alternating the termination adatom type with a desorption of HF molecules as the "waste" gas. The first reaction is that of  $\text{F}_2$  with a uniformly hydrogenated (110) surface:



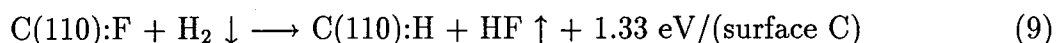
This illustrates the substantial energy gain realized when the hydrogen adatoms are stripped off of the surface when the HF bond is formed. With the breakage of the F<sub>2</sub> bond, the remaining fluorine atom replaces the hydrogen adatom as the terminating adatom. Note that energetically, the reaction simulated is from the completely hydrogenated to the completely fluorinated surface. Thus, any steric repulsions between adatoms is taken into account. One would expect the replacement of a small adatom with a larger adatom to be subject to barriers due to steric repulsion. With the substantial energy gain realized, we can assume that these barriers do not play a significant role in this reaction.

Similarly, the reaction of a flux of atomic F with a uniformly hydrogenated (110) surface

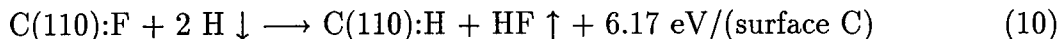


also realizes a large energy gain. The increased energy gain is due to the assumption that a second fluorine atom occupies the surface radical site of the hydrogen which was desorbed as HF after reacting with the first fluorine atom. Thus, there is no F<sub>2</sub> bond to break and the energy gain is increased relative to the last reaction.

Equivalent reactions of atomic and diatomic hydrogen with fluorinated surfaces have also been studied. These reactions,



and



also exhibit large energy gains. The four non-growth mechanisms are obviously self-limiting and are only dependent on the availability of the precursor gas in enough quantity to switch the adatoms.

Reactions (7–10) can be appropriately combined with one of the two growth reactions to obtain monolayer per cycle ALE growth mechanisms. The most promising monolayer ALE mechanism would consist of reaction (3) alternated with reactions (9) or (10) to alternate

the surface adatoms. This mechanism would be self-limiting and exhibits substantial energy gains at each step of the cycle.

In summary, we have identified several favorable diamond growth reactions using hydro- and fluoro-based gas species on the fluorinated and hydrogenated diamond (110) surface. All of the reactions are most likely self-limiting and may be appropriately combined to form monolayer and bilayer growth per cycle ALE mechanisms.  $C_2H_4$  and  $C_2F_4$  were used as the growth precursor gases when exposed to an oppositely terminated surface. Atomic and diatomic hydrogen and fluorine gases reacting with the oppositely terminated surface yielded the end result of switching the species of surface terminating adatoms. All of the reactions relied on the desorption of HF to realize substantial energy gains.

## REFERENCES

- [1] M.L. Yu, Thin Solid Films **224**, 7 (1993)
- [2] J.R. Creighton and B.A. Bansenauer, Thin Solid Films **224**, 17 (1993)
- [3] S.M. Cohen, T.I. Hukka, Y.L. Yang and M.P. D'Evelyn, Thin Solid Films **224**, 155 (1993)
- [4] S. Imai, T. Iizuka, O. Sugiura and M. Matsumura, Thin Solid Films **224**, 168 (1993)
- [5] D.D. Koleske, S.M. Gates and D.B. Beach, Thin Solid Films **224**, 173 (1993)
- [6] V.B. Aleskovski and V.E. Drozd, *Proc. First Inter. Symp. on Atomic Layer Epitaxy*, edited by L. Niinisto, Acta Polytechnica Scandinavica, Chem. Techn. and Metallurgy Ser. **195**, 156 (1990)
- [7] R. Car and M. Parrinello, Phys. Rev. Lett. **55**, 2471 (1985)
- [8] G.B. Bachelet, D.R. Hamman and M. Schlüter, Phys. Rev. B. **26**, 4199 (1982)
- [9] G. Li and S. Rabii, preprint (1992)
- [10] Computational tests of the potentials were performed by calculating and comparing the binding energies and vibrational frequencies of several of the gas species to be used in the reactions. Good agreement with the molecular LDA calculations of Johnson *et al* [11] was exhibited. The atomization energies agreed within 8% and vibrational frequencies and geometries were in close agreement with both molecular LDA and experimental data.
- [11] B.G. Johnson, P.M.W. Gill and J.A. Pople, J. Chem. Phys. **7**, 5613 (1993)

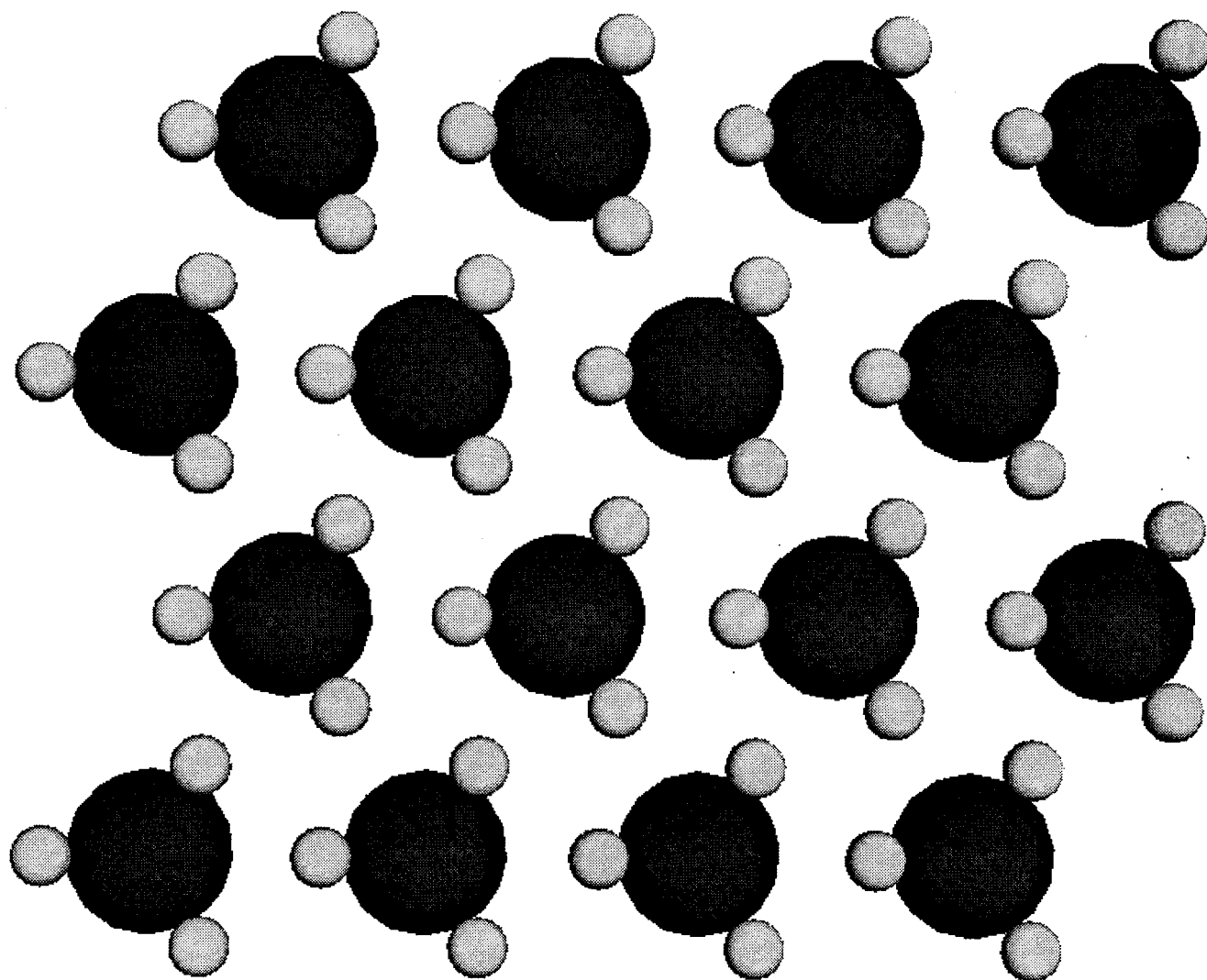


Figure 1. Orientation of 3H terminated (111) surface.

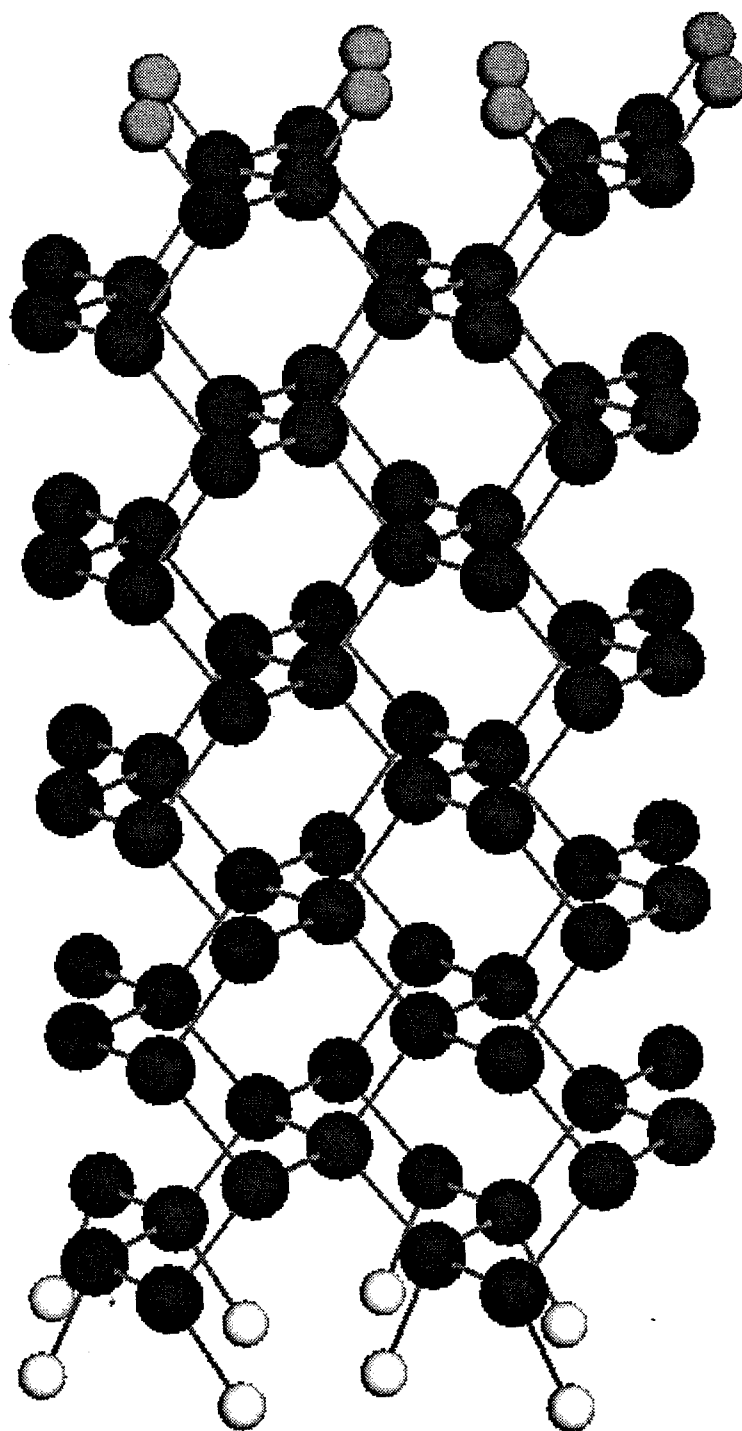


Figure 2. Ten layer C(110):F surface with bottom layer H-passivated.

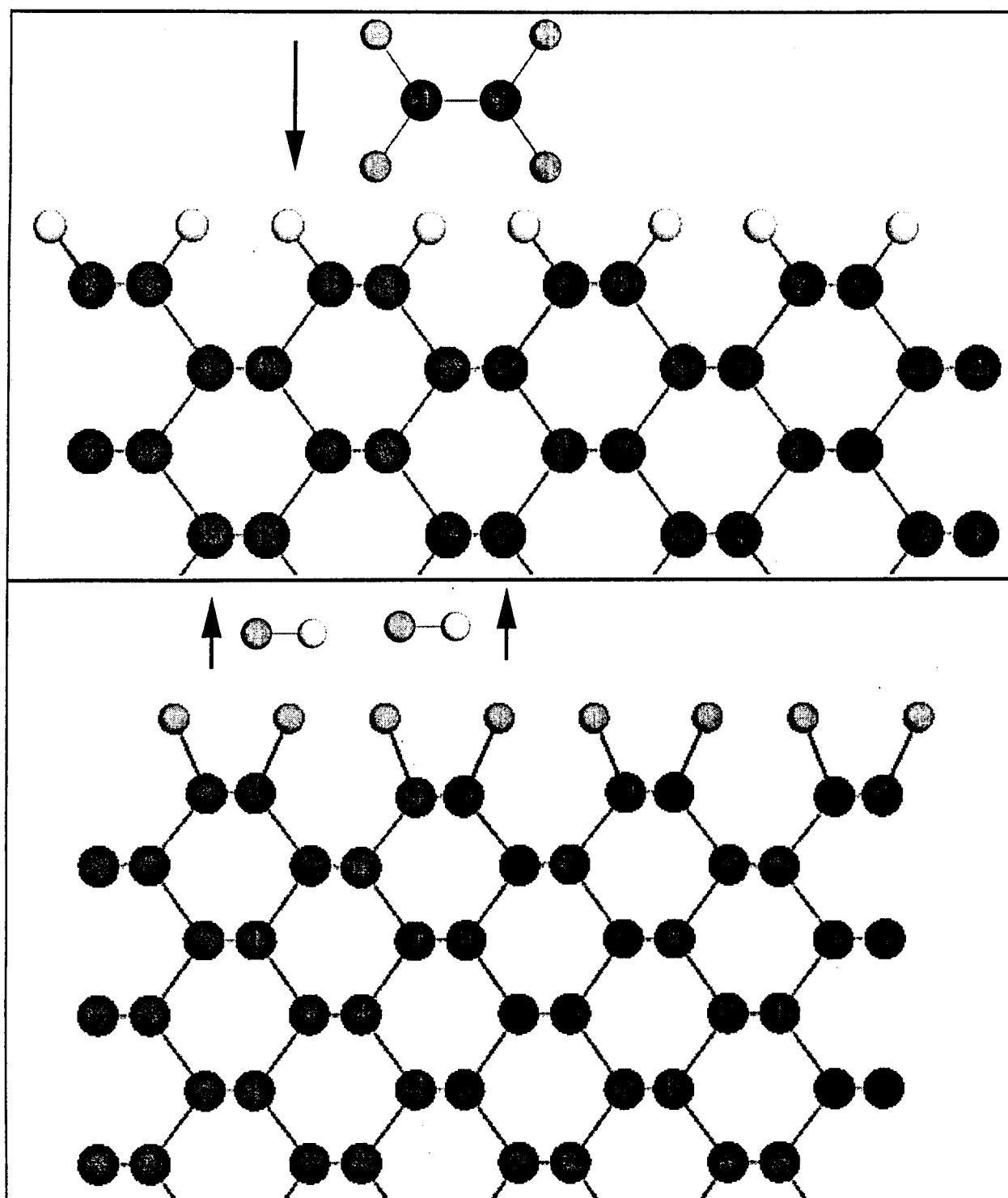


Figure 3. Reaction 3.



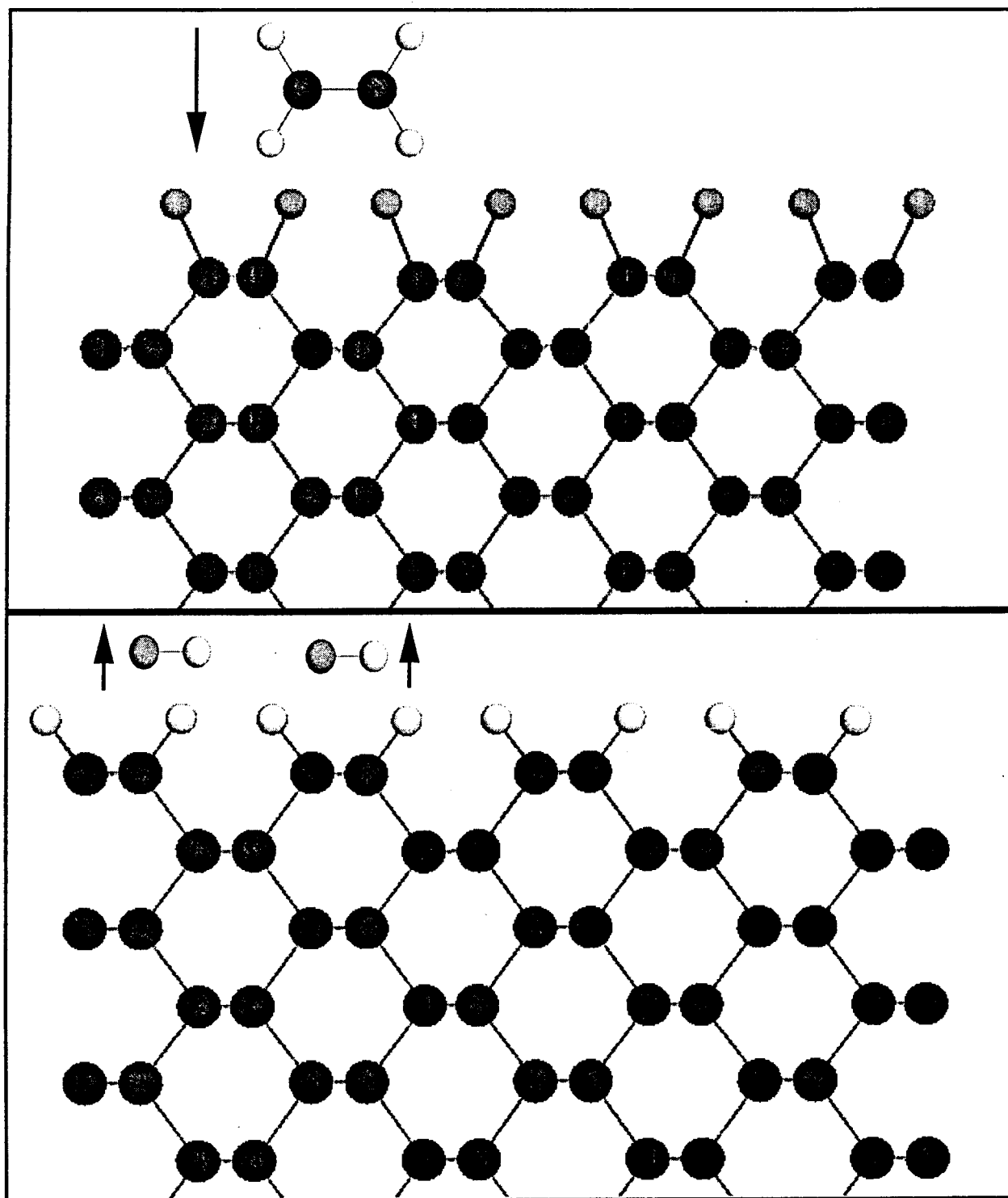


Figure 4. Reaction 4.

## X. Surface Structures and Electron Affinities of Bare and Hydrogenated Diamond C(100) Surfaces

Z. Zhang, M. Wensell, and J. Bernholc

Department of Physics

North Carolina State University

Raleigh, North Carolina 27665-8202

The structure and electronic properties of bare and H-terminated C(100)-2x1 surfaces have been studied by *ab initio* molecular dynamics. Stable 2x1 structures were found for both clean and monohydride-terminated surfaces. The 1x1 dihydride phase is energetically unstable relative to H<sub>2</sub> desorption, although a local minimum, consisting of canted dihydride pairs, was found. The bare diamond (100)-2x1 surface has a positive electron affinity, while a negative electron affinity is obtained for both the 2x1:H and 1x1:2H surfaces. The existence of negative electron affinity for the diamond (100)-2x1:H surface is in good agreement with recent experimental data.

## I. Introduction

Among the three low-index surfaces of diamond, only the (100) orientation sustains high quality growth of homoepitaxial and heteroepitaxial films [1-5]. The flatness of the surfaces grown in this direction can be on a nanometer-to-micrometer scale, making C(100) a good candidate for applications. Recently, the C(100)-2x1:H surface has been found to have a negative electron affinity (NEA), a property that has strong technical and scientific appeal. Normally, a polished C(100) surface shows a 1x1 LEED pattern when heated from 500K to 700K in an UHV environment. At temperatures above 1300 °K the surface reconstructs to a 2x1 structure [6]. The 2x1 phase is believed to be either monohydride-terminated (a single H atom per surface C atom) or bare, depending on its preparation and annealing conditions. While no consensus has been reached on the observed 1x1 structure, it has been suggested that it is either dihydride-terminated 1x1 or a disordered 2x1 structure.

Previous theoretical work has mainly used tight-binding and related approximations [7-9], although an approximate local-density-based calculation has been published recently [10]. The 2x1 phase is believed to be stable with or without adsorbed hydrogen. However, most workers believe that a full dihydride coverage cannot be responsible for the observed 1x1 structure [8, 10], since the calculated steric repulsions are large. Although most calculations find that the dihydride structure is still locally stable [7-9, 11], in the calculations of Ref. [10] the H atoms spontaneously dissociated and formed a H<sub>2</sub> molecule. The original experimental work, utilizing ESD-TOF spectra [6] found two distinct velocities of ions emerging from the 1x1 surface, which would indicate the existence of CH<sub>2</sub> dihydride unit. The slower peak, which persisted to higher temperatures (~1530K) and followed an appearance of a 2x1 reconstruction, was attributed to the hydrogen desorption from monohydride pairs. However, oxygen was also found on the initial 1x1 surface, which might have inhibited the reconstruction of this surface [6, 12]. A more stable 1x1 structure, consisting of alternating dihydride and monohydride units was studied theoretically by Frauenheim *et al* [13], who used semi-empirical simulated annealing MD

techniques. Davidson and Pickett [7] have also considered the possibility of a half-hydride for the 2x1 surface. Frauenheim et al simulations indicate that the 2x1 monohydride structure is stable at ~1200K[13].

The hydrogenated diamond (111) surface has long been known to exhibit negative electron affinity (NEA), *i.e.*, its conduction band edge is above the vacuum level, thus allowing conduction band electrons to be emitted into vacuum. The NEA can be unambiguously detected in photoemission by a presence of a distinct peak at the low energy end of the spectrum [14]. The NEA effect could potentially make diamond useful in applications, such as cold cathode emitters and UV detectors. For C(111), NEA is associated with the 1x1 phase, whereas the (2x1) reconstructed phase exhibits a positive electron affinity [15]. Recently, it was found by a combination of UV photoemission experiments and theoretical calculations that the hydrogenated C(100)-2x1 surface exhibits negative electron affinity while the C(100)-1x1 surface does not [16]. In general, the measured electron affinity has contributions from two different mechanisms, band bending due to the space charge, and surface dipole adjustment. Band bending occurs over a range of about 1000 Å from the surface and is due to the occupation of surface states by impurity and defect-induced carriers from the solid [17, 18]. Surface dipole adjustment occurs on the atomic scale and strongly depends on the surface structure and the adsorbed atoms.

This paper describes the results of extensive *ab initio* molecular dynamics studies of the structure of the bare and hydrogenated diamond (100) surfaces and of their electron affinities. The calculated electron affinities, in conjunction with experimental measurements, also provide information about the surface structure that has led to the identification of the NEA-active diamond (100) surface [16]

## II. Methodology

*Ab initio* molecular dynamics (Car-Parrinello method) utilizes the Lagrangian [19]

$$L = \sum_i \frac{1}{2} \mu \int_{\Omega} d^3 r |\dot{\psi}_i|^2 + \sum_I \frac{1}{2} M_I \dot{\mathbf{R}}_I^2 + \sum_v \frac{1}{2} \mu_v \dot{\alpha}_v^2 - E[\{\psi_i\}, \{\mathbf{R}_I\}, \{\alpha_v\}] \quad (1)$$

where  $\psi_i$  denote the electronic wavefunctions that depend also on constraints  $\{\alpha_v\}$ ,  $\mathbf{R}_I$  the ionic coordinates, and  $E$  is the total energy of the system in the local density approximation [20]. The masses  $\mu$  and  $\mu_v$  are associated with the fictitious dynamics of the electronic wavefunctions and the constraints, respectively. The resulting equations of motion are:

$$\mu \ddot{\psi}_i(\mathbf{r}, t) = -\delta E / \delta \psi_i^*(\mathbf{r}, t) + \sum_k \Lambda_{ik} \psi_k(\mathbf{r}, t) \quad (2a)$$

$$M_I \ddot{\mathbf{R}}_I = -\Delta_{\mathbf{R}_I} E \quad (2b)$$

$$\mu_v \ddot{\alpha}_v = -(\delta E / \delta \alpha_v) \quad (2c)$$

where  $\Lambda_{ik}$  are the Lagrange multipliers associated with the orthonormality constraints of the wavefunctions. After a suitable initialization, the molecular dynamics proceeds while the temperature of the system is slowly reduced to zero. At this point the time derivatives of the wavefunctions are all zero and the equations (2a) are identical, within a unitary transformation, to the well-known Kohn-Sham equations derived variationally from the local density expression for the total energy [21].

The formulation (1-2) allows for band structure calculations, optimization of atomic geometries, as well as truly time-dependent quantum molecular dynamics simulations. The ability to perform time-dependent simulations is also useful in geometry optimization. For example, we have developed a fast relaxation method in which the atoms follow Newtonian dynamics in the presence of a special friction force [22]. This method is substantially faster than either steepest descents or conjugate gradient techniques. It has been used in the present work to relax the various surface structures.

The calculations were carried out using plane waves and soft-core, norm-conserving pseudopotentials, generated using Hamann's procedure [23]. The kinetic energy cutoff in the plane wave expansion was 35 Rydbergs. The diamond surfaces were modeled by a supercell containing ten layers of diamond and a 10 Å vacuum region, in order to avoid interactions between the periodically repeated slab images. Both surfaces of the slab were kept equivalent, thereby avoiding dipole interactions between the surfaces. The clean C(100)-2x1 surface supercell contained eight atoms per layer, or a total of 80 carbon atoms. The monohydride C(100)-2x1:H surface contained twelve carbon atoms per layer. One hydrogen atom was attached to every surface carbon atom. For the C(100)-1x1:2H dihydride surface, two hydrogen atoms were attached to each of the surface carbon atoms. Due to the sizes of the supercells, only the  $\Gamma$  point was used for k-space sampling. Starting from an estimated structure, the equilibrium geometries were obtained by a combination of the steepest descents and fast relaxation methods [22].

The electron affinity of a semiconductor surface is defined as the energy difference between the conduction band minimum inside the solid and the vacuum level. Normally, two factors affect the value of the electron affinity: the surface dipole moment, defined as the potential drop across the first few atomic layers of the surface, and the space charge due to the occupation of surface states by electrons or holes from the bulk. The effect of hydrogen adsorption on the surface states and on the dipole moment can be directly analyzed using the present calculations. However, the space charge, which extends hundreds of angstroms from the surface and depends on bulk doping, must be studied by a different formalism.

By definition, the electron affinity of a semiconductor is

$$\chi = V(\infty) - E_c \quad (3)$$

where  $V(\infty)$  is the position of vacuum level and  $E_c$  denotes the conduction band edge. The formula (3) is easily rewritten as

$$\chi = D - (E_c - V_{\text{bulk}}) \quad (4)$$

where  $D = (V(\infty) - V_{\text{bulk}})$  is defined as the surface dipole strength that determines the relative positions of the bulk electron states and the vacuum level [24], and  $(E_c - V_{\text{bulk}})$  is the position of the conduction band edge relative to the bulk averaged electrostatic potential  $V_{\text{bulk}}$  and is purely a bulk property. To minimize computational errors, we computed the position of the valence band maximum  $E_v$  using a bulk diamond calculation, which gives the value of  $(E_v - V_{\text{bulk}})$ .  $E_c$  was then determined by using the experimental band gap (5.47 eV), since the local density theory underestimates the value of the band gap. The dipole strength  $D$  can be obtained directly from the difference of the electrostatic potential across the surface. More illustratively,  $D$  can also be calculated by integrating the one-dimensional Poisson equation:

$$d^2V/dz^2 = -4\pi\rho(z)$$

where  $\rho(z)$  is the plane-averaged total (electronic and nuclear) charge density.

### III. Results and Discussion

#### *Surface geometries and energetics*

Both clean and monohydride surfaces can have stable 2x1 structures (Figure 1), but the C-C dimer bond length is shorter at the clean surface (1.38Å) than at the monohydride surface (1.63Å). This difference is in the expected range for typical C-C double and single bond lengths. Much larger vertical relaxations were found for the clean surface than for the hydrogenated surfaces. For the 2x1 bare, 2x1 mono-hydrogenated, and 1x1 dihydrogenated surfaces, the spacing between the first and second layers is compressed by 27%, 10% and 6.7%, respectively, while the spacing between second and third layers is stretched by 5.6%, 1.1% and 2.2%, relative to the bulk spacing of 0.89Å (see Table I). However, only small displacements (less than 0.02Å) from the ideal bulk positions were found at the third and fourth layers - an indication that the ten-layer slab used in the calculation is adequate for studying atomic relaxations of these surfaces.

Due to steric repulsion, bonded hydrogen atoms tend to avoid each other. This is the reason for the change in angle between the C-H bond and the surface normal on the monohydride surface from its starting value of  $54.7^\circ$  to its relaxed value of  $23.1^\circ$ . On the dihydride surface the steric repulsion is even stronger. Starting from symmetric initial positions and using the method of steepest descents, a symmetric dihydride structure was obtained (Figure 2a). The stability of the dihydride surface was then examined by a finite temperature simulation where the surface was heated to 300K for about 0.02 ps (about three periods of C-H vibrations). During the simulation the hydrogen atoms deviated from the symmetric positions but no dissociation from the surface was observed. This is in contrast to the results of Ref. [10], where the dihydride structure was found to be unstable, leading to dissociation of  $H_2$  molecules from the surface upon geometry optimization. Starting from the "annealed" structure, we performed a steepest descent quench that led to a canted and twisted structure that is lower by 0.12 eV in energy per 1x1 cell than the symmetric structure. Similar twisting of the dihydride pairs was found by Yang and D'Evelyn [25, 26]. Due to the prohibitive computational cost, we did not attempt higher temperature simulations or a search for a global minimum for the dihydride surface.

The hydrogen removal energies  $\delta E_H$  for the mono- and di-hydride surfaces were computed as differences in total energies between the fully relaxed hydrogenated configurations ( $2 \times 1:H$  and  $1 \times 1:2H$ ) and the relaxed surfaces containing one less H atom per surface unit cell. The results are tabulated in Table II, together with those obtained by previous workers. A large difference (4.36 eV/H atom) in the  $\delta E_H$  was found between the monohydride and the dihydride surfaces. In particular, the dihydride surface is energetically unfavorable by 2.3 eV/ $H_2$  with respect to  $H_2$  desorption, although it is still favored by 1.13 eV relative to desorption to atomic H. Due to a lower  $\delta E_H$ , the desorption of hydrogen from the dihydride surface should occur at a much lower temperature than from the monohydride surface. This is in qualitative agreement with the ESD-TOF measurements [6]. However, the above values were computed by removing an entire hydrogen layer from the surface, rather than a single atom. Furthermore, the measured desorption temperatures reflect the energy barriers for the various desorption paths. Dynamic



simulations are thus necessary to make quantitative comparisons to the measured desorption temperatures.

Accurate experimental measurements of hydrogen coverage on diamond (100) surfaces are not currently available, possibly due to experimental difficulties[6, 26]. In the cases of Si(100) surfaces, Cheng and Yates [27] found a saturation coverage of 1.9 ML (1 ML is defined as one H per surface Si atom) and suggested that the Si(100)-1x1 surface was a disordered phase containing monohydride, dihydride, and trihydride structures. Compared to silicon, the diamond lattice constant is 34% smaller. Thus, the larger steric repulsion will inhibit high density coverage. Yang and D'Evelyn [25, 26] suggested that a disordered dihydride with a local (2+1)x1 structure will most likely give rise to a 1x1 LEED pattern [6]. This model eliminates the large repulsion between two adjacent dihydride units and implies a maximum hydrogen coverage of 1.33 ML at which a 3x1 structure results. In principle, although the steric repulsion is very high for the dihydride surface, it could still exist at zero temperature, since our calculations indicate that it is lower in energy relative to the bare surface and free H atoms. Moreover, a barrier exists for H<sub>2</sub> desorption. However, the conditions required for this phase to occur may be very different from normal laboratory conditions.

### *Electronic Structure*

The electronic wavefunctions were analyzed by examining their Mullikan populations and plane-averaged square moduli. Information about the charge distribution and the bond orientations was obtained from s- and p-projected Mullikan populations. Surface states were identified by the wavefunctions being largely localized in the surface region.

Figure 3a-b shows schematically the electronic levels of the bare and monohydride C(100)-2x1 surfaces in the band gap region. At the bare surface both filled and empty surface states exist in the forbidden gap. They mainly consist of  $\pi$  bonding and anti-bonding orbitals on the dimer atoms. The energy separation between the filled and empty surface states is 1.5 eV. For

the monohydride surface, no occupied surface states were found in the band gap. The C-H bonding states lie about 4 eV below valence band maximum (VBM). However, a broad band of unoccupied states, consisting mostly of C-H anti-bonding orbitals, lies between 1.5 and 2.5 eV below the conduction band edge. Due to the well known inadequacy of LDA in describing excited states, the position of these states cannot be precisely determined.

In their tight-binding calculation for the bare C(100)-2x1 surface, Davidson and Pickett [7] found a 2 eV gap between the highest occupied and the lowest unoccupied states, similar to our value of 1.5 eV. However, Yang *et al* [10] and Mehandru and Anderson [9] found the bare surface to be nearly metallic. While the unoccupied states inside the band gap didn't appear in the calculations of Ref. [9] for the monohydride surface, our results are very similar to theoretical and experimental findings on the monohydride Si(100)-2x1:H surface. Hammers *et al* [28] attributed the peak at 1.0 eV above  $E_f$ , obtained in their STM spectroscopy, to Si-H anti-bonding states previously predicted by Ciraci *et al* [29], using the empirical tight-binding method. Although a strong C-H bond should lead to a large separation between the bonding and anti-bonding states (typically  $\sim 9$  eV in small molecules, such as CH<sub>4</sub>), the interactions with the surface broaden the band so that the empty states drop below the conduction band edge.

Experimentally, for the 2x1 diamond (100) surface, Hamza *et al* [6] found occupied states over a 1.5 eV range of the energies above the valence band maximum and no empty states from 1.2 to 5.5 eV above the Fermi level. Neither of the present calculations for the ideal 2x1 surface (clean or monohydride) results in the electronic structure that exactly matches these data. Since there is a clear indication of occupied gap states, we conclude that the actual surface is at least partially bare. Based on their tight-binding calculations, Davidson and Pickett [7] have shown that a half-hydride structure, with partially filled gap states, would best fit the photoemission data.

The electronic structure of the symmetric dihydride surface is schematically shown in Figure 4. The highest occupied states are surface states induced by hydrogen adatoms. These

states extend the valence band maximum (VBM). A broad band of empty surface states exists 1.5 eV above VBM and is of C-H antibonding character. Although the interactions between the dihydride units are strong, the surface remains insulating. This is in qualitative agreement with the tight-binding calculations of Davidson and Pickett [7]. However, in his self-consistent tight-binding calculation [30], Gavrilenko found the dihydride surface to be metallic. His calculations placed some of the C-H bonding states at the conduction edge, which is more than 5 eV above VBM, where the remaining part of C-H bonding states reside. This is against our intuition, since C-H bonding states should at least be lower in energy than the surface dangling bonds, usually found near the middle of the gap. Regardless of these findings, the existence of a dihydride phase remains controversial.

### *Electron Affinity*

In Figure 5 we plot the plane-averaged self-consistent potentials for the bare, monohydride, and the symmetric dihydride surfaces. For plotting purposes it is convenient to align the potentials inside the bulk. The vacuum level thus appears different for each of the three surfaces, since each of them has a different potential barrier to vacuum. All the potentials agree well inside the bulk and all flatten out in the vacuum region, indicating good convergence with respect to the number of diamond layers and the size of the vacuum included in the calculations. The bare C(100)-2x1 surface has the largest potential barrier (*i.e.*, the largest surface dipole  $D$ ). Its vacuum level lies above the conduction band edge  $E_C$ , giving an electron affinity of +0.8 eV. Compared to the bare C(100)-2x1 surface, the hydrogenated surfaces have less electronic charge spilling into the vacuum, because hydrogen atoms have saturated the dangling bonds. The net effect is that of an additional dipole layer in the opposite direction to the bare surface dipole  $D$ . Hence, the total potential barrier is reduced and the vacuum level lies below the bottom of the conduction band for both the monohydride and the dihydride surfaces. The calculated electron affinities are -2.2 eV and -3.4 eV, respectively.

In the UV photoemission measurements, it was found [16] that the occurrence of NEA was coincident with 2x1 reconstruction, which followed a 1050 °C anneal. While hydrogen cannot be seen in the UV photoemission measurement, we concluded from a comparison between the experimental and our calculated results that hydrogen is present on the 2x1 surface. This is supported by additional experiments [16], which show that exposure to atomic hydrogen does not significantly alter the UPS spectrum. As for the 1x1 unannealed surface, the UPS spectrum does not show the NEA peak and Auger measurements indicate the presence of oxygen. The atomic structure of this surface is yet to be determined.

#### IV. Summary

We have investigated the atomic and electronic structure of bare and hydrogenated diamond (100) surfaces by *ab initio* molecular dynamics. Stable structures have been found for both clean and 2x1 H-terminated surfaces. The 1x1 dihydride surface exhibits large steric interactions and it is energetically unfavorable relative to H<sub>2</sub> desorption. However, a finite temperature simulation at 300K indicates that a local minimum involving canted and tilted dihydride pairs exists.

The hydrogen desorption energies have been calculated. The desorption energy for the dihydride surface is significantly smaller than that of the monohydride, in agreement with the ESD-TOF experiments and previous calculations. The electronic states were analyzed by computing their s- and p-projected Mullikan populations and by direct examination of the wavefunction shape and extent. The clean 2x1 surface has both filled and empty states within the forbidden gap, while for the monohydride surface only empty states appear in the gap. The dihydride surface has a 1 eV gap between the filled and empty states, despite the overcrowding of hydrogen atoms.

Negative electron affinities of 2.2 and 3.4 eV were found, for monohydride and dihydride surfaces, respectively, while the clean 2x1 surface has a positive electron affinity of 0.8 eV. The occurrence of the negative electron affinity is due to surface dipole changes, which lead to

smaller potential barriers for electrons at the hydrogenated surfaces. From these results we conclude the C(100)-2x1 surfaces that exhibit NEA in photoemission experiments are hydrogenated.

## V. Acknowledgments

We would like to thank Dr. J. van der Weide and Professor R. Nemanich for fruitful discussions. This work was supported in part by the National Science Foundation, grant numbers DMR-9100063 and DMR-940837.

1. S. D. Wolter, B. R. Stoner, J. T. Glass, P. J. Ellis, D. S. Buhaenko, C. E. Jenkins, and P. S. Southworth, *Appl. Phys. Lett.* **62**, 1215 (1993).
2. T. Tsuno and T. Imai, *Japanese Journal of Applied Physics* **30**, (1991).
3. R. A. Rudder, J. B. Posthill, G. C. Hudson, D. Malta, R. E. Thomas, R. J. Markunas, T. P. Humphrey, and R. J. Nemanich, *Proc. 2nd Intern. Conf. on New Diamond Science and Technology*, edited by J. T. G. R. Messier J. E. Bulter, and R. Roys, Washington, DC, p. 427 (1990).
4. A. R. Badzian, T. Badzian, X. H. Wang, and T. M. Hartnett, in Ref. 3, p. 549.
5. F. L. Sutcu, C. J. Chu, M. S. Thompson, H. R. Hauge, J. L. Margrave, and M. P. D'Evelyn, *J. Appl. Phys.* **60**, 1685 (1992).
6. A. V. Hamza, G. D. Kubiak, and R. H. Stulen, *Surf. Sci.* **237**, 35 (1990).
7. B. N. Davidson and W. E. Pickett, *Phys. Rev. B* **49**, 11253 (1993).
8. Y. L. Yang and M. P. D'Evelyn, *J. Am. Chem. Chem. Soc.* **114**, 2796 (1992).
9. S. P. Mehandru, and A. B. Anderson, *Surf. Sci.* **248**, 369 (1991).

10. S. H. Yang D. A. Drabold, and J. B. Adams, Phys. Rev. B **48**, 5261 (1993).
11. X. M. Zheng and P. V. Smith, Surf. Sci. **256**, 1-8 (1991).
12. J. van der Weide and R. J. Nemanich, Appl. Phys. Lett. **62**, 1878 (1993).
13. Th. Frauenheim, U. Stephan, P. Blaudeck, D. Porezag, H.-G. Busmann, and W. Zimmermann-Edling, Phys. Rev. B **48**, 18189 (1993).
14. F. J. Himpsel, J. A. Knapp, J. A. Van Vechten, and D. E. Eastman, Phys. Rev. B **20**, 624 (1979).
15. B. B. Pate, Surf. Sci. **165**, 83 (1985).
16. J. van der Weide, Z. Zhang, P. Baumann, M. G. Wensell, J. Bernholc, and R. J. Nemanich, Phys. Rev. B Rapid Communications, in print (1994).
17. C. G. B. Garrett and W. H. Brattain, Phys. Rev. **99**, 376 (1955).
18. B. B. Pate, W. E. Spicer, T. Ohta, and I. Lindau, J. Vac. Sci. Technol. **17**, 1087 (1980).
19. R. Car and M. Parrinello, Phys. Rev. Lett. **55**, 2471 (1985).
20. P. Hohenberg and W. Kohn, Phys. Rev. **136**, B864 (1964).
21. W. Kohn and L. J. Sham, Phys. Rev. **140**, A1133 (1965).
22. C. Wang, Q.-M. Zhang, and J. Bernholc, Phys. Rev. Lett. **69**, 3789 (1992).
23. D. R. Hamann, Phys. Rev. B **40**, 2980 (1989).
24. A. Zangwill, *Physics at Surfaces* (Cambridge University Press, 1988).
25. Y. L. Yang and M. D'Evelyn, J. Vac. Sci. Technol. A **10**, 978 (1991).

26. Y. L. Yang, L. M. Struck, L. F. Sutcu, and M. P. D'Evelyn, Thin Solid Films **225**, 203-211 (1993).
27. C. Cheng and J. G. Yates, Phys. Rev. B **43**, 4041 (1991).
28. R. J. Hamers, P. Avouris, and F. Bozso, Phys. Rev. Lett. **59**, 2071 (1987).
29. S. Ciraci, R. Butz, E. M. Oellig, and H. Wagner, Phys. Rev. B **30**, 711 (1984).
30. V. I. Gavrilenko, Phys. Rev. B **47**, 9556 (1992).
31. X. M. Zheng and P. V. Smith, Surf. Sci. **261**, 395 (1991).

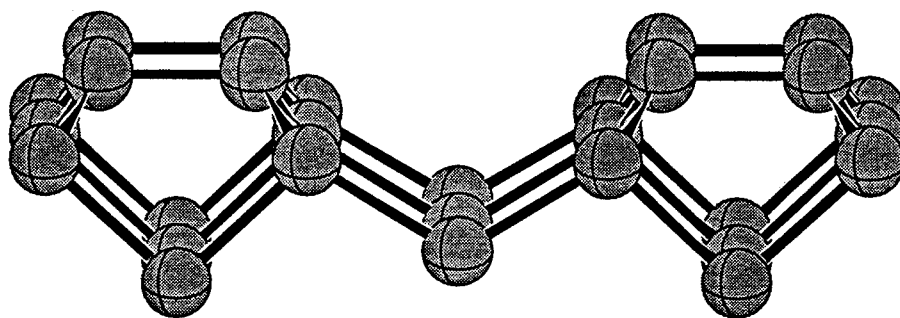
Table I. Calculated C(100) surface geometries.  $r_{\text{dimer}}$  is the surface dimer length and  $r_{\text{CH}}$  the C-H bond length.  $\alpha(\text{dimer-H})$  and  $\theta(\text{H-C-H})$  are, respectively, the angle between the dimer and the C-H bond on the monohydride surface, and the H-C-H angle on the dihydride surface.  $\Delta x_{ij}$  is the spacing between  $i$ th and  $j$ th layers. An average is taken for  $\Delta x_{ij}$  on the 1x1:2H annealed surface, since it is not flat.

	2x1:clean	2x1:H	1x1:2H (symm)	1x1:2H (annealed)
$r_{\text{dimer}}(\text{\AA})$	1.38	1.63	-	-
$r_{\text{CH}}(\text{\AA})$	-	1.11	1.06	1.04 - 1.13
$\alpha(\text{dimer-H})$	-	113.1°	-	-
$\theta(\text{H-C-H})$	-	-	84.72°	93° - 96°
$\Delta x_{12}(\text{\AA})$	0.65	0.80	0.83	0.88
$\Delta x_{23}(\text{\AA})$	0.94	0.90	0.91	0.90
$\Delta x_{34}(\text{\AA})$	0.87	0.89	0.89	0.87

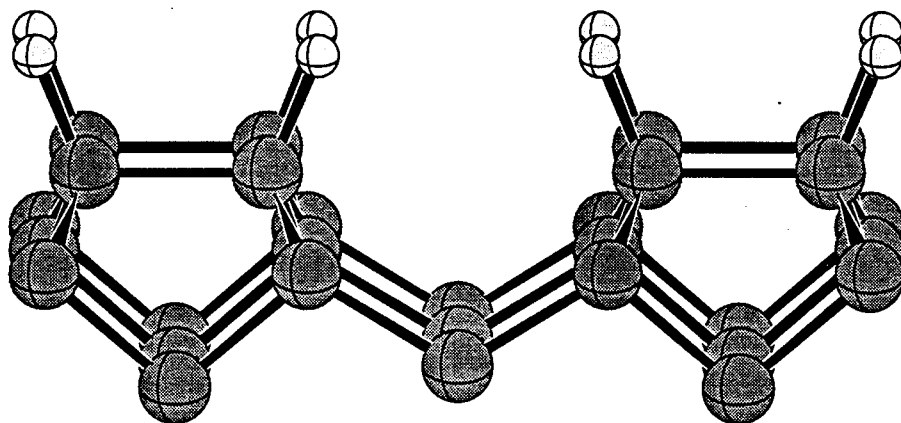


Table II. Energetics of hydrogen binding for C(100)-2x1:H and C(100)-1x1:2H surfaces. Also listed are results of previous studies [8-10, 31].

Surface	This work	Mehandru and Anderson [9]	Yang and D'Evelyn [8]	Yang, Drabold, and Adams [10]	Zheng and Smith [31]
$\delta E_{\text{H-mono}}$ [eV]	5.49	6.63	3.27	6.18	6.32
$\delta E_{\text{H-di}}$ [eV]	1.13	-	1.19	-	4.11

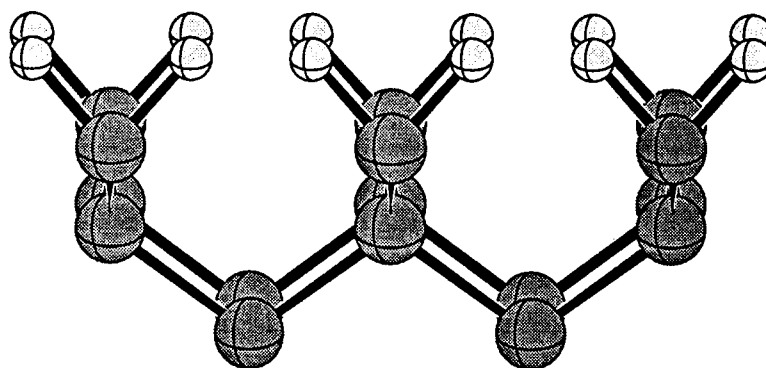


**a) The clean C(100)-2x1**

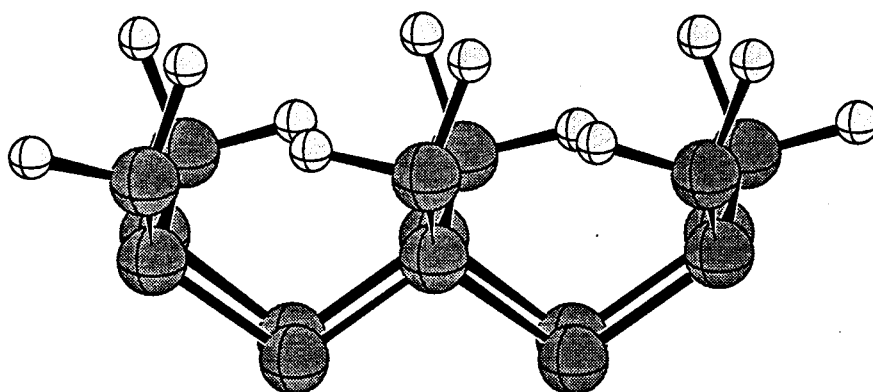


**b) C(100)-2x1:H**

Figure 1. Relaxed structure of clean C(100)-2x1 and C(100)-2x1:H surfaces. The large spheres denote carbon atoms and the small ones hydrogen atoms.

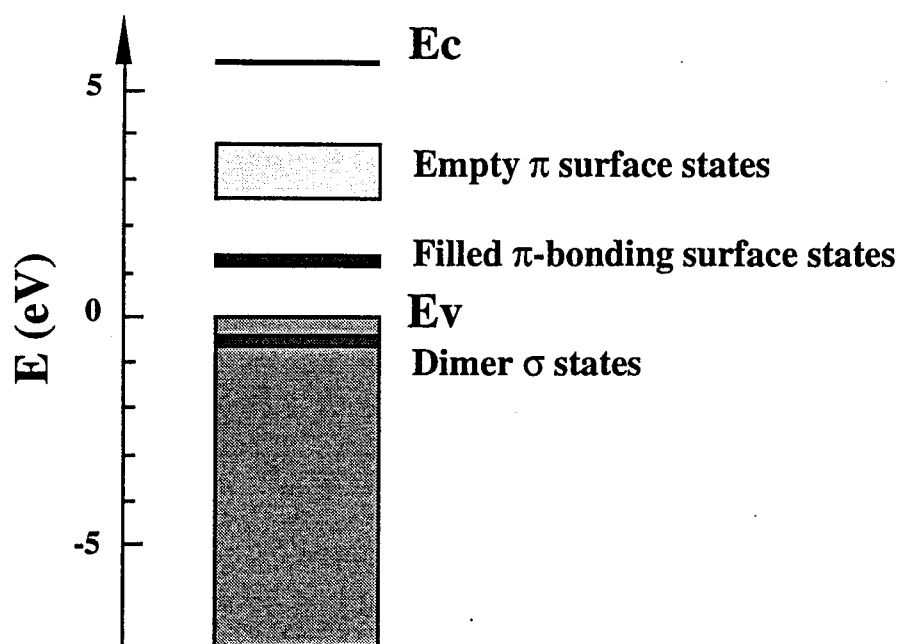


**a) symmetric**

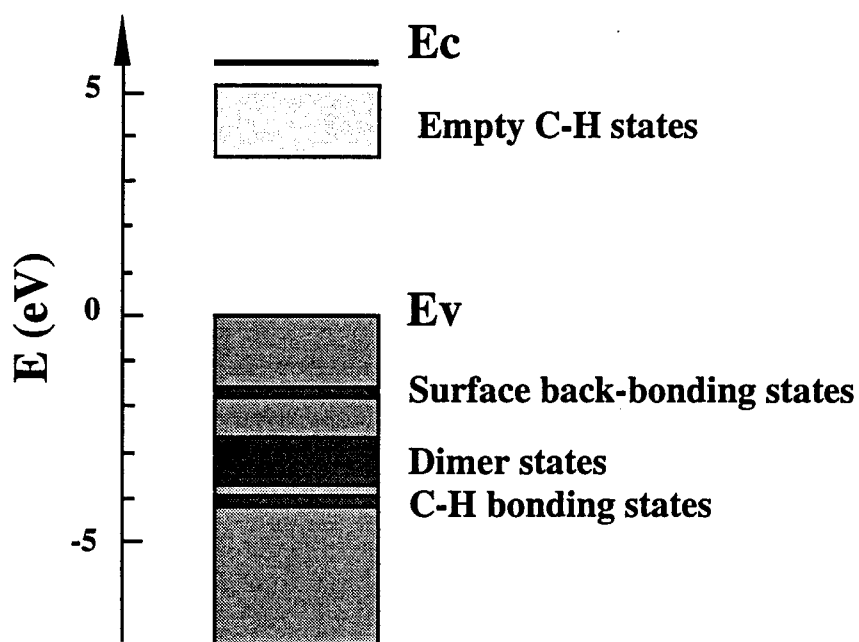


**b) canted**

Figure 2. Structure of  $C(100)-1 \times 1:2H$ . a) Symmetric dihydride, obtained by steepest descent calculation from an originally symmetric geometry. b) Canted dihydride, the structure after simulated annealing.



**a) Bare C(100)-2x1**



**b) C(100)-2x1:H**

Figure 3. The electronic structure of 2x1 diamond surfaces: a) Bare C(100)-2x1; b) Monohydride C(100)-2x1:H. Zero of energy was set at the valence band maximum ( $E_v$ ).

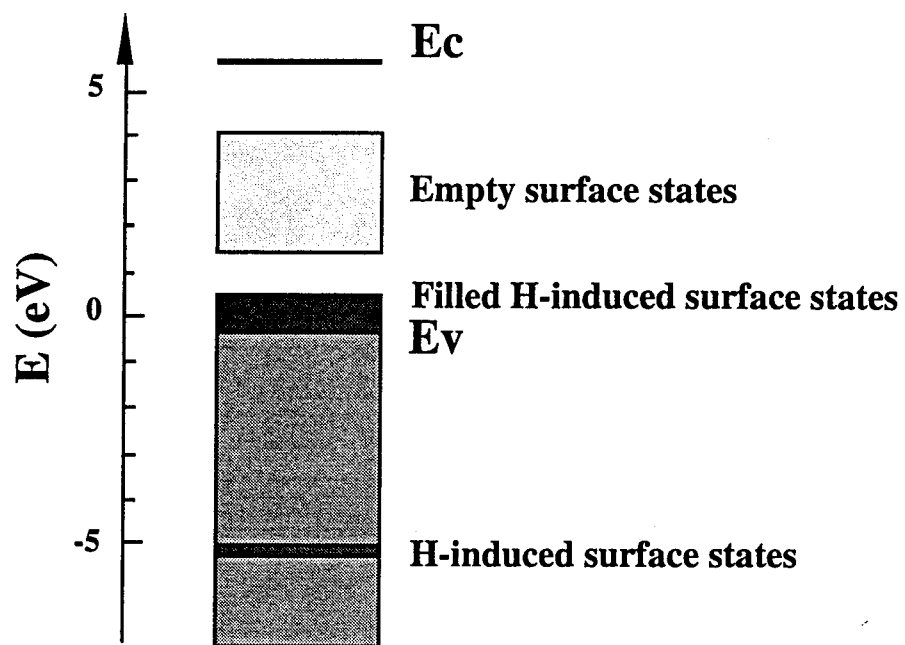


Figure 4. The electronic structure of C(100)-1x1:2H surface.

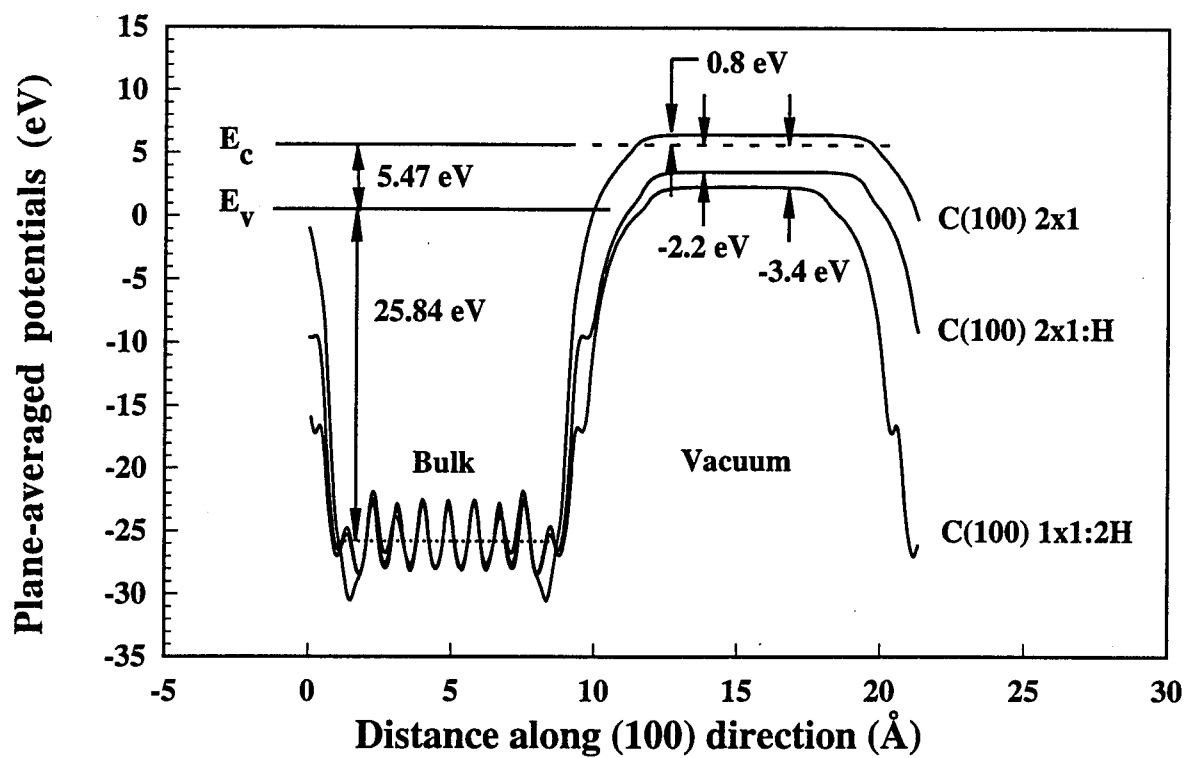


Figure 5. Plane-averaged self-consistent potential for C(100)-2 $\times$ 1, C(100)-2 $\times$ 1:H, and C(100)-2 $\times$ 1:2H surfaces. The energies of the band edges and the electron affinities are indicated by arrows. See text.

## **XI. Negative Electron Affinity Effects on H Plasma Exposed Diamond (100) Surfaces\***

**P. K. BAUMANN, R. J. NEMANICH**

Department of Physics, North Carolina State University,  
Raleigh, North Carolina, 27695-8202 USA

### **Abstract**

The effects of annealing and a H plasma exposure on natural type IIB diamond (100) were investigated by means of ultraviolet photoemission spectroscopy (UPS). The diamond (100) surface was found to exhibit a negative electron affinity (NEA) following a 900°C anneal in UHV. After a H plasma exposure the NEA peak in the UPS spectra had doubled in height. An anneal to 1100°C resulted in the removal of the sharp NEA feature. A second H plasma treatment resulted in the reappearance of the NEA peak like after the first H plasma exposure. A 2x1 reconstructed low energy electron diffraction (LEED) pattern was observed subsequent to the anneals as well as the H plasma treatments. The fact that a NEA can be induced or removed repeatedly by means of a H plasma exposure or a 1100°C anneal, respectively provides evidence to correlate the appearance of a NEA with the presence of a monohydride terminated surface.

### **I. Introduction**

The electron affinity of a semiconductor is defined as the energy difference between the vacuum level and the conduction band minimum. For most materials the vacuum level lies above the conduction band minimum, corresponding to a positive electron affinity. Surfaces of wide bandgap semiconductors like diamond have the potential of exhibiting a negative electron affinity (NEA) since the conduction band minimum lies near the vacuum level. Electrons present in the conduction band have sufficient energy to overcome the workfunction of a NEA surface and can be emitted into vacuum. Indeed, different surface preparation techniques can shift the position of the vacuum level and therefore induce a NEA or remove it [1-3]. Photoemission spectroscopy is very sensitive to determine whether a surface exhibits a NEA or not. Secondary electrons appear as a sharp feature at the low energy end of photoemission spectra for NEA surfaces [4, 5].

---

\*Accepted for publication in the proceedings of DIAMOND FILMS '94, the 5th European Conference on Diamond, Diamond-like and Related Materials, Il Ciocco, Italy, September, 1994: J. Diamond Rel. Mat.

Cleaning of diamond substrates for vacuum investigations oftentimes involves a chemical cleaning step followed by an in-vacuum treatment. A common chemical clean is based on using chromic acid and aqua regia. An electrochemical etch has been suggested as a suitable alternative approach [6]. Previously we have published comparative studies on the influence of this electrochemical cleaning technique versus a conventional chromic acid clean on the diamond (100) surface [1]. In particular it was found that oxygen could be removed from the surface at lower annealing temperatures for samples cleaned by an electrochemical etch than for those cleaned by using chromic acid. Furthermore, we have used both techniques to clean diamond substrates prior to deposition of epitaxial Cu contacts [7]. Various metals like Ti, Ni and Cu have been shown to induce a NEA on diamond [8, 9, 1]. The vacuum cleaning step usually involves annealing the sample or exposing it to a plasma. The effects of annealing diamond (100) have been addressed in several studies [1, 3, 10-12]. Two different structures have been suggested for an unreconstructed, oxygen terminated surface [11]. Arguments for a monohydride terminated surface [1, 3, 12] or a hydrogen free surface [10] after annealing to  $\sim 1000^{\circ}\text{C}$  have been presented. Plasma treatments have been used previously to clean diamond surfaces [2, 3].

In this study natural type IIb diamond C(100) crystals have been chemically cleaned by an electrochemical etch [6] and a HF dip [1]. Following the chemical cleaning step a series of anneals and H plasma exposures at  $500^{\circ}\text{C}$  have been employed. Such a H plasma may be comparable to the environment of diamond growth at low temperatures [13].

## II. Experimental Procedure

The UHV system used in our studies consists of several chambers connected by a UHV transfer line featuring a rail-mounted cart to transport the samples between the chambers. In particular, the chambers used for this study included an ultraviolet photoemission spectroscopy (UPS) chamber, a chamber for low energy electron spectroscopy (LEED) and Auger electron spectroscopy (AES) and a plasma cleaning chamber. The diamond samples used were natural type IIb single crystal C(100)  $3.0 \times 3.0 \times 0.25$  mm wafers. An electrochemical etch was used to chemically clean the samples [6]. For this purpose they were suspended between two Pt electrodes in deionized (DI) water as an electrolyte. For a DC bias of 350V between the electrodes a current of 0.5 mA could be measured. After the electrochemical etch the samples were exposed to UV ozone and rinsed in an HF solution to remove  $\text{SiO}_2$  surface contaminants. The presence of  $\text{SiO}_2$  has been observed previously following the electrochemical etch [1].  $\text{N}_2$  was used to blow the samples dry before they were mounted onto a Mo holder and transferred into the load lock of the UHV system. In vacuum the samples were annealed to  $900^{\circ}\text{C}$  for 15 minutes. A pyrometer was used to determine the surface temperature of the Mo holder on which the



diamond wafers were mounted. The base pressure was  $\sim 1 \times 10^{-10}$  Torr and rose to  $\sim 4 \times 10^{-9}$  Torr during annealing. Following the anneal the samples were exposed to a remote H plasma clean. During the clean the temperature of the sample was kept at 500°C, and the H pressure was held at 50 mTorr. The plasma cleaning system has been described in detail in a previous publication [14]. After the plasma clean the samples were heated to 1100°C which caused the pressure in the annealing chamber to rise to  $\sim 7 \times 10^{-9}$  Torr. Following this anneal the samples were reexposed to a H plasma. Subsequent to each cleaning step the techniques of UPS, LEED and AES have been used to characterize the diamond surface. The photoemission was excited by HeI (21.21 eV) radiation. A 50 mm hemispherical electron analyzer with an angular resolution of 2° was used to analyze the photoemitted electrons. An energy resolution of 0.15 eV was used for these experiments. The sample was biased by 1.0 V to overcome the workfunction of the analyzer and to ensure that low energy electrons from a NEA surface could be detected. The position of the sharp NEA peak at the low energy end of photoemission spectra corresponds to the energy position of the conduction band minimum,  $E_C$  (Fig. 1). Emission from  $E_C$  is positioned at  $E_V + E_G$  in the spectrum, where  $E_V$  is the energy of the valence band maximum and  $E_G$  that of the bandgap. Emission from the valence band maximum appears at  $E_V + hv$  in the spectrum. The spectral width or the distance between emission from the valence band maximum and the conduction band minimum is therefore  $hv - E_G$ . With the values for He I radiation  $hv = 21.21$  eV and the bandgap of diamond  $E_G = 5.47$  eV a spectral width of  $\sim 15.7$  eV is determined for a NEA surface. However, in case of a positive electron affinity surface the low energy cutoff will be determined by the position of the vacuum level and the spectral width will be smaller.

### III. and IV. Results and Discussion

Subsequent to the electrochemical etch and HF dip the as loaded diamond crystals exhibited a positive electron affinity as evidenced from photoemission spectra. In addition, a 1x1 unreconstructed surface and oxygen surface contaminations were detected by means of LEED and AES, respectively. Upon annealing to 900°C in UHV a sharp low energy peak indicating a NEA surface could be observed in UPS spectra (Fig. 2). This peak is positioned 15.7 eV below the position of the valence band maximum,  $E_V$  in the spectrum. Furthermore a weak feature at  $\sim 1.7$  eV below  $E_V$  was also observed after annealing. The NEA effect coincided with the appearance of a 2x1 reconstructed LEED pattern and the removal of oxygen from the surface as seen from AES (Fig. 3). All the spectra in Fig. 2 have been scaled with respect to feature (A). Following a hydrogen plasma clean the NEA peak in the UPS spectra was found to be doubled in intensity. Also the peak at  $\sim 1.7$  eV below  $E_V$  was no longer observed. Furthermore, the 2x1 LEED pattern could be retained and no changes in the AES spectra were detected. After the diamond wafers were heated to

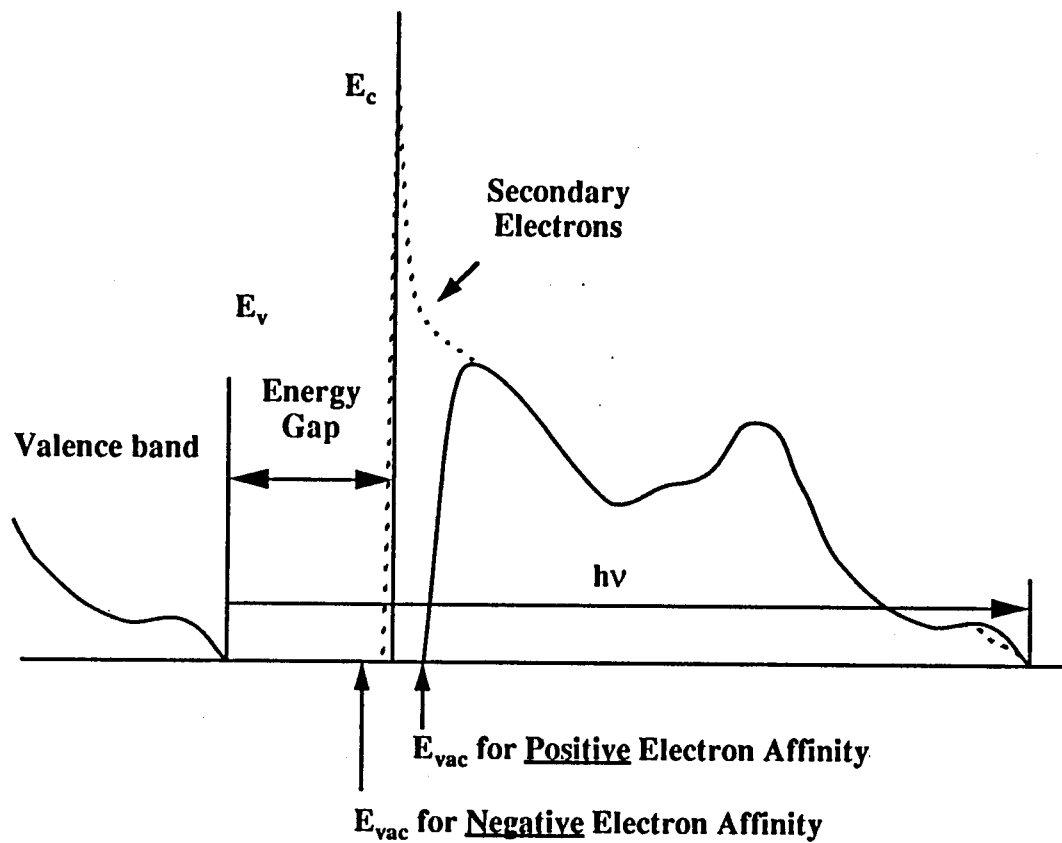


Figure 1. Schematic diagram of photoemission spectra for a negative electron affinity surface (dotted line) and a positive electron affinity surface (solid line).

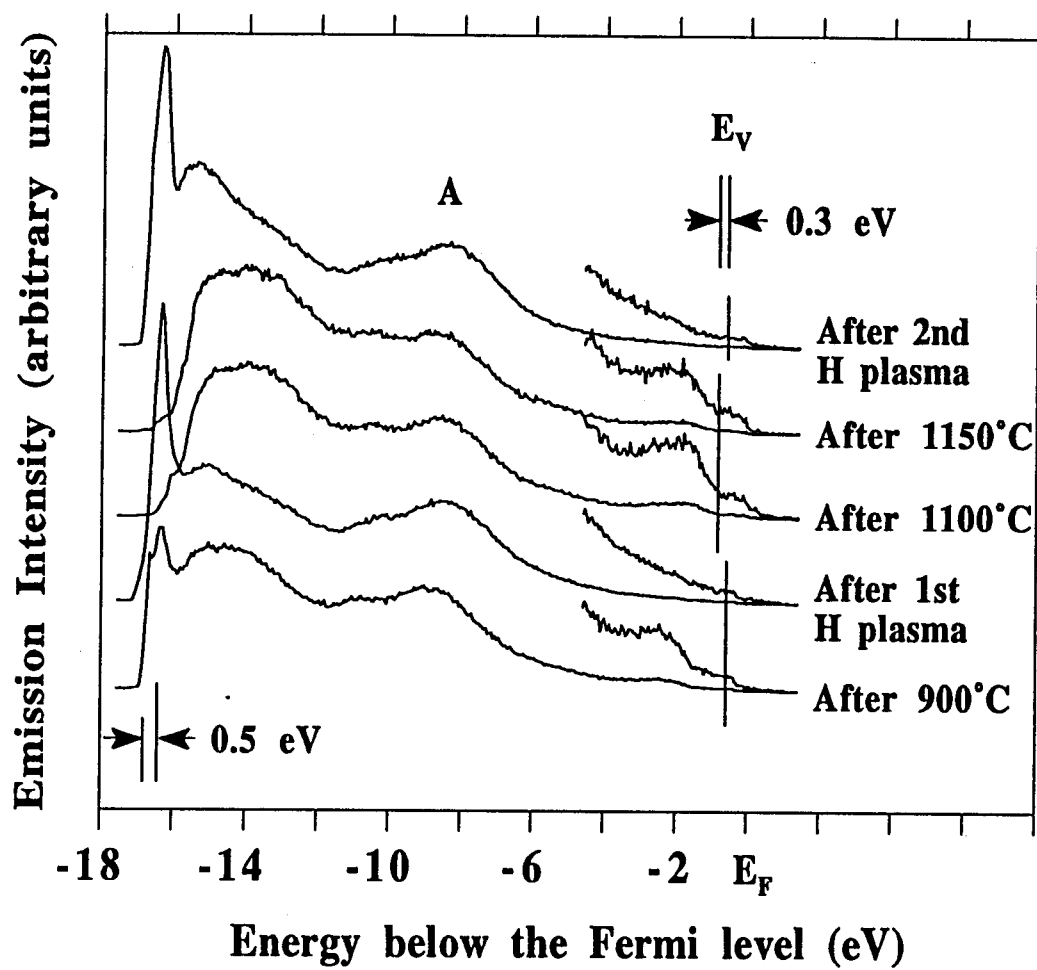


Figure 2. Photoemission spectra of C(100) cleaned by an electrochemical etch. The sequence of spectra follows from bottom to top: a 900°C anneal, a H plasma, a 1100°C anneal, a 1150°C anneal and a second H plasma.

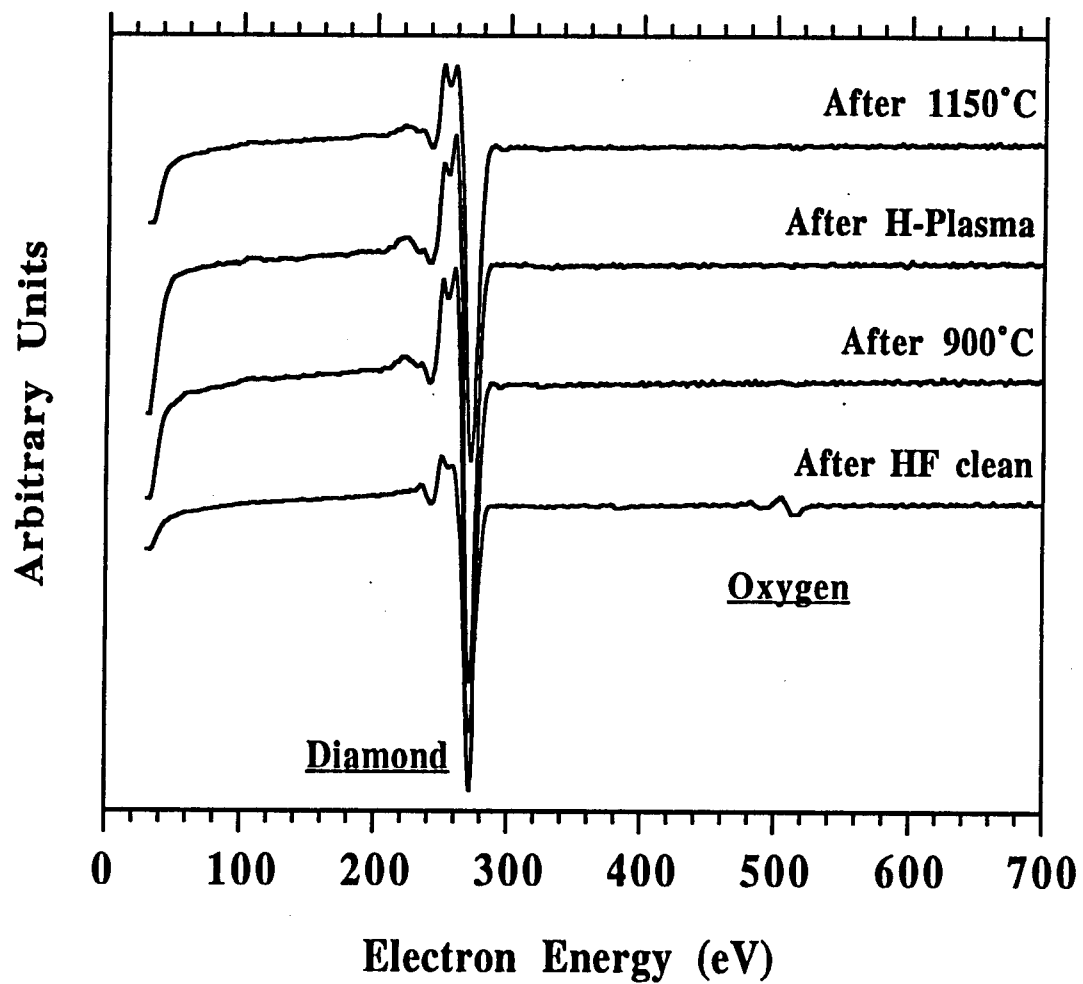


Figure 3. Auger spectra of the diamond (100) surface cleaned by an electrochemical etch, as a function of annealing and H plasma exposure.

1100°C, the sharp low energy peak was removed from the UPS spectra, and the low energy cutoff had moved toward higher energies by  $\sim 0.5$  eV. However, a small low energy shoulder could still be observed. In addition, the whole spectrum was found to be shifted to lower energies by  $\sim 0.3$  eV. Furthermore, the weak feature reappeared at  $\sim 1.0$  eV below the valence band edge. Annealing to 1150°C resulted in the removal of the low energy shoulder. The remaining small low energy feature may still be an indication that the hydrogen has not been removed completely from the surface. Again, after the 1100°C and 1150°C anneals the surface remained 2x1 reconstructed, and the AES spectra did not change. Repeating the H plasma exposure resulted in the appearance of a sharp NEA peak similar to the one observed after the initial H plasma clean. In addition the feature at  $\sim 1.0$  eV below  $E_V$  was removed. The features at  $\sim 1.7$  eV and  $\sim 1.0$  eV below  $E_V$  that appeared subsequent to the 900°C and 1100°C anneal are suggested to be surface states. However, only a LEED pattern with weak secondary spots was observed following the second H plasma exposure. Evidently the second H plasma clean caused a reduction in the domain size of the reconstructed surface. Therefore only a weak secondary interference pattern could form.

From our experiments it is suggested that removing the oxygen from the surface can be correlated to the induction of a NEA effect and a 2x1 reconstruction. This has been described in previous publications [1, 10-12]. It is interesting to note that the intensity of the NEA peak in the UPS spectra could be increased by employing a H plasma clean. Indeed, a H plasma could also induce a NEA on a positive electron affinity surface. However, a reconstructed (2x1) LEED pattern could be detected after every anneal (900°C, 1100°C and 1150°C) and H plasma exposure. It is therefore suggested that a reconstructed surface exhibiting a NEA is terminated by a monohydride. Whereas a reconstructed positive electron affinity surface is believed to be free of hydrogen. Indeed, ab initio calculations for the 2x1 reconstructed surface indicate a NEA for the monohydride terminated surface and a positive electron affinity for the clean surface [3]. Previously Yang et al. suggested that a dihydride terminated surface is energetically unlikely due to steric hindrance of the H atoms [10]. They proposed that a monohydride terminated surface turns into a free surface upon annealing to  $\sim 1000^\circ\text{C}$ . However, Hamza et al. reported the presence of a monohydride terminated surface after annealing to  $\sim 1000^\circ\text{C}$  based on electron-simulated desorption time-of-flight measurements [12]. Furthermore, they report that even after annealing up to  $\sim 1260^\circ\text{C}$  the slow proton peak could be detected in the ESD-TOF spectra. Therefore they argue that large parts of the surface are still terminated by a monohydride. They did not anneal the samples beyond 1260°C since diamond is expected to graphitize at higher temperatures. Our results, however, suggest that upon annealing to 1100°C enough hydrogen has been desorbed from the surface to remove the sharp NEA peak from the photoemission spectra. But if any significant portions of the surface were still terminated by a monohydride,

a peak characteristic of a NEA could clearly be observed in the photoemission spectra (according to Weide et al. [3]). Indeed, spectra obtained upon heating to 900°C exhibited a smaller NEA peak than those taken after a H plasma exposure.

It is suggested that the H plasma clean resulted in a uniform monohydride terminated surface. From the size difference of the NEA peaks we therefore estimate that about half the surface was terminated by a monohydride following the 900°C anneal. Furthermore, the remaining small low energy feature in the photoemission spectra following the 1100°C and 1150°C anneals may be an indication that the hydrogen has not been removed completely from the surface. It may be possible that the portions of the surface terminated by a monohydride were large enough to result in the slow proton peak seen in the ESD-TOF spectra up to ~ 1260°C. However, these portions may have been too small to result in a distinctive low energy peak in the photoemission spectra after heating to 1100°C. It is however interesting to realize that Hamza et al. rapidly heated the diamond surface (up to 1130°C in ~ 45 s). Typical heating rates used for our experiments were ~ 60 °/min. It is, however, unclear whether the different annealing rates would influence the results significantly. Furthermore, it is difficult to measure the temperature of diamond due to its transparent nature. Therefore, the temperature values mentioned in this and other studies may be off somewhat with respect to each other. This may reconcile some of the apparent differences in the results. Also, different surface cleaning processes or the presence of H in the bulk may effect the surface characteristics. Further work will be necessary to clarify these issues.

## V. Conclusions

A NEA effect was induced on the electrochemically cleaned diamond (100) surface by means of a 900°C anneal. A H plasma exposure enhanced this effect. The NEA could be removed following a 1100°C anneal. The UPS spectrum from the initial H plasma clean could be reproduced by reexposing the diamond surface to a H plasma. The surface was found to be 2x1 reconstructed following the 900°C, 1100°C and 1150°C anneals and after each H plasma exposure.

## VI. Future Research Plans and Goals

Fabrication of electron injecting electrical contacts to diamond. Development and testing of cold cathode emitter structures based on diamond NEA surfaces.

## Acknowledgments

This work was supported by the Office of Naval Research (Contract No. N00014-92-J-1477).

## VII. References

- 1 P.K. Baumann, T.P. Humphreys and R.J. Nemanich, in Diamond, SiC and Nitride Wide Bandgap Semiconductors, edited by C.H. Carter, G. Gildenblat, S. Nakamura, R.J. Nemanich, (Mater. Res. Soc. Proc. **339**, Pittsburgh, PA, 1994), in press
- 2 J. van der Weide and R.J. Nemanich, Appl. Phys. Lett. **62**, 1878 (1993)
- 3 J. van der Weide, Z. Zhang, P.K. Baumann, M.G. Wensell, J. Bernholc and R.J. Nemanich, Phys. Rev. B **50**, 5803 (1994)
- 4 F.J. Himpsel, P. Heimann and D.E. Eastman, Solid State Commun. **36**, 631 (1980).
- 5 B.B. Pate, W.E. Spicer, T. Ohta and I. Lindau, J. Vac. Sci. Technol. **17**, 1087 (1980).
- 6 M. Marchywka, P.E. Pehrsson, S.C. Binari and D. Moses, J. Electrochem. Soc., Vol. **140**, No. 2 (1993) L19.
- 7 P.K. Baumann, T.P. Humphreys, R.J. Nemanich, K. Ishibashi, N.R. Parikh, L.M. Porter and R.F. Davis, Proceedings of the Fourth European Conference on Diamond, Diamond- like and Related Materials, (J. Diamond Rel. Mat., Vol. 3/4-6, 1994) pp. 883-886
- 8 J. van der Weide and R.J. Nemanich, J. Vac. Sci. Technol. B **10**, 1940 (1992).
- 9 J. van der Weide and R.J. Nemanich, Phys. Rev. B **49**, 13629 (1994)
- 10 Y.L. Yang, L.M. Struck, L.F. Scutcu and M.P. D'Evelyn, Thin Solid Films **225**, 203 (1993)
- 11 R.E. Thomas, R.A. Rudder and R.J. Markunas, J. Vac. Sci. Technol. A **10**, 2451 (1992)
- 12 A.V. Hamza, G.D. Kubiak and R.H. Stulen, Surf. Sci. **237**, 35 (1990)
- 13 Y. Muranaka, H. Yamashita and H. Miyadera, J. Vac. Sci. Technol. A **9**, 76 (1991)
- 14 T.P. Schneider, J. Cho, Y.L. Chen, D.H. Mahler and R.J. Nemanich, in Surface Chemical Cleaning and Passivation for Semiconductor Processing, edited by G.S. Higashi, E.A. Irene, T. Ohmi (Mater. Res. Soc. Proc. **315**, Pittsburgh, PA, 1993) pp. 197-209.

## XII. Growth and Characterization of Homoepitaxial Diamond Negative Electron Affinity Surfaces

### A. Introduction

Diamond has received much attention in the past due to its unique optical, mechanical, thermal, and electronic properties[1-4]. With the advances in low pressure thin film diamond growth techniques, much emphasis has been placed on electronic applications. However, at present, diamond devices are limited due to the inability to grow conductive n-type films.

Recently, there has been renewed interest in developing diamond cold cathode emitters using negative electron affinity (NEA) emission. An NEA occurs when the vacuum level lies below the conduction band minimum at the surface. If an NEA is present, all electrons in the conduction band have enough energy to overcome the work function of the surface providing a highly efficient mechanism for electron emission. NEA has been observed for the (100), (110), and (111) surfaces of diamond using various *in situ* and *ex situ* surface preparations[5].

Due to diamond's extreme mechanical and chemical properties, it is impossible to obtain atomically flat diamond surfaces, even with modern mechanical and electrochemical polish techniques. High resolution Atomic Force Microscopy reveals residual polishing grooves on the polished surfaces[6]. Since NEA emission is inherently a surface process, it is important to understand the role of surface morphology on NEA electron emission. The objective of this research is to obtain atomically flat diamond surfaces by depositing thin high quality homoepitaxial films. These films will then be characterized using several surface sensitive techniques (described below) to assess this role of surface morphology on NEA electron emission.

### B. Experimental Procedure

The diamond growth system used is shown in Fig. 1. It consists of a commercially available stainless steel ASTeX HPMS microwave plasma CVD chamber. The microwave generator is a 2.45 GHz ASTeX S-1500i rated up to 1500 W. The substrate heater is a graphite susceptor which is inductively heated using a dedicated ASTeX RF power supply. This susceptor is molybdenum capped to prevent the susceptor from providing an uncontrollable carbon source. The temperature is determined using both an optical pyrometer and a standard type-K thermocouple located inside the graphite susceptor. Pressure control is achieved downstream using a MKS Baratron and MKS Butterfly valve. The H<sub>2</sub>/CH<sub>4</sub> process gas mixture is controlled by MKS mass-flow controllers. The process pump is a Leybold D16BCS mechanical pump.



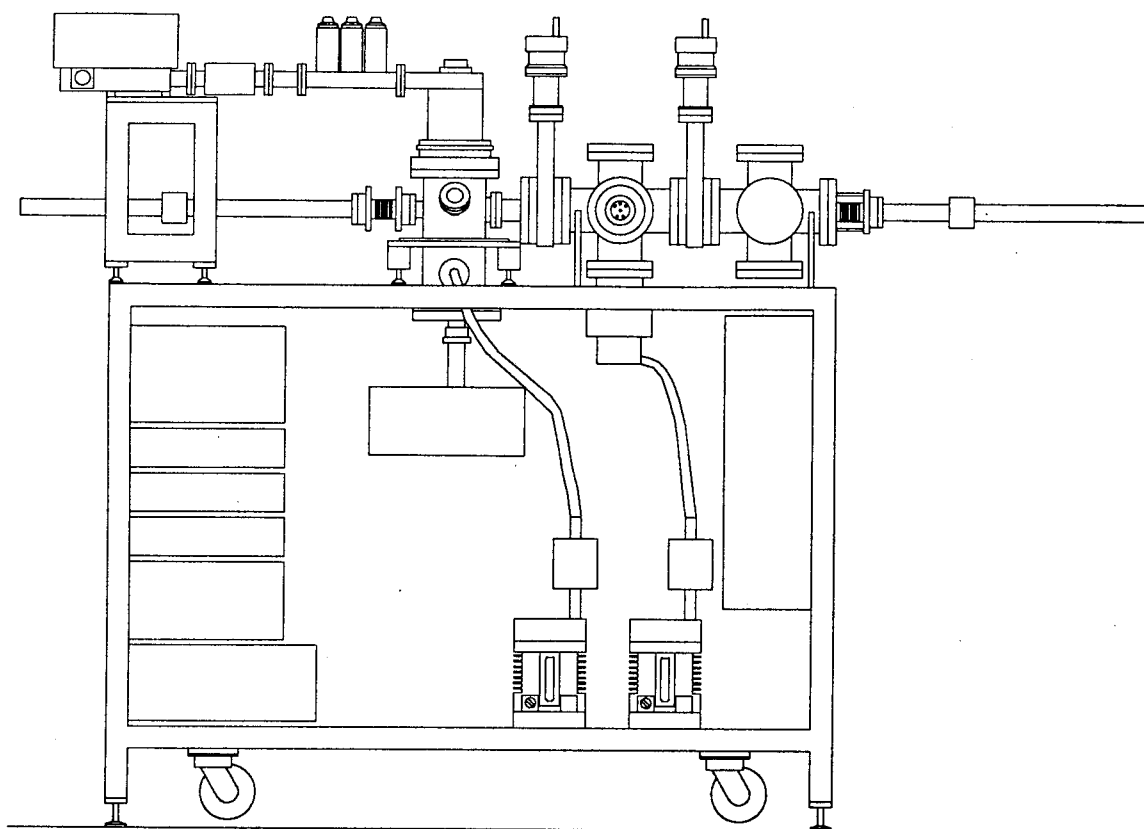


Figure 1. Schematic of the microwave plasma CVD diamond growth chamber.

A schematic of the integrated surface processing/characterization system is shown in Fig. 2. It consists of eight stations which are connected by a 35 ft UHV sample transfer system. These stations include a remote hydrogen plasma cleaning chamber, the HPMS growth chamber, Raman spectroscopy, Ultraviolet Photoemission Spectroscopy (UPS), Auger Electron Spectroscopy (AES), Low Energy Electron Diffraction (LEED), and X-ray Photoemission Spectroscopy (XPS). Raman spectroscopy is routinely used to determine the overall film quality of diamond films. UPS is used to observe whether a surface exhibits an NEA, while XPS and AES are used to determine the chemical composition of species on the surface. Since the HPMS chamber is simply mechanically pumped, it is necessary to have an intermediate chamber which is pumped by a Leybold 180 l/s turbomolecular pump to act as a pressure lock between the growth chamber and the UHV transfer system.

To test the operation of the diamond growth system, diamond was first deposited on (100) silicon substrates. These substrates were scratched using 0.25  $\mu\text{m}$  diamond grit. After scratching, they were degreased using the standard UHV clean procedures (TCE, acetone, methanol, and DI water rinse) and blown dry with  $\text{N}_2$ . The samples were loaded into the HPMS growth chamber via the sample transfer system. The samples were grown at 750  $^\circ\text{C}$  for

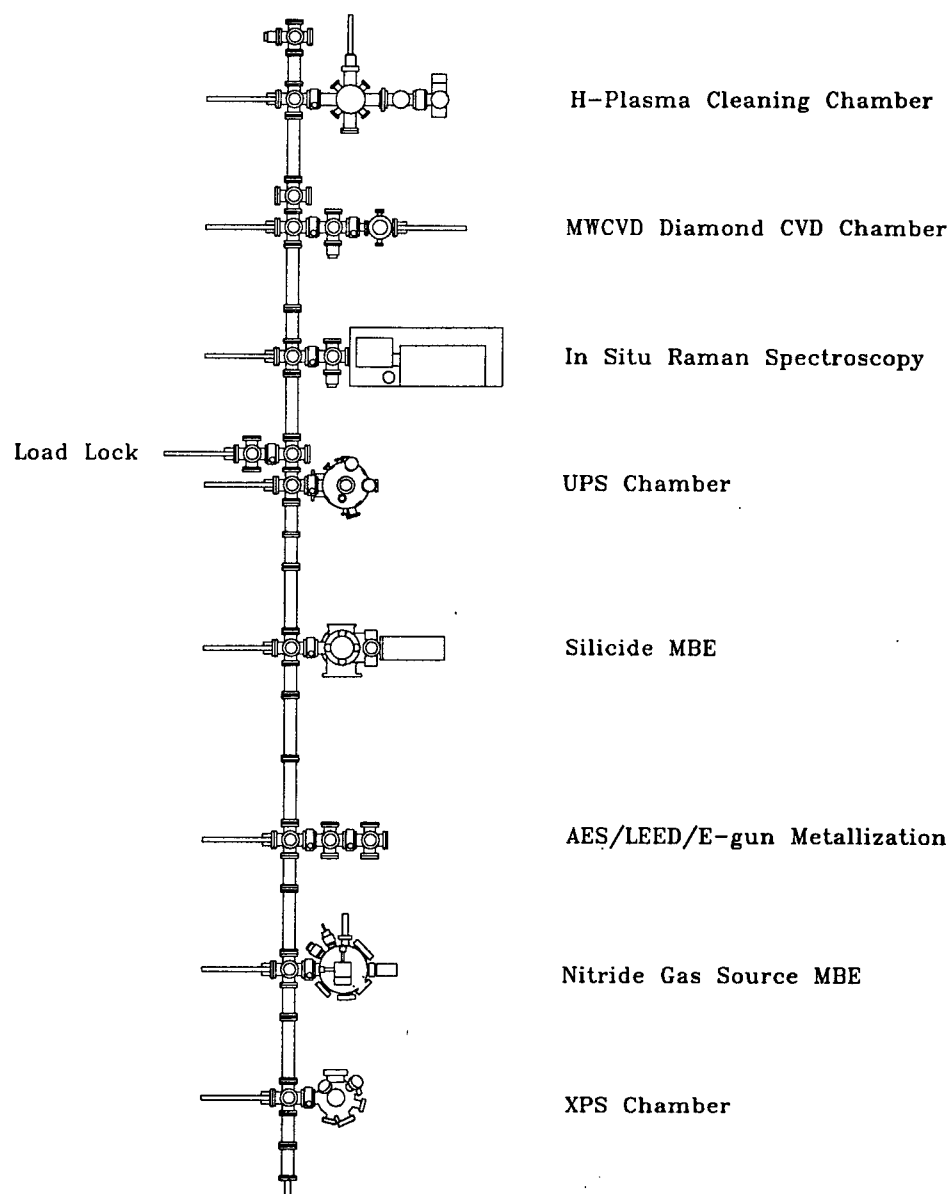


Figure 2. Schematic of the integrated surface processing/characterization system.

7 hours at 20 torr with a  $\text{CH}_4/\text{H}_2$  flow ratio of 0.02 and a total gas flow of 300 sccm and a microwave power of 1000 W. After deposition, the samples were transferred to the Raman spectroscopy chamber and spectra were taken to determine film quality and  $\text{sp}^2/\text{sp}^3$  bonding ratio.

In addition to the *in situ* characterization tools available on the vacuum transfer system, other *ex situ* techniques were used to characterize the morphology and RMS roughness of the samples. These include Atomic Force Microscopy (AFM), Scanning Tunneling Microscopy (STM), and Scanning Electron Microscopy (SEM).

### C. Results and Discussion

Although diamond is considered to possess a highly robust surface, it is imperative for these studies that samples be transferred from chamber to chamber without being exposed to atmosphere. In this way, the surface can be examined and manipulated without possible ambient contaminants. As mentioned earlier, homoepitaxial films will be used to provide atomically flat diamond surfaces. Therefore growth conditions must be determined which will achieve uniform layer by layer growth. In addition, these films must be of extremely high quality in order to eliminate possible competition between the desired electron emission and unwanted recombination through defect centers.

The results to date involve the completion of the design and construction of the ASTeX microwave plasma CVD chamber and its incorporation onto the UHV transfer system. Preliminary testing of the chamber is underway and optimum growth conditions are being evaluated. The nontrivial task of transferring the samples in and out of the growth chamber through customized ports which do not disturb the microwave cavity has been successful. Due to the expense and scarcity of single crystal diamond substrates, the initial testing of the system has been performed using readily available (100) silicon wafers. Figure 3 shows the Raman spectra taken *in situ* of a representative sample. The lack of a large peak at  $\sim 1500\text{ cm}^{-1}$  due to graphitic bonding indicates that the films are of good quality. Figure 4 is an SEM micrograph of the same sample which shows highly faceted nuclei.

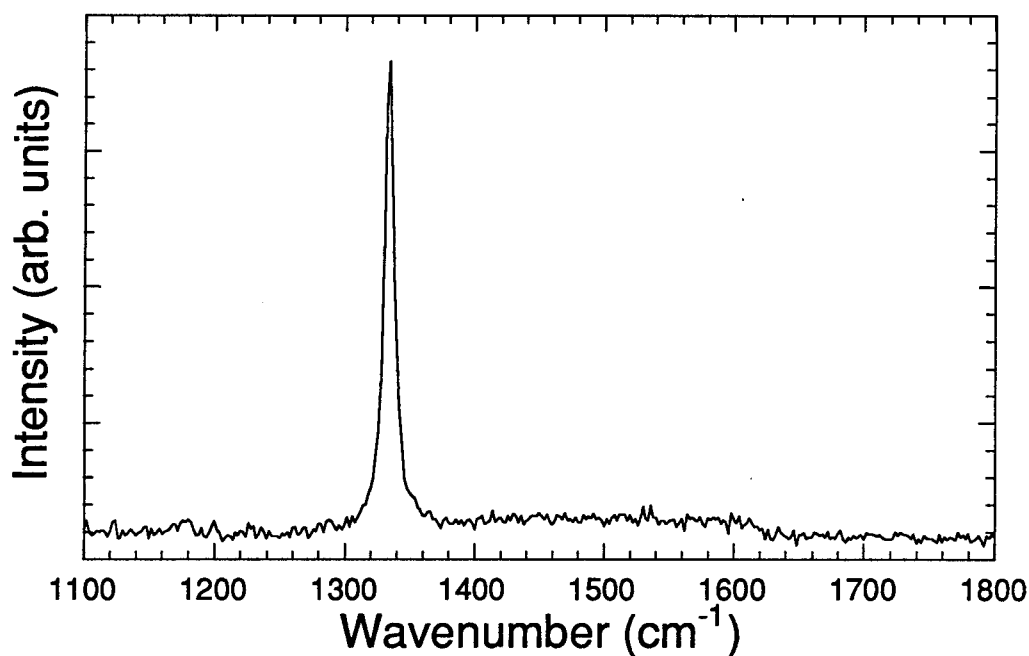


Figure 3. *In situ* Raman spectrum of a CVD diamond film grown on a scratched (100) silicon wafer.

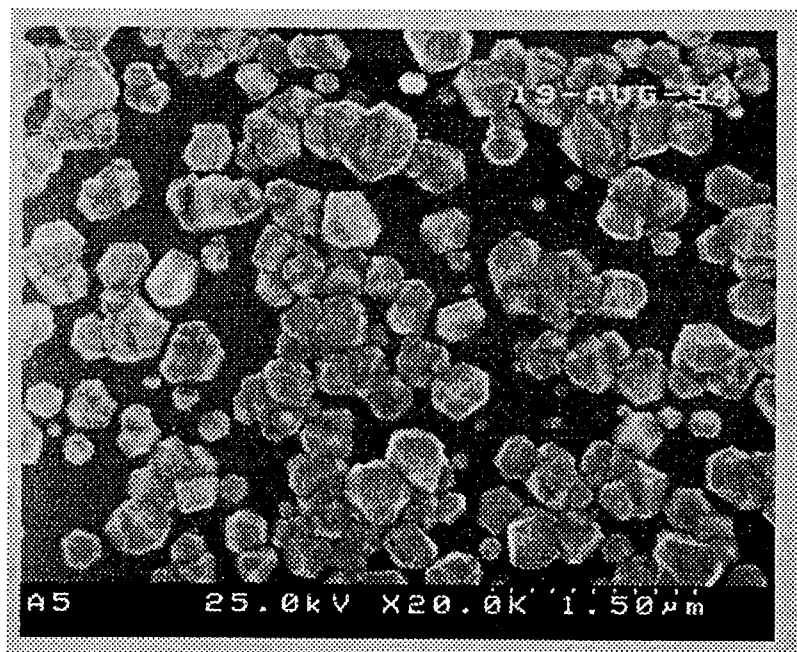


Figure 4. SEM micrograph of the CVD diamond film shown in Figure 3.

#### D. Future Research Plans and Goals

Immediate plans include the continuation of this research as outlined above. Once high quality deposition is achieved on (100) silicon, these parameters will be used as an initial starting point for the deposition on (100) diamond single crystal substrates. Then the next objective will be to obtain high quality epitaxial films. Raman spectroscopy and AFM will be the key techniques in determining the optimum process conditions. Since  $C^{13}$  is heavier than  $C^{12}$ ,  $C^{13}$  labeled methane will be used in order to distinguish the deposited homoepitaxial CVD film from the underlying diamond substrate in the Raman analysis. When pristine films are obtained, the surface sensitive techniques outlined above will be used to examine the role of surface morphology on the NEA characteristics. Work will proceed analogously for the (110) and (111) surfaces of diamond.

#### E. References

1. C. A. Brookes and E. J. Brookes, *Diam. Relat. Mat.* **1**, 13 (1991).
2. L. Wei, P. K. Kuo, R. L. Thomas, edited by R. Messier, J. T. Glass, J. E. Butler, and R. Roy (Materials Research Society, 1990), p.875.
3. J. H. Edgar, *J. Mater. Res.* **7**, 235 (1992).
4. I. M. Buckley-Golder, R. Bullough, M. R. Hayns, J. R. Willis, R. C. Piller, N. G. Blamries, G. Gard, and J. Stephen, *Diam. Relat. Mat.* **1**, 43 (1991).
5. J. van der Weide, Personal Communication (1994).
6. S. E. Wagoner, Personal Communication (1994).

### XIII. Characterization of Electron Emission from Cold Cathode Emitters

#### A. Introduction

The search for cold cathode devices has received much attention recently. To find a device that can emit electrons with just a few volts applied is a goal for both research and industry. In the past, there have been several potential solutions for electron emission. One method uses high electric fields produced by metal tips to cause electrons to tunnel into vacuum. However, these cathodes are unstable at high current densities. Another method uses conventional semiconductors such as Si or GaAs covered with a layer of Cs. Due to band bending, the conduction band of the material lies below the vacuum energy level. When a bias is applied, high current densities of greater than  $1500 \text{ A/cm}^2$  can be measured. The disadvantage of such a device is that it is easily contaminated after exposure to  $\text{O}_2$ . A third method would be to use wide-bandgap materials such as AlN or diamond which can have their conduction band close to the vacuum energy level even in the presence of  $\text{O}_2$  or  $\text{H}_2\text{O}$ . These materials can be doped or grown in different ways to make them acceptable electron emitters[1]. Whatever the method employed, a testing station is needed to characterize the electron emission.

An example of a device pursued by M. Geis *et al.*[2] using diamond is shown in Fig. 1. The diodes are fabricated by carbon ion implantation into p-type diamond and covered with one micron of aluminum. The diode current  $I_D$  was varied from 0.1 mA to 10 mA with a bias voltage  $V_D$  of -60 to -150 V. The voltage between the anode and the p-type diamond substrate was usually 100V, and the anode current  $I_A$  varied from  $1\text{e-}13\text{A}$  to  $5\text{e-}7\text{A}$ .

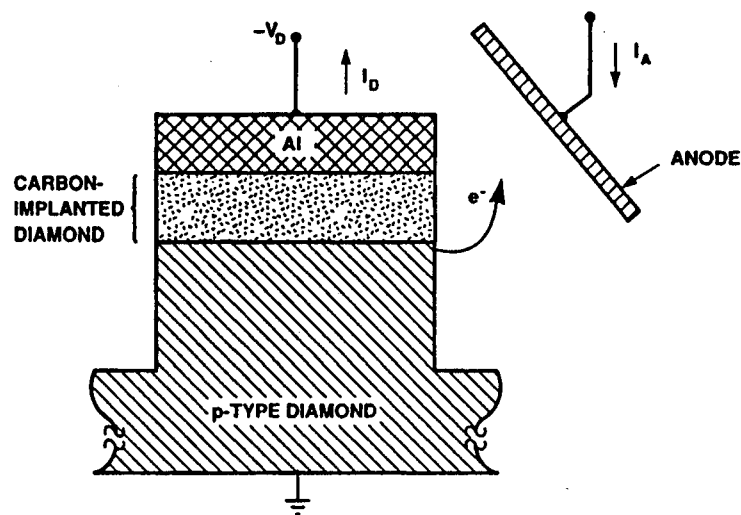


Figure 1. A typical diamond cold cathode built by M. Geis *et al.*

## B. Experimental Procedure

The layout of the High Vacuum I-V / Optics Station is shown in Fig. 2. The chamber, pumps, data acquisition, and source-measure components have been bought and assembled. The chamber will be used for carrying out the measurements described below in vacuum. With the current pumps on the system now, a pressure of  $5\text{e-}8$  Torr can be reached.

The first of the measurements that will be done is a simple two-pole DC measurement as shown in Fig. 3. A collector will be used to draw the electrons out of the sample. An example of a collector would be a spark plug which could withstand up to 25,000 V.

The second DC measurement to be carried out will be a three-pole measurement as shown in Fig. 4. The collector will be attached to a micrometer or a piezo-electric positioner. Electrons are emitted from the surface by applying a voltage across the sample. The current between the sample and the collector will be measured as a function of sample bias.

The third DC measurement will be a four-pole measurement where the set-up would be the same as that for the three-pole measurement with a gate included for amplification of the current. Current-voltage readings between the collector and the sample can be taken as a function of gate bias.

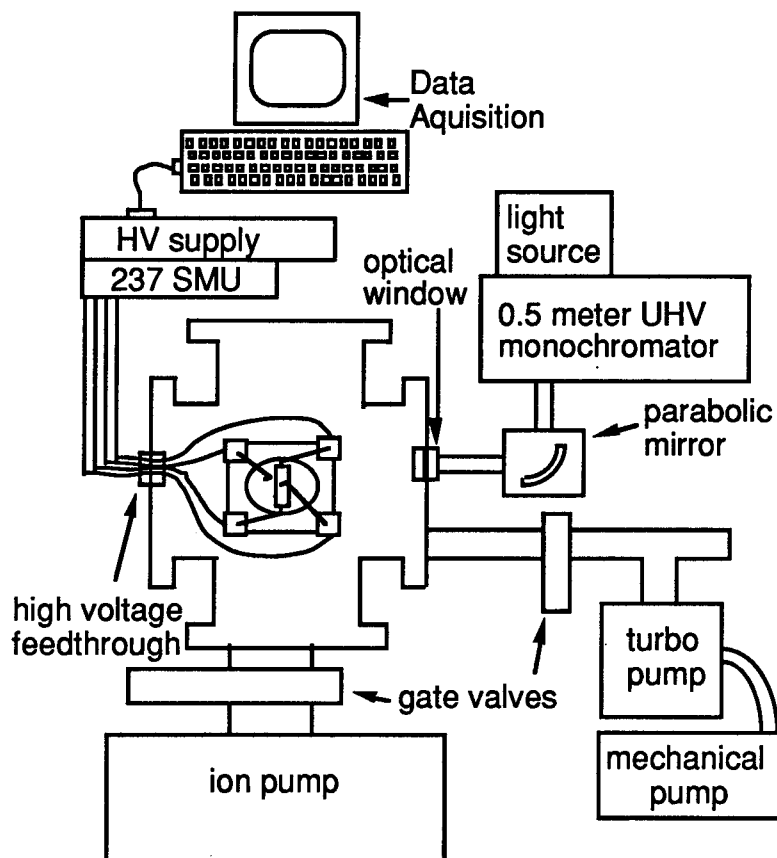


Figure 2. High vacuum I-V / optics station.

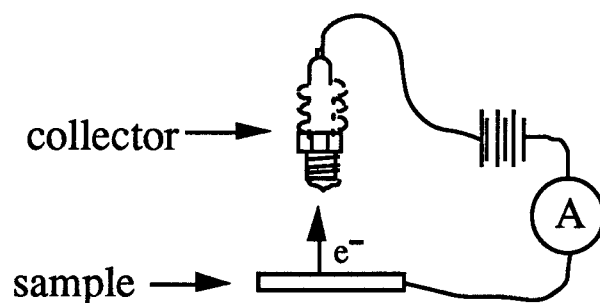


Figure 3. A two-pole DC measurement with a spark plug as a collector.

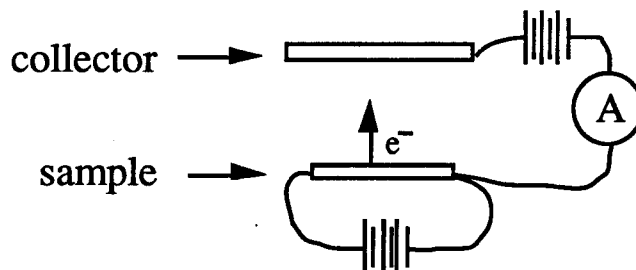


Figure 4. A three-pole DC measurement using a micrometer or piezo-electric positioner as a collector.

A fourth type of measurement that will be done is a quantum efficiency measurement. Quantum efficiency is defined as the ratio of the number of electrons emitted from a sample per photon incident on that sample. The photo-excitation of the sample will be carried out with a monochromatic light source. The wavelength range that can be covered with an ultra-high vacuum monochromator would be from 120nm to 2000nm using a deuterium and Xenon light source. The bandgaps of both diamond and AlN fall well within this range. Operating in this wavelength range would give an understanding of any defect level that may be present in the bandgap of the material. If electrons are emitted from the sample, they can be collected with a grid as shown in Figure 5.

### C. Discussion and Conclusion

The reason for the quantum efficiency measurement, other than applying a merit value to the device in question, would be to study any competing mechanisms which could inhibit electron emission. Quantum efficiency can tell just how much these mechanisms slow electron emission.

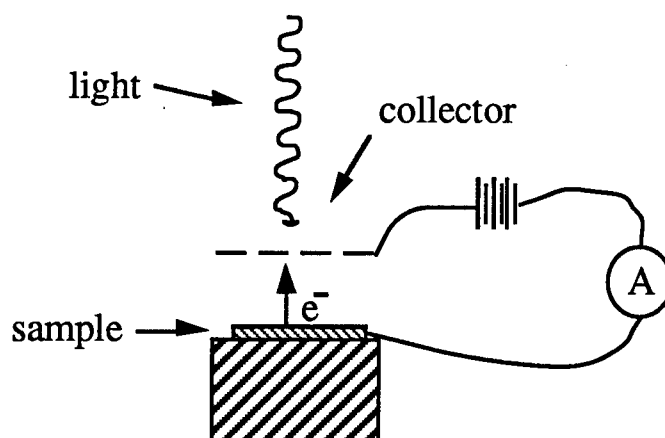


Figure 5. Photo-excitation of the sample with monochromatic light.

As shown in Figure 6, there are two competing mechanisms. After an electron is excited into the conduction band from the valence band, it can go through one of three events. One, if there is a defect level in the lattice, the electron can be captured at an empty center. If the defect happens to capture a hole from the valence band also, then these indirect transitions can affect electron emission drastically. Two, the electron has a certain probability of decaying to the valence band instead of being emitted. Three, if neither of the previous events occurs, then the electron has a probability of being emitted. These two competing mechanisms, indirect transition through a defect level or direct transition to the valence band can inhibit electron emission and cause the device quality to be poor.

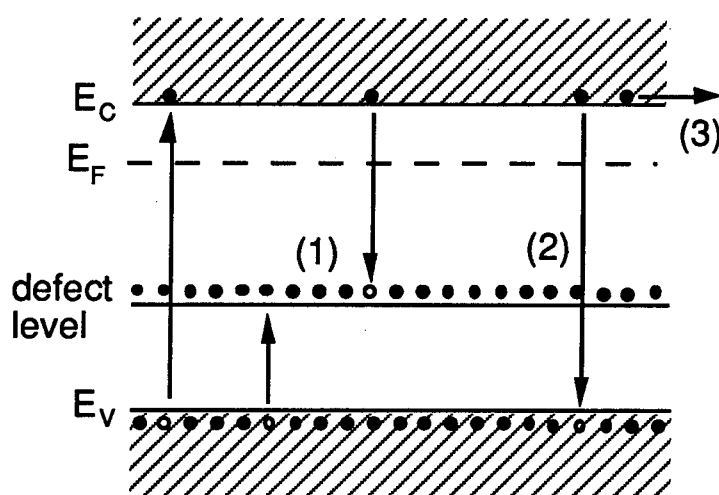


Figure 6. Two competing mechanisms: (1) indirect transition and (2) direct transition. If neither of these events occur then (3) the electron can be emitted.



In conclusion, DC measurements and photo-excitation measurements can give us an understanding of how to design a cold cathode device. Each device that is fabricated can be characterized in vacuum using these methods.

#### D. Future Plans and Goals

Near future work includes annealing the sample to extreme temperatures to see how this affects the measurements discussed above.

#### E. References

1. M. W. Geis, N. N. Efremow, J. D. Woodhouse, M. D. McAleese, M. Marchywka, D. G. Socker and J. F. Hochedez, *IEEE Electron Device Letters* **12**, 456 (1991).
2. M. W. Geis, N. N. Efremow, J. D. Woodhouse and M. D. McAleese, "Diamond Cold Cathodes," in *Proceedings of the First International Conference on the Applications of Diamond Films and Related Materials*, Y. Tzeng, M. Yoshikawa, M. Murakawa and A. Feldman, Ed., Elsevier Science Publishers, 1991, pp 309-310.

# Nitrogen-based Materials

## XIV. High Purity Gallium Nitride Powder Synthesis for Bulk Crystal Growth Studies

### A. Introduction

With the recent developments in the optoelectronic devices manufactured from GaN thin films, availability of single crystal wafers for homoepitaxial growth has gained considerable importance. A panel of experts in the field of wide band gap semiconductors assembled at the 1994 Spring Meeting of the Materials Research Society, were unanimous in their opinion that the greatest hindrance to the rapid advance of the III-V nitrides is the lack of single crystal wafers of these materials [1]. For crystal growth, it will be necessary to have a source of GaN.

Our research has revealed only one supplier of GaN powder in the USA. The supply, purity and cost are limited, poor and extreme, respectively. These constraints are severely limiting bulk crystal growth studies for this material. To conduct the different crystal growth studies, it is necessary to produce kilogram quantities of high purity GaN at reasonable cost. The following sections are concerned with achieving this objective.

### B. Thermodynamic Considerations for GaN Formation

Instability of GaN to sublimation and the very low reactivity between Ga and N<sub>2</sub> ( $\Delta G_f^\circ = -4.4$  Kcal/mol,  $K_p = 17$  @ 500°C) were the two main obstacles faced in selecting a suitable method to synthesize powder. To determine an efficient and economic method of producing high purity GaN powder, the reaction thermodynamics of the systems described by the following equations were investigated over a range of temperatures. A maximum temperature of 800°C was chosen because of the onset of sublimation of GaN.

Reaction	T (°C)	$\Delta G_{\text{reaction}}$ (Kcal/mol)	
$\text{GaBr(g)} + \text{NH}_3\text{(g)} = \text{GaN(s)} + \text{HBr(g)} + \text{H}_2\text{(g)}$	300-800	-4 – +3	(1)
$\text{GaI(g)} + \text{NH}_3\text{(g)} = \text{GaN(s)} + \text{HI(g)} + \text{H}_2\text{(g)}$	300-800	-2 – +6	(2)
$\text{GaCl}_3\text{(g)} + \text{NH}_3\text{(g)} = \text{GaN(s)} + 3\text{HCl(g)}$	300-800	+13 – +4	(3)
$\text{GaF}_3\text{(s)} + \text{NH}_3\text{(g)} = \text{GaN(s)} + 3\text{HF(g)}$	300-800	+33 – +5	(4)
$\text{Ga}_2\text{O}_3\text{(s)} + 2\text{NH}_3\text{(g)} = 2\text{GaN(s)} + 3\text{H}_2\text{O}$	300-800	+49 – +53	(5)
$\text{GaCl(g)} + \text{NH}_3\text{(g)} = \text{GaN(s)} + \text{HCl(g)} + \text{H}_2\text{(g)}$	300-800	-6.6 – +1	(6)
$\text{Ga(l)} + \text{NH}_3\text{(g)} = \text{GaN(s)} + 3/2\text{H}_2\text{(g)}$	300-800	-13 – -12	(7)
$\text{Ga}_2\text{O} + 2\text{NH}_3\text{(g)} = 2\text{GaN(s)} + \text{H}_2\text{O(g)} + \text{H}_2\text{(g)}$	300-800	-47 – -30	(8)

The  $\Delta G_{\text{reaction}}$  values at the temperatures that would be employed in GaN powder production (600-800 °C) for reactions (1-6) are positive and thus indicate that they would not occur. Therefore, reactions (1-6) were ruled out.

GaAs and GaP were not considered as precursor materials due to their higher price/gram in comparison to GaN powder. Furthermore, the conversion of GaAs requires an intermediate conversion step to  $\text{Ga}_2\text{O}_3$ , since a thin layer of GaN forms on the surface of GaAs and prevents complete conversion of GaAs into GaN [1]. Although the same problem was not reported for GaP, in converting GaP into GaN the evaporation of P has been a major problem [2]. In addition its high price makes this route unattractive for GaN production.

Reaction (7) has been proven to yield GaN by the initial research by Pichugin and Yas'kov [3]. The primary advantage of this process route is that it offers a very viable way to produce GaN powder which is as pure as the starting Ga metal and ammonia. With the recent advances in the purification of ammonia such that the water and oxygen levels are  $\leq 1$  ppm and the availability of very pure Ga, the achievement of very high purity GaN at reasonable cost is now possible.

Thermodynamic calculations and a review of the available literature indicate that economic production of bulk quantities of semiconductor purity GaN powder can also be readily achieved via reaction (8). Thermodynamic calculation showed that  $\text{Ga}_2\text{O}_3$  in a  $\text{H}_2$  atmosphere will be reduced to Ga<sub>2</sub>O. Therefore as a second route reaction (8) was chosen, initially starting with  $\text{Ga}_2\text{O}_3$ . This procedure has the advantage of starting with a powder material which provides easy recovery of the end products.

### C. Experimental Procedure

For both of the methods outlined above a 1.5" diameter, 36" long horizontal tube furnace with a quartz inner liner was employed. The source material to be converted into GaN was placed in an alumina or quartz reaction vessel and loaded into the furnace. After reaching the desired reaction temperature ammonia gas was flowed over the vessels. Samples were cooled to room temperature under an increased flow of ammonia in order to minimize the GaN decomposition reaction. A basic sketch of the experimental set-up can be seen in Fig. 1.

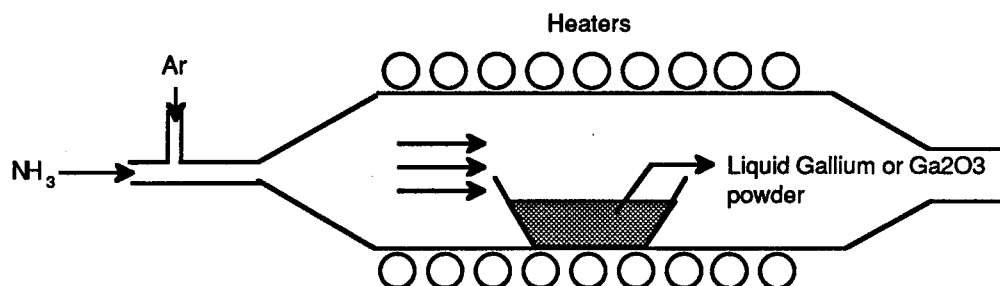


Figure 1. Configuration used for GaN powder synthesis.

*Gallium + Ammonia Route.* Precursor materials used in this route possessed the following purity levels: Ga metal 99.99%, NH<sub>3</sub> 99.999%. A temperature range of 800 to 1150°C was investigated. It is commonly known that GaN dissociates into Ga and N<sub>2</sub> at increasing rates at temperatures above 700°C. This reverse reaction leaves residual Ga metal in the powder produced. Therefore, to optimize the GaN production the lowest temperature where Ga converts fully into GaN was determined. In the temperature range 1000-1150 °C the GaN powder contained  $\geq 2\%$  residual gallium metal. When the temperature was lowered to within the 950-1000°C range, the amount of residual Ga was reduced. The absence of free Ga was indicated by X-Ray diffraction patterns. In this temperature range it is believed that sufficient melt stirring was produced such that the slightly higher density GaN is continually mixed with the Ga. Temperatures below 950°C were also studied at different flow rates and reaction times but in all of the experiments a GaN crust was found on top of the liquid Ga metal. This GaN layer prevented further conversion of Ga into GaN since NH<sub>3</sub> was not able react with Ga.

The placement of the boats in the furnace also has an impact on the quality of the powder produced. To study this point, boats were positioned at different distances from the ammonia inlet. At a flow rate of 300 sccm and a furnace temperature of 950-1000°C it was observed that NH<sub>3</sub> was most efficient in reacting with molten Ga at the end part of the furnace (approximately 24" away from the inlet).

---

---

Table I. Typical Process Parameters for Ga + NH<sub>3</sub> Method

---

Furnace temperature : 950°C - 1000°C

Ammonia flow rate: 300-350 sccm

Pressure : 760 Torr

Total process time : 1-2 hrs

---

---

The resulting GaN had a spongy appearance and had to be scraped from the boats. This material was then crushed into powder form. The X-Ray scans and SEM images of this GaN are presented below.

*Gallium Oxide + Ammonia Route.* In the second route to synthesize GaN powder, 99.5% pure Ga<sub>2</sub>O<sub>3</sub> and 99.999% pure ammonia were used as precursors. Temperatures between 900 and 1050°C were employed. Boats containing 1-2 grams of gallium oxide powder were placed in the furnace. The same ammonia flow rate and furnace location were used as in the previous study. The reaction leading to GaN powder occurred in two steps:



The hydrogen in Equation (10) evolves from the decomposition of ammonia at the reaction temperature. GaN powder obtained by this method was very easily removed from the boat and did not need further crushing.

#### D. Results and Discussion

The GaN powder obtained from both routes was analyzed using XRD. Figure 2 shows the XRD scans of the powders produced and the scan that was taken from a standard material supplied by a commercial source. The reflections in the XRD scans for the GaN produced from Ga, correspond precisely with those in the standard data files compiled by the Joint Committee on Powder Diffraction.

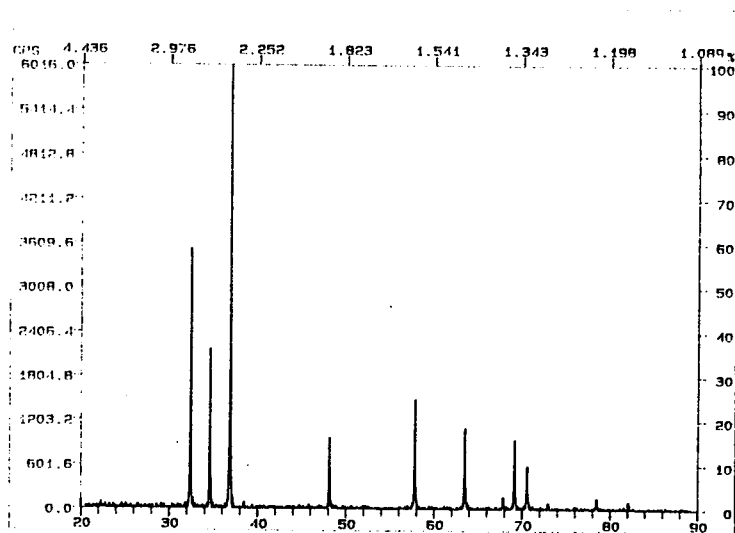
The investigation on the second route, where  $\text{Ga}_2\text{O}_3$  is converted into GaN is yet to be completed. A visible improvement in crystallinity in the XRD pattern was observed when the conversion temperature was raised from 900 to 1000°C (see Fig. 3). It is believed that the reaction time and the amount of material loaded into the furnace has a important effect in obtaining high quality material. X-ray studies suggest a highly distorted GaN lattice. However, it is important to note that no second phase was observed in the X-Ray patterns.

SEM images show that in both production schemes the particle size distribution was between 1 and 5 microns, mainly around 1 micron (Figs. 4 and 5). This information will be valuable during the hot pressing of this material.

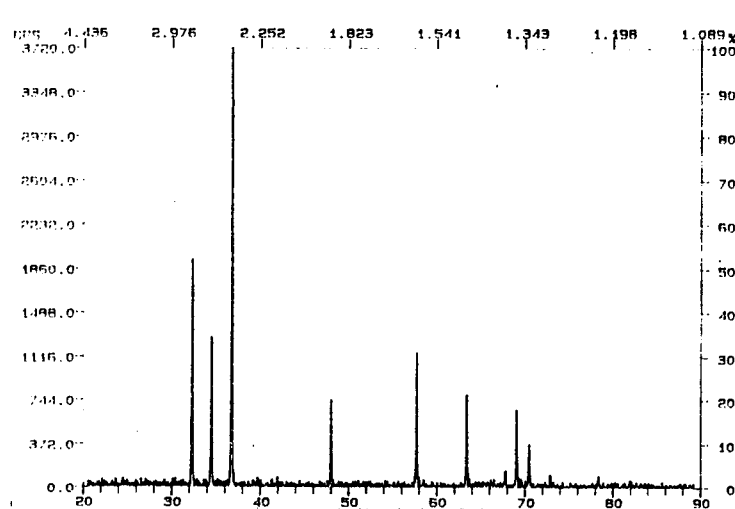
Chemical analysis of the GaN powder synthesized by both methods will be performed in the near future.

#### E. Conclusions

High purity GaN powder in large quantities and low cost can be obtained by reaction of  $\text{NH}_3$  with Ga metal and by reduction of  $\text{Ga}_2\text{O}$ . In converting Ga into GaN it is important to use the right combination of temperature range, ammonia flow rate and furnace location related to ammonia decomposition. The selection of the optimum method among these two routes will depend on the chemical analysis results. However, it is feasible to obtain higher purity material by using the gallium + ammonia approach since here the impurity level of the product depends primarily on the impurity level of the precursors. In the second approach, incomplete reactions and oxygen incorporation in the GaN lattice may lead to a lower purity powder. At present, the only disadvantage of both procedures is that they are batch processes which limit the quantity of material produced to the size of the furnace and the crucible containing the precursors.



(a)



(b)

Figure 2. a) X-Ray Diffraction pattern of commercial GaN, b) X-Ray Diffraction pattern of GaN produced at NCSU.

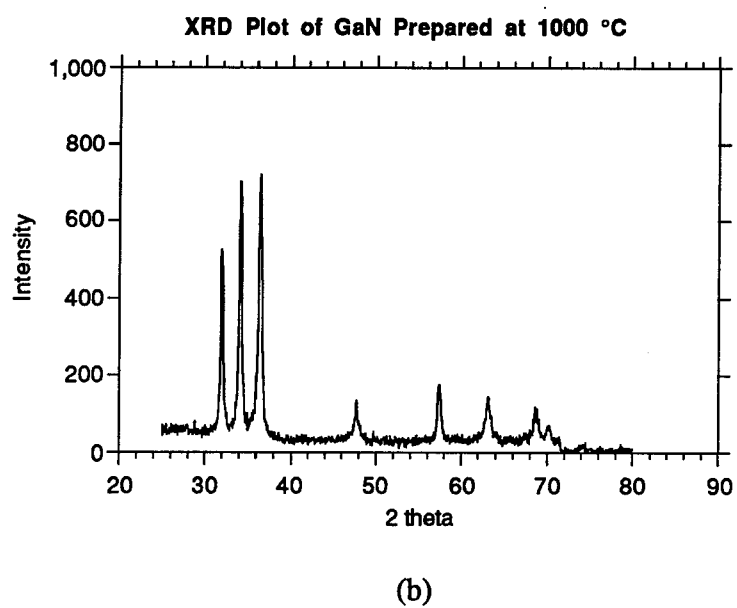
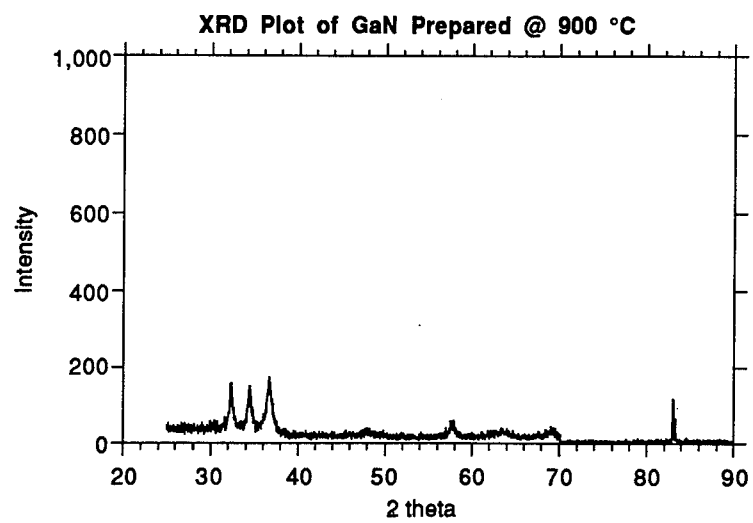


Figure 3. XRD scans of the GaN produced from  $\text{Ga}_2\text{O}_3$ .





Figure 4. SEM image of the powder obtained using the Ga + NH<sub>3</sub> process route.



Figure 5. SEM image of the powder obtained using the Ga<sub>2</sub>O<sub>3</sub> conversion method.

#### E. Future Plans and Goals

The powder production capacity of the system will be increased by installing a larger furnace in the laboratory. This will allow larger amounts of precursor to be used in each batch. The gallium oxide conversion study will be concluded and a comparison of the material produced by the two methods based on purity and cost will be made. Finally, the material synthesized will be consolidated into bulk shapes and thereafter be used in bulk single crystal growth research.

#### F. References

1. R. F. Davis, private communication, (1994).
2. K. R. Faulkner *et al.* J. Mater Sci., **5**, 308, (1970).
3. A. Addamiano, J. Electrochem. Soc. **108**, 1072, (1972).
4. I. G. Pichugin and D. A. Yaskov, Neorg. Mat., **6**, 1973, (1973).

## XV. Atomic Layer Epitaxy of GaN and GaInN

### Introduction

Optical sources made of the InGaN material system can cover all visible range from the UV to the red regions. However, reported epitaxial growth of  $\text{Ga}_{1-x}\text{In}_x\text{N}$  by MOCVD or MBE had been limited to low values of InN percentage of about 20%. Most of reported growth with good optical properties were achieved at high growth temperatures (about 800°C). Higher In contents were achieved at lower growth temperatures (500°C), however poor quality films were reported. The problems with In related compounds can be due to several reasons. First, the high In vapor pressure, relative to Ga and Al, can lead to difficulties in achieving high values of  $x$ , at high growth temperature for all In based III-V compounds, including the nitrides. The second problem is the high  $\text{N}_2$  equilibrium vapor pressure of InN that will require an extremely high V/III ratio. The third problem is the gas phase reaction between In OM sources and  $\text{NH}_3$  in the MOCVD growth. The most obvious solution is the growth of GaN and GaInN at low temperature. However, poor quality and compensated thin films were obtained. This is probably due to the low surface mobility and the poor cracking of  $\text{NH}_3$ . Some of these problems can be avoided by adopting the ALE of growth of nitride compounds.

### Low Temperature ALE Growth of GaN and GaInN

The ALE system used in this work is based on the rotating substrate approach developed in our laboratory during the last decade. A schematic of the ALE approach is shown in Figure 1. This approach allows high growth rate (up to 2  $\mu\text{m}/\text{hour}$ ), short exposure times (0.1 sec or less) and does not rely on gas switching. The ALE growth was done at Spire, in cooperation with Dr. Nasser Karam, using ALE reactor built at NCSU.  $\text{TMGa}$ ,  $\text{TMAI}$ ,  $\text{TMIIn}$  and  $\text{NH}_3$  were used. Growth in the 550-650°C temperature range was used. The substrate rotation speed varies from 30-120 RMP and sapphire substrates were used. The growth was initiated by AlN buffer layer also grown by ALE, followed directly by the ALE growth of GaN or GaInN. The as grown AlN is expected to be single crystal, since no high temperature anneal of this buffer layer was carried out. The gas manifold used did not allow for the MOCVD growth of the AlN buffer layer. GaN and GaInN of about 2000Å was deposited and characterized by TEM, x-ray diffraction, PL and Hall measurement. Hall data was carried at Spire, where as all the other techniques were done at NCSU.

### Properties of ALE GaN and GaInN Grown at 550°C:

TEM data showed that the ALE grown films are single crystal, however, they have high defect density and APD. This may be due to the nonoptimized AlN buffer layer which was grown at low temperature by ALE without any high temperature annealing. This is in contrast to the amorphous AlN layer grown by MOCVD followed by recrystallization at 1000°C. Work is underway to modify the MOCVD manifold to allow the MOCVD growth of this buffer layer.

Double crystal x-ray diffraction (DCXRD) for the ALE grown GaN (2000Å) is shown in Figure 2. The FWHM of the GaN x-ray peak is fairly broad ~ 15 minutes. This broad peak can be due to several reasons, for example, the poor AlN buffer layers, the fairly thin epitaxial films (2000Å) and finally the low growth temperature. It has been previously reported that x-ray FWHM is improved by increasing both the growth temperature and the film thickness. We plan to investigate the effect of the growth rate, and increasing the growth temperature on the quality of these ALE grown films. It may be expected that lower growth rate will improve the crystal quality of these films grown at low temperature.

In contrast and in spite of crystal quality of these films, the optical properties were surprisingly very good. Figure 3 shows the room temperature PL of GaN grown at 550°C and done in Prof. Schetzina's lab. The PL spectrum is dominated by band edge (BE) emission at 3.41 eV. This BE peak is very strong and the spectrometer slits operating at 100 μm were used to avoid overloading the photomultiplier tube. The intensity of this peak is comparable to that obtained by MOCVD grown at 1000°C. A yellow peak is also observed with fairly low intensity.

Resistivity and Hall measurements were carried out at Spire. Data are not conclusive yet, due to the fairly thin films and the problems of ohmic contacts. However, it can be deduced that these ALE grown films have mobility of several hundred and carrier concentrations in the  $10^{16}$  to  $10^{17}/\text{cm}^3$  range.

Preliminary results of the ALE grown GaInN also showed broad XRD peaks and optical properties comparable to that grown by MOCVD as shown in Figure 4.

Thus the ALE grown nitride films have two main features, the first is that the PL is comparable to that grown by MOCVD at 1000° and their carrier concentration is in the  $10^{16}/\text{cm}^3$  range.

### Discussions

GaN grown by MOCVD is usually carried out at temperatures near 1000°C in order to achieve enough cracking of NH<sub>3</sub>. However, such high temperature is also accompanied by an increase in the equilibrium N<sub>2</sub> vapor pressure, especially for In based compounds, that results in a higher concentration of N<sub>2</sub> vacancies. This is believed to be the reason for the reported background carrier in the 10<sup>17</sup>/cm<sup>3</sup> range. Same conclusion can also apply for MBE grown films.

The above results indicate that the ALE process is capable of dissociating NH<sub>3</sub> at lower temperatures than that required for MOCVD. In the ALE process NH<sub>3</sub> is dissociated on a more active surface, that is covered with Ga atoms or monomethylgallium. These observations have been reported by our group earlier for the ALE growth of device quality GaAs, InGaP and GaP at temperatures less than 500°C. Another advantage of ALE is the complete separation of the precursors, thus avoiding any gas phase parasitic reactions. It is not clear at this stage how the parasitic reactions influence the quality of the deposited films and consume part of the NH<sub>3</sub> fragments, such as NH and NH<sub>2</sub>, into reaction pathways that does not contribute to the GaN deposition. ALE will also allow absorbed species (Ga or N) to migrate at the growing surface better than that in the MOCVD or MBE cases. ALE is the ultimate example of migration enhanced epitaxy (MEE).

### Further Activities:

We plan to optimize the AlN buffer layer, the growth temperature and the growth rate. ALE/photo-assisted growth system built in our new lab is currently functional and preliminary tests are being conducted.

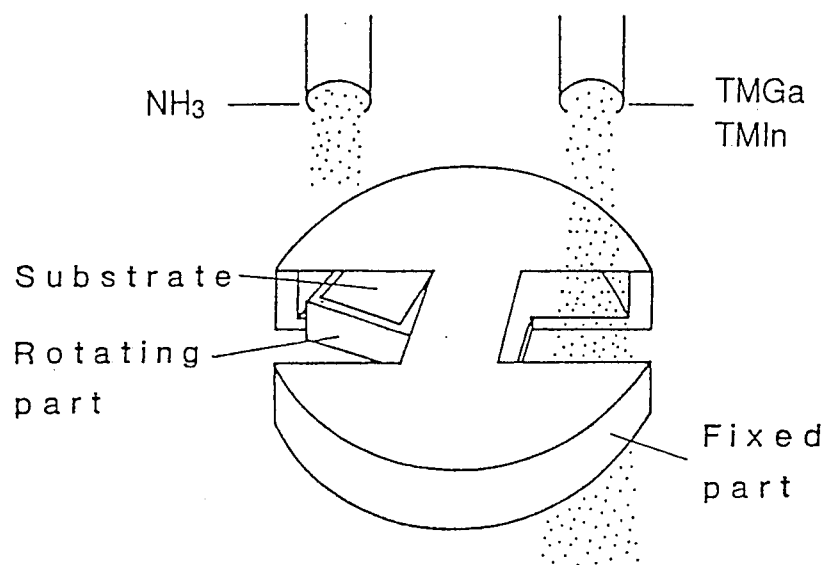


Figure 1. Experimental set-up for ALE of GaN.

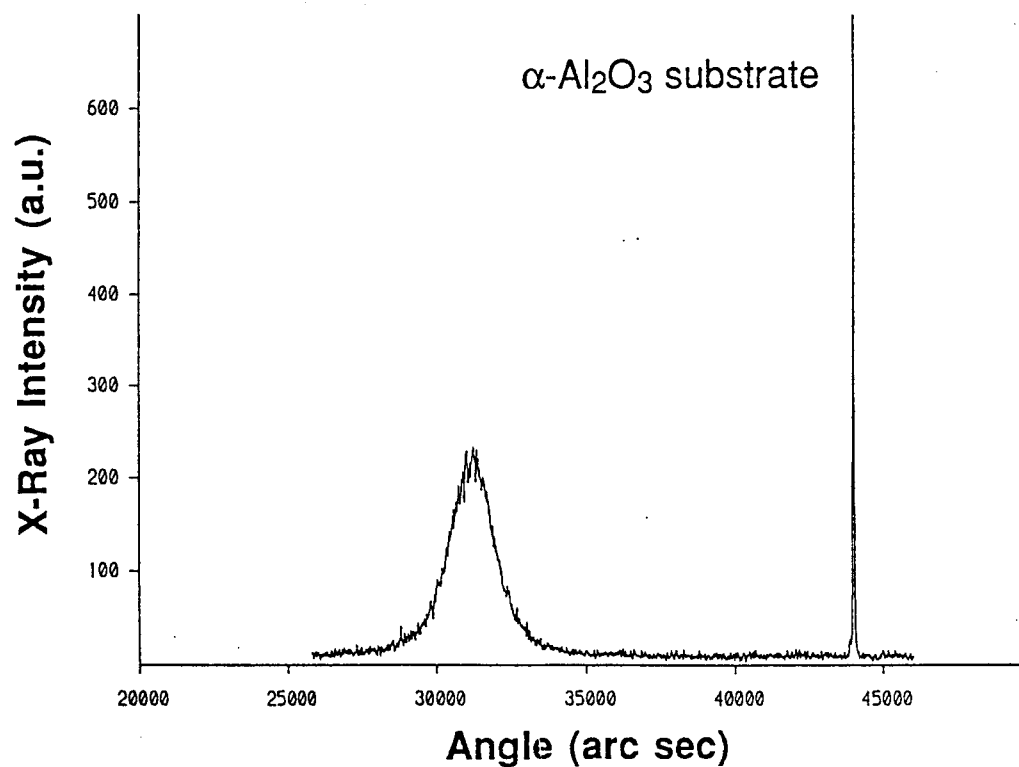


Figure 2. DCXRD of ALE-grown GaN at 550°C.

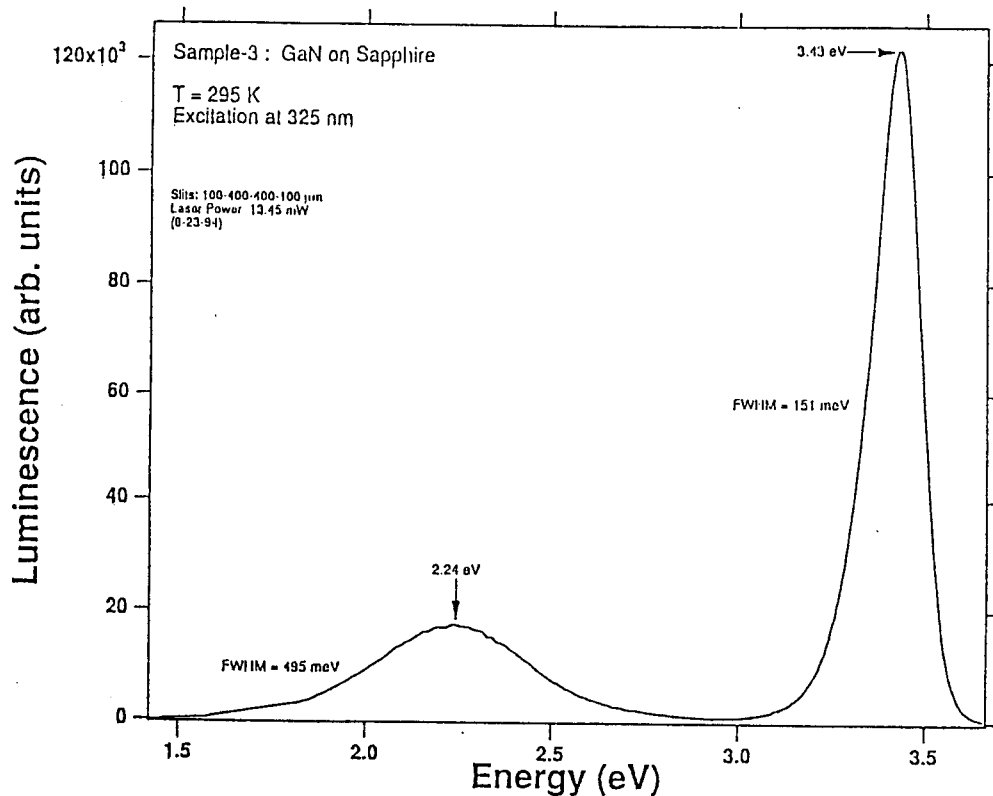


Figure 3. Room temperature PL of ALE-grown GaN.

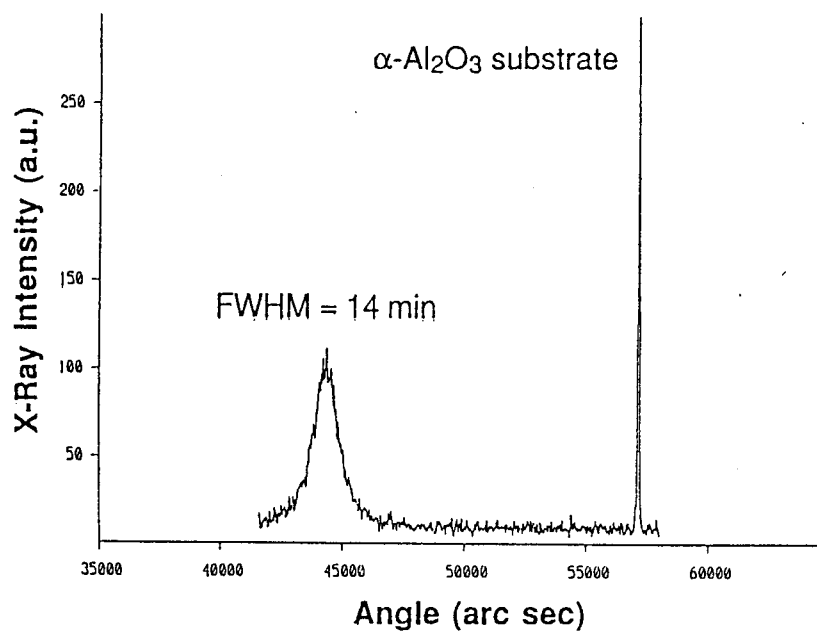


Figure 4. DCXRD of ALE grown In<sub>0.03</sub>Ga<sub>0.97</sub>N at 550C.

## XVI. Characterization of AlN and AlN-SiC Pseudomorphic Heterostructures on $\alpha(6H)$ -SiC(0001) Grown by Plasma-assisted, Gas-source Molecular Beam Epitaxy

### A. Introduction

A marked increase in the interest in wide band gap semiconductor materials for use in high-temperature, -power, -frequency and -speed microelectronic devices resistant to radiation and short-wavelength optoelectronic devices has recently been demonstrated on a global scale. Two candidate materials that have generated much of this interest are SiC and AlN. SiC, the only binary compound in the Si-C system, forms in many different polytypes; the most common being the only cubic polytype,  $\beta$ - or 3C-SiC, and one of the hexagonal polytypes, 6H-SiC. Since the band gap for SiC (3.0 eV for 6H and 2.3 eV for 3C) is indirect, it cannot be used alone for optoelectronic applications. For this reason, AlN, with its direct band gap of 6.28 eV, is of particular interest for use with SiC. Two methods of simultaneously exploiting the favorable characteristics of these materials include the thin film deposition of both pseudomorphic heterostructure and alloys.

Aluminum nitride possesses a direct band gap of 6.28 eV at 300 K [1], a melting point in excess of 2275 K [2] and a thermal conductivity of 3.2 W/cm $\cdot$ K [3]. As such, it is a candidate material for high-power and high-temperature microelectronic and optoelectronic applications with the latter employment being particularly important in the ultraviolet region of the spectrum[1]. This material also has the highest reported surface acoustic wave velocity (Rayleigh  $V_R$ =6-6.2 km/s,  $V_L$ =11-12 km/s [4]-[6]) for any material and a substantial electromechanical coupling coefficient (to 1% [7]). These properties strongly indicate that superior surface acoustic wave devices, operational in aggressive media and under extreme conditions both as sensors for high temperatures and pressures and as acousto-optic devices can be developed [8-10]. However, progress regarding these (and other) applications is hampered by the lack of good single crystal material. The primary objective of the research reported below has been to address this issue via the fabrication of thin films of this material via molecular beam epitaxy (MBE) techniques.

In previous studies, mono- and polycrystalline films of AlN have been grown by chemical vapor deposition (CVD) using  $NH_3$  and  $Al(CH_3)_3$  or  $AlCl_3$  on  $\alpha(6H)$ -SiC [11], sapphire [1,9,12], and Si [13-15]. Chu *et al.* [11] obtained smooth monocrystalline AlN layers to a thickness of 25  $\mu m$  on  $\alpha(6H)$ -SiC{0001} substrates by chemical vapor deposition (CVD) from 1200-1250°C. A high density of defects in these AlN films was revealed by chemical etching. In general, films grown on sapphire and Si substrates possessed a much rougher morphology than those grown on  $\alpha(6H)$ -SiC. This occurred very likely because the difference in lattice



parameters between AlN and SiC is substantially less than between AlN and sapphire or AlN and Si.

Gas source MBE using electron beam evaporated Al and  $\text{NH}_3$  on Si(111) and  $\text{Al}_2\text{O}_3$ (0001) and (01 $\bar{1}$ 2) at 1000-1200°C[16] or thermally evaporated Al and plasma-derived activated nitrogen species on  $\alpha$ (6H)-SiC (0001) and  $\text{Al}_2\text{O}_3$  (0001) at 600-1250°C[17,18] has also been used for single crystal AlN growth.

Pseudomorphic heterostructures of dissimilar semiconductor materials are the basis for quantum well and laser devices. The physical properties (e.g., lattice parameter, crystal structure, melting point and thermal expansion) as well as the optical and electronic properties (e.g., band gap and index of refraction) of SiC and AlN indicate that stable superlattice structures of these materials having the desired properties are feasible. Theoretical calculations regarding electronic structure and bonding at AlN/SiC interfaces [19] and critical layer thickness prior to misfit dislocation formation at interfaces in cubic AlN and SiC have been reported [20]. Rowland *et al.* [21] and Kern *et al.* [22] have described the growth of 3C-SiC/2H-AlN pseudomorphic layers on  $\alpha$ (6H)-SiC(0001) substrates by plasma-assisted, gas-source molecular beam epitaxy (PAGSMBE) using solid Al evaporated from a standard effusion cell and the gas sources of  $\text{Si}_2\text{H}_6$ ,  $\text{C}_2\text{H}_4$  and  $\text{N}_2$ . The resulting SiC layers contained a high density of stacking faults and microtwins caused primarily by interfacial stresses and the low stacking fault energy intrinsic to  $\beta$ -SiC.

## B. Experimental Procedure

In the present research, a specially designed and previously described [23] PAGSMBE system was employed to deposit all AlN-SiC thin films on the Si faces of  $\alpha$ (6H)-SiC(0001) substrates. Both on-axis and off-axis (oriented  $3.5 \pm 0.5^\circ$  off (0001) toward  $[11\bar{2}0]$ ) SiC substrates were used. The substrates were cleaned chemically before growth in a 10% HF solution for 5 minutes, and loaded immediately into the UHV growth chamber. Sources of Si and C were disilane ( $\text{Si}_2\text{H}_6$ , 99.99% purity) and ethylene ( $\text{C}_2\text{H}_4$ , 99.99% purity), respectively. Aluminum (99.9999% purity) was evaporated from a standard MBE effusion cell operated in all cases at 1260°C. A compact electron cyclotron resonance (ECR) plasma source supplied by ASTeX, Inc., operating at 100 W forward power, was used to decompose  $\text{N}_2$  (99.9995% purity). All AlN layers were grown at with the Al effusion cell operating at 1260°C and the ECR at 100W forward power with 3.5 sccm  $\text{N}_2$ . Typical gas flow rates employed for SiC growth for use in heterostructures were 0.1-2.0 sccm  $\text{Si}_2\text{H}_6$ , 0.1-2.0 sccm  $\text{C}_2\text{H}_4$  (Si/C ratio was kept at 1/1). Individual layers of SiC and AlN were grown for variable times ranging from 30 seconds to 5 hours. All layers were grown at 1050°C.

Reflection high-energy electron diffraction (RHEED) at 10 kV and high-resolution transmission electron microscopy (HRTEM) were used for structure and microstructure

analyses. Samples were prepared for HRTEM using standard techniques[7]. A Topcon EM 002B high-resolution transmission electron microscope was used at 200 kV for the HRTEM analysis. X-ray rocking curve measurements were made on a double crystal diffractometer at Brown University by Drs. F. R. Chien and S. R. Nutt. Secondary ion mass spectrometry (SIMS), using a Cameca IMS-3f ion microprobe operating at 10 keV with  $\text{Cs}^+$  ions, was employed to determine the atomic concentration of impurities. Carrier concentrations for undoped SiC films, grown on insulating AlN layers, were measured at room temperature by standard Hall techniques at 3.5 kG. Nickel contacts, RF sputtered at room temperature then annealed at 1000°C for 30 s in Ar, were used on the undoped and films.

### C. Results

*Aluminum Nitride.* Figure 1 shows an x-ray rocking curve of a 2H-AlN/6H-SiC structure grown on vicinal  $\alpha(6\text{H})\text{-SiC}(0001)$  at 1050°C. The AlN layer is approximately 0.75  $\mu\text{m}$  thick. The graph shows the  $(0006)_{\text{SiC}}$  and the  $(0002)_{\text{AlN}}$  Bragg reflections as determined by a double crystal x-ray diffractometer. The full-width half maximum (FWHM) of the AlN peak is 43.2 arc sec. Figure 2 shows an x-ray rocking curve of the same 2H-AlN/6H-SiC structure grown on on-axis  $\alpha(6\text{H})\text{-SiC}(0001)$  at 1050°C. In this case, the AlN layer is also approximately 0.75  $\mu\text{m}$  thick. The full-width half maximum of the  $(0002)_{\text{AlN}}$  Bragg reflection peak is 80 arc sec.

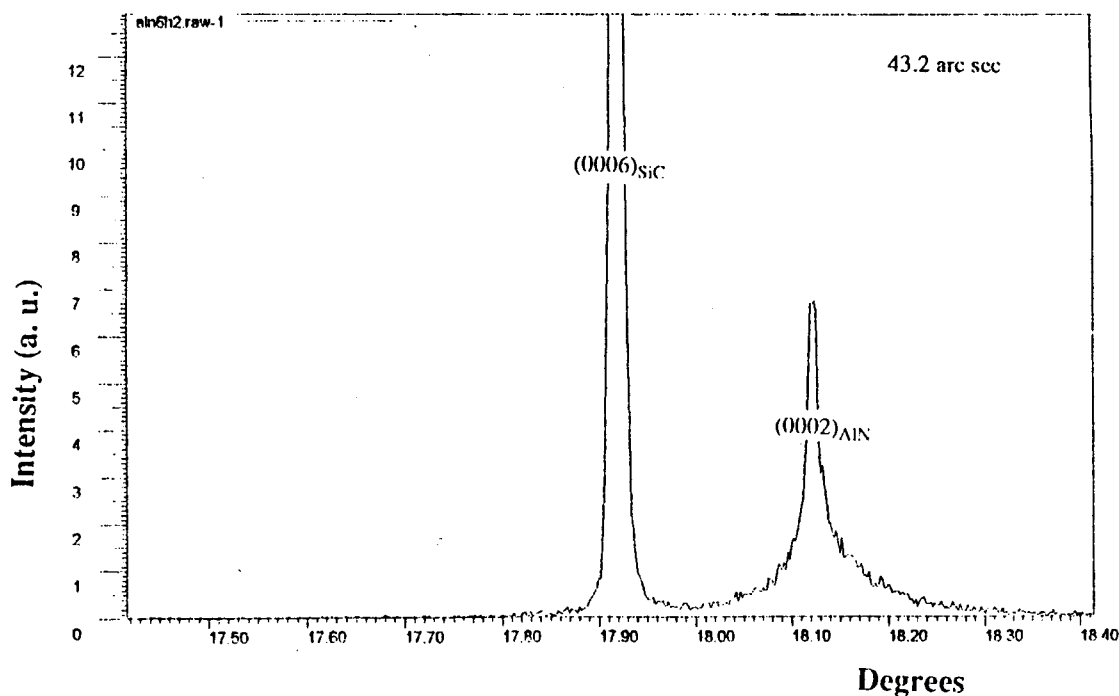


Figure 1. X-ray rocking curve of a 2H-AlN layer grown on vicinal 6H-SiC(0001).

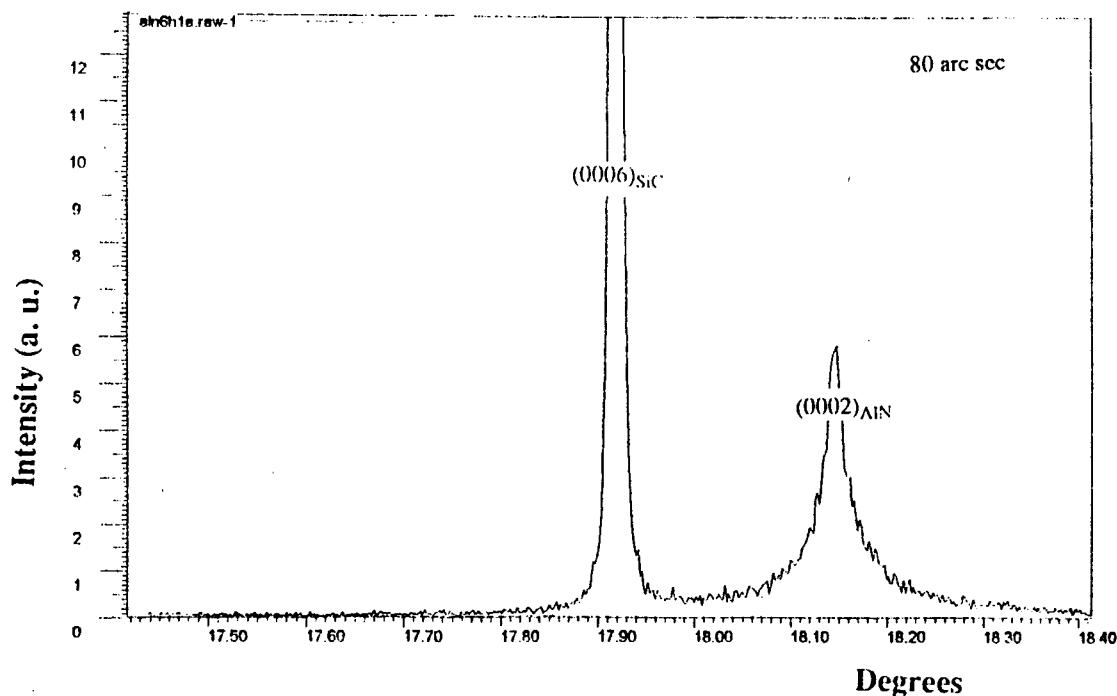


Figure 2. X-ray rocking curve of a 2H-AlN layer grown on on-axis 6H-SiC(0001).

*AlN/SiC Heterostructures.* Undoped films of  $\beta$ -SiC(111) have been grown on thin, insulating layers of 2H-AlN(0001) similar to the structure shown in Fig. 3 at 1050°C using 1.0 sccm Si<sub>2</sub>H<sub>6</sub> and 1.0 sccm C<sub>2</sub>H<sub>4</sub>. Growth rates approaching 1000 Å per hour were achieved. Hall electrical measurements made on some of the thicker SiC films ( $\approx 0.75 \mu\text{m}$ ) have showed the films to be n-type with electron concentrations as low as  $3 \times 10^{15} \text{ cm}^{-3}$  and mobilities as high as  $648 \text{ cm}^2 \text{ V}^{-1} \text{ s}^{-1}$ .

*AlN Doping.* Preliminary attempts to dope AlN with Si (using Si<sub>2</sub>H<sub>6</sub>) and C (using C<sub>2</sub>H<sub>4</sub>) have been undertaken. Secondary ion mass spectroscopy analysis has shown that controllable levels of Si and C can be incorporated into AlN at very constant concentrations. However, the resulting films contained measurable levels of O despite no evidence of water or oxygen in the chamber as measured by a Residual Gas Analyzer (Leybold-Inficon Model H100M). Since standards for these elements in AlN were not available, no quantitative measurements were made. All attempts to measure these samples by the Hall technique were unsuccessful due to the extremely insulating nature of these films.

#### D. Discussion

In both Figs. 1 and 2, the x-ray rocking curve measurements represent the best values reported by any previous researchers. Curiously, films grown on the vicinal substrates, which

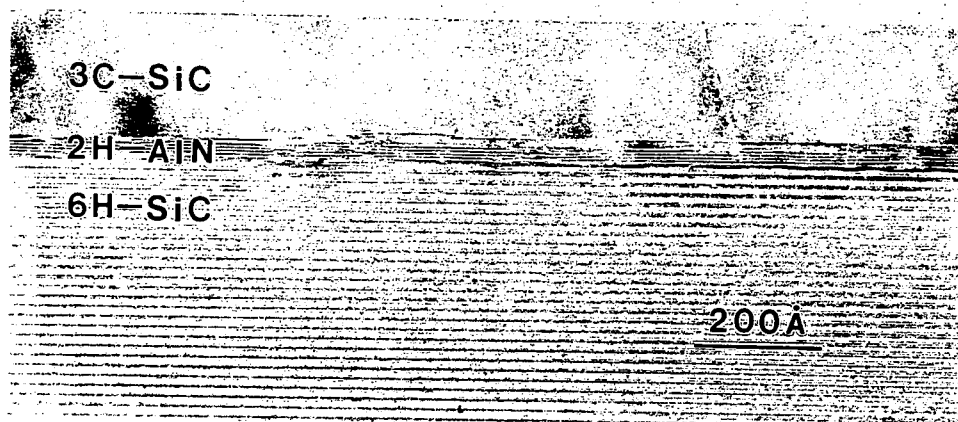


Figure 3. HRTEM micrograph of a SiC/AlN multilayer grown on on-axis 6H-SiC(0001). Electrical characterization of the similar  $\beta$ -SiC(111) layers has been done.

have previously been demonstrated to have rougher surfaces and higher defect densities, have lower value of FWHM for the (0002) Bragg reflection. Previous reports have shown that defects are created in the vicinity of the steps in the vicinal substrates. These defects may play a role in stress relief and contribute to the lower measured values of FWHM.

The results of the Hall measurements on undoped  $\beta$ -SiC, grown on AlN on on-axis 6H-SiC, represent some of the lowest unintentional doping levels ever reported in the cubic polytype. It may be possible to lower these values by more efficient removal from the system of  $N_2$  which makes up the largest mole fraction of the gas present in the chamber prior to SiC growth after the AlN deposition.

Early results in AlN doping have been unsuccessful in creating conducting layers. The presence of measurable quantities of O in the films may be indicative of a problem with the ECR source[24]. In this report, the investigators believe that the ECR source, which has a quartz liner in the vicinity of the plasma, may be the source of Si and O in their GaN films due to erosion of the liner.

#### E. Conclusions

Monocrystalline layers of AlN as well as heterostructures of AlN and SiC have been grown by PAGSMBE on on-axis and vicinal  $\alpha$ (6H)-SiC(0001) substrates. X-ray rocking curve measurements have been made on the AlN layers on vicinal and on-axis 6H-SiC(0001) and have resulted in values of 43.2 and 80 arc sec, respectively. Undoped, cubic SiC(111) layers have been measured electrically and have revealed carrier concentration as low as  $3 \times 10^{15} \text{ cm}^{-3}$  and mobilities as high as  $648 \text{ cm}^2 \text{ V}^{-1} \text{ s}^{-1}$ . Preliminary attempts to dope AlN have been attempted but are inconclusive at this time.

## F. Future Plans and Goals

Further studies into the growth and doping of these materials is planned. In addition, several experiments are planned to try to optimize the source of N used in this research. The first of these is to replace the quartz liner in the existing ECR source with a liner made of pBN. A cooperative effort between NCSU and ASTeX is currently being discussed in an attempt to resolve this situation. Ammonia is also a potential source of N being considered and planned for testing.

## G. References

1. W. M. Yim, E. J. Stofko, P. J. Zanzucchi, J. I. Pankove, M. Ettenberg, and S. L. Gilbert, *J. Appl. Phys.* **44**, 292 (1973).
2. M. G. Norton, B. C. H. Steele, and C. A. Leach, *Science of Ceramics*, **14**, 545 (1988).
3. G. A. Slack, *J. Phys. Chem. Solids* **34**, 321 (1973).
4. M. Kitayama, T. Fukui, T. Shiosaki, and A. Kawabata, *Japan J. Appl. Phys.* **22**, 139 (1982).
5. G. R. Kline and K. M. Lakin, *Proc. IEEE Symp. Ultrasonics* **14**, 495 (1983).
6. K. Tsubouchi, K. Sugai, and N. Mikoshiba, *Proc. IEEE Symp. Ultrasonics* **14**, 340 (1983).
7. M. Sano and M. Aoki, *Oyo Butsuri*, **52**, 374 (1983).
8. J. K. Liu, K. M. Lakin, and K. L. Wang, *J. Appl. Phys.* **46**, 3703 (1975).
9. M. Morita, N. Uesugi, S. Isogai, K. Tsubouchi, and N. Mikoshiba, *Jpn. J. Appl. Phys.* **20**, 17 (1981).
10. G. D. O'Clock, Jr. and M. T. Duffy, *Appl. Phys. Lett.* **23**, 55 (1973).
11. T. L. Chu, D. W. Ing, and A. J. Noreika, *Solid State Electron.* **10**, 1023 (1967).
12. H. M. Manasevit, F. M. Erdmann, and W. I. Simpson, *J. Electrochem. Soc.* **118**, 1864 (1971).
13. M. Morita, S. Isogai, N. Shimizu, K. Tsubouchi, and N. Mikoshiba, *Japan. J. Appl. Phys.* **20**, L173 (1981).
14. Z. J. Yu, J. H. Edgar, A. U. Ahmed, and A. Rys, *J. Electrochem. Soc.* **138**, 196 (1991).
15. A. J. Noreika and D. W. Ing, *J. Appl. Phys.* **19**, 5578 (1968).
16. S. Yoshida, S. Mizawa, Y. Fujii, S. Takada, H. Hayakawa, S. Gonda, and A. Itoh, *J. Vac. Sci. Technol.* **16**, 990 (1979).
17. Z. Sitar, M. J. Paisley, B. Yan, R. F. Davis, J. Ruan, and J. W. Choyke, *Thin Solid Films* **200**, 311 (1991).
18. L. B. Rowland, R. S. Kern, S. Tanaka and R. F. Davis, *J. Mater. Res.* **8**, 2310 (1993).
19. W. R. L. Lambrecht and B. Segall, *Phys. Rev. B* **43**, 7070 (1991).
20. M. E. Sherwin and T. J. Drummond, *J. Appl. Phys.* **69**, 8423 (1991).
21. L. B. Rowland, R. S. Kern, S. Tanaka and R. F. Davis, *Appl. Phys. Lett.* **62**, 3333 (1993).
22. R. S. Kern, S. Tanaka, and R. F. Davis, in *Proceedings of the International Conference on Silicon Carbide and Related Materials*, ed. by M. G. Spencer, R. P. Devaty, J. A. Edmond, M. A. Khan, R. Kaplan and M. Rahman (Institute of Physics Publishing, Bristol, UK, 1994), pp. 389-392.
23. L. B. Rowland, R. S. Kern, S. Tanaka, and R. F. Davis, in *Proceedings of the Fourth International Conference on Amorphous and Crystalline Silicon Carbide*, edited by C. Y. Yang, M. M. Rahman, and G. L. Harris (Springer-Verlag, Berlin, 1992), p. 84-89.
24. R. J. Molnar and T. D. Moustakas, *J. Appl. Phys.* **76**, 4587 (1994).

## XVII. Novel Computer-controlled CVD System for the Deposition and Doping of AlN, GaN, InN and Their Solid Solutions and Heterostructures of These Materials

### A. Introduction

The III-V nitride compounds have good potential for applications in optical semiconductor devices. With band gap energies ranging from 1.9 and 3.4 eV for InN and GaN, respectively, to 6.2 eV for AlN, devices can be made covering the entire visible light range through the UV range. Production and commercial availability of nitride-based optoelectronic devices is now possible due to the advancement of the understanding of the materials and the overcoming of problems in these materials, such as p-type doping of GaN and controlling the In content in In-containing compounds. As a result of these advancements, Nakamura *et al.* have produced a bright blue LED using a Zn-doped  $\text{In}_{0.06}\text{Ga}_{0.94}\text{N}$  active layer with a peak wavelength of 470 nm and an output power of 1500  $\mu\text{W}$  and a quantum efficiency of 2.7% at 20 mA [1]. This compares to 124  $\mu\text{W}$  and 0.22% at 20 mA for the same structure from previous work [2]. Also, Amano *et al.* have shown violet stimulated emission from a photopumped AlGaIn heterostructure demonstrating optical confinement and the feasibility of laser structures in this material system [3]. Other work on microelectronic devices by Khan *et al.* include a AlGaIn/GaN-based heterostructure field effect transistor (HFET) [4]. Although progress has been made in both optoelectronics and microelectronics, further developments are possible, such as complete compositional control of the alloys and doping of AlN. To address these problems and to further demonstrate the capabilities of the III-V nitrides, a novel CVD system has been developed and built. This report will discuss the capabilities of the system and the plans for future work.

### B. Experimental Procedure

Figure 1 shows a schematic of the system which will be used to grow the films. The design is an inverted cold-wall rotating disc MOCVD reactor. Source materials for the system are trimethylaluminum (TMA), triethylgallium (TEG), trimethylindium (TMI) and ammonia ( $\text{NH}_3$ ). The dopants include silane ( $\text{SiH}_4$ ) and germane ( $\text{GeH}_4$ ) for the n-type dopants, and bis-cyclopentadienylmagnesium ( $\text{Cp}_2\text{Mg}$ ) and diethylzinc (DEZ) for the p-type dopants. The metalorganic sources are carried into the chamber using either hydrogen or nitrogen as a carrier gas. All precursors except  $\text{NH}_3$  enter the chamber through a radial gas mixing manifold. The gases are diluted in a flow of either hydrogen or nitrogen as they enter the chamber. In the inverted design, the gases enter the bottom of the chamber and flow in an upward direction past an inverted substrate where the film is grown. Substrate materials are either sapphire (0001) or on- or off-axis SiC(0001). The system has also been designed to be controlled by computer. Using a computer program, the system pressure, temperature, gas flow rates and valve timing

will be regulated during the growth process. This feature will become important as device development progresses where consistency and control become more important.

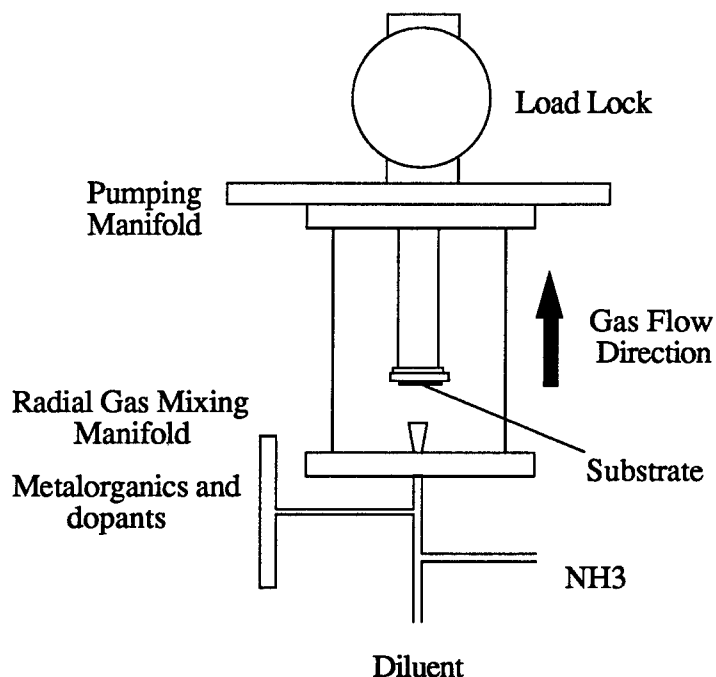


Figure 1. Schematic of CVD system.

Laser Reflection Interferometry (LRI) will be used for in-situ monitoring of film growth. This measurement technique involves detecting a laser reflected off the surface of the sample. As the film grows, the superpositioning of two light waves reflected from the surface of the film and the film-substrate interface generates a periodic interference pattern which corresponds to the thickness of the film, depending on the wavelength and incident angle of the light, and the index of refraction of the material. From this technique, growth rate and film thickness can be measured [5, 6].

### C. Discussion

The choice of reactor design comes from investigating the transport phenomena in the CVD process. The reactor geometry has considerable impact of the flow structure and by appropriately designing the reactor it is possible to minimize the detrimental flow characteristics of vertical cold wall CVD systems. Examining several of the factors governing the transport phenomena in CVD we can see why an inverted geometry design lends itself to the III-V nitride system.

*Thermal Effects and Flow Patterns.* Complex flow structures develop in CVD reactors due to large thermal gradients between the heated substrate and the cold walls. This leads to

buoyancy-driven secondary flows superimposed on the forced flow of gases entering the reactor. In conventional flow reactors, recirculation cells form above the susceptor as result of these recirculations [7]. This effect can be controlled by using high inlet flow rates and placing the inlet close to the substrate, but there are limits to how close the inlet can be to the heated substrate without unwanted gas-phase reaction or predeposition in the inlet. However close the inlet is to the substrate, there will always be a decrease in gas velocity as the gases enter the reactor. This increases the potential for buoyancy-driven recirculation. Inverting the reactor so the buoyancy and inlet flow directions are aligned eliminates the major cause of thermal convections [8]. Radial temperature gradients may still drive flows, but with good temperature uniformity across the substrate this effect can be reduced. With an inverted geometry the flow from the gas inlet to the substrate becomes controlled by the inlet flow rate which improves film thickness uniformity.

*Susceptor Rotation.* A rotating susceptor is often used in CVD systems to produce more uniform films. Rotation of the susceptor emulates a rotating-disk flow which is advantageous in creating a uniform mass-transfer layer. As a result, the film uniformity is increased. The susceptor rotation also stabilizes the flow through the reactor by assisting the forced flow [7].

*System Pressure.* To obtain uniform deposition and abrupt interfaces CVD systems are often operated at reduced pressure with high flow rates. This is a result of a need to decrease the residence time of the reaction gases in the reactor. In conventional systems, residence time increases with increasing pressure as thermally driven convection flows increase [8]. With an inverted geometry the recirculation effect is virtually eliminated due to the alignment of the buoyancy and flow directions, allowing for the operation of the reactor at higher pressures without flow deterioration at higher pressures. This, combined with a rotating susceptor, should allow forced flow conditions at higher pressures than allowed by conventional systems. This is especially pertinent in the InN system, where the equilibrium vapor pressure of nitrogen is high. Using a higher pressure of nitrogen in the system might allow better control in the decomposition of the InN films at higher temperatures. We will be able to investigate the effect of an increased system pressure on the growth of single crystal InN films at higher temperatures without having to compensate for decreased flow stability.

*Junctions/Interfaces.* Abrupt junctions and interfaces are necessary in producing complex devices for optoelectronics applications. As mentioned above, good interfaces require abrupt changes in gas sources which depend on the gas residency time in the reactor. With the inverted geometry, residency times can be decreased, even at increased pressures. Also, the system has been designed with a minimal amount of "dead volume," especially in the mixing manifold, adding to the short switching time.

*Computer Control.* The computer control features of the system offer several benefits to the growth of thin films. When used with the LRI system, the computer control offers precise and



reproducible layer thickness control of the films being deposited. This is a benefit when device structures are being fabricated.

#### D. Future Research Plans and Goals

The first goal of the system described in this report is to optimize film growth parameters for AlN, GaN, and InN films and their alloys, and characterize their properties. Characterization techniques will include PL/CL, SIMS, SEM, TEM, XRC and Hall-effect measurements. Once the optimal film growth parameters are found, work will continue with obtaining controlled n- and p-type doping. This will lead in to developing optoelectronic and microelectronic devices, such as LEDs and HFETs. This work expects much progress in the next six months.

#### E. References

1. S. Nakamura, T. Mukai, M. Senoh. Appl. Phys. Let. 64 (13) 1994 1687.
2. S. Nakamura, M. Senoh, T. Mukai. Jpn. J. Appl. Phys. 31 (1993) L8.
3. H. Amano, T. Tanaka, Y. Kunii, K. Kato, S. Kim, I. Akasaki. 61 (11) 1994 1377.
4. M. A. Kahn, J. N. Kuznia, D. T. Olson, W. J. Schaff, J. W. Burm, M. S. Shur. Appl. Phys. Let. 65 (9) 1994 1121.
5. B. R. Stoner, B. E. Williams, S. D. Wolter, K. Nishamura, J. T. Glass. J. Mater Res., Vol. 7, No. 2, Feb 1992.
6. C. Wu, W. H. Weber, T. J. Potter, M. A. Tamor. J. Appl. Phys. 73 (6) 15 March 1993.
7. Jensen, K. Microelectronics Processing: Chemical Engineering Aspects; American Chemical Society, Washington, DC; 1989, p. 199.
8. Kensen, K. Einset, E. O., Fotiadis, D. I. Annual Review of Fluid Mechanics; Annual Reviews Inc., Palo Alto, CA, 1991, p. 197.

## **XVIII. Deposition, Doping and Characterization of OMVPE Grown GaN on Various SiC(0001) Substrates using High-temperature Monocrystalline AlN Buffer Layers**

### **A. Introduction**

The potential semiconductor and optoelectronic applications of the wide bandgap III-V nitrides has prompted significant research into their growth and development. GaN (wurtzite structure), the most studied in this group, has a bandgap of 3.4 eV and forms continuous solid solutions with both AlN (6.2 eV) and InN (1.9 eV). As such, materials with engineered bandgaps are envisioned for optoelectronic devices tunable from the visible to deep UV frequencies. An AlGaIn/InGaIn/AlGaIn double heterostructure-base blue LED is now commercially available in Japan. The relatively strong atomic bonding of these materials also points to their potential use in high-power and high-temperature devices.

Single crystal wafers of GaN do not exist [1]. Sapphire(0001) is the most commonly used substrate, although its lattice parameter and coefficient of thermal expansion are different than that of GaN. The use of low-temperature (450°C-600°C) buffer layers of AlN [2-5] or GaN film quality and surface morphology. Undoped GaN is typically n-type. To date, p-type behavior has been achieved in chemically vapor deposited Mg- or Zn-doped GaN using post-growth treatments of either low-energy electron beam irradiation [8] or via thermal annealing in a N<sub>2</sub> atmosphere [9, 10]. Acceptor-type behavior has been obtained directly in molecular beam epitaxially grown films [11].

In the present research high quality monocrystalline GaN thin films have been grown on n-type  $\alpha$ -(6H)-SiC(0001) wafers employing high-temperature (HT) monocrystalline AlN buffer layers via organometallic vapor phase epitaxy (OMVPE) in a cold-wall, pancake-style reactor. This is the first known report of the use of *high-temperature* buffer layers to improve subsequent GaN growth. GaN film growth on vicinal and on-axis wafers as well as the different Si- and C-polar planes of SiC(0001) were also investigated. Triethylgallium (TEG), triethylaluminum (TEA) and ammonia (NH<sub>3</sub>) were used as reactants. Controlled n-type Si-doping of GaN using silane (SiH<sub>4</sub>) was demonstrated. Doping with bis-cyclopentadienyl-magnesium (Cp<sub>2</sub>Mg) produced deep blue emission in the PL spectrum. The heteroepitaxial growth of GaN and AlN on SiC was characterized using scanning electron microscopy (SEM), transmission electron microscopy (TEM), photoluminescence (PL) spectroscopy and Hall-effect measurements. Atomic dopant levels were measured using secondary ion mass spectrometry (SIMS). The following sections describe the experimental procedures, detail the results, provide a discussion and conclusions regarding this research and outline future research plans and goals.

## B. Experimental Procedure

GaN thin films were grown on Si-face and C-face, vicinal and on-axis SiC(0001) substrates at 950°C. Vicinal wafers are SiC(0001) 3°-4° off-axis toward the  $\langle 11\bar{2}0 \rangle$ . High-temperature monocrystalline AlN buffers layers were employed in this study. The as-received SiC wafers were cut into 7.1mm squares. The SiC pieces were degreased, dipped into a 10% HF solution for 10 minutes to remove the thermally grown oxide layer and blown dry with N<sub>2</sub> before being loaded onto the pancake-style, SiC-coated graphite susceptor. The reactor was evacuated to less than  $3 \times 10^{-5}$  Torr for one hour prior to initiating growth. The continuously rotating susceptor was rf inductively heated to 1100°C in 3 SLM of flowing H<sub>2</sub> diluent. Hydrogen was also used as the carrier gas for the various metalorganic precursors. Once this growth temperature was reached and stabilized, AlN deposition was started by flowing TEA and NH<sub>3</sub> into the reactor at 23.6  $\mu\text{mol/min}$  and 1.5 SLM, respectively. The system pressure during growth was 45 torr. The AlN was grown for 30 minutes resulting in a thickness of 100 nm. With the NH<sub>3</sub> and H<sub>2</sub> flowing at their prescribed rates, the TEA flow was terminated. The temperature was decreased to 950°C, and the system pressure was increased to 90 torr for the GaN growth. The flow rate of TEG was maintained at 24.76  $\mu\text{mol/min}$ . The growth rate for GaN was 0.9  $\mu\text{m/hr}$ . Si-doped GaN samples were grown by additionally flowing SiH<sub>4</sub> (8.2 ppm in N<sub>2</sub> balance) at flow rates between 0.05 nmol/min and 15 nmol/min. Likewise, Cp<sub>2</sub>Mg was used as the Mg-doping source.

The structural, microstructural, optical and electrical characteristics of the epitaxial GaN thin films were analyzed using several techniques. SEM was performed on a JEOL 6400FE operating at 5 kV. Conventional and high resolution TEM was performed on a Topcon EM-002B microscope operating at 200 kV. The photoemission properties of the GaN films were determined using low-temperature ( $T \approx 7\text{K}$ ) PL obtained using a 15 mW He-Cd laser (325 nm) as the excitation source. The Si-doped GaN films were characterized by Hall-effect measurements using the Van der Pauw geometry. Thermally evaporated Al was used as the contacts to these films with only linear regions of the current-voltage (I-V) curves being used for taking the Hall-effect measurements.

## C. Results and Discussion

*TEM Microstructures.* For growth on SiC(0001) substrates, the use of high-temperature monocrystalline AlN buffers layers dramatically improves the resulting GaN film quality. The GaN film and the HT-AlN buffer layer are monocrystalline as determined by TEM selected area diffraction. The high quality of the GaN on vicinal SiC(0001)<sub>Si</sub> using a HT-AlN buffer layer is apparent in the cross-sectional TEM micrograph shown in Fig. 1. The stacking fault density is noticeably very low. Also, the usually observed double positioning boundaries (DPBs) common in GaN films grown by other CVD and MBE techniques are not observed. Internal

stresses resulting from heteroepitaxial growth appear to be relaxed at the very strained GaN/AlN interface. From initial plan view TEM analysis, the defect density of the GaN film shown in Fig. 1 deposited on a vicinal SiC(0001)<sub>Si</sub> wafer using a HT-AlN buffer layer is roughly  $1\text{e}^8\text{ cm}^{-2}$ .



Figure 1. TEM micrograph of GaN grown on vicinal SiC(0001)<sub>Si</sub> at 950°C by OMVPE employing a high-temperature (1100°C) monocrySTALLINE AlN buffer layer.

Figure 2 shows a cross-sectional TEM micrograph of GaN/HT-AlN deposited on an on-axis SiC(0001)<sub>Si</sub> substrate. The dislocations appear to traverse the GaN perpendicular to the SiC(0001) interface. The dislocations in the vicinal sample shown in Fig. 1 seem to have more random orientations. The dislocation mechanism in both samples is under investigation, beginning with a Burgers vector analysis.

Because of the relative closeness in lattice parameters and coefficients of thermal expansion between wurtzitic AlN and (6H)-SiC, monocrySTALLINE AlN can be deposited directly on SiC at high temperatures. Thus, there is no apparent need to deposit a low-temperature amorphous AlN buffer layer requiring subsequent thermal annealing for growth on SiC(0001) substrates.

*HT-AlN Buffer Layer Surface Morphology.* In several experiments, four different SiC wafer types were simultaneously used for GaN film growth employing the HT-AlN buffer layer technique. These substrates were on- and off-axis SiC(0001)<sub>Si</sub> as well as on- and off-axis SiC(0001)<sub>C</sub>. As observed via SEM, the surfaces of the AlN buffer layers on the vicinal and on-axis C-face wafers were very textured with apparent small hexagonal hillocks. This growth

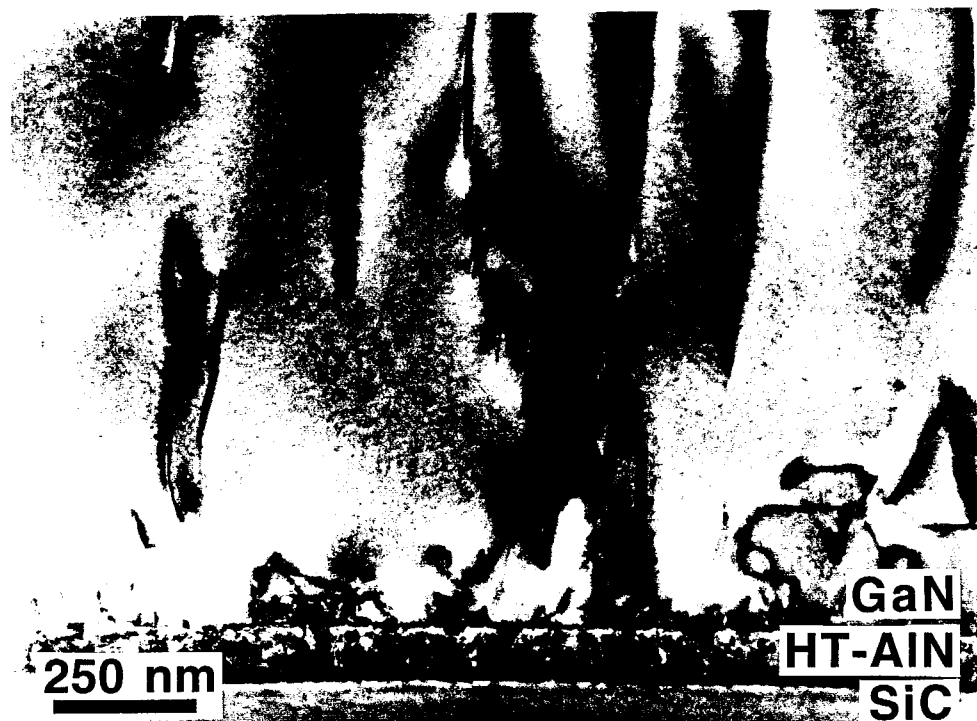


Figure 2. TEM micrograph of GaN grown on an on-axis SiC(0001)<sub>Si</sub> substrate at 950°C by OMVPE employing a high-temperature (1100°C) monocrystalline AlN buffer layer.

template yielded similar hexagonal hillocks on the surface of the subsequently grown GaN film layer. However, the HT-AlN grown on the vicinal and on-axis SiC(0001)<sub>Si</sub> had a rather flat and even surface morphology. However, many small pits (approximately 500Å across) were observed on the AlN surfaces when using both Si-face wafer types. By increasing the AlN deposition temperature from 1100°C to 1200°C for the Si-face substrates, the pit density decreased. This decrease was more appreciable in the on-axis SiC(0001) sample than in the vicinal SiC(0001) sample.

*GaN Film Surface Morphology.* The GaN deposited on the HT-AlN (1100°C) buffer layer on the on-axis SiC(0001)<sub>Si</sub> substrate had a very smooth and flat surface morphology as shown in Fig. 3. Some random pinholes were observed on the otherwise featureless surface. The cause of these pinholes is believed to be submicron particulate contamination of the growth surface. These particles may be from residual contamination in the reaction chamber or be generated by parasitic gas phase reactions. The surface morphology of the GaN on the vicinal SiC(0001)<sub>Si</sub> wafer shown in Fig. 4 was also rather smooth with only random pinholes. However, a slightly textured surface was observable apparently resulting from the step and terrace features of the vicinal SiC substrate.

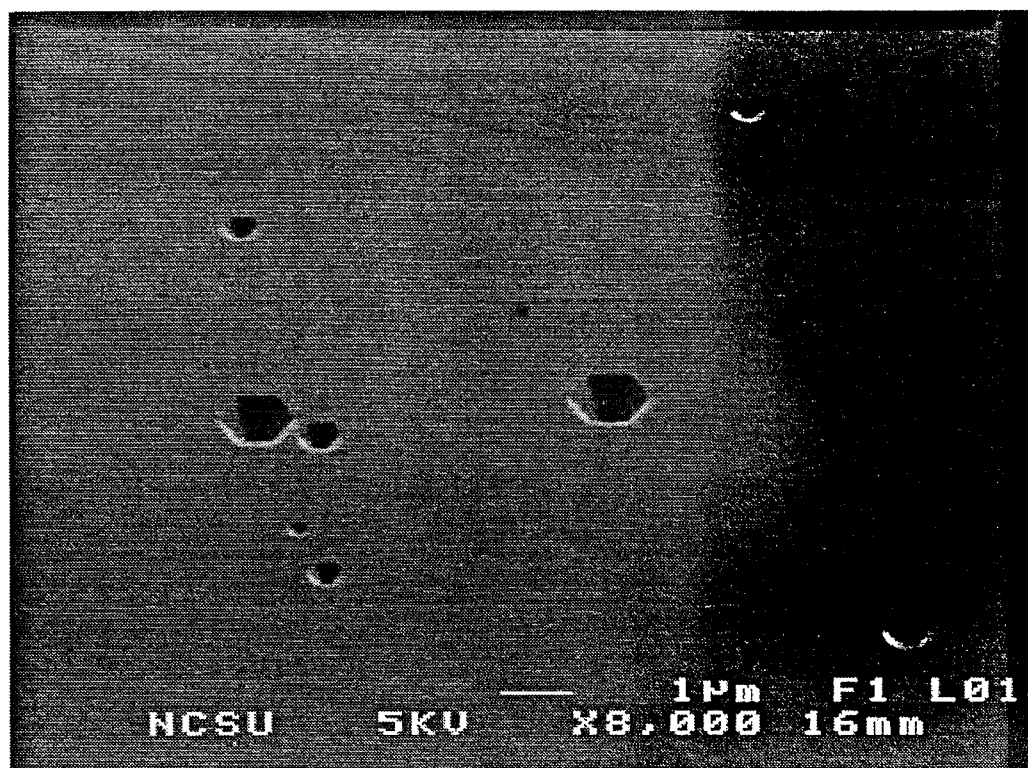


Figure 3. SEM micrograph of GaN deposited on an on-axis  $\text{SiC}(0001)_{\text{Si}}$  substrate using a high-temperature AlN buffer layer.

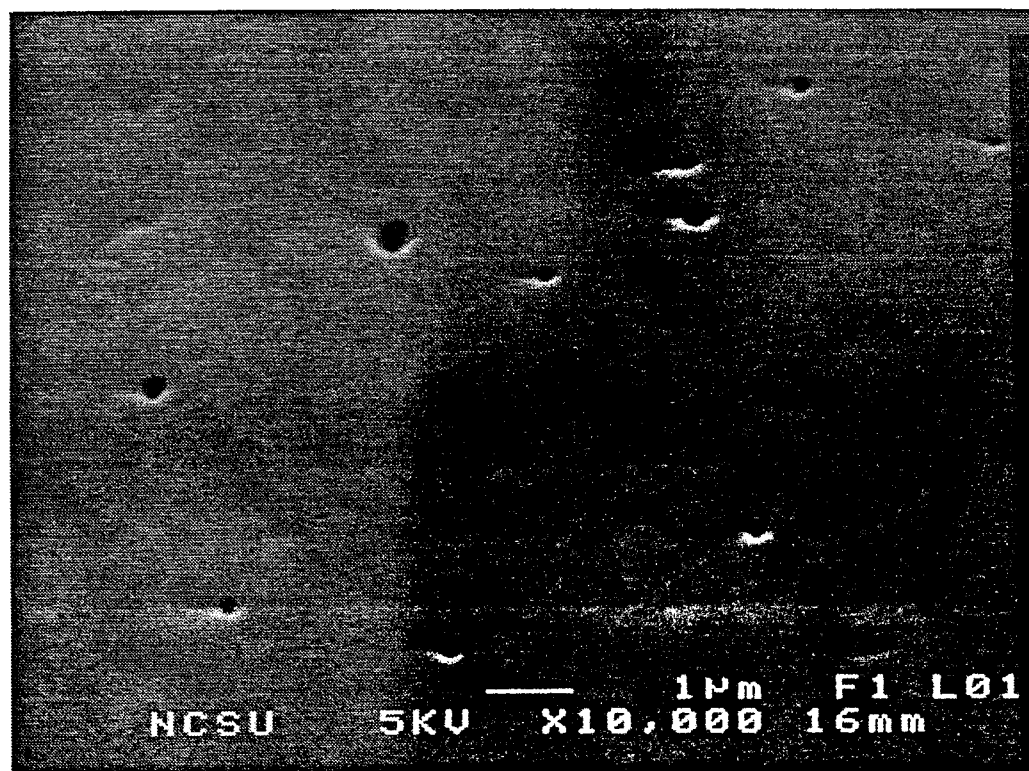


Figure 4. SEM micrograph of GaN deposited on vicinal  $\text{SiC}(0001)_{\text{Si}}$  using a high-temperature AlN buffer layer.

**Photoluminescence.** Low-temperature PL was performed on the various samples. The spectra of the GaN on both vicinal and on-axis SiC(0001)<sub>Si</sub> revealed strong band-edge emission at 3.47 eV. For the GaN on the vicinal sample only two weak defect peaks were observed at 3.26 eV and 2.2 eV, respectively (Fig. 5). However, the spectrum from the GaN sample on the on-axis substrate showed defect peaks at 3.26 eV, 3.0 eV and rather intense yellow emission at 2.2 eV (Fig. 6). Similar variations in the PL spectra also were observed for GaN films grown on the vicinal and on-axis SiC(0001)<sub>C</sub> substrates. The causes of the PL spectral differences are under investigation.

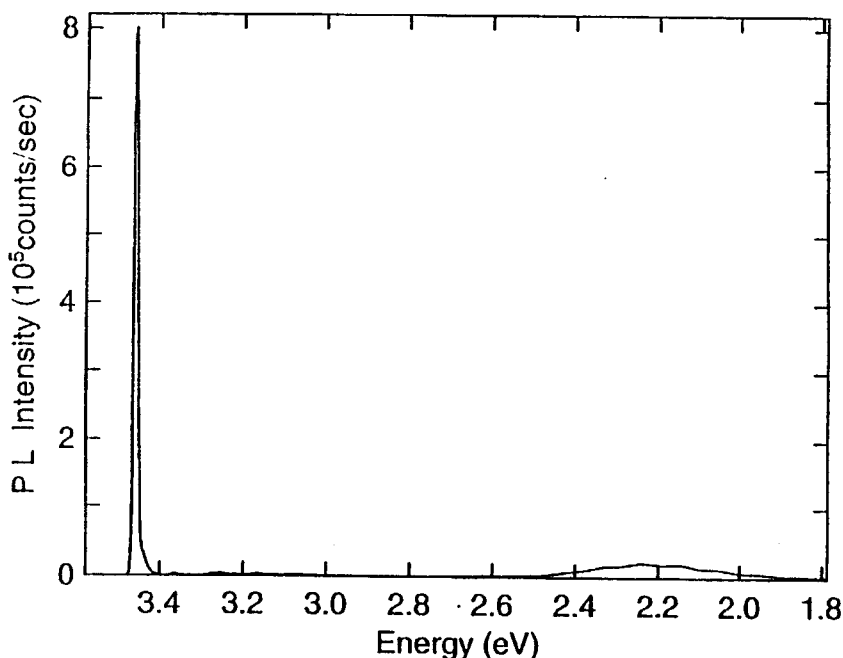


Figure 5. Low-temperature PL of GaN on vicinal SiC(0001)<sub>Si</sub> with a high-temperature AlN buffer layer.

**Si-doping in GaN.** Undoped high quality GaN grown on a HT-AlN buffer layer on SiC(0001) is resistive as deposited. However, GaN was controllably n-type doped with Si from a SiH<sub>4</sub> source for net carrier concentrations ranging from approximately 1e<sup>17</sup> cm<sup>-3</sup> to 1e<sup>20</sup> cm<sup>-3</sup>. The net carrier concentrations and room temperature mobilities versus SiH<sub>4</sub> flow rate are plotted in Fig. 7. As determined by Hall-effect measurements using the Van der Pauw geometry with thermally evaporated Al contacts, Si-doped GaN films with a net carrier concentration of  $n_D - n_A = 2 \times 10^{17} \text{ cm}^{-3}$  had a resulting room temperature mobility of  $\mu = 375 \text{ cm}^2/\text{V}\cdot\text{s}$ .

**Mg-doping in GaN.** GaN was also doped with Mg using Cp<sub>2</sub>Mg. For a magnesium atomic concentration of  $[\text{Mg}] = 6.1 \times 10^{19} \text{ cm}^{-3}$  as determined using a Mg ion-implanted GaN SIMS

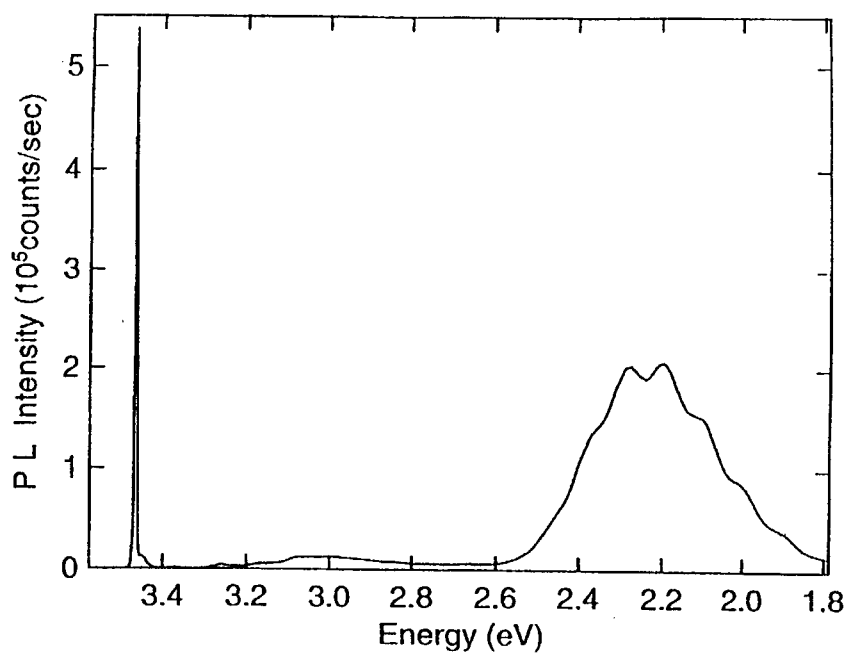


Figure 6. Low-temperature PL of GaN on an on-axis SiC(0001)<sub>Si</sub> substrate with a high-temperature AlN buffer layer.

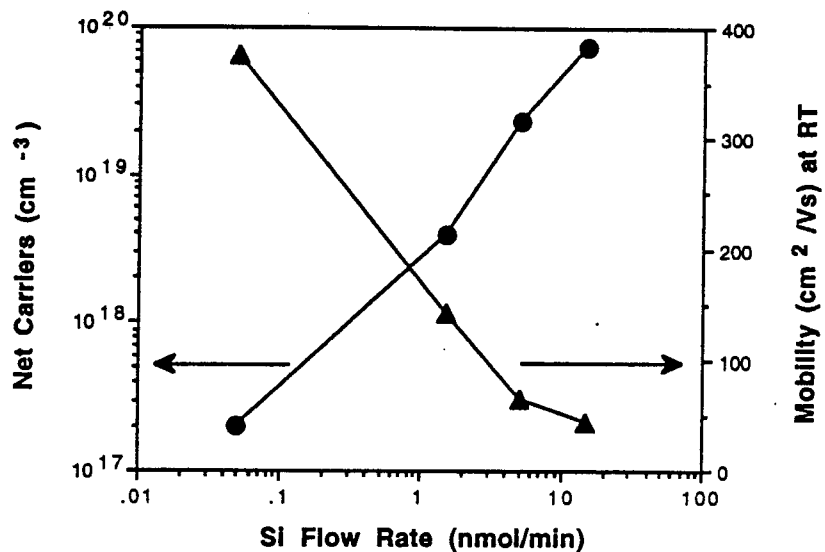


Figure 7. Net carrier concentration and room temperature mobilities in n-type Si-doped GaN as a function of SiH<sub>4</sub> flow rate.



standard, low-temperature PL revealed strong deep blue emission centered at 426 nm (Fig. 8). However, sufficiently ohmic contacts could not be obtained as is necessary for making Hall-effect measurements. Attempts will be made to measure the hole carrier concentrations in Mg-doped GaN films using a Hg-probe C-V system.

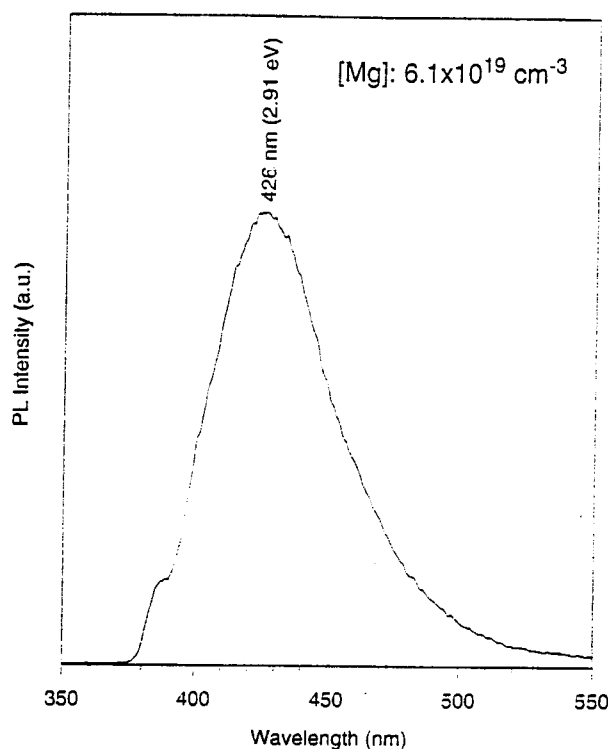


Figure 8. Low-temperature PL of Mg-doped GaN. For a magnesium atomic concentration of  $[Mg] = 6.1 \times 10^{19} \text{ cm}^{-3}$  strong deep blue emission is observed at 426 nm.

#### D. Conclusions

High quality GaN thin films have been deposited on vicinal and on-axis  $\alpha(6H)\text{-SiC}(0001)_{\text{Si}}$  substrates using high-temperature monocrystalline AlN buffer layers. The photoemission properties of the GaN on the vicinal SiC substrate were superior to those on the on-axis substrate. Controlled n-type Si-doping of GaN was demonstrated for net carrier concentrations ranging from  $1 \times 10^{17} \text{ cm}^{-3}$  to  $1 \times 10^{20} \text{ cm}^{-3}$ . Optically active Mg-doped GaN was also observed.

#### E. Future Research Plans and Goals

Reliable and consistent p-type doping of GaN must be obtained. Thus the role of hydrogen passivation needs further investigation. Once p-type conduction in GaN has been verified, pn-junctions will be fabricated and tested. Concurrently, film growth in the InGaN system must be undertaken for use as the active layer in bright-blue LEDs and laser diodes (LDs).

Continued improvements in film quality in the AlGaIn system must occur for use in double heterostructure devices. Also, attempts will be made to controllably dope InGaIn and AlGaIn n- and p-type. Ultimately, both UV and bright-blue LEDs will be demonstrated, as well as microelectronic devices such as MESFETs and MOSFETs.

#### F. References

1. R. F. Davis, *Physica B* **185** (1993) 1.
2. S. Yoshida, S. Misawa and S. Gonda, *Appl. Phys. Lett.*, **42** (1983) 427.
3. S. Yoshida, S. Misawa and S. Gonda, *J. Vac. Sci. Technol.*, **B1** (1983) 250.
4. H.I. Amano, N. Sawaki, I. Akasaki and Y. Toyoda, *Appl. Phys. Lett.*, **48** (1986) 353.
5. I. Akasaki, H.I. Amano, Y. Koide, K. Hiramatsu and N. Sawaki, *J. Cryst. Growth*, **98** (1989) 209.
6. T. Lei, M. Fanciulli, R.J. Molnar and T.D. Moustakas, *Appl. Phys. Lett.*, **59** (1991) 944.
7. S. Nakamura, M. Senoh and T. Mukai, *Jpn. J. Appl. Phys.*, **30** (1991) L1708.
8. H. Amano, M. Kito, K. Hiramatsu and I. Akasaki, *Jpn. J. Appl. Phys.*, **28** (1989) L2112.
9. S. Nakamura, T. Mukai, M. Senoh and N. Iwasa, *Jpn. J. Appl. Phys.*, **31** (1992) L139.
10. S. Nakamura, N. Iwasa, M. Senoh and T. Mukai, *Jpn. J. Appl. Phys.*, **31** (1992) 1258.
11. C. Wang and R.F. Davis, *Appl. Phys. Lett.*, **63** (1993) 990.

## **XIX. Electron Cyclotron Resonance Growth of AlN, GaN, and InN**

### **A. Introduction**

In CVD systems, energy must be supplied to whatever reaction is producing the growth. In thermal CVD, substrate heating provides energy to these surface reactions. Plasma-enhanced CVD provides another method of energy input, a plasma of activated species; therefore, lower substrate temperatures can be used during growth. In an ECR plasma, a magnetic field is added to confine and direct the particles from the plasma. This method will be used to grow the III-V nitrides.

### **B. Experimental Procedure**

The plasma source is a used ASTeX ECR diamond deposition chamber (see Fig. 1). A 2.45GHz microwave source excites a nitrogen plasma in a 875G magnetic field created by two coils. A nitrogen plasma will provide activated nitrogen to the surface reaction. This activated nitrogen flows into a larger growth chamber where the substrate is mounted.

The metalorganic precursors will be trimethylaluminum (TMA), trimethylgallium (TMG), and trimethylindium (TMI) using a nitrogen carrier gas. The metalorganics are kept in constant temperature baths, allowing control of their vapor pressures. The metalorganic injection point is a few inches below the substrate position. The reaction between the metalorganics and the activated nitrogen occurs just below the substrate. The metalorganic gas line is mounted to a Z-stage on the top flange to allow varying the substrate to gas inlet distance.

The growth chamber has a 10-3/4" ID and is water-cooled. An XYZ stage at the center of the growth chamber's top flange supports the substrate which faces down during growth. The sample holder can flip up 90 degrees so samples can be transferred from the transfer line. The Z motion of the sample holder allows varying the substrate distance from the plasma.

### **C. Results**

At present the growth chamber and transfer rod have been designed and are being built. The microwave source, magnets, and plasma chamber are mounted on an aluminum stand which will house the equipment. The gas system and 90 degree flip box for the sample holder are being designed.

### **D. Discussion**

*Applications of the Nitrides.* All the nitrides have optoelectronic applications because of their direct bandgaps. Another important application is negative electron affinity (NEA). GaN has an NEA when cesium is adsorbed on its surface [1]. AlN deposited on  $\alpha(6H)$ -SiC exhibits an NEA [2]. Therefore, it can be used to produce cold cathode emitters. The nitride

alloys with large bandgaps (see Fig. 2) may also exhibit an NEA, and would therefore have device applications similar to AlN.

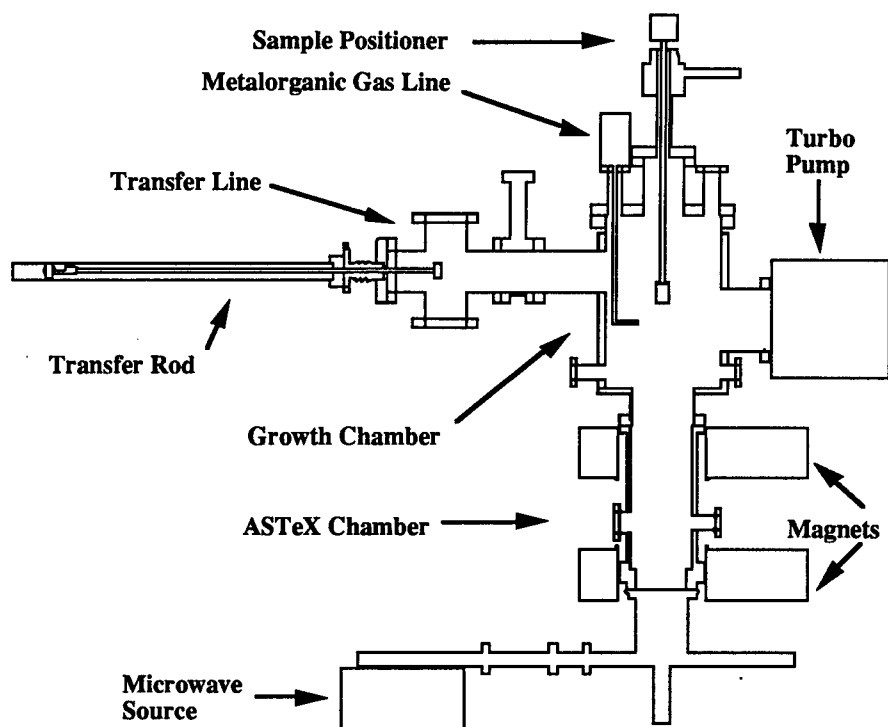


Figure 1. ECR growth system schematic.

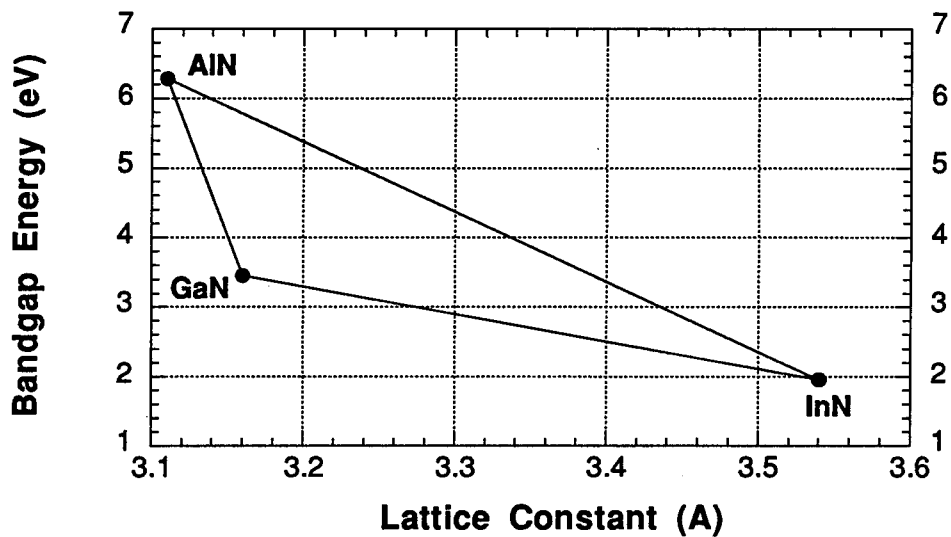


Figure 2. III-V nitride bandgap vs. lattice constant.

*Progress in the Plasma Growth of the Nitrides.* Several groups have grown nitrides using plasma-enhanced CVD. These attempts are being used as models for the growth system being built. Single crystal n-type GaN was grown on sapphire using ECR plasma MOCVD [3]. The precursors were TMG (nitrogen carrier) with an ammonia plasma. The  $\text{NH}_3$  to TMG ratio was about 100. Epitaxial growth occurred from 300-400°C at pressures of .1 - 1 mTorr.

Single crystal InN was grown on sapphire using microwave plasma (non-ECR) MOCVD [4]. The precursors were TMI (nitrogen carrier) in a nitrogen plasma. The  $\text{N}_2$  to TMI ratio was 5000. Epitaxial growth occurred from 400-600°C at 1.3 Torr.

Thin AlN films were grown using ECR plasma MOCVD [5]. The precursors were TMA (nitrogen & hydrogen carriers) and a  $\text{N}_2/\text{H}_2$  plasma. Growth was at 10m Torr and only at 500°C. At higher growth temperatures, epitaxial growth of AlN may be attained.

AlN, GaN, and InN are completely miscible, so four different alloys can be formed. Single crystals of AlGaIn, InGaIn, and InGaAlN have been grown using MOCVD [6,7]. No reports have been found of growth using plasma-enhanced (ECR or non-ECR) CVD.

#### F. Conclusions

AlN, GaN, InN and their alloys will be grown by the method of ECR plasma-enhanced MOCVD. The ECR method especially suits growth of InN which dissociates at low temperatures. The nitride growth system will eventually be part of the transfer line; thus, connecting it to characterization and plasma cleaning systems.

#### G. Future Research Plans and Goals

The nitrides will be used to make devices and will be studied for their NEA properties. One specific device of interest is the cold cathode emitter

#### H. References

1. J. I. Pankove and H. E. P. Schade, Appl. Phys. Lett. **25**, 53 (1974).
2. M.C. Benjamin, Cheng Wang, R. F. Davis, and R. J. Nemanich, Appl. Phys. Lett. **64**, 3288 (1994).
3. Sakae Zembutsu and Toru Sasaki, Appl. Phys. Lett. **48**, 870 (1986).
4. A. Wakahara, T. Tsuchiya, and A. Yoshida, J. Crystal Growth, **99**, 385 (1990).
5. H. Nomura, S. Meikle, T. Nakanishi, and Y. Hatanaka, J. Appl. Phys. **69**, 990 (1990).
6. M. Matloubian and M. Gershenson, J. Electron. Mater. **14**, 633 (1985).
7. T. Matsuoka, N. Yoshimoto, T. Sasaki, and A. Katsui, J. Electron. Mater. **21**, 157 (1992).

## XX. Luminescence Studies of GaN, AlN, InN and Their Solid Solutions

### A. Introduction

Luminescence is the emission of photons due to excited electrons in the conduction band decaying to their original energy levels in the valance band. The wavelength of the emitted light is directly related to the energy of the transition, by  $E=h\nu$ . Thus, the energy levels of a semiconductor, including radiative transitions between the conduction band, valance band, and exciton, donor, and acceptor levels, can be measured.[1,2] Various methods exist to excite the electrons, including photoluminescence (photon excitation), and cathodoluminescence (electron-beam excitation). In each technique, signal intensity is measured at specific wavelength intervals using a monochromator and a detector. The intensity versus wavelength (or energy) plot can then be used to identify the characteristic energy band gap and exciton levels (intrinsic luminescence) of the semiconductor, and the defect energy levels (extrinsic luminescence) within the gap.[1]

Both photo- and cathodoluminescence analysis has been performed on AlN, GaN, InN and their solid solutions.[3-20] Much of the work has been in measuring the low temperature luminescence of GaN. High quality, unintentionally doped GaN exhibits a strong donor-bound exciton peak at 357.3 nm (3.47 eV).[16] Defect peaks due to donor-acceptor (DA) transitions and accompanying phonon replicas are also prevalent, with peak wavelengths at 380.3, 391.2 and 402.9 nm. The identity of the acceptor is not clear. A deep emission at 540 nm (2.2 eV) is also common in GaN. Currently the source of this emission is not know, although various models exist to explain it.[19,20] It is of utmost importance to limit the defect transitions, as it can reduce the transition probability of the near-gap emission.

Although undoped GaN is always n-type, recent advances in film growth have lowered the carrier concentration to  $10^{16}/\text{cm}^3$ . For device applications it is important to have a high carrier concentration at a controlled level. Common dopants for n-type doping of GaN include Si and Ge. Nakamura, *et al.* found that for Si-doped GaN two peaks dominate the spectrum.[12] The first is a UV emission peak at 380 nm. The second peak is the deep level (DL) emission previously discussed; this transition is enhanced by Si-doping. Conflicting results were shown by Murakami, *et al.*, who saw a band edge peak at 358 nm dominate their spectrum.[8] The DL emission at 540 nm in their samples was very weak.

The development of light emitting diodes (LEDs) and laser diodes using GaN-based materials has been limited by the difficulty in obtaining quality p-type films.[12] Common dopants include Zn, Cd, and Mg.[3] Recent work has proven successful, with low resistivity Mg-doped GaN obtained by thermal annealing or low energy electron beam irradiation

(LEEBI) as a post-growth process step. The luminescence from these films typically show a broad peak located at 450 nm, with no emission near the band-edge.

Work on AlN and  $\text{Al}_x\text{Ga}_{1-x}\text{N}$  has been limited by the energy gap of 6.2 eV for AlN. This corresponds to a wavelength (200 nm) that is lower than most of the optical light sources. An excimer laser using the ArF line (193 nm) could possibly be used, although very little work on this has been done to date. Cathodoluminescence of AlN is possible, however, and most of the results have been obtained via this method.[16-18].  $\text{Al}_x\text{Ga}_{1-x}\text{N}$  with low amounts of Al can also be investigated using frequency doubled and tripled lasers that have lines down to 260 nm.

## B. Experimental Procedures

A combined photo- and cathodoluminescence system is used to measure the luminescence from the III-V nitrides. A schematic view is shown in Fig. 1, and a block diagram is shown in Fig. 2. Each sample is attached to a cryostat that allows for a test temperature range of 8 to 400 K. A McPherson model 219 vacuum monochromator with a focusing mirror chamber is used to collect the emitted light. The focal length of the monochromator is .5 m, with a wavelength resolution of .04 nm at 313.1 nm for a 1200 G/mm grating. A photon counting detection scheme is used to measure the light intensity, with a photomultiplier tube (PMT) used that has a wavelength range of 180-650 nm. A GaAs PMT that is efficient from 185-930 nm will be added to the system shortly.

A Liconix He-Cd laser is the photoexcitation source. It is a continuous wavelength laser that operates at a wavelength of 325 nm (3.8 eV), with a power of 15 mW. It is used for PL of GaN and  $\text{In}_x\text{Ga}_{1-x}\text{N}$ , but a lower wavelength source is needed to test the full range of  $\text{Al}_x\text{Ga}_{1-x}\text{N}$  solid solutions. A pulsed excimer laser is proposed as the other optical source; it operates at wavelengths of 193 nm (6.4 eV) and 248 nm (5.0 eV).

A Kimball Physics electron gun is used for cathodoluminescence measurements. It has maximum beam voltage of 10 keV and a maximum beam current of 450  $\mu\text{A}$ . By varying the beam voltage it is possible to perform depth-resolved spectroscopy.

The beam blanking capability of the electron gun will allow for time-delay studies of the semiconductors.

## C. Results and Discussion

Photoluminescence measurements were performed on GaN films grown via OMVPE on vicinal  $\alpha(6\text{H})\text{-SiC}(0001)\text{Si}$  wafers. The buffer layer for each sample was AlN. All of the tests were performed at 8 K, unless otherwise noted.

The photoluminescence of undoped GaN grown at 950 °C is shown in Fig. 3. The sample thickness was .68  $\mu\text{m}$ . The peak at 357.2 nm is attributed to the recombination of excitons at neutral donors. The FWHM of this peak, 4 meV, indicates the high quality of the sample. The

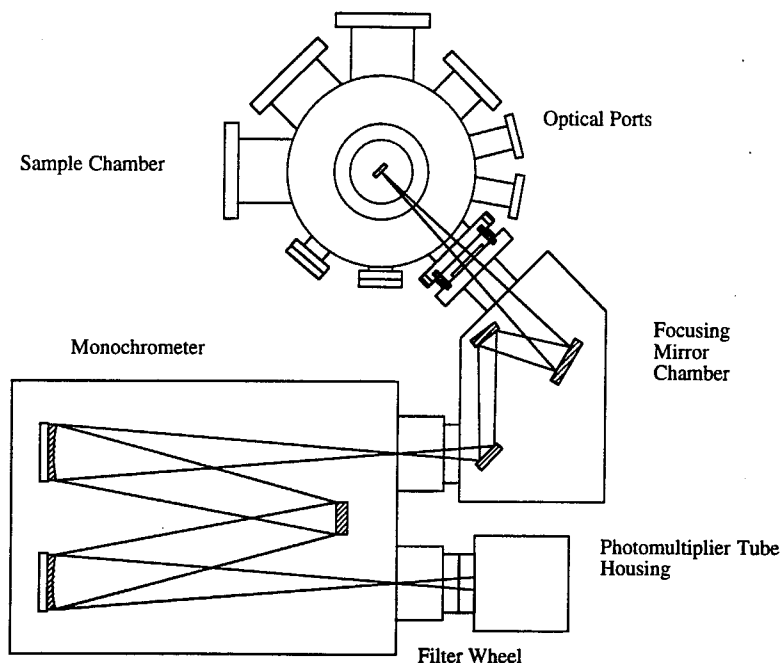


Figure 1. Schematic view of combined photo- and cathodoluminescence system.

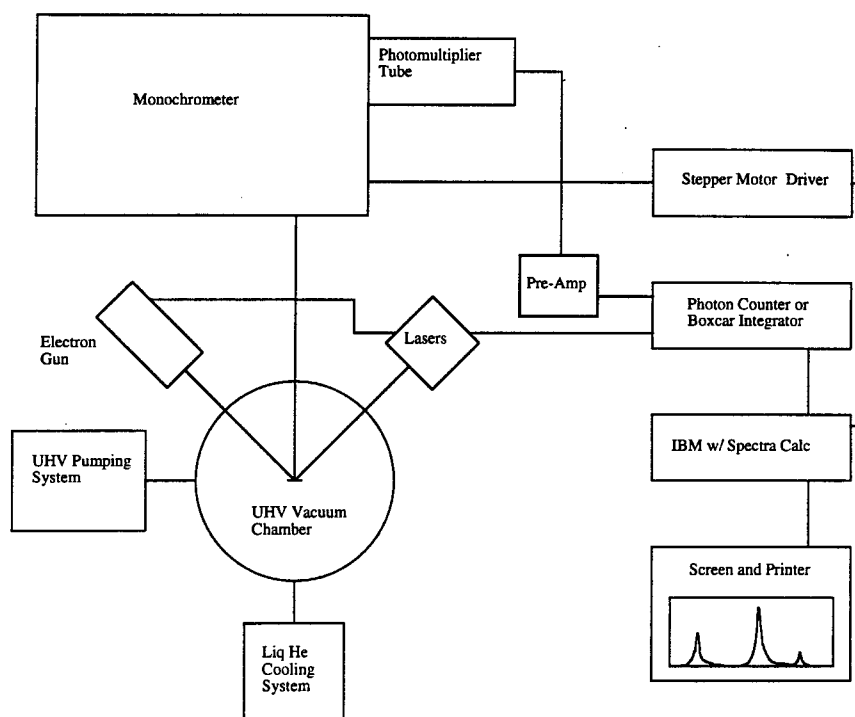


Figure 2. Block diagram of combined photo- and cathodoluminescence system.



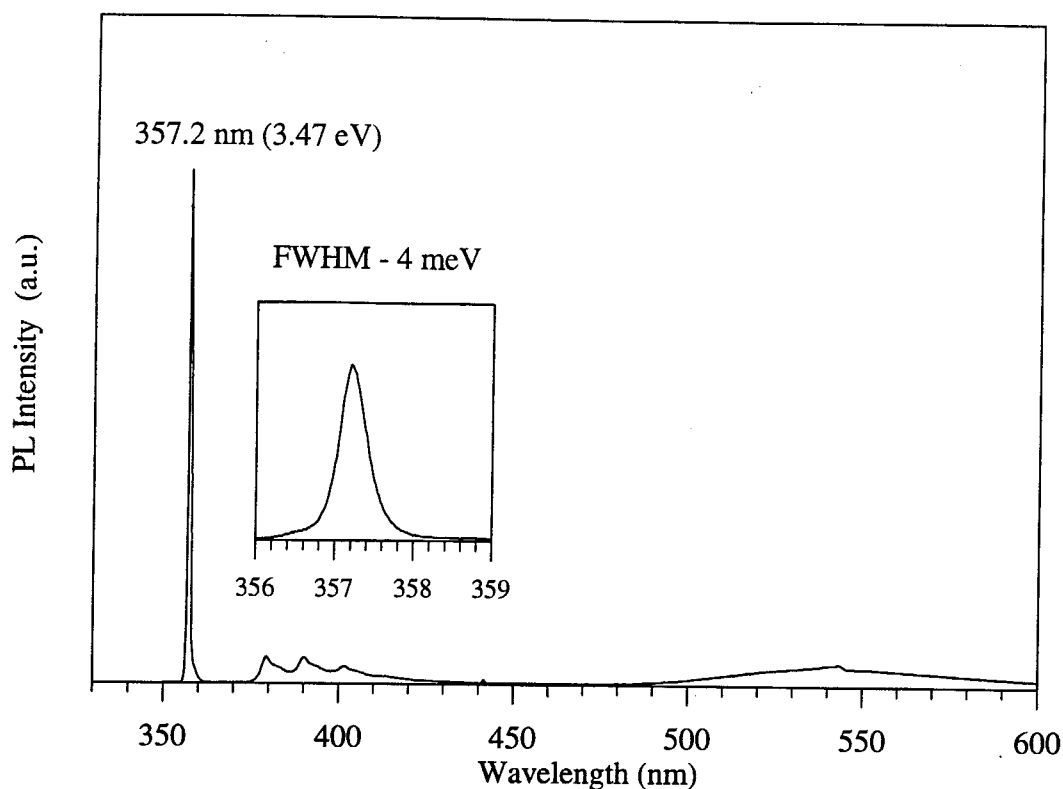


Figure 3. PL of undoped GaN at 8K.

donor-acceptor (DA) defect peaks were relatively weak in this sample, as was the deep level (DL) emission at 540 nm.

The effect of growth temperature on the photoluminescence of GaN is shown in Fig. 4. All three samples were .6-.7  $\mu\text{m}$  thick. At the higher growth temperatures the DA peaks increased in intensity relative to the band-edge emission. The sample grown at 900  $^{\circ}\text{C}$  exhibited the best luminescence. Subsequent tests showed that 950  $^{\circ}\text{C}$  was the optimal growth temperature, as judged by electrical, microstructural, and structural characterization. Modifications of the growth parameters improved the PL as well (Fig. 3).

The PL of Si-doped GaN is shown in Fig. 5, as a function of carrier concentration. The two main peaks in the spectrum are the band edge emission at 358 nm and the DL peak at 540 nm. The peak at the band edge broadened and moved to lower wavelengths as the doping level was increased, with the peak wavelengths at 358.3 nm, 358.24 and 358.0 for the three samples. This is typical behavior for n-type semiconductors. It is believed that the band-edge peak is due to donor to valance band transitions, but lower carrier concentrations are needed to verify this. The deep level emission at 540 nm also increased in intensity as the doping level increased.

The PL of Mg-doped GaN exhibited blue emission, as shown in Fig. 5. These results proved to be repeatable. This sample was annealed in flowing  $\text{N}_2$  for 90 minutes at 800  $^{\circ}\text{C}$ .

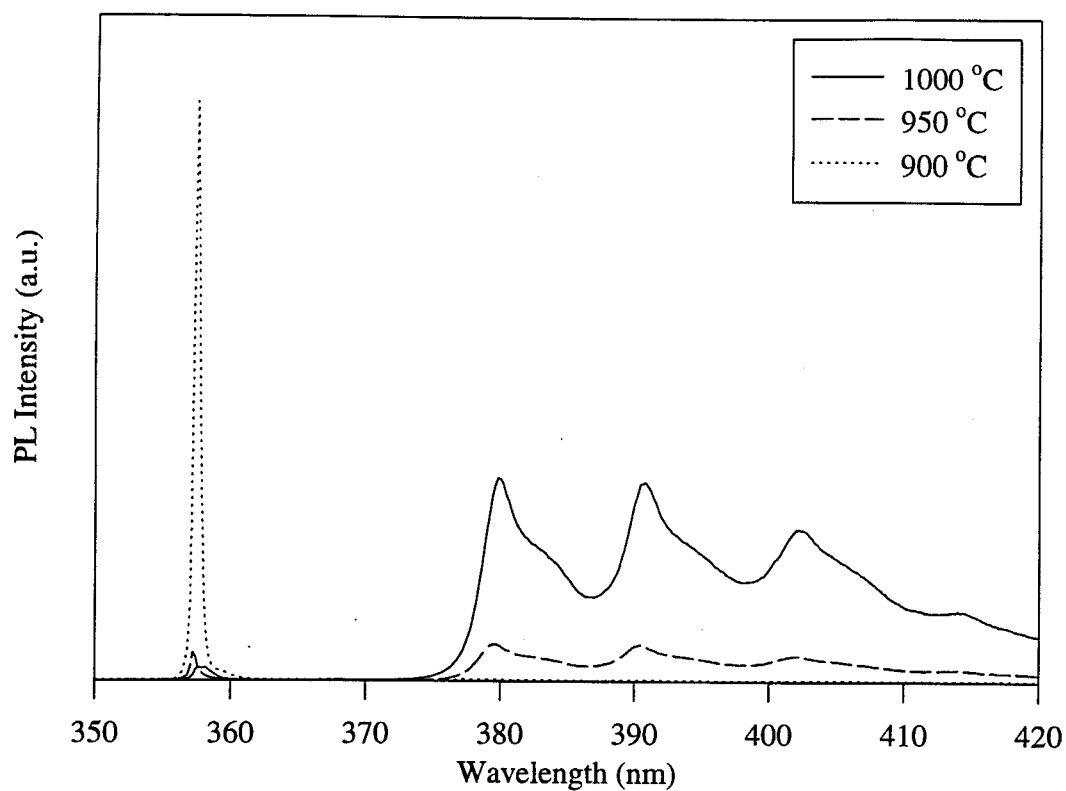


Figure 4. PL of GaN as a function of growth temperature.

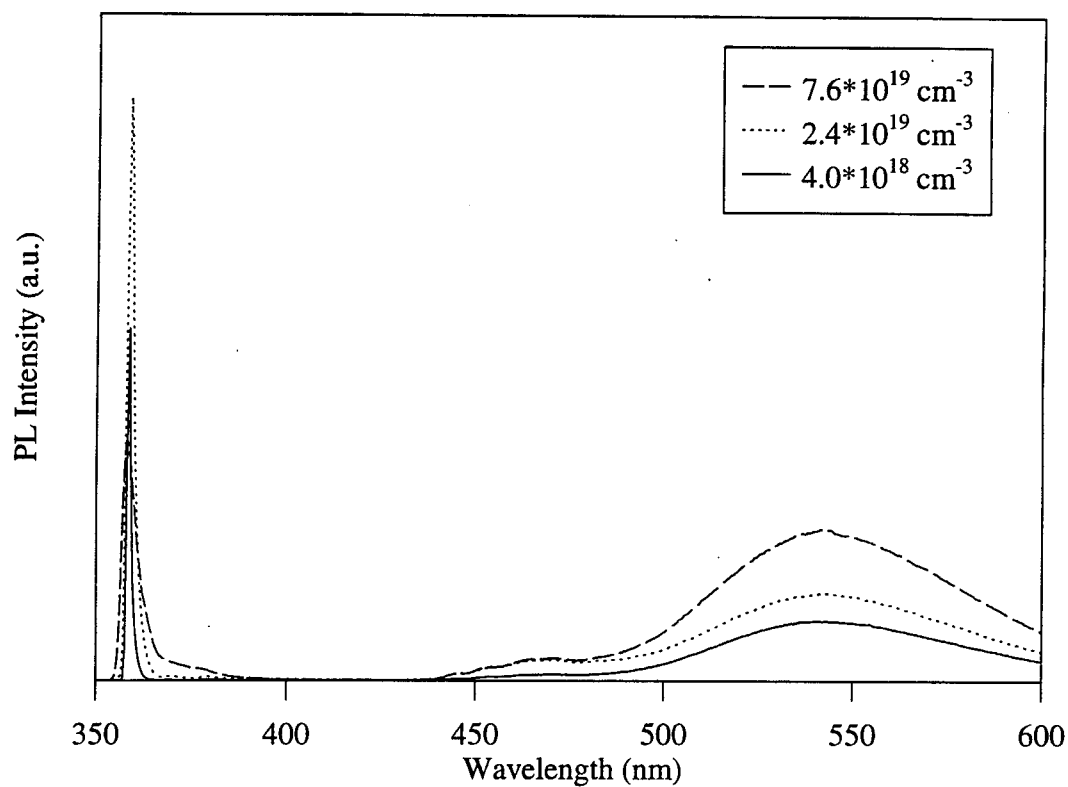


Figure 5. PL of GaN as a function of growth temperature.

The peak wavelength of 426 nm was typical for the samples tested. PL performed at room temperature showed that the samples exhibited blue emission at a lower intensity.

Cathodoluminescence was performed on two  $\text{Al}_x\text{Ga}_{1-x}\text{N}$  samples, and the results are shown in Fig. 6. Each sample was doped with silicon. The results indicate that near band-edge emission was obtained for both samples. Further tests are needed to better understand the origin of the deep emissions seen in each sample.

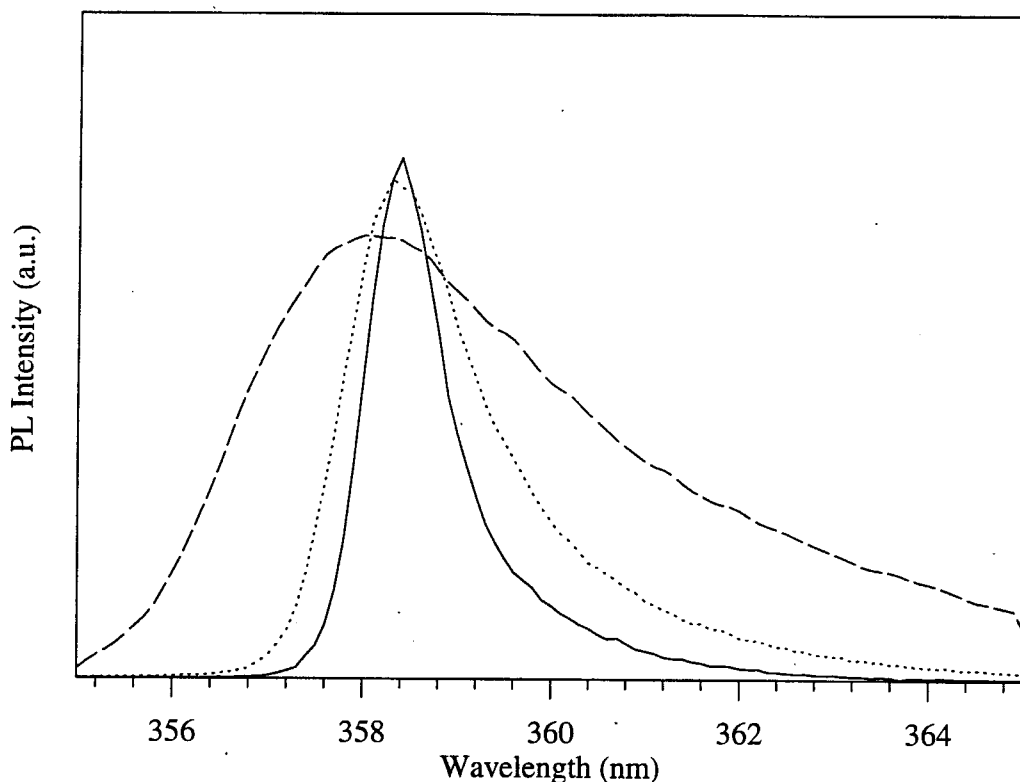


Figure 6. PL of GaN as a function of growth temperature.

#### D. Conclusions

Low temperature (8K) photoluminescence has been used to characterize both undoped and doped GaN films deposited on vicinal  $\alpha(6H)\text{-SiC}(0001)\text{Si}$  wafers by OMVPE. Unintentionally doped GaN exhibited a sharp peak at 357.2 nm that is due to the recombination of excitons at neutral donors. The FWHM of 4 meV of the peak is an indication of the high quality of the films. The film thicknesses for the results reported were all below 1  $\mu\text{m}$ , which indicates that thicker films are not required to improve the PL data.

The PL of Si-doped GaN showed two peaks that dominate the spectrum, a near-band edge peak at 358 nm which is probably due to donor to valance band transitions, and a peak at 540 nm due to DL emission. As the carrier concentration increased the band-edge peak

broadened and moved to higher energies, while the DL peak increased in intensity. Mg-doped GaN exhibited a broad blue spectrum that peaked at 426 nm. These samples were annealed in flowing N<sub>2</sub> for 90 minutes at 800 °C.

Cathodoluminescence was used to characterize two Si-doped Al<sub>x</sub>Ga<sub>1-x</sub>N films. The results indicate that CL is a useful tool for analyzing films which have a band gap higher than that which can be tested by the He-Cd laser. In the future the CL of both undoped and doped Al<sub>x</sub>Ga<sub>1-x</sub>N films will also be performed to measure their quality.

#### E. Future Research Plans and Goals

Photoluminescence and cathodoluminescence will continue to be used to measure the quality of GaN films grown by OMVPE. CL measurements of Al<sub>x</sub>Ga<sub>1-x</sub>N films through the full composition range will also be performed. In addition, PL will be used to guide the growth of In<sub>x</sub>Ga<sub>1-x</sub>N. A new GaAs photomultiplier tube (PMT) with a wavelength range of 180-930 nm will be added to the system to assist in this. This PMT will also make it possible to measure deep levels that occur in Mg-doped GaN, which have been found in samples that were not fully annealed.[5]

The present system will be improved by placing the monochrometer on an optical table. This will allow for a variety of experiments outside of the sample chamber shown in Fig. 1. One application will be to measure the spectral output, external quantum efficiency, and total output power of LEDs with the aid of an integrating sphere. PL measurements will also be made using the breadboard.

Future collaboration include working with Dr. J. J. Song at Oklahoma State on photopumping and time-decay studies of Al<sub>x</sub>Ga<sub>1-x</sub>N and In<sub>x</sub>Ga<sub>1-x</sub>N. Deep level transient spectroscopy (DLTS) measurements will be made with the assistance of Dr. Nobel Johnson at Xerox PARC. A collaboration with Dr. Barbara Goldenberg of Honeywell will study the photoluminescence of AlN and Al<sub>x</sub>Ga<sub>1-x</sub>N using an ArF excimer laser.

#### F. References

1. B. G. Yacobi and D.B. Holt, Cathodoluminescence Microscopy of Inorganic Solids, Plenum Press, New York (1990).
2. Micheal D. Lumb, Ed., Luminescence Spectroscopy, Academic Press, New York (1978).
3. S. Strite and H. Morkoç, J. Vac. Sci. Technol. B, **10** (4) 1237-1266 (1992).
4. R. A. Youngman and J. H. Harris, J. Am. Ceram. Soc., **73** [11] 3238-46 (1990).
5. S. Nakamura, T. Mukai, and M. Senoh, Jpn. J. Appl. Phys., **30** (10A) 1708-1711 (1991).
6. V. F. Veselov, A. V. Dobrynin, G. A. Naida, P. A. Pundur, E. A. Slotensietse, and E. B. Sokolov, Inorganic Materials, **25** (9) 1250-4 (1989).
7. J. N. Kuznia, M. A. Kahn, D. T. Olson, R. Haplan, and J. Freitas, J. Appl. Phys. **73** (9) 4700-4702 (1993).
8. H. Murakami, T. Asahi, H. Amano, K. Hiramatsu, N. Sawaki, and I. Akasaki, J. Crystal Growth, **115** 648-51 (1991).

9. K. Maier, J. Schneider, I. Akasaki, and H. Amano, *Jpn. J. Appl. Phys.*, **32** (6) 846-848 (1993).
10. I. Akasaki, and H. Amano, *J. Crystal Growth*, **99** 375-80 (1990).
11. S. Yoshida, H. Okumura, S. Misawa, and E. Sakuma, *Surf. Sci.*, **267** (7) 50-53 (1992).
12. S. Nakamura, T. Mukai, and M. Senoh, *Jpn. J. Appl. Phys.*, **31** (9) 2883-90 (1992).
13. S. Nakamura, N. Iwasa, T. Mukai, and M. Senoh, *Jpn. J. Appl. Phys.*, **31** (5) 107-15 (1992).
14. S. Nakamura, T. Mukai, and M. Senoh, *Jpn. J. Appl. Phys.*, **30** (12A) 1998-2001 (1991).
15. S. Strite, J. Ruan, Z. Li, N. Manning, A. Salvador, H. Chen, D. J. Smith, W. J. Choyke, and H. Morkoç, *J. Va. Sci. Technol. B* **9** (4) 1924-29 (1991).
16. W. J. Choyke and I. Linkov, *Inst. Phys. Conf. Ser.*, **137** 141-147 (1993).
17. S. Pacesova and L. Jastrabik, 1979 *Phys. Stat. Sol. B* **93** K111.
18. S. Yoshida, S. Misawa, Y. Fujii, S. Takada, H. Hayakawa, S. Gonda, A. and Itoh, *J. Vac. Sci. Technol.*, **16** (4) 990-3 (1979).
19. E. R. Glaser, T. A. Kennedy, H. C. Crookham, J. A. Freitas, Jr., M. Asif Khan, D.T. Olson, and J. N. Kuznia, *Appl. Phys. Lett.* **63** (19) 2673-2675 (1993).
20. E. R. Glaser, T. A. Kennedy, J. A. Freitas, Jr., M. Asif Khan, D. T. Olson, and J. N. Kuznia, *Inst. Phys. Conf. Ser.*, **137** (1993).
21. T. Sasaki, T. Matsuoka, A. Katsui, *Appl. Surf. Sci.* **41/42** 504-508 (1989).

## XXI. Native Defects in Wurtzite GaN and AlN

### Abstract

The results of an extensive theoretical study of native defects in GaN and of vacancies in AlN are presented. We have considered cation and anion vacancies, antisites, and interstitials. The computations were carried out using quantum molecular dynamics, in supercells containing 72 atoms. Due to the wide gap of nitrides, the formation energies of defects depend strongly on the position of the Fermi level. The N vacancy in GaN introduces a shallow donor level that may be responsible for the *n*-type character of as-grown GaN. Other defects introduce deep states in the gap, with strongly localized wave functions.

### 1. Introduction

Wide gap nitrides hold substantial promise for electronic applications. Since the electronic quality of a semiconductor is largely determined by the nature and number of its native defects and impurities, it is important to understand their properties. In wide gap semiconductors, impurity-induced shifts in the Fermi level position will have a major effect on the abundance of native defects, and thus on self-compensation and diffusion. Therefore, they will also affect growth and processing.

In GaN, *n*- and recently also *p*-type doping has been achieved [1, 2]. The quality of the material could still be improved, and the role of native defects needs to be understood, in particular for light-emitting applications, where a presence of recombination centers could lead to severe degradation. AlN has so far resisted any doping attempts, either *n*- or *p*-type. This may be due to its very wide band gap (6.3 eV), or be caused by a presence of a large number native defects.

We have embarked on a comprehensive study of native defects and impurities in GaN and AlN, focusing on identifying the dominant native defects, stoichiometry effects, and a search for effective dopants. In the following, we describe our first results regarding the electronic structure and formation energetics of point defects. We have also considered substitutional impurities and contaminants. These results will be presented elsewhere.

### 2. Calculations and Theoretical Aspects

The calculations were carried out using *ab initio* molecular dynamics (MD) [3] and the local density approximation (LDA). A soft non-local pseudopotential for N was generated according to the procedure of Lee and Rabii [4], while for Ga a standard non-local potential was used [5]. The kinetic energy cutoff for the plane wave basis set was 30 Ry. The accuracy of the pseudopotentials was tested by computing the lattice constants, the cohesive energies, and the bulk moduli of zinc-blende GaN and AlN. The results were in good agreement with previous calculations and experimental data [6]. Calculations for defects were carried out in a large supercell that would contain 72 atoms in the case of the perfect crystal. Due to the size of the cell, only the  $\Gamma$  point was used for Brillouin zone summations. To speed up the search for minimum energy configurations, the atoms were relaxed according to an efficient scheme that uses Newtonian dynamics with a special friction force for the atoms [7], while the electrons follow the motion of the atoms according to the Car-Parrinello equations [3].

Considering the limitations of the above approach, the use of supercells allows for the application of the powerful *ab initio* MD formalism, but results in broadening of the defect-

and impurity-induced energy levels. This leads to an uncertainty in level positions of up to 0.5 eV in the supercell we are using. (The total energy and thus the calculated formation energies converge much more rapidly with supercell size.) The remaining source of error is due to the use of local density theory, which seriously underestimates band gaps and overestimates the cohesive energy. Even when the positions of the levels are measured from the nearest band edge, the band gap problem introduces an *additional* uncertainty of the order of 0.5 eV for deep levels. The overbinding problem is less severe, affecting the formation energies by less than 10%.

For the purposes of the present paper, we define the formation energy  $E_{form}$  of a neutral defect, *e.g.*, a nitrogen vacancy, as

$$E_{form} = E[GaN : V_N] + E_{at}(N) + \mu(N) - E[GaN], \quad (1)$$

where  $E$  is the total energy of the supercell,  $E_{at}(N)$  is the total energy of the isolated N atom, and  $\mu$  is taken as the experimental cohesive energy of the solid [8] except for N, where we use the binding energy of  $N_2$ .

For charged defects, the formation energy depends on the position of the Fermi level  $E_F$  as

$$E_{form}(\Delta n) = E_{form}^0 - E_F \Delta n, \quad (2)$$

where  $E_{form}^0$  is the formation energy for the neutral defect, and  $\Delta n$  is its charge.

One should stress that the definition of the formation energy (1) is not unique, since it depends on the chemical potential(s) of the atom(s). These, in turn, depend on the conditions at which the defects form during growth, processing, or annealing. If the growing solid can be assumed to be in local equilibrium with other solid phases, one can constrain the variation of the chemical potential in (1) to a range determined by the difference in the cohesive energy of the compound and that of its elements [9, 10, 7]. In some cases, the assumption of a good quality material (*i.e.*, with a low concentration of defects), restricts the values of the chemical potential to a narrow range [7, 11].

Provided that the growth proceeds under quasi-equilibrium conditions, the concentration of a defect is given by

$$Conc = N_{sites} \exp(S_{form}/k_B - E_{form}/k_B T) \quad (3)$$

where  $N_{sites}$  is the number of available sites and  $S_{form}$  is the formation entropy. Usually, the formation entropy is in the range of 4-10  $k_B$  and the formation energy dominates.

It should be pointed out that the local equilibrium with competing solid phases may not be maintained. This is especially true if the growth process involves local excitations with ion sources and/or energetic beams, or specific kinetic conditions, *e.g.*, those corresponding to atomic layer epitaxy. In CVD, the use of complex precursors may also preclude the attainment of local equilibrium with the solid phases. In annealing experiments, the chemical potentials are determined by the nature and pressure of the gases in the annealing ampoule, rather than by equilibrium with the solid phases [11]. We postpone the investigation of these effects to a future publication and use equation (1) as a benchmark for an approximate comparison of the energetics of formation of various types of defects.

Turning to crystal symmetry issues, it is convenient to analyze the results obtained for the wurtzite structure in terms of zinc-blende symmetry with a superimposed hexagonal perturbation. In the zinc-blende structure, a substitutional defect, *e.g.*, a vacancy, has four equivalent nearest neighbors, which may be subject to both fully symmetric (breathing mode) and asymmetric relaxations. In the wurtzite structure, the atom along the  $c$  axis relative to the defect (called here type-1 neighbor) becomes inequivalent to the three remaining neighbors (called here type-2 neighbors). The lowering of the point symmetry is also reflected in the electronic structure: the defect states that are three-fold degenerate in the zinc-blende structure split into singlets and doublets in the wurtzite structure. In the following, we refer to such singlet and doublet pairs as quasi-triplets.

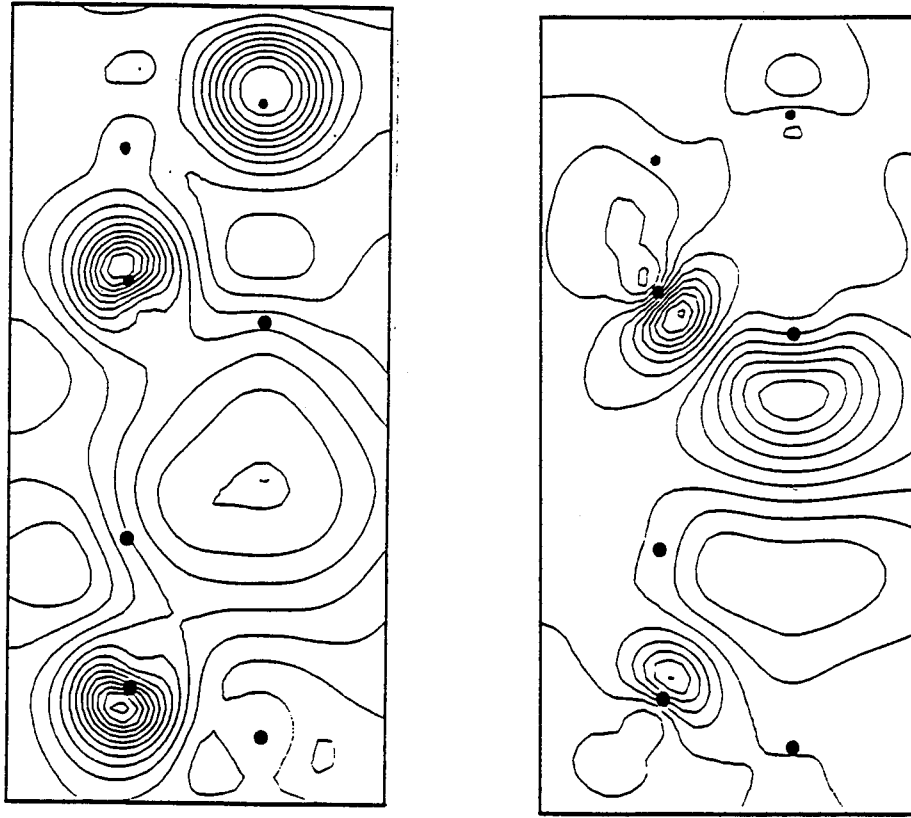


Figure 1: Contour plots of the wave functions of  $V_N$  a) the shallow donor state; and b) the conduction band resonance.

### 3. Native Defects in GaN

#### 3.1. Nitrogen vacancy

The nitrogen vacancy has long been thought to be the dominant native defect in GaN, responsible for the  $n$ -type character of as-grown crystals. Our results show that the neutral N vacancy is indeed a shallow donor, with a level just below the conduction band edge. The effective-mass character of this state follows not only from the position of its energy level, but also from its wave function, which is mainly built up from wave functions at bottom of the conduction band of the perfect GaN, see Fig. 1a. This is what one expects for a shallow donor state from the effective mass theory.

The dangling-bond-like quasi-triplet state expected for the vacancy is a resonance in the conduction bands. The hexagonal symmetry results in a 0.5 eV splitting, with the singlet being lower than the doublet. The singlet is located 0.8 eV above the bottom of the conduction band. In the dangling bond model of the vacancy, the quasi-triplet level, which would have held six electrons in the perfect GaN, should contain one electron once the vacancy was created by removing the five-valent N atom. However, since the quasi-triplet is a resonance, the electron autoionizes to the bottom of the conduction bands, where it forms an effective mass state bound by the Coulomb tail of the vacancy potential.

The lattice relaxation around  $V_N$  is not very pronounced. The Ga nearest neighbor shell relaxes outwards, by 0.407 and 0.125 a.u. for type-1 and type-2 neighbors, respectively. For the neutral vacancy, the energy gain is 0.38 eV and the computed formation energy becomes 4.8 eV. It will be strongly reduced in  $p$ -type material by electron transfer from its donor level to the Fermi level. In  $n$ -type GaN, the high formation energy of  $V_N$  would indicate that it cannot be formed in sufficient concentration to account for the  $n$ -type character of the as-grown material. However, the assumption of phase equilibrium during growth may not be valid for GaN, since MBE growth involves supplying highly excited  $N_2$  to the surface



( $N_2$  in its ground state is unreactive) which could result in N-deficient material. In CVD, thermal equilibrium should be easier to achieve, but thermal decomposition of TGM and ammonia may involve complicated intermediates, making simple formation energy estimates less reliable. Attainment of local equilibrium between the various solid phases also requires that the diffusion rate in the surface layers be faster than the deposition rate. At this time little is known about the mechanisms of growth of GaN, and thus the reliability of formation energy arguments cannot be assessed.

Recent high-pressure measurements in as-grown *n*-type GaN show that when high pressure is applied, the electrons that were initially in the conduction bands become localized [12]. This result indicates the presence of a resonant state in the conduction bands that emerges into the forbidden gap as the bottom of the conduction bands moves up with pressure. The electrons in the conduction bands would then become trapped in the just emerged deep level, rendering the sample insulating. We have performed calculations for  $V_N$  under pressure, and found that the quasi-triplet indeed emerges into the gap in agreement with the experimental data. The wave function of the lower (singlet) level is shown in Fig. 1b. Additional results regarding the pressure calculations will be published elsewhere.

Obviously, further data are needed for a final identification, but the good agreement between the theoretical and experimental results suggests that N vacancies are present in the samples of Ref. [12].

### 3.2. Gallium Vacancy

Since the formation of the Ga vacancy creates N dangling bonds, its levels should be close to the top of the valence bands. Indeed, the quasi-triplet is located about 0.4 eV above the valence bands edge, and the hexagonal splitting is only 0.1 eV. Since the quasi-triplet is populated by 3 electrons in the neutral charge state,  $V_{Ga}$  can trap both electrons and holes. In spite of the proximity to the valence band, the quasi-triplet wave functions are very localized. The wave function of the singlet is composed mainly of the  $p_z(N)$  orbital of the type-1 neighbor. The contributions of the type-2 neighbors are smaller by an order of magnitude. The wave functions of the doublet are built up from the  $p(N)$  orbitals of the type-2 neighbors. In this case, the contribution of the type-1 neighbor is negligible.

The formation energy of the neutral  $V_{Ga}$  is very high, 8 eV. However, since  $V_{Ga}$  can release or accept three electrons, its formation energy depends very strongly on the position of the Fermi level. In particular, in *n*-type samples the formation energy of  $V_{Ga}^-$  may become very low. The thermodynamic levels for 0/-, -/2-, and 2-/3- transitions are at 0.5, 0.8, and 1.3 eV above the top of the valence band, respectively.

### 3.3. Nitrogen antisite, $N_{Ga}$

In the neutral charge state,  $N_{Ga}$  introduces a doubly occupied singlet at  $E_v+0.4$  eV, and an empty doublet at  $E_c-0.2$  eV. For both levels, the contribution of the type-1 neighbor is about 5 times smaller than those of type-2 neighbors. However, the singlet and the doublet do not originate from one quasi-triplet. In the initial unrelaxed configuration, there is a resonant quasi-triplet located at 0.3 eV above the bottom of the conduction band, with a vanishing hexagonal splitting. After relaxation, the splitting becomes 2.3 eV and the doublet moves to  $E_c-0.2$  eV.

The dominant contribution of the type-1 neighbor is due to a strong distortion of  $N_{Ga}$  along the *c* axis. Specifically, the bond distance to the type-1 neighbor is reduced by 29% (from 3.70 to 2.62 a.u.) and becomes comparable with the bond length in the  $N_2$  molecule, 2.07 a.u. Due to the distortion, the remaining bond lengths increase by 11%. The relaxation energy is 0.6 eV.

The formation energy of the neutral  $N_{Ga}$  is 7.3 eV. This value can be slightly reduced in strongly *p*-type samples, due to electron transfer to the Fermi level. The empty doublet at  $E_c-0.2$  eV cannot be occupied even by one electron, due to the large value of the electron-electron repulsion parameter for this level (0.95 eV).

### 3.4. Gallium antisite, $\text{Ga}_N$

The gallium antisite introduces a quasi-triplet close to the middle of the band gap. In the neutral charge state, the singlet at  $E_v+1.4$  eV and the doublet at  $E_v+2.1$  eV contain two electrons each. The wave function of the singlet is mainly a bonding combination of the  $p_z$  orbitals of  $\text{Ga}_N$  with the orbitals of the type-1 neighbor. Similarly, the doublet is mainly a bonding combination of  $p_{x,y}$  of  $\text{Ga}_N$  with  $p$  orbitals of the type-2 neighbors. However, the  $p$  orbitals from the second neighbor N atoms contribute considerably to both the singlet and the triplet.

As expected, we find an outward relaxation around  $\text{Ga}_N$ , with a large relaxation energy of 3.9 eV. The bond lengths with type-1 and type-2 neighbors are 4.12 and 4.27 a.u., respectively. The formation energy of  $\text{Ga}_N$  in the neutral state is 6.0 eV, but it is reduced strongly in highly doped samples due to electron transfer to/from the Fermi level.

### 3.5. Interstitials

For substitutional defects, the local topologies of zinc-blende and wurtzite lattices are similar, since in both cases each atom has four first neighbors with tetrahedral symmetry. The difference between the two structures begins at the second shell of neighbors. This is why the electronic structures of vacancies and interstitials in both structures are similar. In contrast, the local topologies of interstitials are quite different in the two lattices. In zinc-blende crystals there are two interstitial sites with tetrahedral symmetry, surrounded by four cations and four anions, respectively. In the wurtzite structure, there are two high-symmetry interstitial positions, referred to as 'tetrahedral' ( $T$ ) and 'octahedral' ( $O$ ) in the literature [13]. These terms are misleading, since they do not correspond to the actual point group symmetry, which is  $C_{3v}$  in both cases. In the ideal wurtzite lattice, an atom at the  $O$  site has six first neighbors, three cations and three anions. An atom at the  $T$  site has two first neighbors, one cation and one anion, and six second neighbors (three anions and three cations). Due to the point symmetry, neither  $T$  nor  $O$  can be the equilibrium position of an interstitial defect, except by accident. In particular, a relaxation along the  $c$  axis is expected.

Indeed, we find that both  $T$  and  $O$  positions are highly unstable for native interstitials. The interstitials move towards the first neighbor of the same kind. For the N interstitial, starting from both  $T$  and  $O$  positions leads to the same final configuration. At present, we are investigating whether an analogous effect also holds for the Ga interstitial.

After relaxation,  $\text{N}_I$  assumes a bridge-bond configuration similar to the bridge-bond geometry of As interstitial in GaAs, as discussed by Chadi [14]. The N-N bond length is 2.64 a.u., which is very close to the N-N distance in the case of  $\text{N}_{\text{Ga}}$ . Both N atoms move off the  $c$ -axis, and the resulting configuration is asymmetric. The relaxation energy is 7.6 eV, due to interstitial motion of over 2 a.u. Considering the electronic structure,  $\text{N}_I$  introduces two closely spaced deep levels at about  $E_v+1.0$  eV, separated by 0.06 eV. Both are built up from the orbitals of the N-N pair and are occupied by three electrons. The formation energy of  $\text{N}_I^0$  is 2.9 eV, but it will be strongly reduced in highly doped samples.

The  $\text{Ga}_I$ , initially at the  $T$  position, undergoes a displacement of 1.2 a.u., which leads to an energy gain of 8.9 eV. As mentioned above, the equilibrium configuration is similar to the bridge-bond geometry of interstitial Ga found by Chadi, but in GaN both Ga atoms are exactly along the  $c$  axis. The Ga-Ga distance is 4.17 a.u., which is close to the average Ga-Ga distance for  $\text{Ga}_N$ .

Turning to the electronic structure,  $\text{Ga}_I^0$  introduces a deep level at  $E_v+0.5$  eV, occupied by two electrons, and a resonance at  $E_c+0.8$  eV. The remaining Ga electron autoionizes from the resonance and is trapped in a shallow, effective mass state. The deep  $\text{Ga}_I$  state is composed of displaced host Ga orbitals and the three N neighbors. The formation energy of a neutral  $\text{Ga}(T)$  is 5.1 eV, but it will be strongly reduced in p-type samples.

#### 4. Vacancies in AlN

We have extended the computations to the second important nitride, AlN, and considered both vacancies. Their electronic structures and formation energies are very close to the corresponding values in GaN. Specifically,  $V_{Al}^0$  introduces a quasi-triplet at  $E_v+0.4$  eV, split by 0.05 eV. It is occupied by 3 electrons. Its formation energy is 8.05 eV, which is smaller by 0.05 eV from that of  $V_{Ga}^0$ .  $V_N$  introduces a quasi-triplet at  $E_c+0.2$  eV. The hexagonal splitting is 0.6 eV and the singlet is below the bottom of the conduction band. The formation energy of  $V_N^0$  is 5.4 eV, compared to 5.0 eV in GaN.

#### 5. Summary

We have calculated the electronic structure and formation energies of native defects in wurtzite GaN by *ab initio* molecular dynamics. In most cases, the relaxation around the defect is substantial, strongly influencing the energy levels and formation energies. This is particularly true for interstitials. We have investigated two possible high-symmetry interstitial sites, the so-called *T* and *O*. In these high-symmetry positions both Ga and N interstitials are highly unstable. After a displacement of 1-2 a.u., both atoms form split interstitial configurations that are lower in energy by 5-9 eV. Due to the large value of the forbidden gap, formation energies depend strongly on the position of the Fermi level. The low-formation energy defects are  $V_{Ga}$ ,  $Ga_N$ , and  $N_I$  in n-type samples, and  $V_N$ ,  $Ga_N$ ,  $Ga_I$ , and  $N_I$  in p-type samples. Our results confirm the widely held hypothesis that  $V_N$  is a shallow donor, which may be responsible for the n-type character of as-grown GaN. We have also considered common dopants and contaminants in GaN and AlN. The results of these investigations will be presented elsewhere.

This work is supported by ONR and NSF.

#### 6. References

1. R. F. Davis, *Physica B* **185**, 1 (1993).
2. S. Strite and H. Morkoc, *J. Vac. Sci. Technol. B* **10**, 1237 (1992).
3. R. Car and M. Parrinello, *Phys. Rev. Lett.* **55**, 2471 (1985).
4. G. Li and S. Rabii, preprint.
5. G. B. Bachelet, D. R. Hamann, and M. Schluter, *Phys. Rev. B* **26**, 4199 (1982); X. Gonze, R. Stumpf, and M. Scheffler, *Phys. Rev. B* **44**, 8503 (1991).
6. R. W. L. Lambrecht and B. Segall, *Mat. Res. Soc. Symp. Proc.* **242**, 367 (1992); V. Fiorentini, M. Methfessel, and M. Scheffler, *Phys. Rev.* **47**, 13353 (1993); K. Miwa and A. Fukumoto, *Phys. Rev. B* **48**, 7897 (1993).
7. C. Wang, Q.-M. Zhang, and J. Bernholc, *Phys. Rev. Lett.* **69**, 3789 (1992).
8. C. Kittel, *Introduction to Solid State Physics*, Wiley and Sons, New York (1986).
9. S. B. Zhang and J. E. Northrup, *Phys. Rev. Lett.* **67**, 2339 (1991).
10. D. B. Laks, C. G. Van De Walle, G. F. Neumark, and S. T. Pantelides, *Phys. Rev. Lett.* **66**, 648 (1991).
11. B. Chen, Q.-M. Zhang, and J. Bernholc, *Phys. Rev. B* **49**, 2985 (1994).
12. P. Perlin, H. Teyssie, and T. Suski, to be published.
13. R. Boyn, *Phys. Stat. Solidi (b)* **148**, 11 (1988). M. A. Robertson and S. K. Estreicher, *Mat. Res. Soc. Symp. Proc.* **242**, 355 (1992), denote these sites by *T* and *R*, respectively.
14. J. D. Chadi, *Phys. Rev. B* **46**, 9400 (1992).

## XXII. Theory of Native Defects and of Carbon Doping in Wurtzite GaN

### Abstract

The results of an extensive theoretical study of point native defects and substitutional carbon in GaN are summarized. The computations were carried out using quantum molecular dynamics, in supercells containing 72 atoms. Both the N vacancy and the interstitial Ga introduce shallow donor levels that may be responsible for the *n*-type character of as-grown GaN.

### 1. Introduction

Gallium nitride together with other wide gap nitrides hold substantial promise for electronic applications [1, 2]. In order to improve the quality of the material, the role of native defects needs to be understood. This is because the quality of a semiconductor is largely determined by the nature and number of its native defects, an issue particularly important in light-emitting applications, where a presence of recombination centers could lead to severe degradation effects.

Here, we summarize the results of our study of native defects and impurities in GaN. We focus on the electronic structure, formation energies, and identification of the dominant native defects. A more complete discussion will be published elsewhere [3]. We also present the results for the substitutional C impurity.

### 2. Theoretical Method

The calculations were carried out using *ab initio* molecular dynamics [4], the local density approximation, and non-local atomic pseudopotentials. The plane wave cutoff was 30 Ry. We used large supercells containing 72 atoms + defect. All atoms were relaxed using a fast relaxation procedure [5]. Details of the calculations, comparison with previous calculations [6], and other results concerning vacancies and interstitials were presented elsewhere [7].

The formation energy of a defect in a charge state  $\Delta n$  is given by

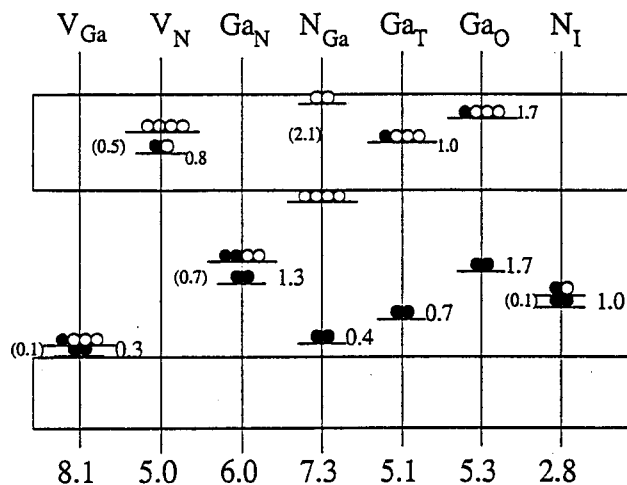
$$E_{form}(\Delta n) = E_{tot}(\Delta n) - n_{Ga}\mu_{Ga} - n_N\mu_N - \Delta n E_F, \quad (1)$$

where  $E_{tot}$  is the total energy of the supercell with defect,  $n_{Ga}$  and  $n_N$  are the number of Ga and N atoms,  $\mu_{Ga}$  and  $\mu_N$  are the chemical potentials, and  $E_F$  is the Fermi energy. Here, we use the chemical potentials of metal Ga and the  $N_2$  gas.

### 3. Vacancies and Antisites

Our results are summarized in Fig. 1, which shows both the energy level scheme and, at the bottom of the Figure, the calculated formation energies. The defect states that are three-fold degenerate in the zinc-blend structure split into singlets and doublets due to the wurtzite symmetry. In such cases, we give in Fig. 1 the

Figure 1. Energy levels in eV (in parentheses: hexagonal splittings), and formation energies in eV of native defects in GaN (bottom line).



energy of the lower level, and in parentheses the value of the splitting. In the following, we refer to such singlet and doublet pairs as quasi-triplets. The quoted  $E_{form}$  may be modified by two factors: (i) a possible transfer of electron(s) to/from the Fermi level, which lowers  $E_{form}$ , and (ii) a change of the chemical potentials, which are determined by the actual growth conditions.

**Gallium vacancy.** The Ga vacancy introduces a quasi-triplet located at about 0.4 eV above the valence bands edge, with hexagonal splitting of only 0.1 eV. Since the quasi-triplet is populated by 3 electrons in the neutral charge state,  $V_{Ga}$  can trap both electrons and holes. The formation energy of the neutral  $V_{Ga}$  is high, 8 eV.

**Nitrogen vacancy.** The dangling-bond-like quasi-triplet state expected for a vacancy is a resonance in the conduction band. For the neutral vacancy, the one electron occupying the resonance autoionizes to the bottom of the conduction band, where it forms an effective mass state bound by the Coulomb tail of the vacancy potential. The computed formation energy is 5 eV.

**Gallium antisite,  $Ga_N$ .** The gallium antisite introduces a quasi-triplet close to the middle of the band gap. In the neutral charge state, the singlet at  $E_v+1.4$  eV and the doublet at  $E_v+2.1$  eV contain two electrons each. The formation energy of  $Ga_N$  in the neutral state is 6.0 eV.

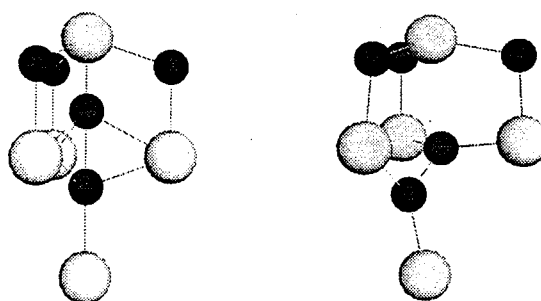
**Nitrogen antisite,  $N_{Ga}$ .** In the neutral charge state,  $N_{Ga}$  introduces a doubly occupied singlet at  $E_v+0.4$  eV, and an empty doublet at  $E_c-0.2$  eV. The formation energy of the neutral  $N_{Ga}$  is 7.3 eV. The empty doublet at  $E_c-0.2$  eV cannot be occupied even by one electron, due to the large value of the electron-electron repulsion parameter for this level (0.95 eV).

Recently, native defects in GaN were studied also by Neugebauer and Van De Walle [8], who obtain comparable results both for vacancies and antisites.

#### 4. Interstitials

In the wurtzite structure, there are two high-symmetry interstitial positions, referred here to as  $T$  and  $O$ . The point symmetry is  $C_{3v}$  in both cases. In the ideal wurtzite lattice, an atom at the  $O$  site has six first neighbors, three cations and three anions. An atom at the  $T$  site has two first neighbors, one cation and one anion, and six second neighbors (three anions and three cations).

Figure 2. Initial and relaxed configuration for the interstitial N(*T*).



We find that the *T* position is highly unstable for native interstitials, which move towards the first neighbor of the same kind. In equilibrium, both Ga(*T*) and N(*T*) assume bridge-bond configurations, similar to the bridge-bond geometry of self-interstitials in GaAs [9]. Moreover, for the N interstitial, starting from both *T* and *O* positions leads to the same final configuration.

The relaxed configuration of  $N_I$  is shown in Fig. 2. Both N atoms move off the *c*-axis, and the resulting configuration is asymmetric. Considering the electronic structure,  $N_I$  introduces two closely spaced deep levels at about  $E_v+1.0$  eV, separated by 0.1 eV. The formation energy of  $N_I^0$  is 2.9 eV. For this defect, a similar structure of energy levels but a higher  $E_{form}$  was found in [8].

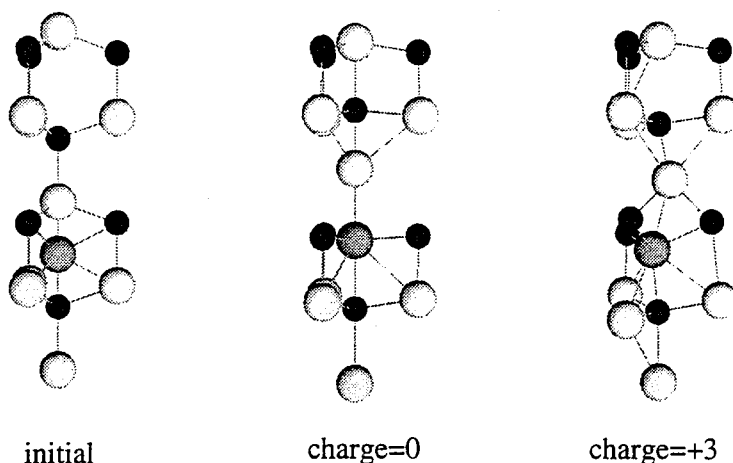


Figure 3. Initial and relaxed configurations for the interstitial Ga(*T*).

Figure 3 shows the relaxation of the interstitial Ga, placed initially at the *T* site. As follows from the figure, the equilibrium configuration depends strongly on the charge state. In particular, for  $\Delta(n)=+3$  the relaxation breaks the  $C_{3v}$  symmetry, and Ga(*T*) moves off the *c* axis. Turning to the electronic structure,  $Ga_T^0$  introduces a deep level at  $E_v+0.5$  eV, occupied by two electrons, and a resonance at  $E_c+0.8$  eV. The electron that should occupy the resonance autoionizes and is trapped in an effective mass state. According to our results Ga(*T*) is a negative-U system: the charge state +2 is unstable, i.e., the gap state will be populated by two electrons or it will be empty. The formation energy of a neutral Ga(*T*) is 5.1 eV.

The *O* site is a locally stable position for Ga interstitial, and we find only a weak breathing-mode relaxation of its nearest neighbors. The formation energy and the energy level scheme are close to that of Ga(*T*), see Fig. 1.

## 5. Dominant Defects

The calculated formation energies were used to study stoichiometry effects and defect concentrations in GaN. For the high-temperature growth at Ga-rich conditions (used to obtain bulk samples [10]) we find that the dominant defects are  $V_N$ , Ga(I), and N(I); their relative abundances are dependent on the external doping. A detailed discussion of this issue will be published elsewhere [3].

Comparison of our findings with experimental data must be tentative, since no native defects in GaN have been unambiguously identified at present. The nitrogen vacancy is considered to be the dominant native defect in GaN, responsible for the  $n$ -type character of as-grown crystals [11]. Our results are consistent with this conjecture. In particular, we find that the neutral N vacancy is indeed an effective-mass donor. Furthermore, recent high-pressure measurements [10] in as-grown  $n$ -type GaN indicate a presence of a resonant state in the conduction band that emerges into the forbidden gap as the bottom of the conduction band moves up with pressure. We have performed calculations for  $V_N$  under pressure [3], and found that the quasi-triplet indeed emerges into the gap in agreement with the experimental data.

However, the experimental facts above may be explained by the presence of Ga(I), which also is a shallow donor with a resonance in the conduction band. Pressure calculations for this defect are in progress.

## 6. Amphoteric C impurity

In GaN, the group-IV element C may substitute for either Ga or N. We have considered both possibilities, finding that  $C_N$  is a shallow acceptor, with a low formation energy of 1.5 eV, while  $C_{Ga}$  is a shallow donor, with a higher  $E_{form}=4.1$  eV. In the latter case, the DX-like configuration of  $C^-$  is metastable. Due to the relatively low values of  $E_{form}$ , the substitutional C may be amphoteric, with the possibility of self-compensation.

The calculations were performed at the Pittsburgh Supercomputing Center, and at ICM, Warsaw University. This work is supported in part by Grants ONR N00014-92-J-1477, NSF DMR-9408437, and KBN 2-P302-124-07.

## References

1. R. F. Davis, *Physica B* **185**, 1 (1993).
2. S. Strite and H. Morkoc, *J. Vac. Sci. Technol. B* **10**, 1237 (1992).
3. P. Boguslawski, E. Briggs, and J. Bernholc, to be published.
4. R. Car and M. Parrinello, *Phys. Rev. Lett.* **55**, 2471 (1985).
5. Q. Zhang, J.-Y. Yi, and J. Bernholc, *Phys. Rev. Lett.* **66**, 2633 (1991).
6. R. W. L. Lambrecht and B. Segall, *Mat. Res. Soc. Symp. Proc.* **242**, 367 (1992); V. Fiorentini, M. Mathfessel, and M. Scheffler, *Phys. Rev.* **47**, 13353 (1993); K. Miwa and A. Fukumoto, *Phys. Rev. B* **48**, 7897 (1993).
7. P. Boguslawski, E. Briggs, T.A. White, M. G. Wensell, and J. Bernholc, *Mat. Res. Soc. Symp. Proc.* **339**, ed. C. Carter, G. Gildenblat, S. Nakamura, and R.J. Nemanich, in print.
8. J. Neugebauer and C. Van De Walle, *Phys. Rev.*, to appear.
9. J. D. Chadi, *Phys. Rev. B* **46**, 9400 (1992).
10. P. Perlin, H. Teissyre, T. Suski, M. Leszczynski, I. Grzegory, J. Jun, and S. Porowski, this conference.
11. E.R. Glaser *et al.*, *Appl. Phys. Lett.* **63**, 2673 (1993), and the references therein.

## XXIII. Reactive Ion Etching of GaN, AlN and InN

### A. Introduction

Semiconductor devices are the principle components of electronic and telecommunications systems [1]. In order to densely pack these microscopic components, unidirectional, or anisotropic, etching techniques are required to produce a fine network of uniformly thick lines. Wet etching processes found in many semiconductor manufacturing steps produce a multi-directional, or isotropically, etched features with variable thickness through its depth. This is undesirable for microcircuitry since the goal is to produce the smallest devices possible. Therefore, plasma-assisted processes, such as reactive ion etching (RIE), combine the physical characteristics of sputtering with the chemical activity of reactive species to produce a highly directional feature. RIE has the added advantage of providing a more uniform etch and a higher degree of material etch selectivity.

RIE has been employed to etch a wide variety of semiconductor materials including silicon-based materials [2-11], metals, like aluminum [7, 12-18] and III-V compounds, such as GaAs and InP [19-21]. Plasma-assisted etching of newer III-V compounds, such as GaN, AlN and InN, has also been investigated in depth by Pearton *et al.* [22-27] and other investigators [20, 21, 28-31]. There has been wide spread interest in using these nitrides for semiconductor device applications requiring visible light emission, high temperature operation and high electron velocities. Since these materials possess wide bandgaps and optical emissions spectra in the blue to near ultraviolet range, they are prime candidates for ultraviolet detection devices.

The objectives of this report are to discuss recent progress made in the field of reactive ion etching of gallium, aluminum and indium nitride. In the following sections, a brief review of pertinent literature on plasma-assisted etching of III-V nitride compounds is provided along with a description of the reactive ion etching system, choice of process gases and results to date.

### B. Literature Review

*Etching of GaN.* Since GaN is a direct transition material with a bandgap ranging from 3.4-6.2 eV at room temperature, it is an ideal candidate for the fabrication of shortwave length light emitters [20, 32]. High quality GaN films have been successfully grown by MOVPE [32], ECR-MBE [33, 34], MOCVD [35] and a layer-by-layer process [36] on a number of substrate. In order to fabricate complete device structures, reliable etching processes need to be developed. Though wet etchants for GaN have been employed, including NaOH/H<sub>2</sub>O [23, 37] and hot H<sub>3</sub>PO<sub>4</sub> [37-40], patterning for device fabrication with wet etchants has not been studied or characterized. Thus, RIE is an effective method for the production of fine line



patterning in GaN and does not involve direct exposure to heated, concentrated acid and base solutions.

There have been many reports of etching GaN by plasma-assisted processes in the past few years [20-23, 25, 27-31]. The more conventional technique of plasma etching of III-V nitrides, i.e. reactive ion etching, has been employed by several research groups [21-23, 25, 28, 31]. Fairly high etch rates have been attained with chlorine-based plasmas, as shown in Table I. In the chlorine-based plasmas, the higher etch rates are the result of more active Cl species diffusing to the nitride surface. Thus, as the pressure increases more Cl species are available for reaction and the etch rates increase (as shown in the case for BCl<sub>3</sub>/Ar plasma). The addition of H<sub>2</sub> to a Cl<sub>2</sub> plasma is believed to tie up nitrogen atoms on the surface as volatile NH<sub>x</sub>, resulting in increased etch rates with increasing H<sub>2</sub> flow rates [23]. In addition, there is evidence from auger electron spectroscopy (AES) [25, 28, 31] that GaN surface remains stoichiometric after etching and that Cl species are completely reacted and removed. The AES results from these studies concurrently showed that the concentration of oxygen had increased after etching, probably the result of oxygen diffusion to the damaged surface. The source of

Table I. Etch Rate Parameters for RIE of GaN.

Maximum Etch Rate (Å/min)	Plasma Gases	Pressure (mtorr)	Power* (watts)	DC Bias (-V)	Ref.
175	BCl <sub>3</sub> /Ar	1	200 (MW)	250	[23]
510	BCl <sub>3</sub> /Ar	50	200 (RF)	NM <sup>#</sup>	[31]
750	Cl <sub>2</sub> /H <sub>2</sub>	1	1000 (MW)	150	[25]
200	Cl <sub>2</sub> /H <sub>2</sub>	1	200 (MW)	150	[25]
200	CCl <sub>2</sub> F <sub>2</sub> /Ar	1	200 (MW)	250	[23]
139	CCl <sub>2</sub> F <sub>2</sub> /Ar	20	40 (RF)	NM	[21]
80	CH <sub>4</sub> /H <sub>2</sub> /Ar	1	200 (MW)	300	[23]
350	CH <sub>4</sub> /H <sub>2</sub> /Ar	1	1000 (MW)	250	[25]
500	SiCl <sub>4</sub> /Ar	20	NM	400	[28]
330	SiCl <sub>4</sub> /Ar	50	200 (RF)	NM	[31]

\* MW designates a microwave power supply, whereas RF designates a radio frequency power supply.

# NM designates a parameter that was not mentioned in the reference.

oxygen was not elucidated, however, water vapor present in the vacuum system may account for a reaction with the GaN surface. Lastly, Adesida *et al.* [28] have demonstrated that fluorine plasmas are impractical to use as etchant gases due to the formation of involatile fluorides with Ga, Al and In at the surfaces. Addition of a fluorine-containing gas ( $\text{SiF}_4$ ) was added to their  $\text{SiCl}_4$  plasma to facilitate removal of atomic nitrogen from the surface. As expected, this addition had no effect on the etch rate probably due to the competitive formation of  $\text{GaF}_x$  and volatile  $\text{GaCl}_x$  at the surface.

Methane-based plasmas have been employed [23, 25] because of the speculation that methyl species and group III metal atoms, in this case Ga, will form a volatile metalorganic compound, such as trimethylgallium. Unfortunately, there is no mass spectrometer data to support this hypothesis. In general, etch rates of GaN are slow, as compared to chlorine-based plasmas, and a DC bias of about -175 V is required for initiation of the surface reaction.

More novel approaches to etching GaN have also been employed. Reactive fast atom beam etching was employed early on by Tanaka *et al.* [20] to etch GaN on sapphire in a  $\text{Cl}_2$  plasma at substrate temperatures ranging between 80-150°C during etching. Etch rates of up to 1000-1200 Å/min produced relatively smooth surfaces and a well defined pattern of elongated rectangular bars. More recently, Adesida *et al.* [30] have employed chemically assisted ion beam etching to etch GaN with an Ar beam in a  $\text{Cl}_2$  gas ambient. Results of their work should be available in the near future. Lastly, Pearton *et al.* [27] have employed a novel processing technique, called sidewall-etchback processing, to fabricate nanostructures of GaN as small as 300 Å wide. This technique involves the following steps: photolithography of defined photoresist features, deposition of a thin (300-1000 Å) layer of mask material (dielectric or metal) over the photoresist features, anisotropic etching of the mask material leaving the vertical sidewalls intact, removal of the photoresist and anisotropic etching of the underlying GaN film. Dry etching in a  $\text{CH}_4/\text{H}_2/\text{Ar}$  plasma (1 mtorr, -200 Vdc, 350 W microwave power) was employed to etch the GaN film slowly to preserve the integrity of the circular nanostructures. The etch-back technique is an important tool allowing one to produce sub-micron features without requiring advanced photolithography processing.

*Etching of AlN.* Aluminum nitride is a candidate material for optoelectronic devices because it possess a high electrical resistivity, high thermal conductivity, low dielectric constant and has a direct transition bandgap of 6.3 eV [41]. AlN films have been grown by several techniques including CVD, MBE and ALE, and on a variety of substrate materials including sapphire, silicon, spinel, silicon carbide and quartz [42]. Etching fine features in the AlN films is an important step in the fabrication of such devices. AlN has been wet etched for various applications including synthesis of AlN powders from nitrided steels etched in  $\text{FeCl}_3$  [43] and development of piezolayer field effect transistors employing phosphoric acid [44]. In addition, mention of wet etchants, including  $\text{NH}_4\text{F}$ -based solutions [45, 46], NaOH solutions [47], hot

H<sub>3</sub>PO<sub>4</sub> [48] and several other strong acids and bases [49], can be found in several Japanese patents regarding device fabrication.

There have been a few reports of etching AlN in chlorine-based and methane-based plasmas by Pearton *et al.* [22, 23, 25]. High etch rates have been attained, as shown in Table II, especially for Cl<sub>2</sub>/H<sub>2</sub> plasmas. As the case is for GaN, an increase in pressure produces an increase in the etch rate as a result of a high concentration of Cl at the nitride surface. In addition, the morphology of the etched surfaces becomes more smooth as the flow of H<sub>2</sub> is increased. This effect is thought to be the result of more efficient removal of the nitrogen etch product from the surface [25]. However, a threshold bias of about -100 V is required for removal of the native oxide and initiation of a surface reaction [23]. Examination of the AlN surfaces before and after etching, using AES, revealed no change in the stoichiometry, but a 2% atomic concentration of Cl was found on the surface. This would seem to indicate that slightly higher surface temperatures are necessary for complete removal of the AlCl<sub>x</sub> species.

Table II. Etch Rate Parameters for RIE of AlN.

Maximum Etch Rate (Å/min)	Plasma Gases	Pressure (mtorr)	Microwave Power (watts)	DC Bias (-V)	Ref.
110	BCl <sub>3</sub> /Ar	1	200	250	[23]
200	CCl <sub>2</sub> F <sub>2</sub> /Ar	1	200	300	[23]
25	CH <sub>4</sub> /H <sub>2</sub> /Ar	1	200	300	[25]
300	CH <sub>4</sub> /H <sub>2</sub> /Ar	1	1000	250	[25]
550	Cl <sub>2</sub> /H <sub>2</sub>	1	200	150	[25]
1100	Cl <sub>2</sub> /H <sub>2</sub>	1	1000	150	[25]

*Etching of InN.* Indium nitride also has a direct bandgap of 1.9 eV making it a promising candidate for visible light optoelectronic devices and high efficiency, low cost solar cells. Since the InN growth system is coming on line in our labs, it is desirable to be able to etch InN and fabricate patterned device structures. At the current time, wet etching has been accomplished by exposing (0001) InN samples to NaOH/H<sub>2</sub>O and KOH/H<sub>2</sub>O solutions at temperatures between 20-60°C [50]. Etch rates of up to 600 Å/min and 300 Å/min at 60°C in KOH and NaOH,

respectively, were achieved. Smooth surfaces free of etch pits were obtained, but no patterning was demonstrated.

Reactive ion etching has recently been employed to etch InN. Pearton *et al.* [22, 23, 25] have been conducting reactive ion etching on InN at low pressures (1-30 mtorr) in ECR discharges of chlorine- and methane based plasmas. Fairly high etch rates were attained at low pressure and high DC bias, as shown in Table III. With regard to chlorine-based plasmas, InN has a lower etch rate than GaN or AlN which can be attributed mainly to the low volatility of the  $\text{InCl}_x$  species at normal cathode temperatures (around 25°C). Though significant heating of the samples can occur during etching by ion bombardment, the temperature of the samples surface is not high enough for the  $\text{InCl}_x$  species to become volatile. The result is a rough, In-rich surface. AES results from Pearton's work [25] showed a nitrogen deficiency on the etched surface in addition to 6% atomic concentration of chlorine probably due to incomplete reaction of Cl radicals with In atoms on the nitride surface. Interestingly enough, since the chlorine-based plasma produces fairly slow etch rates, relative to GaN and AlN, layers of InN could be used as etch stops for etching AlGaIn/GaN heterostructures. Methane-based plasmas, on the other hand, require significant DC bias to obtain comparable etch rates (as compared to etch rates attained in Cl-based plasmas), i.e. a threshold bias of -175V was required before etch rates of 300 Å/min were attained [25]. High biases may induce significant damage to the surface, a characteristic that is undesirable for optimal device performance.

Table III. Etch Rate Parameters for RIE of InN.

Maximum Etch Rate (Å/min)	Plasma Gases	Pressure (mtorr)	Power* (watts)	DC Bias (-V)	Ref.
175	$\text{BCl}_3/\text{Ar}$	1	200	300	[23]
300	$\text{Cl}_2/\text{H}_2$	1	200	300	[24]
190	$\text{CCl}_2\text{F}_2/\text{Ar}$	1	200	300	[24]
100	$\text{CH}_4/\text{H}_2/\text{Ar}$	1	200	300	[24]
350	$\text{CH}_4/\text{H}_2/\text{Ar}$	1	1000	250	[24]

*Etching of Ternary Compounds.* A low pressure (1 mtorr) ECR plasma discharge was employed by Pearton *et al.* [26] for reactive ion etching on  $\text{In}_x\text{Ga}_{1-x}\text{N}$  and  $\text{In}_x\text{Al}_{1-x}\text{N}$  compounds. Etch rates were fairly high ( $\approx 200$ -350 Å/min) over the entire composition range even at high microwave power (1000 W) and DC bias (-250 V) when using a  $\text{CH}_4/\text{H}_2/\text{Ar}$

plasma, and a slight increase in the etch rate (up to  $\approx 400 \text{ \AA/min}$ ) was observed with increasing In mole fraction. This behavior, Pearton believes, is a result of the In-methyl etch product being more volatile than its Ga- and Al-methyl counterparts. Smooth surfaces and anisotropically etched features were observed over the whole range of composition. Higher etch rates were obtained for  $\text{Cl}_2/\text{H}_2$  and  $\text{Cl}_2/\text{SF}_6$  plasmas for low In mole fraction. As the In mole fraction increased from 0% (all GaN and all AlN) to 100% (all InN), the corresponding etch rates dropped from 1000  $\text{\AA/min}$  and 700  $\text{\AA/min}$ , for  $\text{In}_x\text{Al}_{1-x}\text{N}$  and  $\text{In}_x\text{Ga}_{1-x}\text{N}$  respectively, to 200  $\text{\AA/min}$ . Again, this result is expected since at high In mole fraction the  $\text{InCl}_x$  species are more difficult to remove from the surface at normal cathode temperatures. More recently, Adesida *et al.* [30] have reported on reactive ion etching and chemically assisted ion beam etching of GaAlN. Details of their work have not yet been published.

### C. Experimental Procedure

**Experimental Apparatus.** A schematic of the reactive ion etching system is shown in Fig. 1. The main components of the system include gas handling/storage, etcher, gas scrubber and mass spectrometer. Since toxic gases, such as  $\text{BCl}_3$  and  $\text{Cl}_2$ , may be used to etch GaN and AlN, the system is designed for safe shutdown in the event of a power or water failure and/or inadvertent shutdown of the exhaust systems in the building.

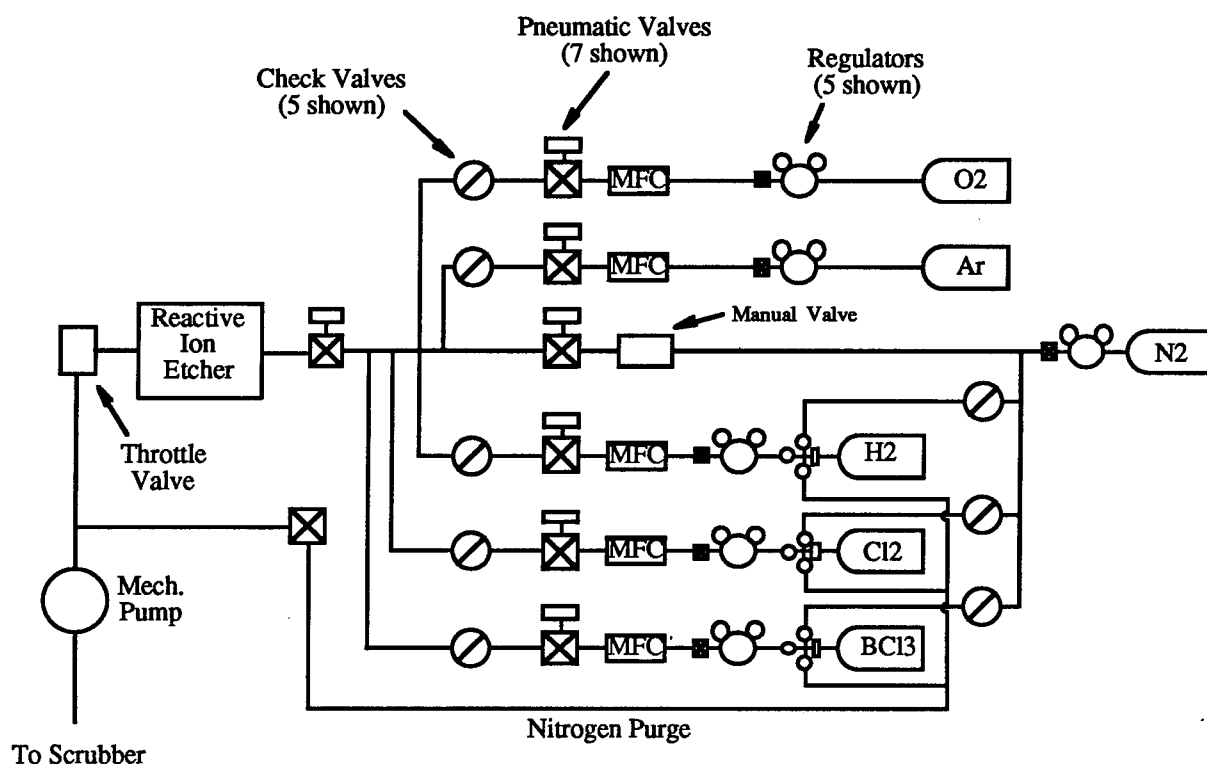


Figure 1. Schematic diagram of the reactive ion etching system.

The gas handling/storage sub-system consists of the gas storage cabinets, gas bottles, bottle regulators and necessary valves and tubing. Dry nitrogen is used to purge the gas lines before and after every run to remove moisture and chlorine from the lines, thus reducing the probability of corrosion of the gas lines. Mass flow controllers are employed for accurate control of the process gases. In the event of a power failure, interruption of the water supply or shutdown of the exhaust system, the solenoid actuated pneumatic valves will isolate the gas lines from the etch chamber.

The design of the etcher is based on that of the standard parallel-plate diode configuration, Fig. 2, in which the bottom electrode is powered by a RF power supply. The electrical potential applied across the parallel plate configuration results in ionization of the gas molecules, creating a plasma of neutrals, ions and electrons. The etcher, a Technics 85 series RIE, consists of an anodized aluminum chamber with an anodized aluminum water-cooled, driven lower electrode. A 350 Watt, 13.56 MHz RF generator with auto impedance matching network produces the power required to maintain a glow discharge in the chamber. Safety interlocks are supplied by Technics to disable the power when the system is vented or a panel is removed. The chamber pressure is measured by a capacitance manometer (absolute pressure) which is mounted to the underside of the chamber. The six channels of process gas (made from stainless steel tubing) are isolated from the injection manifold by means of air-operated electrically actuated isolation valves. In addition, an 19 CFM two-stage corrosive-series direct drive rotary vane pump provides the vacuum on the etch chamber.

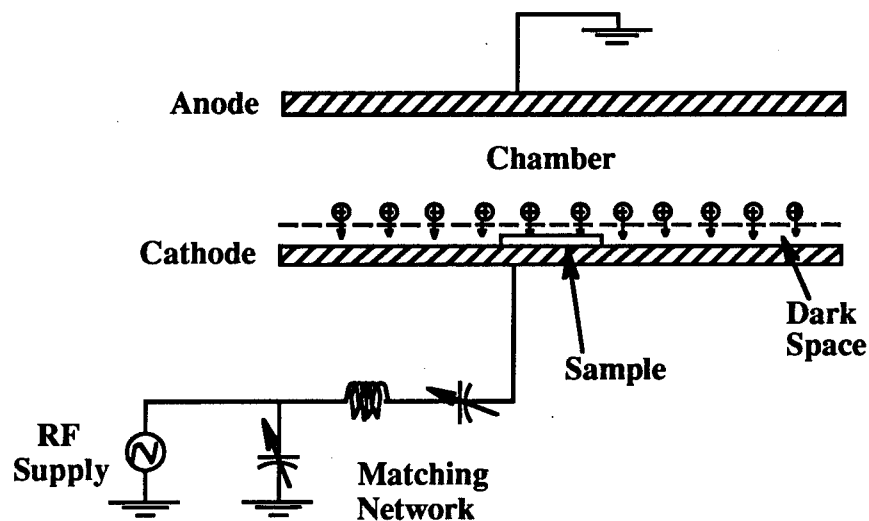


Figure 2. Schematic Diagram of the Parallel Plate Configuration

Residual process gases and reaction by-products from the etcher will pass through a wet scrubber, which is equipped with a water recirculation line. These lines are monitored for water

flow and exhaust ventilation and are an integral part of the control system. Interruption of the water flow or inadequate ventilation will trip the pneumatic valves and close the gas lines. In addition, the pH level of the scrubber water is tested and monitored prior to each days etching runs.

In the near future, an infrared heating assembly with optical pyrometer will be installed to provide heating and measurement of the sample surfaces during etching.

*Choice of Process Gases.* There are a number of process gases that can be used to produce anisotropically etched features. For GaN, AlN and InN, fluorine plasmas are impractical because involatile fluorides are formed with Ga, Al and In at the surfaces, see Table IV, therefore limiting desorption of reaction species from the surface. Chlorine plasmas, on the other hand, have been used extensively for etching these compounds, see Section B above.

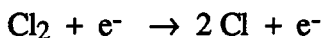
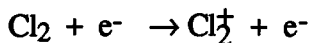
Table IV. Thermodynamic Data for Various Etchant Species.

Species	$\Delta G_f^\circ$ (kJ/mole) at RT <sup>#</sup>	$T_m(^{\circ}\text{C})^*$	$T_b(^{\circ}\text{C})^*$
GaF <sub>3</sub> (g)	-1203	sublim. 800	-
GaCl <sub>3</sub> (g)	-565	78	201
AlF <sub>3</sub> (g)	-1530	sublim. 1291	-
AlCl <sub>3</sub> (g)	-738	sublim. 177	-
InF <sub>3</sub> (g)	-950	1170	> 1200
InCl <sub>3</sub> (g)	-475	sublim. 300	-

\* From Reference [37].

# From Reference [51].

Based on the success of Pearton *et al.* [22, 23] and others [20, 21, 28] Cl<sub>2</sub> and BCl<sub>3</sub> are currently being used as the main process gases in addition to Ar and N<sub>2</sub> as diluent and purge gases. The chlorine-based gases provide the following ionic and chemically reactive components via reaction of Cl<sub>2</sub> with electrons generated by the plasma:



Experimentation with other gases, such as iodine- and/or bromine-containing gas mixtures and other chlorinated gases, is possible in order to obtain smooth, anisotropic features with reasonably high etch rates.

*Etching Procedure.* Prior to etching, the samples are patterned with an oxide mask via the following steps: deposition of a low temperature CVD silicon dioxide and photolithography, which includes spinning the photoresist onto the oxide, exposing unmasked areas of the resist to UV light and developing the hardened resist. The exposed oxide areas are etched away using a buffered HF solution and the resist is removed by acetone in an ultrasonic cleaner.

The RIE system is checked for proper water, air and exhaust supply. Samples are loaded into the etching chamber and process gas lines are pumped down to  $\approx 5 \times 10^{-4}$  torr. A typical etch run includes the following steps: argon plasma to remove water vapor and hydrocarbon contamination from the sample and etch chamber;  $\text{Cl}_2/\text{Ar}$  or  $\text{BCl}_3/\text{Ar}$  plasma for processing; nitrogen purge to remove chlorinated process gases from the chamber; vent chamber to atmosphere with nitrogen.

After the samples are removed from the etcher, the oxide is removed in a buffered oxide etch solution and the step heights of the etched features are measured with a Dektak stylus profilometer. In addition, SEM is used to observe the surface roughness and etched steps, and XPS and AES are used to observe the residual gas species on the sample surface.

#### D. Results

A reactive ion etching system has been installed and tested and is now operational. GaN has been etched in  $\text{Cl}_2$  and  $\text{BCl}_3$  plasmas with varying flow rates, pressures, power and DC bias. Typical etching parameters are: 1-10 sccm total gas flow, 35-75 mtorr, 125-200 W power and -(200-300)V bias. Etch rates of up to 200 Å/min and 150 Å/min have been achieved with  $\text{Cl}_2/\text{Ar}$  and  $\text{BCl}_3/\text{Ar}$  plasmas, respectively.

#### E. Future Research

In the future, parametric studies will be conducted to determine how the power, pressure, gas load and flow rates affect the etching rate of III-V nitrides in various chlorine-based plasmas. Alternative Cl-containing gases such as methyl and nitrosyl chloride may be used in the future in order to establish etch rates of the nitrides and to study the underlying etch mechanisms. Surface analysis techniques such as AES and XPS will be employed to determine the contamination levels and surface condition of the nitrides before and after etching. In the future, scanning tunneling microscopy and atomic force microscopy may be employed to observe the surface morphology and to correlate etching parameters with surface damage. With the addition of the heating assembly to the reactive ion etching system, the effects of increasing substrate temperature on the etch rate and surface morphology will be studied. In addition, experimentation with different cathode materials (such as graphite and quartz) is possible if



there is any micromasking from the cathode material. The ultimate goal of this research is to etch features necessary for optoelectronic and semiconductor devices fabrication.

## F. References

1. *Plasma Processing of Materials: Scientific Opportunities and Technological Challenges*, National Research Council—Panel on Plasma Processing of Materials, (National Academy Press, Washington, D.C., 1991).
2. D. L. Smith, R. H. Bruce, *J. Electrochem. Soc.* **129**, 2045 (1978).
3. C. J. Mogab, A. C. Adams, D. L. Flamm, *J. Appl. Phys.* **49**, 3796 (1978).
4. L. M. Ephrath, *J. Electrochem. Soc.*, (August 1979), 1419.
5. S. Matsuo, *J. Vac. Sci. Technol.* **17**, 587 (1980).
6. L. M. Ephrath, *Solid State Technol.*, (July 1982), 87.
7. D. L. Smith, P. G. Saviano, *J. Vac. Sci. Technol.* **21**, 768 (1982).
8. Y. H. Lee, M. M. Chen, *J. Appl. Phys.* **54**, 5966 (1983).
9. M. Zhang, J. Z. Li, I. Adesida, E.D. Wolf, *J. Vac. Sci. Technol. B* **1**, 1037 (1983).
10. A. J. van Roosmalen, *Vacuum* **34**, 429 (1984).
11. J. W. Palmour, R. F. Davis, T. M. Walleit, K.B. Bhasin, *J. Vac. Sci. Technol. A* **4**, 590 (1986).
12. R. H. Bruce, G. P. Malafsky, *J. Electrochem. Soc.* **136**, 1369 (1983).
13. S. Park, L. C. Rathburn, T. N. Rhodin, *J. Vac. Sci. Technol. A* **3**, 791 (1985).
14. H. F. Winters, *J. Vac. Sci. Technol. B* **3**, 9 (1985).
15. D. A. Danner, D. W. Hess, *J. Appl. Phys.* **59**, 940 (1986).
16. N. N. Efremow, M. W. Geis, R. W. Mountain, G. A. Lincoln, J.N. Randall, N.P. Economou, *J. Vac. Sci. Technol. B* **4**, 337 (1986).
17. Y. Ochiai, K. Shihoyama, T. Shiokawa, K. Toyoda, A. Masuyama, K. Gama, *J. Appl. Phys.* **25**, L527 (1986).
18. R. J. A. A. Janssen, A. W. Kolfshoten, G. N. A. van Veen, *Appl. Phys. Lett.* **52**, 98 (1988).
19. G. Smolinski, R. P. Chang, T. M. Mayer, *J. Vac. Sci. Technol.* **18**, 12 (1981).
20. H. Tanaka, F. Shimokawa, T. Sasaki, T. Matsuoka, *Optoelect. Dev. Technol.* **6**, 150 (1991).
21. J. S. Foresi, M.S. Thesis, Boston University, Boston, MA, 1992.
22. S. J. Pearton, C. R. Abernathy, F. Ren, J.R. Lothian, P.W. Wisk, A. Katz, C. Constantine, *Semicond. Sci. Technol.* **8**, 310 (1993).
23. S. J. Pearton, C. R. Abernathy, F. Ren, J.R. Lothian, P.W. Wisk, A. Katz, *J. Vac. Sci. Technol. A* **11**, 1772 (1993).
24. C. R. Abernathy, F. Ren, S.J. Pearton, in *IEEE 6th International Conference on InP and Related Materials*, (IEEE, Piscataway, NJ, 1994), p. 387.
25. S. J. Pearton, C. R. Abernathy, F. Ren, *Appl. Phys. Lett.* **64**, 2294 (1994).
26. S. J. Pearton, C. R. Abernathy, F. Ren, *Appl. Phys. Lett.* **64**, 3643 (1994).
27. S. J. Pearton, F. Ren, C. R. Abernathy, J.R. Lothian, *Semicond. Sci. Technol.* **9**, 338 (1994).
28. I. Adesida, A. Mahajan, E. Andideh, *Appl. Phys. Lett.* **63**, 2777 (1993).
29. I. Adesida, A. T. Ping, C. Youtsey, T. Dow, M. Asif Khan, D.T. Olsen, J.N. Kuznia, *Appl. Phys. Lett.* **65**, 889 (1994).
30. I. Adesida, A.T. Ping, in *Second International Workshop on Wide Band Gap Nitrides* (St. Louis, MO, 17-18 October 1994).
31. M. E. Lin, Z. F. Fan, Z. Ma, L.H. Allen, H. Morkoc, *Appl. Phys. Lett.* **64**, 887 (1994).
32. I. Akasaki, H. Amano, *Physica B* **185**, 428 (1992).
33. C. Eddy, Ph.D. Thesis, Boston University, Boston, MA, 1990.
34. T. Lei, T. D. Moustakis, *J. Appl. Phys.* **71**, 4933 (1992).
35. Z. J. Yu, B. S. Sywe, A. U. Ahmed, *J. Electr. Mater.* **21**, 782 (1992).

36. J. Sumakeris, Z. Sitar, K. S. Ailey-Trent, *Thin Solid Films* **225**, 244 (1993).
37. *CRC Handbook of Metal Etchants*, P. Walker, Ed. (CRC Press, Boca Raton, LA, 1991).
38. Y. Morimoto, *J. Electrochem. Soc.* **121**, 1383 (1974).
39. A. Shintani, S. Minagawa, *J. Electrochem. Soc.* **123**, 706 (1976).
40. V. V. Malinovskii, L. A. Marasina, N. V. Mitusova, I.G. Pichugin, *Izv. Leningr. Elektrotekh. Inst. im. V.I. Ul'yanova* **281**, 76 (1981).
41. E. S. Dettmer, B. M. Romenesko, H. K. Charles, B.G. Charkuff, D.J. Merrill, *IEEE Trans. Comp. Hybrids Manuf. Technol.* **12**, 543 (1989).
42. L. R. Rowland, Ph.D. Thesis, North Carolina State University, Raleigh, NC, 1992.
43. A. V. Omel'Chenko, M. A. Shelagarov, A. N. Frolov, M.E. Getmanova, G.S. Belousov, "Manufacture of Nitrides by Alloy Nitridation Followed by Selective Leaching," Small Enterprise Jilpa Ltd., Russia, PCT Int. Appl., 1992.
44. B. Matthes, E. Broszeit, O. Zucker, P. Gauer, *Thin Solid Films* **226**, 178 (1993).
45. M. Nagaoka, "Annealing Method for Compound Semiconductor Device Fabrication," Toshiba Corp., Japan, Jpn. Kokai Tokkyo Koho, 1987.
46. H. Kato, M. Sugata, T. Ikeda, "Manufacture of Silicon-Supported X-Ray Mask having Aluminum Nitride-Based Film," Canon K.K., Japan, Jpn. Kokai Tokkyo Koho, 1989.
47. A. Sasame, K. Shibata, H. Sakagami, "Aluminum Nitride Sintered Body with a Metalized Layer and Its Manufacture," Sumitomo Electric Industries, Ltd., Japan, Jpn. Kokai Tokkyo Koho, 1986.
48. "Group IIIA Pnictide Semiconductor Device," Fujitsu Ltd., Japan, Jpn. Kokai Tokkyo Koho, 1982.
49. N. Yamaguchi, S. Ogawa, I. Yoshizawa, S. Kajita, K. Waki, "A Method for Manufacturing a Nitride-Type Ceramic Circuit Board," Matsushita Electric Works, Ltd., Japan, Jpn. Kokai Tokkyo Koho, 1986.
50. Q. X. Guo, O. Kato, A. Yoshida, *J. Electrochem. Soc.* **139**, 2008 (1992).
51. *HSC Chemistry*, Version 1.11, Outokumpu Research Oy, Inc., Pori, Finland, 1993.

## XXIV. Contact Formation to n-type and p-type GaN

### A. Introduction

The formation of ohmic contacts with semiconductor materials and devices is a fundamental component of solid state device architecture. As device size has diminished and the scale of integration has increased, the quality of these interfaces has become an increasingly important concern. In addition, the presence of parasitic resistances and capacitances, such as those existing at contact interfaces, becomes more detrimental at higher operating powers and higher oscillation frequencies. For many devices, the losses that occur at the contact interfaces account for a large fraction of the total losses, and as such are responsible for significant impact on device performance.

The development of adequate and reliable ohmic contacts to the compound semiconductors, particularly those with wider band gaps, has met a number of challenges. The subject of ohmic contacts to p- and n-type III-V compounds, mostly GaAs, AlGaAs, and InP, has received a great deal of attention over the past decade, and significant advances have been made [1-12]. By comparison, the III-V nitrides have received little attention in this regard. However, interest in these materials has been renewed in recent years as thin film growth techniques have improved, p-type doping in GaN and AlGaN solid solutions has been achieved, and p-n junctions have been fabricated.

The majority of successful ohmic contact systems that have so far been implemented with the more conventional compound semiconductors have relied upon alloying (liquid-phase reaction) or sintering (solid-phase reaction) via post-deposition annealing treatments, and/or the presence of high carrier concentrations near the interface [1,2,6,12]. However, many otherwise successful ohmic contact systems have only limited thermal stability and are subject to degradation, usually in the form of extensive interdiffusion, interfacial reaction, and interphase growth, accompanied by increase in contact resistivity, under subsequent thermal processing steps. It is reasonable to suppose that the cleanliness and preparation of the semiconductor surface prior to contact deposition plays a significant role in the behavior of the interface, and there are indications in the recent literature that support this [2,11-13]. Thorough oxide removal is especially important, though it may well prove to be a persistent challenge with Al-containing compounds in particular.

In this study, two main approaches are being taken in the development of ohmic contacts to GaN and AlN. The first approach is similar to that which has resulted in the majority of successful ohmic contacts to the more conventional compound semiconductors such as GaAs: the creation of high carrier concentrations in the semiconductor at the metal interface by means of alloying, sintering, or implantation of dopant species. The so-called pinning of the Fermi level at this surface, particularly with GaAs, results in a more or less fixed potential barrier at

the metal interface. In the case of the pinned Fermi level of GaAs, the approach has generally been to shrink the width of the depletion layer by means of increasing the carrier concentration to the point where carrier tunneling through the barrier occurs readily. Even with optimization of contact composition and annealing times and temperatures, the lowest contact resistivities ( $\rho_c$ ) have been obtained only on the most heavily doped materials. Though there are indications that high doping levels and extensive interfacial reactions through alloying and sintering are not essential for ohmic contact formation in all cases, these processes have proven useful for minimizing  $\rho_c$  [2,11-13].

The other approach toward ohmic contact formation to be taken in this study involves the Schottky-Mott-Bardeen (SMB) model of semiconductor interfaces [14,15]. In this model the relative values of work function of the materials involved determine the band structure of the interface and thus the nature of any potential barriers present. The presence of interfacial states at the semiconductor surface can interfere with the alignment of the Fermi level across the interface and overshadow the effect of the inherent difference in work function between the two materials. The III-V nitride compounds are more ionically bonded than their phosphide and arsenide counterparts, as a result of larger electronegativity differences between the component elements. According to the observations of Kurtin *et al.* [16], this fact indicates that the nitrides should experience less Fermi level stabilization or "pinning" at the surface than do the more covalent compounds. Thus, the barrier heights of contacts to the nitrides should be more dependent on the contact material than is the case with the more conventional and more covalent semiconductors such as Si, GaAs, InP, SiC, etc. With the work of Foresi and Moustakas [17,18], this concept is beginning to be investigated. The SMB model also indicates that the cleanliness of the interface plays an important role in its electrical behavior, particularly in the minimization or elimination of any insulating layers at the interface.

To date, several alloyed and sintered contact strategies, having demonstrated effectiveness with GaAs - and, in the case of Au, with GaN - have been undertaken with GaN and AlN. The tighter bonding of Ga and Al to N, in comparison to As, suggests that higher temperatures and possibly longer times are required for interfacial reactions to take place, and that some reactions may be inhibited or prevented. The behavior of the systems examined so far has been consistent with these suppositions. Contact strategies involving the concentration of active dopant species at the contact interface will continue to be characterized in this study, as well as the investigation of the roles of work function differences and interfacial cleanliness. In the present reporting period, both of these approaches to contact formation were continued.

One area of contacts development that has received a significant amount of attention is that of the metal silicide compounds. Silicide thin films have been extensively studied and applied as contacts and interconnects, mostly for silicon-based technology [19-24]. In comparison, the properties of the metal germanides are not well documented. As a general rule, germanides

have been found to be more resistive than silicides and their chemistry with Si-based materials more complex. However, in a series of studies, M. O. Aboelfotoh *et al.* have shown that a particular phase of copper germanide, specifically the ordered monoclinic phase  $\epsilon_1$ -Cu<sub>3</sub>Ge, is an exception to these rules [25-28]. Thin films of Cu<sub>3</sub>Ge exhibit remarkably low resistivities, unlike Cu<sub>3</sub>Si, and, unlike both Cu and Cu<sub>3</sub>Si, are surprisingly stable with respect to oxygen and air exposure. As such, Cu<sub>3</sub>Ge presents itself as a potentially useful contact metal. Indeed, preliminary experimentation with Cu<sub>3</sub>Ge contacts on GaAs and GaN, primarily on n-type and heavily-doped p-type material, has produced some favorable results in terms of ohmic contact formation. For these reasons copper-germanium contacts were investigated during this reporting period as possible candidates for high-quality, low-resistivity ohmic contacts.

## B. Experimental Procedure

*Film Deposition.* The substrates used for III-nitride film growth were 6H-SiC wafers supplied by Cree Research, Inc. Two growth methods have been used for the deposition of III-N films for these contacts studies: ECR plasma-enhanced molecular beam epitaxy (MBE) and metalorganic vapor phase epitaxy (MOVPE). The growth reactors used for the nitride film deposition are described in other sections of this report. Magnesium incorporated into the films during growth as the p-type dopant; Ge was used to grow n-type material via MBE and Si was used as the more effective donor impurity for the MOVPE-grown films.

Six different contact systems were examined during this reporting period. Contacts deposited on n-GaN (Si or Ge-doped) were: (1) single Al layers, (2) an alloyed compound of Cu<sub>3</sub>Ge, and (3) TiN layers. The contacts deposited on Mg-doped GaN were: (1) single Au layers, (2) single Pt layers, and (3) a Au/Mg/Au multilayer contact. Prior to metals deposition, the nitride films were cleaned with a 50:50 HCl:H<sub>2</sub>O dip and carefully pulled dry from the solution. Any remaining cleaning solution was blown dry with N<sub>2</sub>. A shadow mask was used during deposition to create rectangular-bar TLM (transmission line model) patterns for contact resistivity ( $\rho_c$ ) measurements, as described in the earlier semiannual report of June 1993. The variety of contact metals used in this study has necessitated the use of different deposition systems with differing capabilities. The Au layers, Cu/Ge layers, and Au/Mg/Au layers were deposited by means of electron beam evaporation using a Thermionics evaporation system having a 3 kW 5-source electron gun. The 5-source capacity of the e-beam hearth allowed the deposition of multiple layers of different metals in the same vacuum run. Film thicknesses were monitored using a quartz crystal oscillator. The Al layers were deposited in a standard thermal evaporator, while the much more refractory Pt films were deposited by means of Ar ion sputtering. Lastly, the TiN films were grown by means of ion-beam assisted deposition (IBAD) in a UHV electron-beam evaporation system containing a Kaufman-type ion source for N<sub>2</sub> activation.

*Contact Characterization.* After deposition, I-V measurements were taken between separate pads of the TLM patterns, using tungsten probe tips and an HP 4145C Semiconductor Parameter Analyzer. Measurements were made at room temperature and at elevated temperatures ranging from 100 to 500°C. Annealing treatments were performed in a flowing N<sub>2</sub> atmosphere at successively higher temperatures using a Heatpulse 410 rapid thermal annealing (RTA) furnace. TLM measurements were taken by measuring the total resistance between identical contact pads as a function of separation distance  $l$ . The contact resistivity was obtained from the plot of  $R(l)$  vs.  $l$ , as described by Reeves and Harrison [29]. The mathematical assumptions and pattern geometry inherent in this model yield values for  $\rho_c$  that represent an upper limit; thus, the measured values are conservative assessments of performance. In addition, for every test pattern geometry there is a lower limit of  $\rho_c$  below which it is not possible to obtain precise  $\rho_c$  calculations. This is due to the fact that the linear  $R(l)$  plot becomes very steep and too close to the origin with decreasing  $\rho_c$ . For the shadow-mask test geometry used in this study to date, and for many of the TLM results reported by other researchers in the field, the practical lower limit for precise  $\rho_c$  calculation is about  $10^{-6} \Omega \text{ cm}^2$ .

In addition to electrical characterization, the contact samples in this study were also prepared for cross-sectional TEM analysis by Dr. Moon Kim and Dr. Yi Huang at the Center for Solid State Science at Arizona State University. At the time of the writing of this report, microstructural and crystallographic characterization had been performed on several of the contact systems and compositional analysis by means of energy-dispersive x-ray analysis (EDS) and electron energy loss spectroscopy (EELS) was being undertaken.

### C. Results

*Al Contacts on Ge:GaN.* Aluminum contacts (single Al layers 2500 Å thick) deposited on Ge-doped GaN were ohmic and exhibited low contact resistivity in the initial as-deposited condition. The I-V behavior of the as-deposited contacts is shown in Fig. 1. As the plot shows, the I-V relationship of the Al contacts on Ge:GaN is completely linear. In addition, this contact system, at temperatures below 550°C, exhibited a much lower contact resistivity than others yet investigated in this study: from TLM measurements the contact resistivity  $\rho_c$  was found to be  $8.6 \times 10^{-5} \Omega \text{ cm}^2$  at room temperature and  $6.2 \times 10^{-5} \Omega \text{ cm}^2$  at 500°C. These results compare very favorably with those reported by Foresi and Moustakas [17,18], and, more recently, Lin *et al.* [30], who obtained  $\rho_c$  values of  $1 \times 10^{-3} \Omega \text{ cm}^2$  and approximately  $1 \times 10^0$  respectively. The samples were heat-treated at 450°C, 550°C, and 650°C for 3 min at each temperature; TLM measurements were performed at room temperature and elevated temperatures - 200°C, 350°C, and 500°C - after every heat treatment. The effects of this heat treatment on the contact resistivity is plotted in Fig. 2. For each given heat treatment

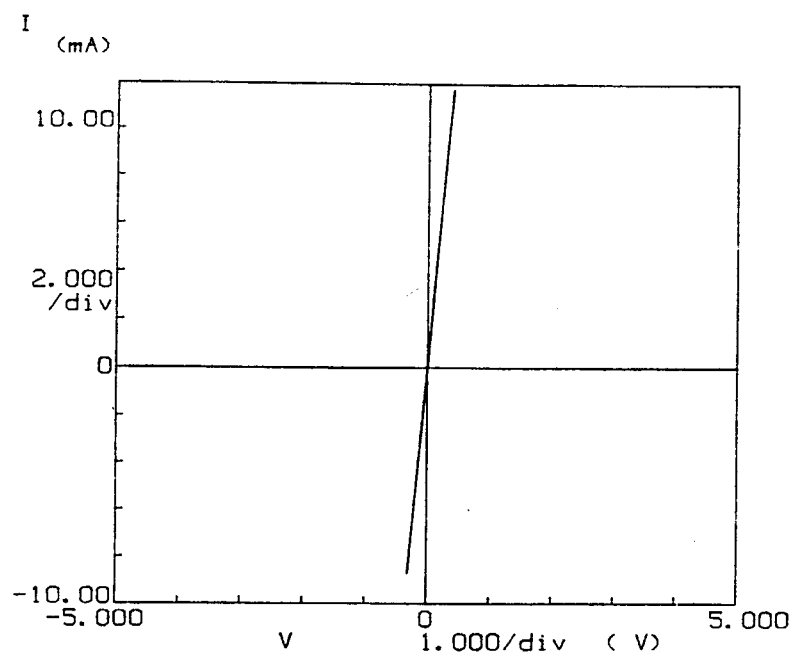


Figure 1. I-V data for as-deposited Al contacts on n-type GaN.

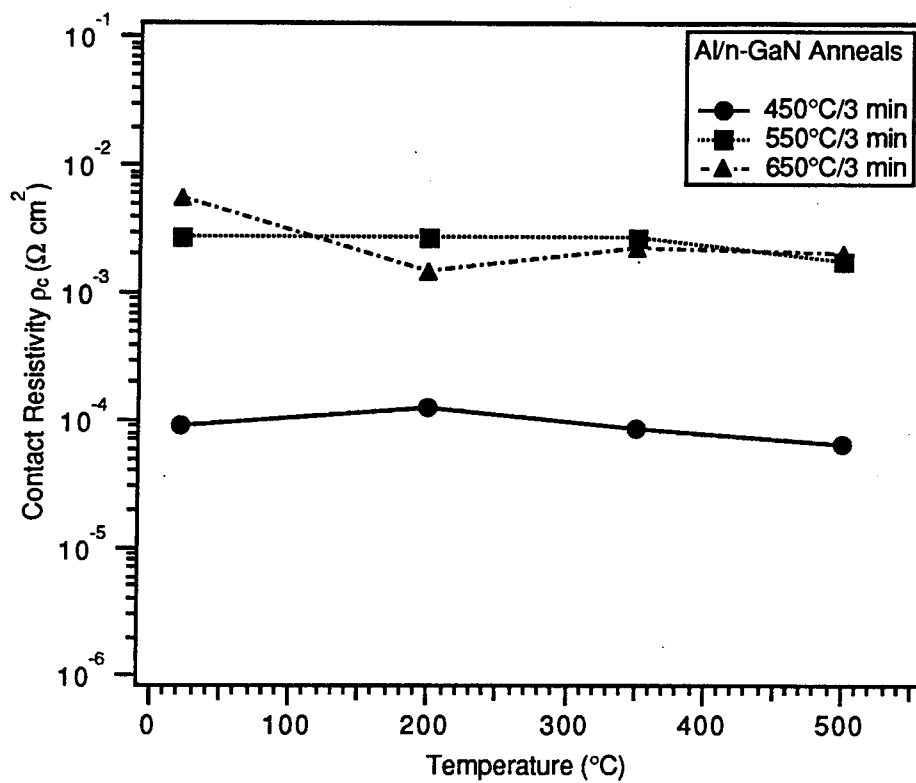


Figure 2. Contact resistivities of Al/Ge:GaN as a function of measurement temperature and heat treatment.

condition, the measured resistances and contact resistivities decreased slightly with increasing temperature due to the greater thermal availability of free charge carriers. After annealing at 450°C, the behavior of the Al contacts was essentially unchanged from the as-deposited condition. However, the 550°C and 650°C anneals resulted in an overall increase of contact resistivity, even with the reduced resistances that occurred at higher measurement temperatures. After annealing to 650°C, the contact resistivity stabilized at approximately  $2 \times 10^{-3} \Omega \text{ cm}^2$ .

Characterization by means of cross-sectional TEM (X-TEM) is being performed on the contact systems in this study by our collaborators at Arizona State University to investigate the interfacial structures in detail. The Al film as initially deposited was polycrystalline with somewhat columnar growth, oriented randomly with respect to the GaN surface. Annealing resulted in grain growth in the Al layer, but no change in the random orientation with respect to the GaN lattice. In addition, this analysis of the Al/n-GaN contact interface shows that a new phase formed at the Al/GaN interface as a result of heat treatment. Cross-sectional TEM images of the Al/GaN interface, annealed at 650°C for 3 min, are shown in Fig. 3. The appearance of this interfacial phase as a result of annealing correlates with an increase in contact resistivity, which suggests the formation of higher-resistivity materials at the interface and thus may indicate the presence of an Al nitride phase. Selected-area diffraction analysis (SAD) of these second phase regions indicates a cubic structure with a lattice parameter of 7.84 Å. These second phase particles at the interface, which do not form a continuous layer, range in size from about 50-800 Å; smaller particles of the same phase were found farther into the Al layer, about 10-100 Å in size. Spectroscopic analysis via EELS revealed the presence of nitrogen in the Al layer, but no appreciable amounts of Ga. Some oxygen was also found in the Al layer, though at this time it is not clear how much of this oxygen originated at the sample surfaces and how much of it was incorporated in to the Al film during thermal evaporation in a non-UHV environment.

*Cu<sub>3</sub>Ge Contacts on Ge:GaN.* The Cu<sub>3</sub>Ge contacts on n-type GaN (MBE, Ge-doped) were deposited at IBM's Yorktown Heights research facility in a UHV e<sup>-</sup>-beam evaporation system. The Cu and Ge components of this contact system were deposited sequentially, 800 Å layers of Cu followed by 1200 Å of Ge; the alloying of the layers was accomplished by heating at 400°C for 15 minutes, while in vacuum after the metal evaporation, as described by Aboelfotoh *et al.* [25-28]. Current-voltage data for Cu<sub>3</sub>Ge contacts on Ge-doped GaN, shown in Fig. 4, reveal ohmic behavior with low overall resistance. In addition, the contacts retained a shiny, smooth surface, indicative of little or no roughening or reaction at the interface. This good contact behavior contrasts with the results reported in the last semi-annual report for this project (June 1994), in which the Cu/Ge layers were sequentially deposited in a non-UHV, bell jar-type evaporation system and alloyed at 1 atm (N<sub>2</sub>) in an RTA furnace. Subsequent SIMS analysis of these earlier, non-UHV-deposited Cu<sub>3</sub>Ge films revealed a substantial presence of



oxygen in the metal. These observations indicate that the deposition and alloying environment plays an important role in the character and performance of the electrical contacts that form. Further characterization of the  $\text{Cu}_3\text{Ge}$  contact system, including TLM measurements and microstructural analysis, will be performed in the coming weeks.

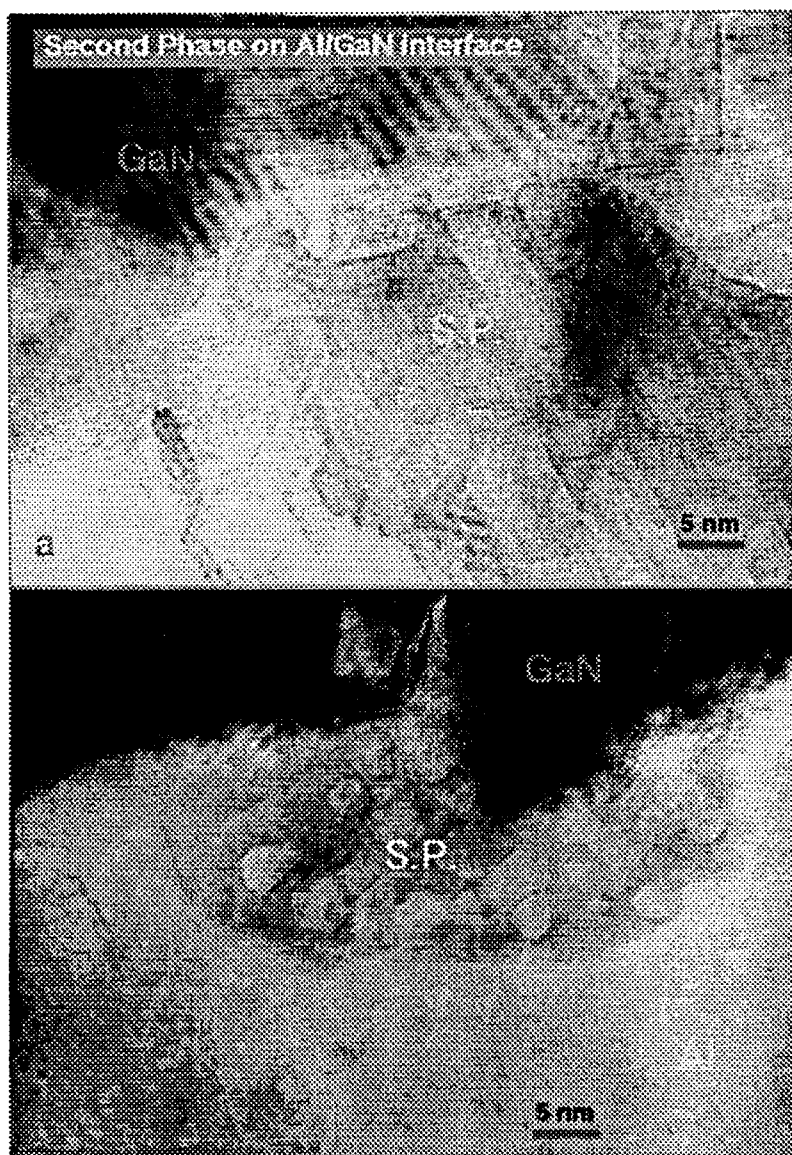


Figure 3. High-resolution X-TEM images of Al /GaN interface, annealed at 650°C for 3 min. Both images, taken at the same magnification in two different regions of the interface, show a new crystalline phase forming at the Al/GaN interface.

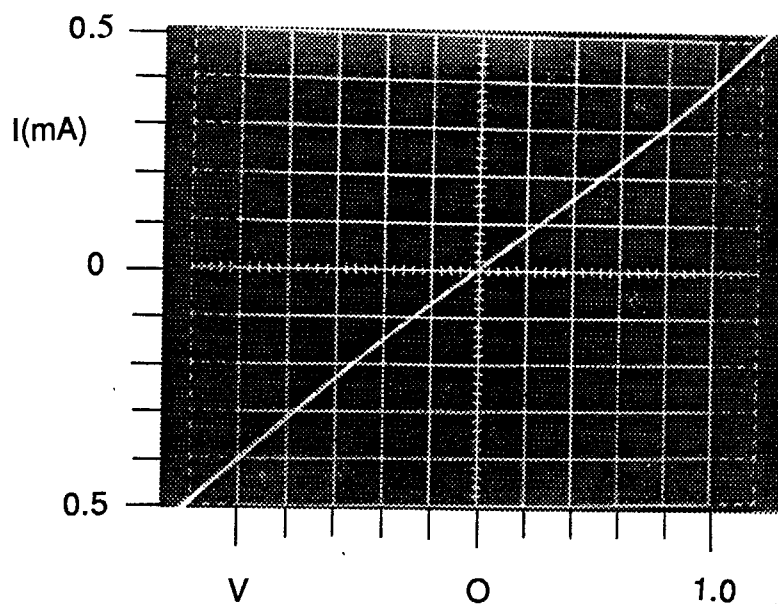


Figure 4. I-V data for as-alloyed  $\text{Cu}_3\text{Ge}$  contacts on Ge-doped GaN.

*TiN Contacts on Si:Ga<sub>N</sub>.* Titanium nitride was grown on Si-doped GaN (MOVPE-grown) by means of ion beam-assisted deposition (IBAD), using e-beam evaporation of Ti and purified  $\text{N}_2$  activated by a Kaufman-type ion gun. The TiN growth was performed at a substrate temperature of  $350^\circ\text{C}$  and a deposition rate of  $10\text{--}15 \text{ \AA}/\text{min}$ . Auger depth-profiling analysis of films grown under these conditions have revealed them to be stoichiometric TiN and uniform through the thickness even when variations in pressure and deposition rate occurred during growth. In addition, the metallic gold-like appearance of the TiN compound is a reliable indicator of stoichiometry.

Current-voltage measurements of TiN/n-GaN contacts, shown in Fig. 5, reveal them to be linearly ohmic in the as-deposited condition. TLM measurements of this contact system yield a very low specific contact resistivity at room temperature, estimated to be in the low  $10^{-7} \Omega \text{ cm}^2$  range; the lower limit of  $\rho_c$  measurement has been discussed above in the Experimental Procedure section. Elevated-temperature TLM measurements showed that the  $\rho_c$  increased with increasing temperature, into the  $10^{-3} \Omega \text{ cm}^2$  range, and returned to its room-temperature behavior after cooling.

*Au contacts on Mg:Ga<sub>N</sub>.* The preliminary electrical characterization of Au contacts on p-type Mg:Ga<sub>N</sub> was described in last year's annual report for this project (December 1993). These Au/p-GaN contacts were rectifying as-deposited, though not close to being ideal Schottky contacts, and were found to yield linearly ohmic I-V behavior after annealing at sufficiently high temperatures ( $>650^\circ\text{C}$ ). Annealing at  $800^\circ\text{C}$  for 10 minutes, after earlier

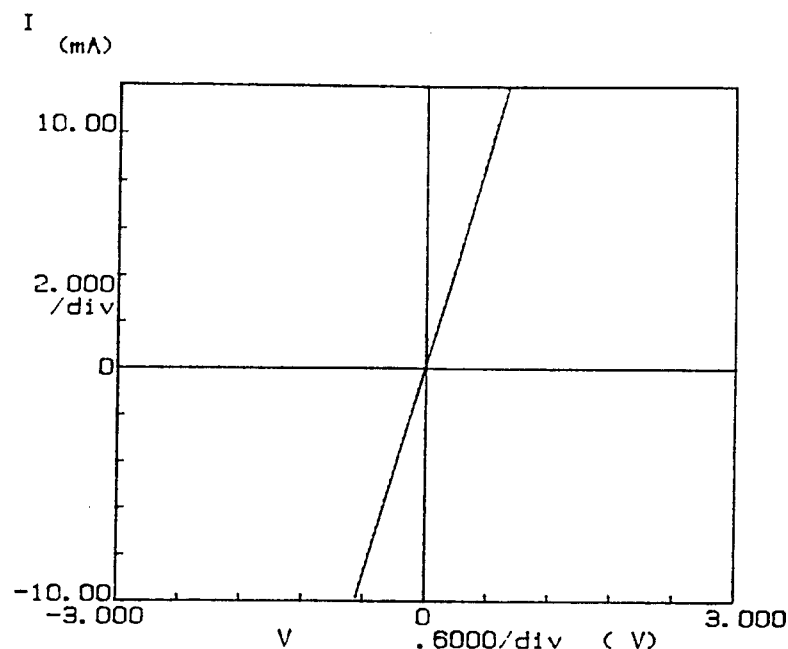


Figure 5. I-V data for as-deposited TiN contacts on Si-doped GaN.

anneals at lower temperatures, resulted in a  $\rho_c$  drop of over 3 orders of magnitude into the  $10^1 \Omega \text{ cm}^2$  range. This change in contact behavior, shown in Fig. 6, was associated with some visible roughening of the Au surface, indicative of interfacial roughening, and noticeable intermixing of the metallic elements at the interface was observed in Auger depth-profiling analysis.

Cross-sectional microstructural characterization has since been performed on this contact system by means of X-TEM, and high-resolution images reveal that interfacial reaction did indeed occur as a result of annealing at high temperature. In addition, during the preparation of TEM specimens, it was observed that there was poor adhesion of the Au to the GaN surface in both the as-deposited and annealed conditions. Figure 7 shows the formation of an amorphous phase at the annealed Au-GaN interface, extending into the apparently decomposing GaN lattice. Some cavities were also seen at the interface, which almost certainly contribute to the poor adhesion. Spectroscopic analysis by means of EELS revealed the presence of nitrogen throughout the Au layer; compositional characterization of the amorphous regions is currently underway. The Au layer (2500 Å thick) was polycrystalline as-deposited, and while grain growth in the Au film occurred during annealing, no particular crystallographic orientation or relationship was observed between the Au and the GaN.

*Au/Mg/Au contacts on Mg:GaN.* A three-layer Au/Mg/Au (320 Å/320 Å/1700 Å overlayer on top) contact system was deposited on Mg-doped GaN by means of e-beam evaporation. In contrast to the Au single-layer contacts, the Au/Mg/Au contacts with only

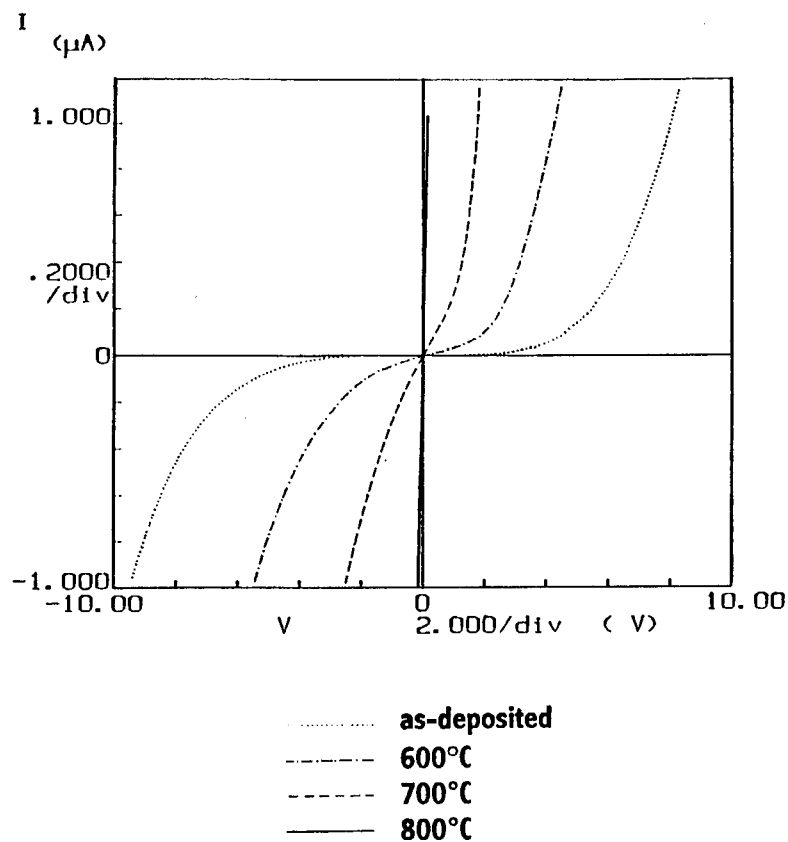


Figure 6. I-V behavior of Au/Mg:GaN contacts as a function of annealing temperature, showing transition to ohmic behavior.



Figure 7. High-resolution X-TEM image of Au/GaN interface, annealed at 800°C for 10 min, showing formation of amorphous phase as a result of high-temperature annealing.

320 Å in direct contact with the GaN surface, followed by the Mg layer, were linearly ohmic in the as-deposited condition; this is shown in Fig. 8 below. Contact resistivity measurements yielded a room-temperature  $\rho_c$  of  $214 \Omega \text{ cm}^2$ . Figure 9 shows the results of elevated-temperature  $\rho_c$  measurements. The  $\rho_c$  dropped off substantially at elevated temperatures, down to  $2.7 \times 10^{-1} \Omega \text{ cm}^2$  when measured at  $350^\circ\text{C}$ . This behavior remained essentially unchanged after heat treatments of  $575^\circ\text{C}$  and  $650^\circ\text{C}$ , for 15 s each. After a further annealing treatment at  $725^\circ\text{C}$  for 15 s, the contacts became substantially more resistive. Cross-sectional microstructural characterization of this contact system, both as-deposited and annealed, is currently underway.

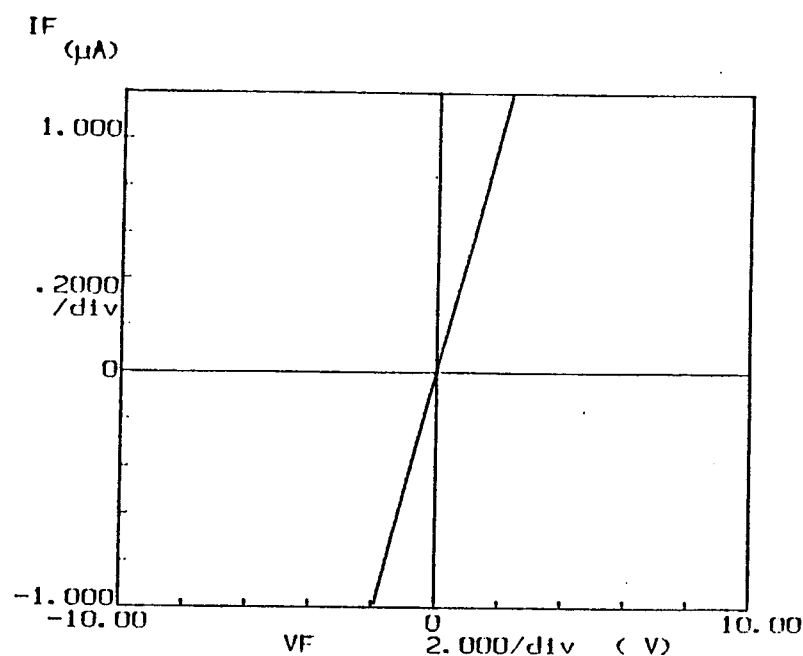


Figure 8. I-V data for as-deposited Au/Mg/Au contacts on Mg-doped GaN.

*Pt Contacts on Mg:GaN.* Pt contacts were deposited on Mg-doped GaN by means of Ar-ion sputtering. There was no deposition thickness monitor in the sputtering system, but from reported deposition rates the Pt film thickness is estimated to be 500-600 Å. These contacts were found to be ohmic as-deposited, as shown in Fig. 10 below, and to have a  $\rho_c$  that is evidently substantially lower than the range of precise calculation, which means much less than  $10^{-6} \Omega \text{ cm}^2$ . When measured at elevated temperatures up through  $400^\circ\text{C}$ , this behavior remained throughout well below the range in which it could be calculated. These initial results are very promising and demand further confirmation and more precise characterization. Annealing studies of this contact system, as well as further depositions, will be performed in the coming weeks. Microstructural characterization is also upcoming in the very near future.

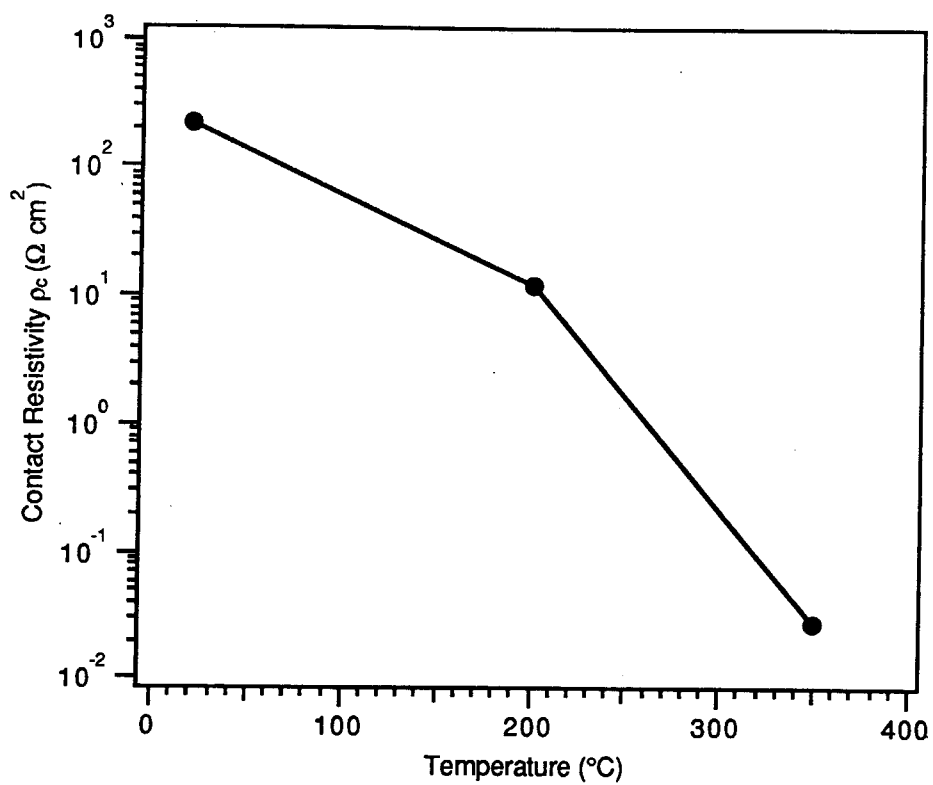


Figure 9. Contact resistivities of Au/Mg/Au/p-GaN system as a function of temperature.

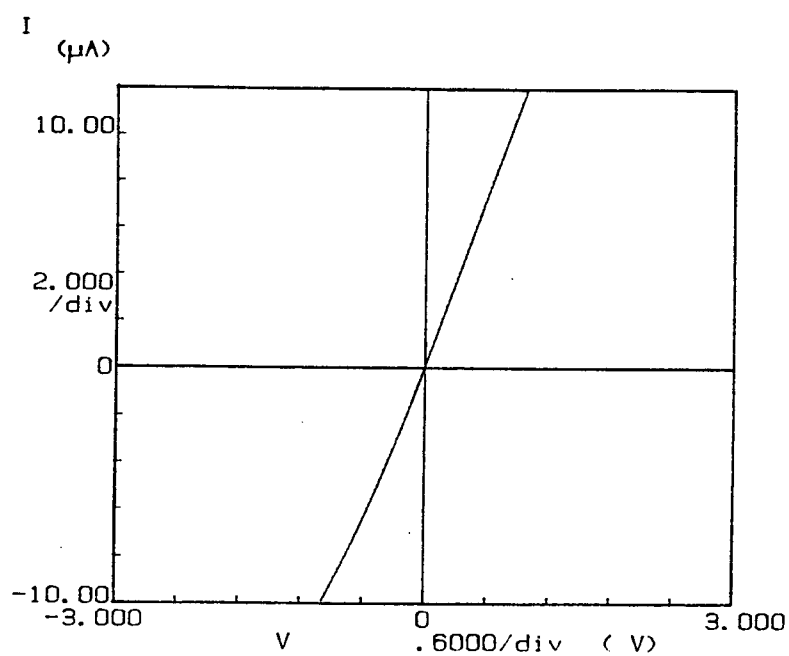


Figure 10. I-V data for as-deposited Pt contacts on Mg-doped GaN.

#### D. Discussion

*Al Contacts on Ge:GaN.* That the as-deposited Al contacts on Ge-doped GaN would prove to be ohmic is consistent with the Schottky-Mott-Bardeen model, based on the relationship of the work functions of the two surfaces. Aluminum is a relatively low work function metal ( $\phi_{Al}=4.2$  eV) and thus provides a favorable band offset for ohmic contact formation to an n-type semiconductor ( $\phi_{GaN}$  estimated to be 4.1 eV). However, it should be pointed out that the exact value for the work function and/or electron affinity of GaN and their dependence upon doping levels have not been reproducibly and precisely established as yet. As stated above, the results of these contact resistivity measurements compare very favorably with those reported by Foresi and Moustakas [17,18], and, more recently, Lin *et al.* [30]. The GaN materials used by both of these groups were different than those used in this study; theirs were unintentionally doped and inherently n-type, indicative of high background carrier concentrations (about  $10^{17}$  cm<sup>-3</sup> in both cases) and defect densities. Hall measurements of Ge:GaN films similar to those used for contact deposition and TLM measurements in this study yielded carrier concentrations of about  $3 \times 10^{19}$  cm<sup>-3</sup> with mobilities of approximately 100 cm<sup>2</sup> V<sup>-1</sup> s<sup>-1</sup>. Given the fact that contact resistivities tend to be strongly affected by bulk and surface carrier concentrations, it is not surprising that these highly doped Ge:GaN films produced low-resistivity contacts. However, contacts need to be made to more lightly doped material as well, and steps can be taken to improve the performance of such contacts, as described above.

The samples were annealed for short periods of time in an RTA furnace under flowing N<sub>2</sub>. The purpose of performing the annealing under N<sub>2</sub> at atmospheric pressure for short times was to reduce the likelihood of generating N vacancies which are believed to be shallow donors that contribute to the background carrier concentration. While increasing the background carrier concentration may contribute to greater current transport in the semiconductor and across the contact interface and apparently reduce the  $\rho_c$ , in general such behavior would be detrimental to overall electronic properties and device performance. More extensive characterization of the electronic properties of our nitride films is needed to better correlate and understand the relationship between dopant concentration, carrier concentration and mobility, Fermi levels, and contact behavior. Improvements in our measurement capabilities, in terms of both equipment and sample preparation techniques, are underway.

The results of the X-TEM analysis show that an intermediate phase formed at the Al/GaN interface, possibly a form of AlN, as a result of annealing. The correlation of the formation of this interfacial phase with an increase in contact resistivity is suggestive. Aluminum nitride has a very large and negative free energy of formation and thus the reaction is energetically favored where there is sufficient thermal mobility. The presence of nitrogen and the formation of intermediate phase particles within the Al layer indicates that this is very likely occurring.

*CuGe Contacts on Ge:GaN.* To date, the properties of  $\text{Cu}_3\text{Ge}$  films have been documented by Aboelfotoh *et al.*, but the interfacial properties of CuGe contacts to semiconductor surfaces are only beginning to be investigated. The results of preliminary TLM measurements, reported in the last semi-annual report for this project (June 1994) show that  $\text{Cu}_3\text{Ge}$ , and also Cu contacts in the as-deposited state, form ohmic contacts on both Ge:GaN and Mg:GaN. The results of I-V measurements of UHV-deposited, alloyed-*in situ*  $\text{Cu}_3\text{Ge}$  contacts indicate low-resistivity ohmic behavior. At the present time the work function and electron affinity properties of CuGe compounds have not yet been studied, so it is not known how this contact system compares with the Schottky-Mott-Bardeen model. It is possible that even if a contact metal does not have a favorable work function relationship to a semiconductor for ohmic contact formation according to the Schottky model, the role of a barrier at the surface can be bypassed by means of other current transport mechanisms. The time intervals and temperatures of the alloying and/or contact annealing steps, along with the cleanliness of the deposition environment, have significant effects on the resulting current-carrying abilities of the contacts. The details of the alloying and annealing procedures would influence the rate and amount of any interfacial diffusion that take place and the reactions that occur at the interface. Film composition is also evidently of critical importance in the behavior of this contact system, given the difference between the UHV and non-UHV-deposited contacts. All of these factors have an effect on the behavior of the contacts. Given the success of this contact system with GaAs materials and its promise for the nitrides, investigations will continue.

*TiN Contacts on Si:GaN.* TiN is a low work function metal ( $\phi_{\text{TiN}}=3.74$  eV), and thus according to the Schottky-Mott-Bardeen model should be likely to form ohmic contacts to n-type semiconductors. It has the NaCl structure and has a reasonably close lattice match to hexagonal GaN (-5.9 %) and AlN (-3.6 %) in the close-packed (111) planes. In earlier work at NCSU it was shown that TiN forms an epitaxial and ohmic contact on n-type 6H-SiC, which has a lattice parameter similar to that of AlN. In addition, TiN is thermally very stable and highly resistant to oxidation, forming only a thin passive oxide film on the surface. Since in the TiN the Ti is already stoichiometrically nitrided and strongly bound to N, the likelihood of detrimental interfacial reaction is virtually eliminated. As such, it is a good contact candidate, and this experiment was performed to test this supposition.

The TiN/n-GaN contacts did indeed turn out to be ohmic and to have low specific contact resistivity in the as-deposited condition. These recent results may provide some insight into the good performance seen from annealed Ti/Al contacts on n-type GaN [30]: given that thermodynamic data suggest that TiN formation is favored, the presence of TiN at the interface of annealed Ti/Al contacts may be responsible in whole or in part for the observed low contact resistivities. Annealing treatments will be conducted on the TiN contact samples in the coming weeks to investigate the thermal stability of the system. The increase in  $\rho_c$  with increasing



measurement temperature contrasts with the results observed with Al/n-GaN and Au/Mg/Au/p-GaN contacts. More detailed study of the temperature-dependent  $\rho_c$  behavior is planned in order to understand the current transport mechanisms and establish the utility of this contact system for high-temperature device applications. After the annealing study, X-TEM samples of as-deposited and heat-treated contacts will be sent to ASU for high-resolution microstructural characterization to look for epitaxial relationships and any compositional changes that take place.

*Au Contacts on Mg:GaN.* The rectifying nature of the as-deposited Au contacts on undoped n-GaN was observed by Foresi and Moustakas in their contacts investigation [17,18]. However, the GaN material used by Foresi *et al.* was different than that used in this study; theirs was undoped and inherently n-type, indicative of a high background carrier concentration and defect density. By contrast, the GaN material used in the present study was Mg-doped; Mg:GaN films grown under the same conditions as these have been found to be p-type, with carrier concentrations of  $10^{18} \text{ cm}^{-3}$  and low mobilities of about  $10 \text{ cm}^2 \text{ V}^{-1} \text{ s}^{-1}$  [32]. According to the Schottky model, Au should form an ohmic contact on p-type GaN and a rectifying contact on n-type material. However, it should be pointed out that the exact value for the work function and/or electron affinity of GaN and their dependence upon doping levels have not been reproducibly and precisely established as yet; Foresi and Moustakas obtained ohmic contacts with Au on undoped n-GaN after annealing at  $575^\circ\text{C}$  for 10 minutes in a reducing atmosphere; according to their TLM measurements they achieved contact resistivities in the range  $1.6\text{-}3.1 \times 10^{-3} \Omega \text{ cm}^2$ . In the present study, the contact resistivities obtained from Au on Mg-doped GaN were higher. Also, the samples in this study were annealed for short periods of time in an RTA furnace under flowing  $\text{N}_2$ . It is possible that more extensive interfacial reaction than seen in this study would occur in a conventional annealing furnace, as used in the other studies, over longer periods of time.

The change in appearance and texture of the Au surface after high-temperature annealing was evidently due to reactions and/or interdiffusion taking place between the Au and GaN. Interfacial reactions with contacts on GaAs typically show a significant amount of interphase formation and roughening of the interface. The roughening of the interface due to reaction and phase formation may help to lower  $\rho_c$  by increasing the area of contact between the metal layer(s) and the semiconductor. The lumpiness of the annealed Au film is indicative of metallurgical reaction and phase formation, and the balling-up effect implies a lack of good "wetting" of the GaN surface. The lack of good wetting of the GaN by Au is also indicated by the poor adhesion of Au to GaN, in both the as-deposited state and the annealed state. The results of X-TEM characterization indicate that under thermal activation N diffused out of the GaN and into the Au layer, thereby freeing the Ga to react and possibly form compounds with the Au. Gallium nitride lacks the very mobile As species of GaAs and has stronger interatomic

bonding, but sufficiently high temperatures and favorable chemistry can nevertheless free the Ga and N from one another. The results of elemental analysis of the amorphous interfacial phase should help determine its composition. Amorphous Au-Ga alloys have been observed before in thin-film deposition, that remain amorphous even up to room temperature [33], which may be forming at the Au/Ga interface upon annealing. On the other hand, the presence of holes and cavities in the annealed Au contact films may have allowed epoxy adhesive, used to prepare the TEM specimens, to seep into the interface in many locations during sample preparation and may be responsible for the amorphous material at the interface. These issues will be resolved in the near future.

*Au/Mg/Au Contacts on Mg:GaN.* The ohmic behavior of the Au/Mg/Au contact system on p-GaN contrasts with the rectifying behavior of as-deposited Au contacts. While pure Au was the first layer deposited on the GaN in the sequence, the layer was relatively thin (320 Å) and Mg followed immediately afterward. Cross-sectional TEM samples of both as-deposited and annealed contacts have been sent to our collaborators at ASU for microstructural characterization. It is important to determine the nature of the metal in contact with the GaN surface and whether the proximity of the Mg changes the structure and/or composition of the thin Au layer so as to result in behavior different from that of a thick solid Au contact.

A study of Au/Zn/Au ohmic contacts on Zn-doped GaAs was reported last year by X.W. Lin *et al.* [34]. In contrast to the more familiar Zn/Au contacts for p-GaAs, little or no interfacial reaction with the GaAs surface was seen with annealing when a thin Au layer was deposited on the GaAs first before following with the Zn dopant layer. Au<sub>3</sub>Zn phases were found to form at room temperature; no layered structure of the Au/Zn/Au contact system was seen in the as-deposited state. This contact system remained planar and stable even after annealing and did not result in roughening or protrusion formation at the GaAs interface. In this light, it will be informative to characterize both the as-deposited and annealed Au/Mg/Au/p-GaN.

The substantial decrease in  $\rho_c$  with increasing measurement temperature is consistent with the thermal ionization of acceptor impurities and consequent increased availability of charge carriers. An Arrhenius-type calculation on the  $\rho_c(T)$  data yielded a carrier activation energy of approximately 0.27 eV; this value is close to an estimated value for the Mg acceptor level in GaN reported by Strite and Morkoç in their review of the III-nitride literature [35]. The increase in overall resistance and  $\rho_c$  observed as a result of annealing above 650°C may be due to the formation of higher-resistivity compounds. These contacts were deposited in a non-UHV evaporation system; the presence of oxygen may be an issue in this case, particularly with respect to the Mg content. Magnesium is well known for its reactive and easily oxidized behavior. Compositional analysis of the cross-sectional samples will help resolve these issues.

*Pt Contacts on Mg:GaN.* As has been observed with Al contacts on n-type GaN, the fact that as-deposited Pt contacts on Mg-doped GaN would prove to be ohmic is consistent with the Schottky-Mott-Bardeen model, based on the relationship of the work functions of the two surfaces. Platinum is a very high work function metal ( $\phi_{\text{Pt}}=5.65$  eV) and thus provides a favorable band offset for ohmic contact formation to a p-type semiconductor. In addition, Pt is thermally very stable and highly resistant to oxidation.

The truly linear ohmic behavior and very low  $\rho_c$  observed in these measurements are very promising and are the lowest contact resistivities for contacts to p-type GaN reported to date. Investigation of Pt as an ohmic contact candidate for p-type GaN was conducted earlier in this study, as described in the semi-annual report for June 1993, but the results were not as promising at that time. Substantial improvements in GaN film quality and electrical properties have been made since then. The newer Mg:GaN described here were grown by MOVPE instead of MBE, as was the case when the earlier study was conducted. However, it should be pointed out that Mg doping procedures in the MOVPE system at NCSU are still undergoing improvement and optimization, and it is necessary to confirm the type and carrier concentrations in the Mg:GaN films being grown currently. In addition, these results should be compared with Pt contacts deposited using another method besides sputtering, in order to determine how much the ion bombardment experienced during deposition contributed to the observed contact behavior. Annealing studies and upcoming cross-sectional examination will also help assess the value of this promising contact material.

#### E. Conclusions

The work conducted in this study so far has shown that it is possible to form metal contacts with ohmic, linear I-V behavior and low specific contact resistivity to both n-type and p-type GaN films. The Al contacts on n-type GaN had very good low-resistivity characteristics and remained stable to at least 500°C. The TiN/n-GaN contact system exhibits better performance characteristics than any other investigated in this study to date, and better characteristics than most contacts yet reported for GaN. The Cu<sub>3</sub>Ge contacts deposited in a UHV environment have offered very encouraging results and will be undergoing more complete investigation in the coming weeks. Recently, very encouraging results have also been observed with p-type ohmic contacts, particularly with the Pt/Mg:GaN and Au/Mg/Au/Mg:GaN samples. The achievement of as-deposited ohmic contacts to p-GaN is a valuable new development of great importance for device fabrication. Further characterization of these contacts, particularly the microstructural information obtained from X-TEM analysis, will yield greater understanding of the chemical and structural contributions to contact behavior and will allow more rapid and knowledgeable development of improved contact schemes and their capabilities.

## F. Future Plans and Goals

In addition to further chemical and structural characterization of the contact systems described in this report, other schemes for improving contact performance will be investigated. One potentially useful approach involves the deposition of high carrier concentration, moderate band gap InN as an interlayer to provide improved band offsets and better carrier transfer across the metal-nitride interface, as proposed by Abernathy *et al.* [31]. Combined with the search for improved contacts to the III-nitrides is the ongoing investigation of Fermi-level pinning and defect states, and the role played by work function and electron affinity differences in contact properties. The evidence examined to date indicates that GaN does indeed experience much less Fermi-level pinning than its more covalently bonded relatives such as GaAs; further work will help to clarify this issue and assist the development of advanced microelectronic and optoelectronic devices.

Another area of study having importance for contact behavior is the issue of surface cleaning and sample preparation. Preliminary investigations of surface cleaning methods by means of XPS analysis have already been performed, and will continue in order to develop a more complete picture of the effects of surface preparation on contact behavior. The role of oxygen and other contaminants at the contact interface is important to understand, and will become even more critical for AlGaN and AlN-based devices due to the strong affinity of Al for oxygen. For such cases the cleanliness of the contact deposition environment will probably be of greater importance as well.

## G. References

1. T. C. Shen, G. B. Gao, H. Morkoç, J. Vac. Sci. Technol. B **10**(5) 2113 (1992).
2. R. Williams, *Modern GaAs Processing Techniques* (Artech House, Norwood, MA, 1990).
3. M. Murakami, Materials Science Reports (5) 273 (1990).
4. A. Piotrowska and E. Kaminska, Thin Solid Films **193/194** 511 (1990).
5. A. Piotrowska, A. Guivarc'h and G. Pelous, Solid-St. Electron. **26**(3) 179 (1983).
6. V. L. Rideout, Solid-St. Electron. **18** 541 (1975).
7. K. Tanahashi, H. J. Takata, A. Otsuki and M. Murakami, J. Appl. Phys. **72**(9) 4183 (1992).
8. H. J. Takata, K. Tanahashi, A. Otsuki, H. Inui and M. Murakami, J. Appl. Phys. **72**(9) 4191 (1992).
9. M. C. Hugon, B. Agius, F. Varniere, M. Froment and F. Pillier, J. Appl. Phys. **72**(8) 3570 (1992).
10. W. O. Barnard, G. Myburg and F. D. Aurret, Appl. Phys. Lett. **61**(16) 1933 (1992).
11. G. Stareev, Appl. Phys. Lett. **62**(22) 2801 (1993).
12. E. D. Marshall and M. Murakami, in *Contacts to Semiconductors*, edited by L. J. Brillson (Noyes, Park Ridge NJ, 1993).
13. F. W. Ragay, M. R. Leys and J. H. Wolter, Appl. Phys. Lett. **63**(9) 1234 (1993).
14. H. K. Henisch, *Semiconductor Contacts*. (Clarendon Press, Oxford, 1984).
15. E. H. Rhoderick, *Metal-Semiconductor Contacts* (Oxford University Press, New York, 1988).
16. S. Kurtin, T. C. McGill and C. A. Mead, Phys. Rev. Lett. **22**(26) 1433 (1969).

17. J. S. Foresi, *Ohmic Contacts and Schottky Barriers on GaN*, M.S. Thesis, Boston University (1992).
18. J. S. Foresi and T. D. Moustakas, *Appl. Phys. Lett.* **62**(22) 2859 (1993).
19. B. L. Crowder and S. Zirinski, *IEEE Trans. Electron Devices* **ED-26**, 369 (1979).
20. S. P. Murarka, *Silicides for VLSI Applications*, Academic Press, New York (1983).
21. L. Krusin-Elbaum, J. Y.-C. Sun, and C.-Y. Ting, *IEEE Trans. Electron Devices* **ED-34**, 58 (1987).
22. J. C. Hensel, R. T. Tung, J. M. Poate, and F. C. Unterwald, *Appl. Phys. Lett.* **44**, 913 (1984); *Phys. Rev. Lett.* **54**, 1840 (1985).
23. P. H. Woerlee, P.M. Th.M. van Attekum, A.A.M. Hoeben, G.A.M. Hurkx, and R.A.M. Wolters, *Appl. Phys. Lett.* **44**, 876 (1984).
24. M. T. Huang, T. L. Martin, V. Malhotra, and J. E. Mahan, *J. Vac. Sci. Technol. B* **3**, 836 (1985).
25. L. Krusin-Elbaum and M.O. Aboelfotoh, *Appl Phys. Lett.* **58**(12) 1341 (1991).
26. M. O. Aboelfotoh, H. M. Tawancy, and L. Krusin-Elbaum, *Appl. Phys. Lett.* **63**(12) 1622.
27. M. O. Aboelfotoh, K. N. Tu, F. Nava, and M. Michelini, *J. Appl. Phys.* **75**(1) (1994).
28. M. O. Aboelfotoh, H. M. Tawancy, *J. Appl. Phys.* **75**(4) (1994).
29. G. K. Reeves and H.B. Harrison, *IEEE Electron Device Lett.* **EDL-3** 111 (1982).
30. M. E. Lin, Z. Ma, F.Y. Huang, Z.F. Fan, L.H. Allen, and H. Morkoç, *Appl. Phys. Lett.* **64**(8) 1003 (1994).
31. C. R. Abernathy, S. J. Pearton, F. Ren, and P. W. Wisk, *J. Vac. Sci. Technol. B* **11**(2) 179 (1993).
32. C. Wang, K. S. Ailey, K. L. More, and R. F. Davis, *Inst. Phys. Conf. Ser. No.* 137, 417 (1994).
33. D. Korn, H. Pfeifle, and G. Zibold, *Z. Physik* **270**, 195 (1974).
34. X.W. Lin, Z. Lilienthal-Weber, and J. Washburn, *J. Vac. Sci. Technol. B* **11**(1) 44 (1993).
35. S. Strite and H. Morkoç, *J. Vac. Sci. Technol. B* **10**(4) 1237 (1992).

## XXV. AlN/SiC Electronic Structures

### A. Introduction

For electronic device engineering, there is interest in materials having negative electron affinities (NEA) for electron emission. NEA surfaces are desired for cold cathode devices, vacuum microelectronics, and photodetectors[1,4]. Thin films of AlN grown on 6H SiC have been shown to exhibit a negative electron affinity (NEA) under bias[15]. The presence of a NEA can be determined by ultraviolet photoemission spectroscopy (UPS) [5-7]. This technique involves directing 21.2 eV light (the He I resonance line) to the surface of the sample and detecting the spectrum of the emitted photo excited electrons as a function of electron kinetic energy. Typically, UPS is used to obtain a profile of the valence band (VB) electronic states. As such, most studies of UPS of semiconductors present data of the most energetic electrons emitted from the surface. Electrons scattered to lower energy and secondary electrons will be displayed in the spectra at lower kinetic energies. In addition, for a semiconductor which exhibits a NEA surface, a distinctive peak may be observed at the low kinetic energy (highest binding energy) end of the photoemission spectra. Fig. 1 depicts a schematic representation of the photoemission spectra from a semiconductor with a negative or positive electron affinity. The low kinetic energy feature is due to secondary electrons which (quasi) thermalize to the conduction band minimum.

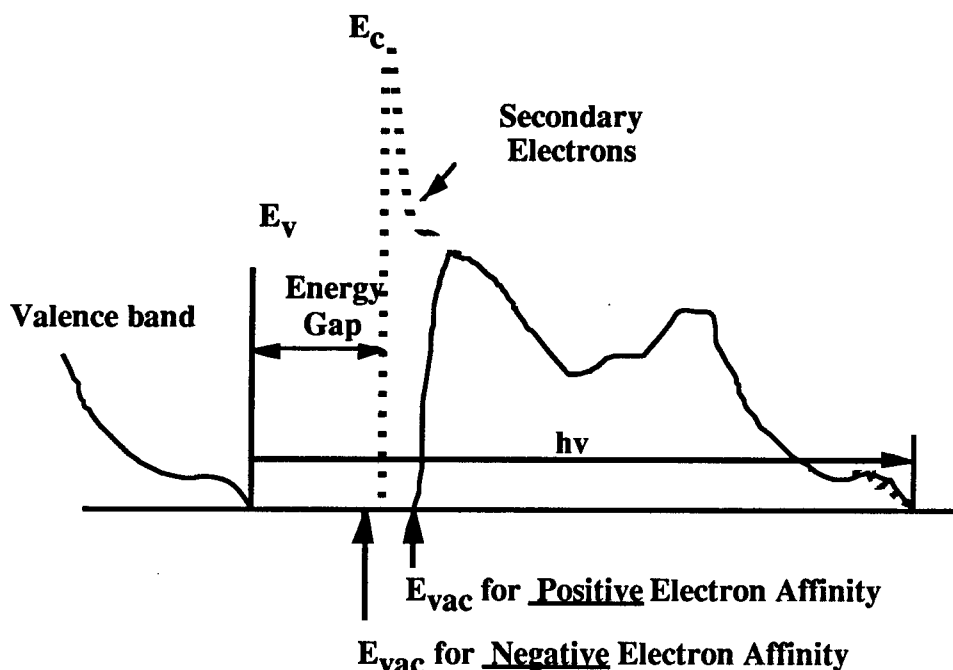


Figure 1. Representative spectra for samples with positive and negative electron affinities.

The sharp features typical of a NEA have been observed from spectra of (111) and (100) diamond surfaces [5-9]. In the studies of diamond, a correlation was made between the presence of hydrogen and the NEA peak [6,7]. In addition, it was also shown that thin metal layers such as Ti or other low workfunction metals could induce a NEA on the diamond surface [9,10]. These measurements verify that the surface dipole can be influenced by surface processing and that the effects contribute to the observation of a NEA.

For the AlN UPS studies presented here, the SiC substrate is important for two reasons. The first is that from wide bandgap semiconductors there would be charging problems, and the photoemission would be quickly quenched. Because it is a wide bandgap semiconductor, the AlN acts as an insulator and will charge up. This problem is avoided by growing a thin layer of AlN on a conducting doped SiC substrate. The n-type SiC substrates used in this study, being more conductive than bulk AlN, provide a source of electrons for photoemission. The second benefit of the SiC substrate is the small lattice mismatch between SiC and AlN (3.08 Å vs. 3.11 Å). The small lattice mismatch enables heteroepitaxial growth.

In this report, we present the first UPS studies of Ge doped AlN samples. These samples have carrier concentrations on the order of  $10^{20}/\text{cm}^3$ . Also we present studies of *in situ* grown AlN surfaces. These samples were never exposed to atmosphere and thus are very clean.

## B. Experimental Procedure

The SiC substrates used in this study were supplied by Cree Research, Inc. The samples were n type with doping concentrations of  $10^{16}$  to  $10^{18}/\text{cm}^3$ .

The samples for the most part have been grown in a remote location and transported in air to the analysis system.

The AlN was deposited on the SiC substrate by a modified gas source MBE system. The substrate was a vicinal wafer of 6H polytype (0001) (oriented 3-4 degrees towards [1120]) SiC which resulted in the growth of hexagonal (2H) AlN. The MBE system consists of three parts: a load lock (base pressure of  $5 \times 10^{-8}$  Torr), a transfer tube (base pressure of  $1 \times 10^{-10}$  Torr), which also was used for degassing the substrates, and the growth chamber (base pressure of  $5 \times 10^{-11}$  Torr). Knudson effusion cells with BN crucibles and Ta wire heaters were charged with 6N pure aluminum. Ultra-high purity nitrogen, further purified by a chemical purifier, was used as the source gas. The nitrogen gas was excited by an ECR plasma source, which was designed to fit inside the 2.25 inch diameter tube of the source flange cryoshroud. The details of the system can be found elsewhere. [2,3,11]

The SiC substrates were obtained from Cree Research Inc. Prior to loading into the chamber, the substrates were cleaned by a standard degreasing and RCA cleaning procedure. After undergoing a degassing procedure in UHV (700 °C for 30 minutes), the substrates were

transferred into the deposition chamber. Epitaxial AlN films were deposited under the conditions shown below in Table I. The films examined were roughly 100 Å thick.

---

Table I. Deposition Conditions for MBE AlN Film Growth.

---

Nitrogen pressure:	$2 \times 10^{-4}$ Torr
Microwave power:	50W
Aluminum cell temp:	1120 °C
Substrate temperature:	1100 °C
Deposition Rate:	1000 Å/hr

---

The samples were transported in air to the surface analysis system. The analysis system is made up of several chambers linked by a linear UHV transfer line. The details of the system are described elsewhere [8,10]. Among the capabilities available are UPS, XPS, LEED, hydrogen and argon plasma cleaning, and Auger electron spectroscopy. Recently added is the capability of Gas source MBE (GSMBE) to grow undoped AlN films.

The presence of a NEA can be determined by ultraviolet photoemission spectroscopy (UPS) as mentioned earlier. Light of energy 21.2 eV (the He I resonance line) is directed to the surface of the sample. Emitted electrons are collected at a hemispherical energy analyzer to give a profile of electron kinetic energy.

The UPS chamber has a base pressure of  $2 \times 10^{-10}$  Torr. Operating conditions involve pressures up to  $1 \times 10^{-9}$  Torr, but the higher pressure is due to the helium inflow and does not contaminate the sample. The UPS system utilizes a helium resonance lamp (the He I line) to provide a source of 21.2 eV light. Photoemitted electrons are measured with a 50 mm mean radius hemispherical electron analyzer operated at a 0.15 eV energy resolution and a 2° angular resolution. The analyzer (VSW HA50) is mounted on a double goniometer and can be tilted with respect to the sample in two independent directions. The AlN/SiC samples were fastened with tantalum wire to a molybdenum sample holder. The sample holder is biased by up to 4 V to allow low energy electrons to overcome the workfunction of the analyzer. The Fermi level of the system (sample and analyzer) is determined by UPS measurement of the sample holder with no sample bias (i.e., grounded). The sample holder can be heated to 1150 °C.

For the studies presented, the SiC substrate is important for several reasons. The first is that with wide bandgap semiconductors charging would occur, and the photoemission would be quickly quenched. This problem is avoided by growing a thin layer of AlN on a conducting doped SiC substrate. The n-type SiC substrates used in this study, being more conductive than



bulk AlN, provide a source of electrons for photoemission. The second benefit of the SiC substrate is the small lattice mismatch between SiC and AlN (3.08 Å versus 3.11 Å). The small lattice mismatch enables heteroepitaxial growth.

### C. Results

The UPS measurements were carried out on the initial AlN/SiC sample as loaded, and after anneals of 700 °C and 1000 °C. Auger Electron Spectroscopy (AES) and Low Energy Electron Diffraction (LEED) were also performed on the sample as-loaded, and after the anneals. The UPS data for the as-loaded AlN/SiC sample are displayed in Fig. 2. The spectra were obtained with different sample bias to overcome the workfunction of the analyzer. In the figure, all spectra have been displaced by the applied bias so that the Fermi level aligns. Two aspects indicate the presence of the NEA. The first is the detection of a low energy peak clearly observable with a sample bias of 3.0 Volts, with onset occurring at a bias of 1.5 Volts. The two low energy peaks of roughly the same height present at the 3.0 Volt bias are attributed to the normal secondary emission typical of UPS while the low energy feature is attributed to electrons thermalized to the conduction band minimum. This second peak is considered as the NEA peak since the electron count drops off so quickly. The large (~3V) bias is needed because the workfunction of the AlN is apparently less than that of the analyzer. The analyzer workfunction is between 4 and 5 eV.

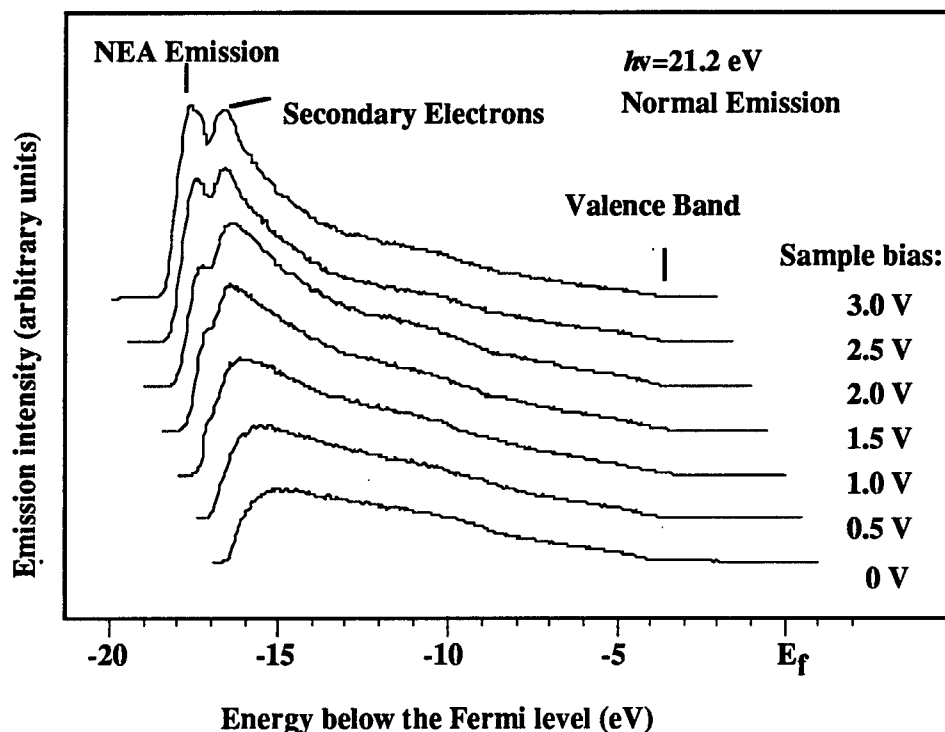


Figure 2. The uv-photoemission from AlN on 6H-SiC. The spectra were obtained at different sample bias to overcome the workfunction of the electron analyzer.

The second indication of the NEA is that the widths of the photoemission spectra are consistent with the model described in Fig. 1. Here the width  $W = h\nu - E_g$  where  $W$  extends from the low energy limit to the valence band maximum. We have used this relation to determine the position of the valence band maximum in the spectrum obtained with a 3V bias. The low energy limit was determined by linear extrapolation of the back edge to zero intensity. Then using the band gap of AlN as 6.2 eV and the 21.2 eV photon energy, the valence band maximum should then occur at 15.0 eV above this limit. The vertical line labeled Valence Band was obtained in this way. As is evident from the spectra, the valence band emission extends to this energy. We also note that the results indirectly verify that the band gap of the AlN film is the same as the bulk value of 6.2 eV. As mentioned earlier, the Fermi level is determined from the onset of electron emission from a metal sample.

The effect of annealing in vacuum was explored. After annealing to 700 and 1000 °C the photoemission spectra showed a decrease in the relative intensity of the NEA related peak (Fig. 3). Auger Electron Spectroscopy (AES) of the as-loaded surface showed oxygen and carbon contaminants in addition to the Al and N signals. After an anneal of 700 °C the AES showed a small reduction of the oxygen and a similar scale increase in the surface carbon, a trend that continued with the 1000 °C anneal. A LEED pattern was not visible from the sample as loaded or after the anneals of 700 °C and 1000 °C. We note that after a short H-plasma clean a faint 1×1 pattern was visible with an electron beam energy of 80 eV and the C signal was removed. The lack of a LEED pattern for the as-loaded and the annealed samples is possibly related to the carbon and oxygen on the surface. The reduction of the NEA related features indicates that the effect is related to the surface structure and termination of the AlN.

Another sample investigated was capped with a thin ( $<10\text{\AA}$ ) layer of silicon to prevent oxidation during transit. While the processing parameters were similar [14], the photoemission spectra were different as can be seen in Fig. 4. A peak sharper than that of the NEA surface in Fig. 2 appeared with a bias of 3.0 Volts, but the width of the spectra was not consistent with the known band gap. We attribute this to the presence of the silicon. Even after two plasma exposures, one of which was a deep etching exposure, we were unable to remove all of the silicon. A band alignment model is presented in Fig. 5.

In comparison to the UPS spectra obtained from diamond surfaces which exhibit a NEA, [5-8] the feature in diamond is significantly sharper than that observed here for the AlN. There are several possible causes that could contribute to a broader signature. These could be related to a more disordered surface or to the intrinsic properties of the AlN (e.g., direct bandgap). Future research will explore these issues.

In Fig. 6, the doped samples show features indicative of an NEA surface without application of a bias. The surface appears to be p type. The *in situ* grown sample appears in Fig. 7. We see sharp and strong emission with a 4 volt bias applied.

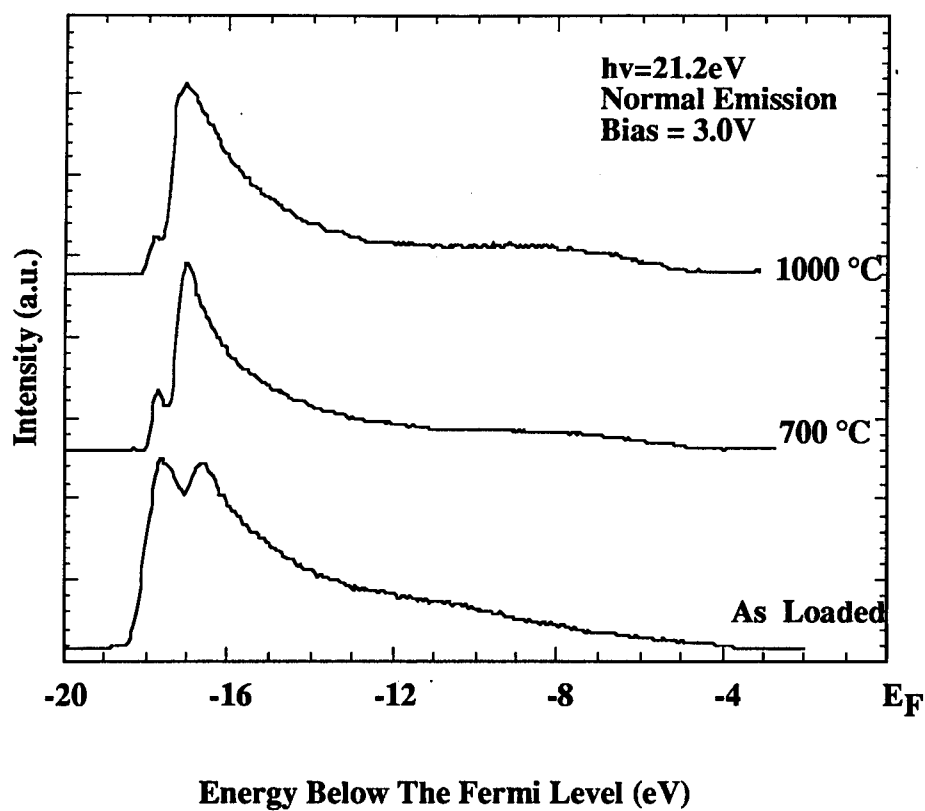


Figure 3. The uv-photoemission spectra of the AlN on 6H-SiC as-loaded and after vacuum annealing at the indicated temperatures. All spectra were obtained with a sample bias of 3.0 V.

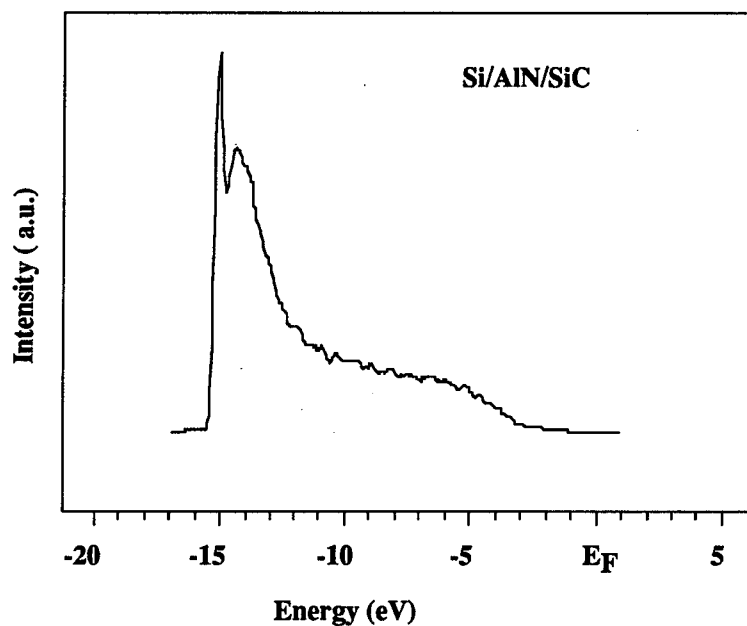


Figure 4. UV-photoemission spectra of Si capped AlN on 6H-SiC sample studied. This spectrum was obtained with a sample bias of 3.0 V

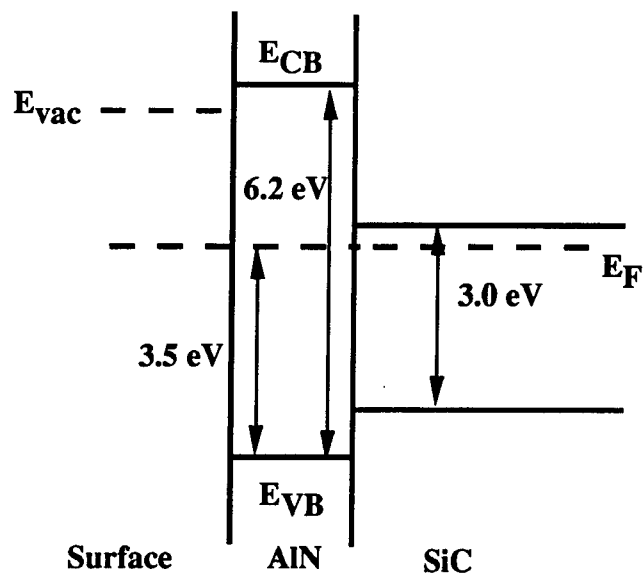


Figure 5. Possible band alignment model.

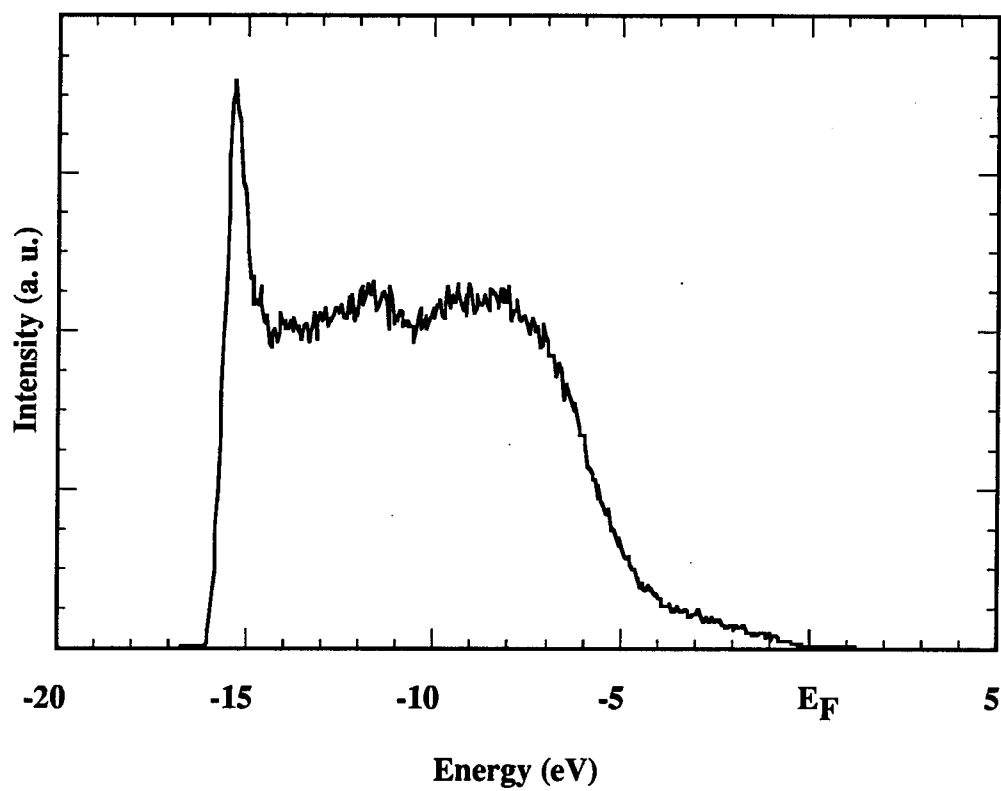


Figure 6. Ge doped sample. Note no bias is applied.

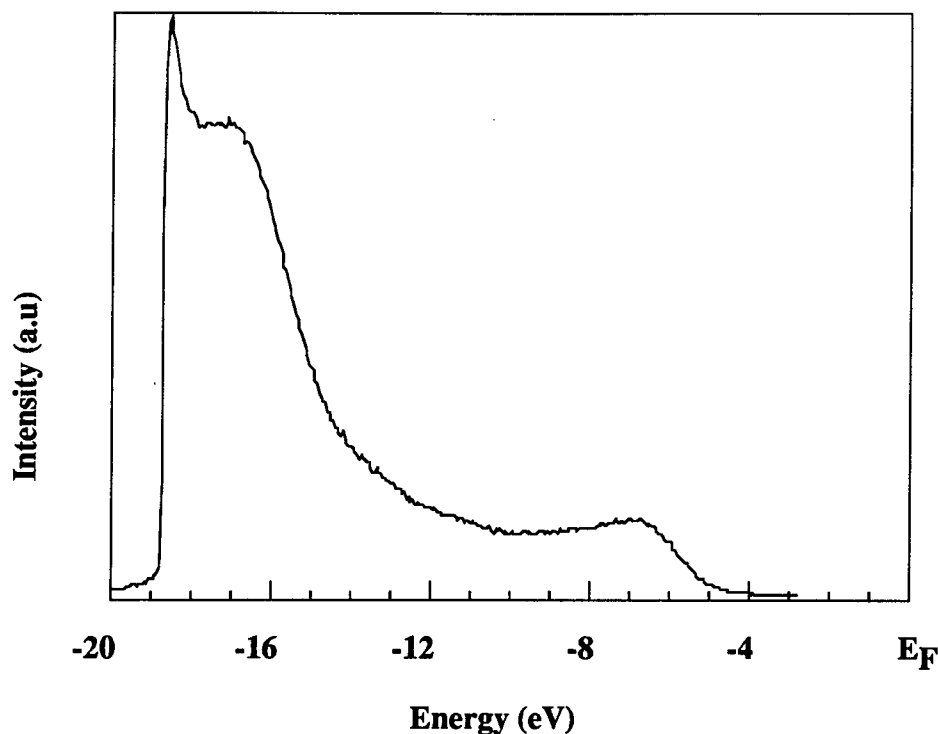


Figure 7. *In situ* grown sample.

#### D. Conclusions

In summary, we have observed features in the UPS spectra indicative of a NEA surface on as-loaded and annealed AlN on SiC. The measurements were made possible by the structures of thin AlN layers on SiC.

The UPS measurements were carried out on the AlN/SiC sample as loaded, and after anneals of 700 °C and 1000 °C. Auger Electron Spectroscopy (AES) and Low Energy Electron Diffraction (LEED) were also performed on the sample as-loaded, and after the anneals. The UPS data for the as-loaded AlN/SiC sample are displayed in Fig. 2. The spectra were obtained with different sample bias to overcome the workfunction of the analyzer. In the figure, all spectra have been displaced by the applied bias so that the Fermi level aligns. Two aspects indicate the presence of the NEA. The first is the detection of a low energy peak clearly observable with a sample bias of 3.0 Volts, with onset occurring at a bias of 1.5 Volts. The two low energy peaks of roughly the same height present at the 3.0 Volt bias are attributed to the normal secondary emission typical of UPS while the low energy feature is attributed to electrons thermalized to the conduction band minimum. This second peak is considered as the NEA peak since the electron count drops off so quickly. The large (~3V) bias is needed because the workfunction of the AlN is apparently less than that of the analyzer. The analyzer workfunction is between 4 and 5 eV.

The second indication of the NEA is that the widths of the photoemission spectra are consistent with the model described in Fig. 1. Here the width  $W = h\nu - E_g$  where  $W$  extends from the low energy limit to the valence band maximum. We have used this relation to determine the position of the valence band maximum in the spectrum obtained with a 3V bias. The low energy limit was determined by linear extrapolation of the back edge to zero intensity. Then using the band gap of AlN as 6.2 eV and the 21.2 eV photon energy, the valence band maximum should then occur at 15.0 eV above this limit. The vertical line labeled Valence Band was obtained in this way. As is evident from the spectra, the valence band emission extends to this energy. We also note that the results indirectly verify that the band gap of the AlN film is the same as the bulk value of 6.2 eV. As mentioned earlier, the Fermi level is determined from the onset of electron emission from a metal sample.

The effect of annealing in vacuum was explored. After annealing to 700 and 1000 °C the photoemission spectra showed a decrease in the relative intensity of the NEA related peak (Fig. 3). Auger Electron Spectroscopy (AES) of the as-loaded surface showed oxygen and carbon contaminants in addition to the Al and N signals. After an anneal of 700 °C the AES showed a small reduction of the oxygen and a similar scale increase in the surface carbon, a trend that continued with the 1000 °C anneal. A LEED pattern was not visible from the sample as loaded or after the anneals of 700 °C and 1000 °C. We note that after a short H-plasma clean a faint 1×1 pattern was visible with an electron beam energy of 80 eV and the C signal was removed. The lack of a LEED pattern for the as-loaded and the annealed samples is possibly related to the carbon and oxygen on the surface. The reduction of the NEA related features indicates that the effect is related to the surface structure and termination of the AlN.

The second sample investigated was capped with a thin (<10Å) layer of silicon to prevent oxidation during transit. While the processing parameters were similar [14], the photoemission spectra were different as can be seen in Fig. 4. A peak sharper than that of the NEA surface in Fig. 2 appeared with a bias of 3.0 Volts, but the width of the spectra was not consistent with the known band gap. We attribute this to the presence of the silicon. Even after two plasma exposures, one of which was a deep etching exposure, we were unable to remove all of the silicon.

In comparison to the UPS spectra obtained from diamond surfaces which exhibit a NEA, [5-8] the feature in diamond is significantly sharper than that observed here for the AlN. There are several possible causes that could contribute to a broader signature. These could be related to a more disordered surface or to the intrinsic properties of the AlN (e.g., direct bandgap). Future research will explore these issues.

We also address the position of the Fermi level in the AlN. From Fig. 2, it is evident that the surface Fermi level occurs at ~3.5 eV above the valence band maximum. This is near the center of the 6.2 eV bandgap. From this data we suggest a possible band alignment of AlN and

SiC. Here we have assumed that there is no band bending in the AlN or in the SiC near the interface. Because of the wide band gap of the AlN, it seems unlikely that there is significant band bending in the thin film. The bulk Fermi level of the SiC has been determined from the doping level of the substrates to be  $\sim 0.3$  eV below the SiC conduction band edge [12]. The results are summarized in Fig. 5. The band offsets are -0.8 eV at the valence band and 2.4 eV at the conduction band. The largest uncertainty in this proposed band offset is probably in the band bending in the SiC. Such band bending would result in an increase in the magnitude of the valence band offset and a decrease in the conduction band offset. While we are not aware of any calculations of the heterojunction band offsets of wurtzite AlN on 6H-SiC, there has been a calculation of the offsets of the (110) interfaces of cubic AlN/SiC [13]. The theoretical results also indicate a type I offset with band discontinuities of 1.5 eV at the valence band and -1.2 eV at the conduction band. This is qualitatively similar to the results presented in Fig. 5.

Doped films show emission without bias. This is promising as devices will have to be doped to make full use of the NEA property.

Study of *in situ* grown samples allow insight into the effect that atmosphere-borne contaminants have on the observed NEA. To date, the only effect seems to be attenuation of emission intensity.

#### E. Future Plans

The preparation of the AlN films will be studied to determine the effect on the observed NEA. The aim will be to understand what parameter in the process dominates. Plasma cleaning will be incorporated. Doped films will be further investigated as we move towards actual devices.

#### Acknowledgment

This work was supported in part by the Office of Naval Research through grants N0014-92-J-1477 and N0014-92-J-1604. The SiC substrates used were supplied by Cree Research.

#### F. References

1. J.H. Edgar, J. Mater. Res., **7**, 235 (1992)
2. H.S. Kong, J.W. Palmour, J.T. Glass, and R.F. Davis, Appl. Phys. Lett. **51**, 442 (1987)
3. C. Wang, R.F. Davis, Appl. Phys. Lett. **63**, 990 (1993).
4. M.D. Williams, M.D. Feuer, S.C. Shunk, N.J. Sauer, and T.Y. Chang, J. Appl. Phys. **71**, 3042 (1992).
5. F.J. Himpsel, J.A. Knapp, J.A. van Vechten and D.E. Eastman, Phys. Rev. B **20**, 624 (1979).
6. B.B. Pate, Surf. Sci. **165**, 83 (1986).
7. B.B. Pate, M.H. Hecht, C. Binns, I. Lindau and W.E. Spicer, J. Vac. Sci. Technol. **21**, 364 (1982).
8. J. van der Weide and R.J. Nemanich, J. Vac. Sci. Technol. B **10**, 1940 (1992).
9. J. van der Weide and R.J. Nemanich, Appl. Phys. Lett. **62**, 1878 (1993).

10. J. van der Weide and R.J. Nemanich, Phys. Rev. B15 **49** 13629 (1994).
11. Z. Sitar, M.J. Paisley, D.K. Smith and R.F. Davis, Rev. Sci. Instrum.. **61**, 2407 (1990).
12. J. Pelletier, D. Gervais, and C. Pomot, J. Appl. Phys. **55**, 994 (1983)
13. Walter R.L. Lambrecht and Benjamin Segall, Phys. Rev. **B43**, 7070 (1991).
14. L.B. Rowland, R.S. Kern, S. Tanaka, and R.F. Davis, in *Proceedings of the Fourth International Conference on Amorphous and Crystalline Silicon Carbide*, edited by C.Y. Yang, M.M. Rahman, and G.L. Harris (Springer, Berlin, 1992) p. 84.
15. M.C. Benjamin, C. Wang, R.F. Davis, R.J. Nemanich Appl. Phys. Lett. **64**, (1994)



## XXVI. Distribution List

Mr. Max Yoder Office of Naval Research Electronics Division, Code: 314 Ballston Tower One 800 N. Quincy Street Arlington, VA 22217-5660	3
Administrative Contracting Officer Office of Naval Research Regional Office Atlanta 101 Marietta Tower, Suite 2805 101 Marietta Street Atlanta, GA 30332-0490	1
Director, Naval Research Laboratory ATTN: Code 2627 Washington, DC 20375	1
Defense Technical Information Center Bldg. 5, Cameron Station Alexandria, VA 22314	2